Functional characterization of the MICOS protein MIC13 defining its role for mitochondrial ultrastructure

Inaugural-Dissertation

zur Erlangung des Doktorgrades
der Mathematisch-Naturwissenschaftlichen Fakultät
der Heinrich-Heine-Universität Düsseldorf

vorgelegt von

Jennifer Urbach
aus Remscheid

Düsseldorf, November 2020

aus dem Institut für Biochemie und Molekularbiologie I

der Heinrich-Heine-Universität Düsseldorf

Gedruckt mit der Genehmigung der
Mathematisch-Naturwissenschaftlichen Fakultät der

Heinrich-Heine-Universität Düsseldorf

Berichterstatter:

1. Prof. Dr. Andreas Reichert

2. Prof. Dr. Lutz Schmitt

Tag der mündlichen Prüfung: 10.02.2021

For Frodo!

Table of Contents

1. Introduction

1.1. Origin and Functions of Mitochondria

Mitochondria are vital cell organelles, that are present in almost all eukaryotic cell types [1]. These cell organelles were first described in 1894 by Richard Altman and in 1898 the term “mitochondrion” was introduced by Carl Benda [2]. Endosymbiosis is widely accepted to be the origin of mitochondria in eukaryotic cells [3]. Mitochondria are suggested to originate from α-proteobacteria, which were introduced into eukaryotic cells by endosymbiosis about 2 billion years ago [4, 5]. This origin was found by analyzing the mitochondrial specific genome, the mitochondrial DNA (mtDNA), that was kept during evolution from their bacterial origin [4]. The mtDNA has the same fundamental role in all eukaryotes by encoding proteins and RNA important for the mitochondrial function [6]. This circular, extrachromosomal genome with a size of about 16 kb encodes a total of 37 genes in humans [7]. Most importantly it encodes for 13 subunits of the electron transport chain and F_1F_0-ATP synthase, as well as the ribosomal RNA (rRNA) and transfer RNA (tRNA) [8]. In other organisms, the number of proteins and the size of mtDNA can vary from about only 6 kb, coding only for three protein genes in *Plasmodium falciparum* [9] to over 200 kb to about 11.000 kb, the largest known mitochondrial genome in land plants [10]. The 69 kb mtDNA of *Reclinomonas Americana*, a eukaryotic microbe, contains more genes than any other characterized mitochondrial genome and also exhibits bacterial characteristics, underlining the endosymbiotic origin of this DNA [11]. The endosymbiotic origin is not only supported by the mtDNA, but also by proteins encoded by the nuclear DNA, like the mitochondrial protein MIC60, part of the MICOS, which will be described later in this work. MIC60 orthologues were found in α-proteobacteria with the same membrane deforming activity as in higher mammals [12]. Studies on the yeast mitochondrial proteome showed, that 50% – 60% of the mitochondrial proteins are prokaryote specific with a counterpart in prokaryotic genomes [13, 14]. With this conserved, but also highly variable proteome of mitochondria, these organelles fulfil several important functions in eukaryotic cells.

Mitochondria are mostly known for their ability to provide energy by generating ATP, which contributes to cell survival. As stated above, the mtDNA encodes for proteins of the electron transport chain and F_1F_0-ATP synthase to perform oxidative phosphorylation (OXPHOS). These proteins are located in mitochondria and together with the tricarboxylic acid cycle (TCA-cycle) they provide the main source of ATP for the cell [15]. Energy conversion is known as the most important function of mitochondria in the cell, but by far not the only one. Mitochondria in interaction with the endoplasmatic reticulum play a crucial role in the regulation of calcium homeostasis [16-18]. They are capable of accumulation and release of Ca^{2+} through a Ca^{2+} uniporter (MCU) and a Na^+ / Ca^{2+} antiporter. Calcium homeostasis is linked to many biological functions and can play a part in apoptosis [19]. With the release of caspase-activating proteins

from mitochondria, they also play an essential role in the apoptotic pathway [20]. Several other functions are known for mitochondria, for example, the involvement in heme biosynthesis and synthesis of Fe/S clusters, as well as the β-oxidation of fatty acids [21]. During oxidative phosphorylation, reactive oxygen species (ROS) can be generated as a side product. ROS is known to contribute to aging and disease, but can also act as a signaling molecule in the cell to support vital cellular functions [22, 23]. In the following two chapters the role of mitochondria in respiration and apoptosis will be explained further.

1.1.1. Mitochondrial Role in Apoptosis

Apoptosis as part of the programmed cell death is a mechanism that protects the organism from damaged or mutated cells, that can disturb normal cellular homeostasis [24, 25]. Defects in apoptosis are linked to several pathological conditions such as autoimmune and neurodegenerative diseases and cancer [26-28]. Apoptosis can be mediated by two pathways, the intrinsic and extrinsic pathway, both resulting in the activation of caspases, a class of proteases, and ultimately in cell degradation (Figure 1) [29].

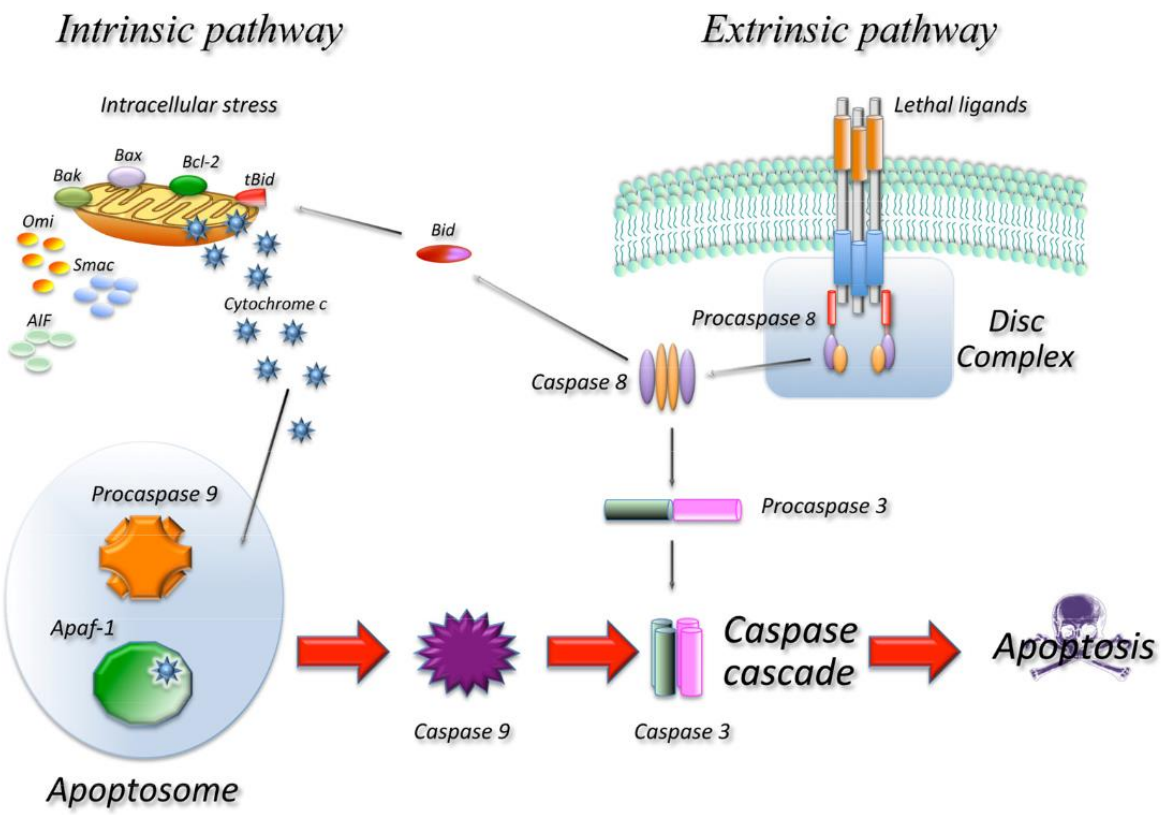

Figure 1. Schematic representation of the intrinsic and extrinsic pathway of apoptosis. The extrinsic pathway activates caspase 8, after activation through ligand binding to the DISC complex. Caspase 8 can activate the caspase cascade to lead to apoptosis. The intrinsic pathway can be activated by intracellular stress, which leads to mitochondrial outer membrane permeabilization and release of proapoptotic proteins such as cytochrome *c*, apoptosis-inducing factor (AIF), and

DIABLO/SMAC. By binding to APAF-1, cytochrome *c* induces the formation of the apoptosome that activates caspase 9, which can activate downstream caspases and lead to apoptosis (image taken from Favaloro et al. [29]).

The intrinsic pathway of apoptosis is closely linked to mitochondria. This pathway can be activated by a variety of factors, inducing irreversible damage to the cell, such as oxidative stress, resulting in DNA damage. Upon induction of apoptosis, two molecular mechanisms can mediate mitochondrial outer membrane permeabilization (MOMP). One mechanism involves the permeability transition pore complex (PTPC), that requires the Adenine Nucleotide Transporter (ANT) and the Voltage Dependent Anion Channel (VDAC) [26, 30]. The other one involves Bcl-2 family proteins at the outer membrane to generate a pore [31]. The key apoptotic proteins in the latter are BAK and BAX [32, 33]. Upon apoptosis induction, BAX accumulates at the mitochondria in large oligomers and inserts into the outer mitochondrial membrane [34-36]. A recent study shows with stimulated emission depletion (STED) microscopy, that BAX clusters appear attached to the outer mitochondrial membrane, but not embedded. In addition to these clusters, also ring-like structures were observed, which remodeled the outer membrane and lead to cytochrome *c* release but are not sufficient for it [37]. Both mechanisms lead ultimately to permeabilization of the outer membrane and allow the release of apoptotic proteins, like cytochrome *c*, apoptosis inducing factor (AIF), endonuclease G (endo G), direct IAP-binding protein with low PI (DIABLO/SMAC), and others into the cytosol [29]. It was shown recently, that also mtDNA is released from apoptotic mitochondria through BAX/BAK foci and the results of inner mitochondrial membrane remodeling [38]. Mitochondrial morphology is changed during apoptosis, with not only the permeabilization of the outer membrane but also hyperfused cristae and widening of the crista junctions, mediating the release of cytochrome *c* from the cristae lumen to the intermembrane space and through BAX/BAK foci into the cytosol [39]. Details on the mitochondrial ultrastructure and remodeling of it will be explained in a later chapter. The release of cytochrome *c* leads to the formation of the apoptosome by binding of cytochrome *c* to APAF-1 and to the activation of caspase 9, which then activates more caspase 9 and the caspase cascade to ultimately lead to degradation of the cell [29].

1.1.2. Mitochondrial Role in Respiration

Being known as the “powerhouse” of the cell, mitochondria are the main site of cellular respiration. Cellular respiration is the process of converting energy from reducing equivalents like nicotinamide adenine dinucleotide (NADH) and flavin adenine dinucleotide ($FADH_2$) into a usable form for the cell, adenosine triphosphate (ATP). Mitochondria hold the major enzymatic system to store energy in form of ATP by oxidation of sugars, fats, and proteins [40]. These different substrates can enter the mitochondrial energy metabolism after being catabolized to

acetyl-CoA through the TCA-cycle, which is located at the mitochondrial matrix [41, 42]. The TCA-cycle converts the energy from acetyl-CoA to the cofactors NADH and $FADH_2$, which carry the energy to the mitochondrial electron transport chain, also known as the respiratory chain (Figure 2) [43].

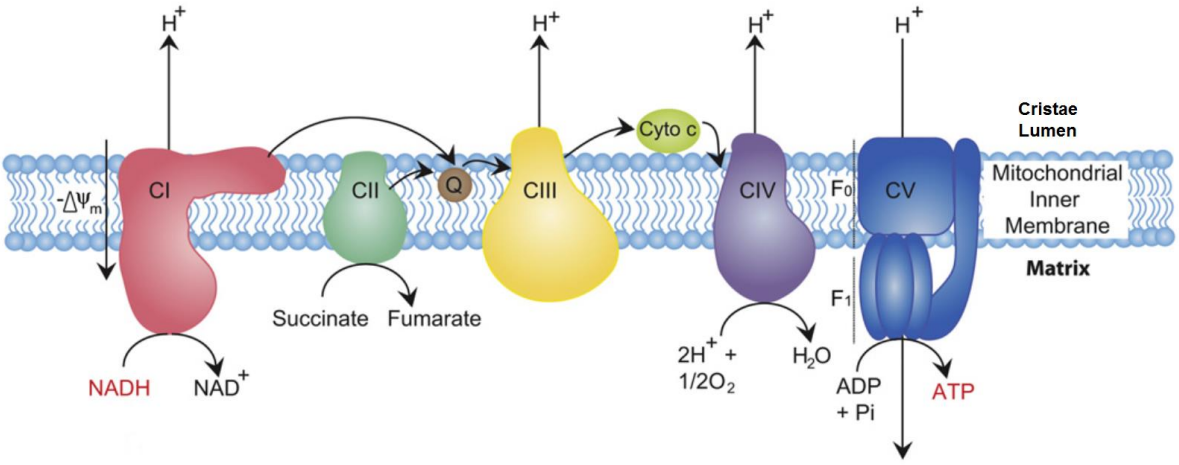

Figure 2. Bioenergetics of the electron transport chain. NADH provided by TCA-cycle is converted to NAD^+ to drive oxidative phosphorylation. Electron transport through the respiratory chain complexes leads to proton pumping into the cristae lumen. The proton gradient is used in a final step to phosphorylate ADP through the F_1F_0-ATP synthase (complex V) and generate ATP (image modified from Osellame et al. [43]).

The respiratory chain, consisting of different protein complexes, transports the electrons from NADH and $FADH_2$ to generate a proton gradient across the inner mitochondrial membrane. The proton gradient is used in the last step to generate ATP through the phosphorylation of adenosine diphosphate (ADP) by the F_1F_0-ATP synthase (complex V). The NADH binds to the NADH dehydrogenase (complex I) of the respiratory chain as one possible entry point for electrons. The binding of NADH leads to the donation of two electrons, which enter via a flavin mononucleotide prosthetic group and are transported through the protein via a series of Fe/S-clusters onto the redox carrier coenzyme Q. $FADH_2$ enters the respiratory chain at the second entry point, the succinate dehydrogenase (complex II). The succinate dehydrogenase is also part of the TCA-cycle and directly contains a bound flavin adenine dinucleotide (FAD) as a cofactor and catalyzes its reduction to $FADH_2$ by the oxidation of succinate to fumarate. Again Fe/S-clusters help to transport the electrons to coenzyme Q. In this case, no protons are pumped through the membrane. Coenzyme Q, which can be reduced by both complexes, diffuses through the inner mitochondrial membrane and donates the electrons to the cytochrome *c* reductase (complex III). Coenzyme Q is oxidized and cytochrome *c* reduced at this protein complex, passing the electrons from one coenzyme Q on two molecules cytochrome *c* acting in a two-step mechanism. This again results in a proton transfer across the membrane. The final protein of the electron transport chain is the cytochrome *c* oxidase

(complex IV). At this protein complex, four molecules of cytochrome *c* donate their electrons to produce two H_2O molecules from one O_2 molecule. The reduction of oxygen consumes matrix protons and therefore contributes to the proton gradient. The final step of oxidative phosphorylation is the phosphorylation of ADP to produce ATP by the F_1F_0-ATP synthase (complex V) with help of the proton gradient [43]. These respiratory complexes form large supermolecular assemblies, called respiratory supercomplexes or 'respirasomes' to optimize electron transport during respiration [44, 45]. These 'respirasomes' are mainly located at the cristae membrane, making the cristae the main site of oxidative phosphorylation [46]. This shows the strong connection between mitochondrial function and mitochondrial ultrastructure, which is explained in a later chapter.

1.1.3. Role of Mitochondria in Disease

For a long time, mitochondrial diseases were described as a disease caused by a mutation in the mtDNA, therefore only diseases caused by a clinical defect of the respiratory chain were described as mitochondrial diseases [47]. If a mitochondrial disease is suggested in a patient and no clear biochemical and clinical evidence point to a nuclear origin, usually the mtDNA is analyzed [48]. This analysis covers only the diseases caused by a defect in the respiratory chain. Defects in the respiratory chain can affect a wide range of systems with different effect from minor health issues to diseases which are progressive and have a severe, if not fatal outcome. For example, the cytochrome *c* oxidase deficiency, which display symptoms like profound hypotonia and lactic acidosis [49]. However, in most cases, these diseases manifest in the brain or skeletal muscles due to the high energy demand of these tissue types [50]. Changes in mitochondrial DNA can also lead to a reduction in fatty-acid oxidation and therefore inhibit glucose transport and play a role in diabetes [51]. Another mitochondrial disease is MELAS syndrome (mitochondrial encephalomyopathy, lactic acidosis, and stroke-like episodes), in which symptoms are stroke-like episodes and infarctions in the brain [52]. Therapies for mitochondrial diseases are limited and mostly targeted at the symptoms. Stem cell therapy can be used to target the cause of the disease [53]. To reduce the risk of mtDNA-related diseases reproductive technologies were developed to uncouple the inheritance of mtDNA from nuclear DNA. This allows affected women to have a healthy genetically related child [54].

1.2. Mitochondrial Ultrastructure

Mitochondria display a distinct ultrastructure, which is closely linked to its function. As already mentioned mitochondria have a double membrane with an inner membrane (IM) and an outer membrane (OM) with a small space in between, the intermembrane space (IMS) [55, 56]. A characteristic feature of the IM are invaginations into tubular or lamellar structures called

cristae, that increase the surface of the membrane, providing more space for processes such as oxidative phosphorylation. The shape and appearance of cristae are highly dependent on tissue type and physiological and developmental stages. It can vary from tubular structures to lamellar appearance and even triangle-shaped cristae were observed in astrocytes [57]. After the first visualization of mitochondria, with help of electron microscopy, three models were proposed for the morphology of cristae (Figure 3).

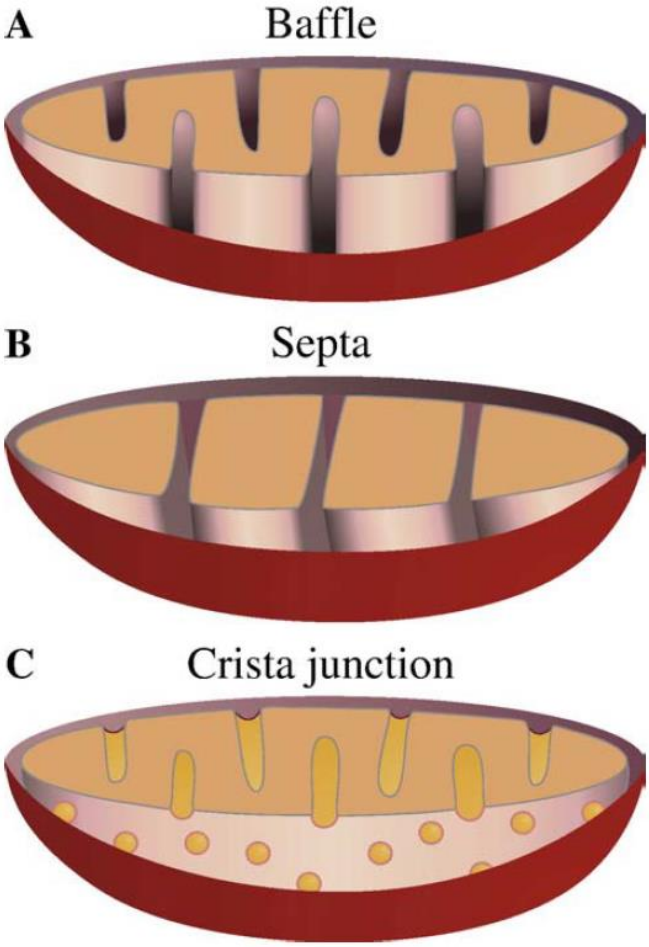

Figure 3. Models of mitochondrial inner membrane invaginations. (A) 'Baffle model' with broad openings of the cristae into the intermembrane space and a baffle-like structure. (B) 'Septa model' dividing the mitochondria into several distinct compartments with cristae as septa spanning through the matrix. (C) 'Crista junction model' suggesting the connection of cristae to the inner membrane by small tubular structures with a small diameter, termed crista junctions (CJs). This model is currently widely accepted (image taken from Zick et al. [57]).

The baffle model, developed by Palade in the 1950s shows the cristae invaginations with broad openings to the IMS in a regularly spaced manner [55, 58]. The 'septa model' proposed by Sjöstrand depicted the cristae as septa to increase the inner membrane surface and therefore divide the mitochondria into distinct compartments [56]. Later upon analysis of very thin serial sections of mitochondria by transmission electron microscopy, small tubular structures were

observed at the invaginations of cristae [59]. These structures were confirmed to be narrow tubular openings in the IM and were termed crista junctions (CJs) [60-63]. The 'crista junction model' is now widely accepted in the field and proposes a subcompartmentalization of the IM into the inner boundary membrane (IBM), which lies opposite to the OM and the cristae membrane (CM) enclosing the cristae lumen and being divided from the IBM by the CJs (Figure 4) [46, 64]. Mitochondrial OM and IBM lie closely together and help proteins to be transported into the matrix through both membranes at once. There is also proof of contact sites between OM and IBM, providing a functional region for different mitochondrial needs like protein transport, metabolite transport, or correct fusion and fission of mitochondria [65].

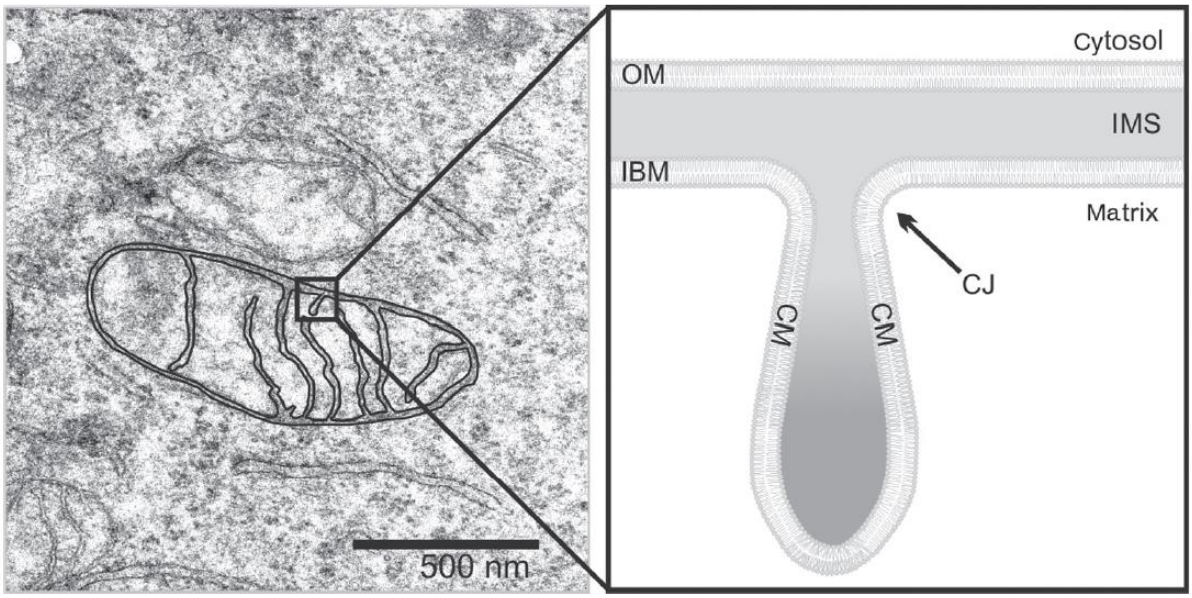

Figure 4. Subcompartments of mitochondria. Left: Electron microscopy picture of mitochondria with an overlay of mitochondrial membranes. Right: Schematic view of mitochondrial membranes and subcompartments. The outer membrane (OM) and inner boundary membrane (IBM) enclosing the intermembrane space (IMS). IBM and the cristae membrane (CM) together as the inner membrane enclosing the mitochondrial matrix. Crista Junction (CJ) divides IBM from the CM (image taken from Koob and Reichert [66]).

1.2.1 Function of Crista Junctions

CJs are small, ring-like structures with a diameter of 12 to 40 nm and are uniform in size and shape suggesting a distinct role in mitochondrial function [62, 67, 68]. These small pore-like structures are supposed to act as a diffusion barrier for membrane and soluble proteins [61, 63]. By acting as a diffusion barrier, CJs can limit or prevent diffusion of membrane proteins from CM to IBM and vice versa, but also limit the diffusion of soluble molecules and proteins like cytochrome *c* or ADP to assure optimal mitochondrial function. This is supported by the fact, that there is an uneven distribution of mitochondrial inner membrane proteins, with proteins of the mitochondrial protein import machinery mainly located at the IMS and proteins involved in OXPHOS and Fe/S cluster biogenesis enriched at the CM [64]. This localization is

not completely strict and also redistribution of Tim23p, a protein involved in mitochondrial protein import, was observed depending on the physiological state [46]. Therefore CJs do not act as a strict diffusion barrier, but still allow a dynamic reorganization between the different subcompartments of the mitochondrial inner membrane and between cristae lumen and IMS [57]. The formation and maintenance of CJs play an important role in mitochondrial function and are highly dependent on a protein complex termed mitochondrial contact site and cristae organizing system (MICOS), which will be described in a later chapter.

1.2.2. Cardiolipin in Mitochondrial Membranes

An important factor for the curvature of mitochondrial membranes is the phospholipid cardiolipin (CL). CL is a conical shaped phospholipid, that can form non-bilayer structures that are thought to play important roles in membrane fusion, vesicle formation, and cell division and is specifically found only in mitochondria [69, 70]. There, CL is mainly located at the IM with an asymmetric distribution and CL mainly in the matrix facing leaflet of the IM, where cardiolipin biosynthesis is located [70-72]. Other studies found CL to be enriched at the negatively curved inner leaflet of the CM facing the cristae lumen [73]. CL facilitates budding, fission, and fusion of mitochondria by imposing curvature stress onto the membrane [74]. It is also required for the assembly of the complete MICOS and therefore contributes to CJ formation [75]. It was shown *in vitro* that CL is essential for the formation of cristae like structures in giant unilamellar vesicles (GUVs) [76]. In addition to its role for mitochondrial ultrastructure, CL is important for fusion and fission of mitochondria through interaction with OPA1 and Drp1 [77-79]. CL is also involved in protein import [80] and assures the stability of respiratory supercomplexes [81-83].

1.2.3. Mitochondrial Dynamics

Mitochondria are often simplified in textbooks and models, as shown in Figure 3 and Figure 4. They are depicted as small bean-shaped single organelles. As said before mitochondria can have a variety of shapes and form tubular networks. Mitochondrial networks can span through the whole cell and are highly dynamic and undergoing continuous fusion and fission events [84]. This dynamic network assures optimal mitochondrial quality through content mixing of dysfunctional mitochondria with the functional mitochondrial network mediated by mitochondrial fusion. In addition, dysfunctional mitochondria are removed from the network by fission and fragmentation and undergo mitophagy as a part of the autophagy mechanism [85]. The dynamin-like GTPases play an important role in this mitochondrial dynamic [86, 87]. Mitochondrial fission is mainly mediated by dynamin-related protein 1 (Drp1) in mammals, which is predominantly found in the cytosol [88]. Drp1 forms large homomultimeric complexes to encircle the mitochondrion and mediate fission in an energy-dependent manner [89]. Defects in Drp1 lead to a block in mitochondrial fission and a formation of highly interconnected mitochondrial tubules [90, 91]. The fusion of mitochondria is also regulated by GTPases.

Mitofusin 1 and 2 (Mfn1 and Mfn2) are located at the mitochondrial outer membrane, facing the cytosol, and can bind to Mfn proteins on neighboring mitochondria to perform fusion of the OM [92]. Mutations in the Mfn proteins lead to a loss of fusion and fragmented mitochondria [88]. The fusion of the IM is mediated by the dynamin-like GTPase Mgm1 in yeast and optic atrophy 1 (OPA1) in mammals [93, 94]. Interestingly OPA1 is capable of heterotypic membrane fusion by binding of CL in trans, which overcomes the requirement of OPA1 being present on both membranes, like known for Mfn proteins [77]. OPA1 is present in two forms in mitochondria, the long form (L-OPA1), which is anchored to the IM and a short, soluble form (S-OPA1), which occurs after proteolytic processing by the IM protease OMA1 or YME1L in yeast, regulating the activity of OPA1 [87, 95-97]. Mutations in the OPA1 gene lead to optic atrophy, a disease that results in progressive vision loss [88]. On an organellar level, the loss of OPA1 results in the loss of mtDNA and also causes accumulation of swollen cristae, as well as CJ widening, hinting to a function in CJ regulation [94, 98-100].

1.2.4. Role of Cristae Remodelling in Apoptosis

As already described in chapter 1.1.1. mitochondria are involved in the intrinsic pathway of apoptosis, with the release of apoptogenic proteins like cytochrome *c* as an important trigger for the postmitochondrial pathway [101, 102]. Cytochrome *c* resides mainly in the cristae lumen with only 15% - 20% residing in the IMS [39, 103]. Mitochondrial outer membrane permeabilization alone cannot be sufficient to release cytochrome *c*, for CJs are supposed to act as a diffusion barrier and hinder cytochrome *c* release into the IMS. The apoptotic protein tBID can induce a BAK independent mobilization of cytochrome *c* to increase its availability for release upon MOMP. This redistribution was shown to be the result of a cristae remodeling with widening of CJ and fusion of individual cristae [39]. The exact mechanism of cytochrome *c* release is still not fully understood. Different mitochondrial proteins are suggested to contribute to this mechanism. Loss of the fusion protein OPA1 delays staurosporine induced apoptosis [104]. In contrast, former studies stated an antiapoptotic effect of OPA1 [94, 98, 105]. OPA1 was also shown to prevent loss of mitochondrial membrane potential upon apoptosis and to be involved in the regulation of CJ remodeling during apoptosis [98, 106]. To control the CJ width, S-OPA1 and L-OPA1 act together as an oligomer. The soluble S-OPA1 connects the membrane bound L-OPA1 at the sites of CJ or CM to control the width of CJ or cristae lumen. This interaction is disrupted upon the addition of the apoptosis factor tBID and therefore CJ widening occurs [98]. OPA1 interacts with MICOS component MIC60 to control CJ biogenesis and acts upstream of MIC60. Upon apoptosis, OPA1/MIC60 multimers are destabilized, which affects CJ stability and also promotes CJ widening [107]. Contrary to the stated antiapoptotic effect of OPA1, these findings do not clarify the mechanism of CJ remodeling and cytochrome *c* release completely but indicate an involvement of the fission and fusion machinery. This is supported by a study stating the knockdown of the fission protein

Drp1 affects cytochrome *c* release even upon BAX assembly [37]. In this study additionally, the involvement of MICOS component MIC60 was questioned. Another study showed that the loss of MIC60 leads to a faster cytochrome *c* release, proposing a role of MICOS in this mechanism [108]. MIC60 is proposed to be an antiapoptotic protein and apoptosis is affected by cristae remodeling, directly controlled by MIC60 [108, 109]. MIC60 and also MICOS component MIC27 were shown to redistribute during apoptosis more uniformly, but this has no direct effect on cytochrome *c* release, suggesting that MICOS is not immediately involved in cytochrome *c* release [37].

1.2.5. Role of Mitochondrial Ultrastructure in Cellular Respiration

The mitochondrial ultrastructure contributes to efficient cellular respiration. A disrupted mitochondrial ultrastructure with loss of CJ, as observed upon loss of several MICOS components is associated with a defect in mitochondrial respiration [110-112]. The increased inner membrane surface of mitochondria enhances the capacity of oxidative phosphorylation and from the early 1950s, the CM was hypothesized as a specialized compartment to ensure optimal conditions for ATP production [55]. As stated before, proteins of the respiratory chain mainly reside in the CM and therefore this mitochondrial subcompartment is suggested to be the preferential site of OXPHOS [64, 113, 114]. With CJs as diffusion barriers, the cristae lumen is an ideal subcompartment for building up the proton gradient, which is needed for ATP synthesis. Indeed, the F_1F_0-ATP synthase was found to be located at the edges of tightly curved cristae, whereas complex I is mainly located in the flat part of the CM [57, 115]. The F_1F_0-ATP synthase is not only located at this subcompartment but also required for the cristae formation and cristae tips [57]. F_1F_0-ATP synthase together with MIC60 mediates negative and positive membrane curvature in an antagonistic manner [116]. Also, F_1F_0-ATP synthase dimer can form higher order oligomers, which are responsible for tubulation of the IM [57]. A lack of subunit e and subunit g of this complex, two subunits which are not important for ATP synthesis, but for oligomerization of this complex, leads to a disrupted mitochondrial ultrastructure with loss of CJ in yeast [117-120]. The MICOS components MIC26 and MIC27 are required for the integrity of the respiratory chain supercomplexes [121]. All this leading to a structural dependence of efficient respiration and regulation of ATP synthesis. This was shown already in the 1960s, where an excess of ADP leads to a condensed state of mitochondria with swollen cristae and vice versa limited ADP led to an orthodox confirmation with a smaller cristae lumen [122, 123]. Furthermore, the shape and size of CJs could contribute to the regulation of ATP by limiting the ADP flux [60, 62].

1.2.6. Cristae Dynamics

Dynamic remodeling of cristae was observed early by the definition of an orthodox and condensed state, upon ADP concentration as stated before (chapter 1.2.5.) [60, 62, 122, 123].

Also upon changes in the physiological state, proteins dynamically redistribute across the IM between CM and IBM [46]. The CM can act as a reservoir for protein complexes of IBM with CJ as diffusion barriers, but still allowing a dynamic redistribution between the subcompartments, hinting to possible cristae dynamics. CM reorganization involves membrane fission and fusion events [61]. Upon apoptosis mitochondria develop changes in IM shape, connectivity, and volume [39], further supporting the model of cristae, that can dynamically change their structure. The function of OPA1 in controlling CJ width upon apoptosis also shows the dynamics of these structures [107]. The structure of the OPA1 yeast homolog Mgm1 was recently solved and authors predict the involvement of S-Mgm1 in the formation of an unstable membrane tip, which leads to fusion in *trans* [124]. Early studies suggested, that perturbation of mitochondrial membrane potential in one part of the mitochondrion affects the whole cell organelle and mitochondria exhibit a homogenous voltage across the whole mitochondrial membrane according to the "cable theory" [125, 126]. Recently with the help of extended-resolution airyscan microscopy and stimulated emission depletion (STED) super resolution nanoscopy, it was shown that the mitochondrial membrane potential in cristae is different from the IBM, as well as different cristae from one mitochondrion can have different membrane potentials and are independent bioenergetic units [127]. More recent studies provided an insight into the mechanism of CJ dynamics in living cells [111, 128]. CJs are frequently arranged in a helical pattern in budding yeast mitochondria and human mitochondria [129]. The dynamic movement of cristae was recently shown by STED nanoscopy [111, 128]. The cristae dynamic was supported by the finding, that MICOS components MIC10 and MIC60, marking the CJ, move towards each other to merge and subsequently split in a balanced manner. These movements of cristae and CJ inside the mitochondria and the membrane-remodelling events happen on a timescale of seconds [111]. The merging of cristae is MICOS dependent and the merging patterns resemble the letters 'X' and 'Y', which is in line with earlier observations of static cristae showing Y-like structures, which are connected to the IBM by multiple CJ [111, 130]. This cristae dynamic could be beneficial for trapping protons or other metabolites in isolated cristae and the exchange of metabolites by fusion of cristae [131]. These new findings may help understand the contribution of the ultrastructure to mitochondrial functions, such as respiration and apoptosis.

1.2.7. Mitochondrial Ultrastructure and Association to Diseases

Meanwhile, all changes in mitochondrial proteins, also the nuclear encoded ones, are suggested to be a mitochondrial disease, including defects in lipid milieu, mtDNA translation, and mitochondrial fission and fusion [47, 132]. It was shown that mitochondrial ultrastructure plays an important part in mitochondrial health and is also linked to different diseases. Abnormal mitochondrial morphology was observed in cancer, neurological disorders such as Alzheimer's and Parkinson's diseases, obesity, diabetes mellitus, liver dysfunction,

degenerative muscle disease, and cardiovascular diseases [133-136]. With CL as an important factor for mitochondrial ultrastructure, changes in this phospholipid are associated with morphology changes in mitochondria and a disease called barth syndrome with abnormal mitochondrial morphology displaying characteristic honey-comb patterns of the cristae and hyperfused mitochondria (Figure 8) [137]. Barth syndrome is a rare, infantile-onset, X-linked recessive mitochondrial disorder with a highly variable phenotype. Common symptoms are cardiomyopathy, growth retardation, dysmorphism, cognitive impairment, and 3-methylglutaconic aciduria [138]. This disease is caused by a mutation in the nuclear gene encoding for the cardiolipin transacylase tafazzin TAZ [139]. This leads to a defect in cardiolipin synthesis and therefore lower levels of CL, which ultimately affects mitochondrial ultrastructure and function. In Barth syndrome patient cells, the abundance of the MICOS complex and the whole MIB was significantly increased, as well as the levels of OPA1, linking this disease to morphology as well as fusion and fission [140].

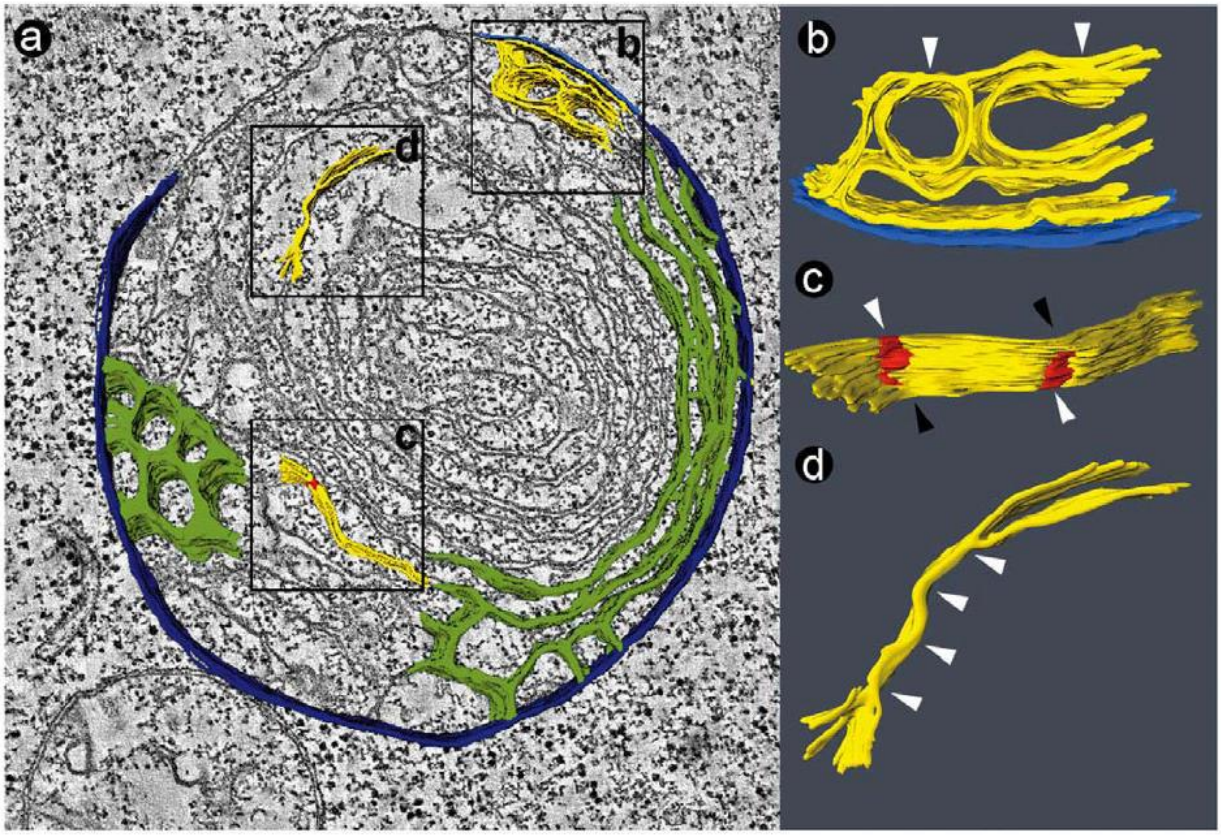

Figure 8. Tomogram of a mitochondrion from a Barth syndrome patient (50 nm section). Outer membrane depicted in blue (a, b), inner membrane depicted in yellow (a, b, c, d) and green (a), cristae depicted in green (a). Adhesions of the inner membrane marked in red, white arrowheads point to areas with collapsed intracristae space and black arrowheads point to areas with open intracristae space (image taken from Acehan et al. [137]).

Other mitochondrial functions can also be affected in diseases, for example, calcium homeostasis. Neurodegenerative diseases like Alzheimer's disease, Parkinson's disease, and Huntington's disease are linked to defects in calcium homeostasis. In these diseases, reactive oxygen species (ROS) can affect calcium levels or other mitochondrial functions [141]. The importance of mitochondrial quality control by fusion and fission can be shown in the case of the GTPase OPA1, which is related to dominant optic atrophy, a neuropathy of the *nervus opticus* which leads to severely impaired vision. OPA1 is associated with different mitochondrial functions including fusion of mitochondria, maintenance of the respiratory chain, membrane potential, and cristae organization, underlining the importance of all these mitochondrial functions for the cell [142]. Changes in the protein DISC1 (Disrupted in Schizophrenia-1), which is supposed to play a role in correct mitochondrial ultrastructure were found to correlate with schizophrenia and other major affective disorders in a large Scottish family [143, 144].

1.3. Mitochondrial contact site and cristae organizing system (MICOS)

The existence of CJs was suggested already over 50 years ago, however, the mechanism of how these structures were build was not understood [59]. Only recently a large heterooligomeric protein complex, the mitochondrial contact site and cristae organizing system (MICOS), was identified and shown to locate as CJs [116, 145-151]. Mitofilin, later termed MIC60, was shown to play a role in cristae morphology [109]. Later it was shown, that this protein together with other mitochondrial proteins builds a complex, important for CJs formation and maintenance, the MICOS [116, 151, 152]. This large protein complex was described first in 2011 by different studies, which found this complex to be located at the CJs and important for their formation. They termed the protein complex either MINOS, for mitochondrial inner membrane organizing system [145], MitOS, for mitochondrial organizing structure [147] or MICOS [146]. In 2014 a uniform nomenclature for this complex was established, using the term MICOS for the complex and referring to the proteins as MICX, with X as the approximate weight in kDa [151]. This complex was shown to be evolutionary conserved and the presence of MICOS in an organism correlates with the presence of characteristic cristae structures in mitochondria [153-156]. Since the first description of MICOS, at least seven proteins were found to be part of this complex in mammals [157]. The loss of the MICOS or even some of its proteins lead to a loss of CJs, so the cristae have no stable connection to the IBM anymore and can appear as stacks of lamellar cristae or as concentric rings [110, 116, 145-148]. The MICOS protein MIC60 interacts with outer membrane proteins and builds contact sites (CS) of the inner and outer membrane, which promote the import of a subset of precursor proteins into the mitochondria [145, 158]. As mentioned before, MICOS proteins are known to contribute to

several mitochondrial functions and the downregulation of this complex leads to impaired respiration, fragmentation of the mitochondrial network, and can also affect apoptosis [108, 112, 154, 158-161]. Additionally, a link between MICOS and the phospholipid CL was shown in several studies. MICOS components and cardiolipin biosynthetic enzymes display a strong genetic interaction and mammalian MIC27, as well as plant MIC60, can even bind CL *in vitro* [75, 147, 160, 162]. CL is required for the focal localization of the MIC10-MIC12-MIC27 subcomplex of MICOS in yeast upon the loss of MIC60 [75]. Whereas the connection to CL is shown, the functional consequences of this interaction are not understood yet [66].

1.3.1. MICOS and the mitochondrial intermembrane space bridging complex (MIB)

The MICOS complex interacts with several proteins and was also described to be part of a big intermembrane space spanning protein complex, which was found at the CS of mitochondrial IM and OM, the mitochondrial intermembrane space bridging (MIB) complex (Figure 5) [149, 152].

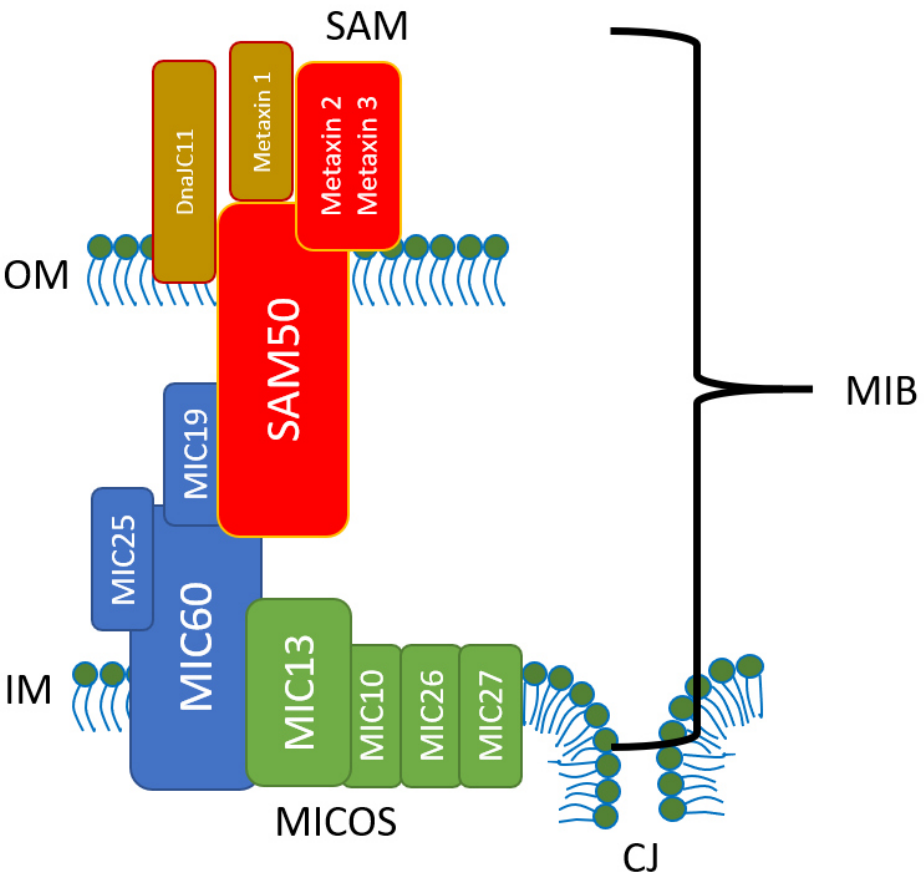

Figure 5. Mitochondrial intermembrane space bridging complex (MIB). The intermembrane space complex spans the intermembrane space and connects the IM to the OM. It consists of the SAM complex (red), DnaJC11, Metaxin1 in the outer membrane, which are linked to the MICOS at the inner membrane near the CJ. The MICOS is divided into MIC60-subcomplex (blue) and MIC10-subcomplex (green).

The MIB consist of MICOS in the inner membrane and the SAM complex, metaxin 3, and the long form of DnaJC11 in the outer membrane, that interact with MICOS to bridge the intermembrane space. The MICOS complex alone migrates at 700 kDa on a Blue-Native-PAGE and forms the bigger MIB complex, which migrates at more than 1 MDa, possibly around 2200 – 2800 kDa [163]. The crucial proteins for the formation of this intermembrane spanning complex are SAM50 in the OM and MIC19 and MIC60 in the IM, which take part in the stability of the MIB and cristae organization [164]. MICOS/MIB, as stated before, is important for the mitochondrial ultrastructure and also contributes to other mitochondrial pathways, such as protein import, the stability of mtDNA, and mitochondrial respiration. MIC60 was not only shown to interact with SAM in the OM but also with the protein translocase TOM and the oxidoreductase Mia40 of the MIA machinery. Therefore it stimulates the TOM-SAM-mediated import of β-barrel proteins into the OM, as well as the MIA mediated import of intermembrane space proteins [157]. In humans, it was furthermore shown that levels of SAM50 and metaxins highly depend on MIC60 and MIC19, therefore also affecting the TOM-SAM-mediated protein import [149]. Additionally, MICOS is required for the efficient import of carrier proteins into the mitochondrial membrane in humans [165]. The mechanistic role of MICOS in protein import however is still unclear. Besides its function in protein transport, MICOS was also linked to the fusion and fission of mitochondria [157]. Upon disruption of MICOS, reduced levels of OPA1 were observed [159]. The yeast protein Ugo1 and its mammalian homolog SLC25A46, which act as an adapter of the mitochondrial fusion machinery were also shown to interact with MICOS [146, 166]. The finding that the loss of MIC60 leads to impaired fusion and fission, as well as enlarged mitochondria, supports the link of MICOS to mitochondrial fission and fusion and therefore the inner membrane architecture to the mitochondrial membrane dynamics [167]. MICOS is linked to further mitochondrial functions. Upon loss of MICOS altered inheritance or even decreased levels of mitochondrial DNA were observed [144, 146]. The loss is also linked to an altered distribution of respiratory chain complexes and loss of respiratory competence [75, 146]. Here most likely the change of the functional ultrastructure caused by the loss of CJs as diffusion barriers and lack of connection between cristae and IMS leads to the defect in mitochondrial respiration. Alterations in MICOS are linked to many human mitochondrial diseases. Displaying the abnormal cristae morphology, a lot of diseases linked to this morphology are caused or accompanied by alterations in MICOS proteins, which will be described in a later chapter (1.3.3.).

1.3.2. Components of MICOS

The MICOS itself consists of at least seven proteins in mammals, namely MIC10, MIC13, MIC19, MIC25, MIC26, MIC27, and MIC60 (Figure 5). The MICOS was shown to assemble in two subcomplexes, one consisting of MIC60 as a core component with attached MIC25 and MIC19, as the only MICOS proteins not inserted into the membrane. The other one consisting

of MIC10 as a core component together with the remaining MICOS proteins MIC26, MIC27, and MIC13 [75, 112, 158, 168]. The assembly of the MIC10-subcomplex is dependent on the respiratory complexes and CL, whereas the MIC60-subcomplex assembly seems to be independent [75].

MIC60, also known as mitofilin is the first identified protein of MICOS and also the most evolutionary conserved one. It was found to be enriched at CJs and important for their formation [116, 152]. Orthologues of MIC60 are found even in α-proteobacteria, which confirms the endosymbiotic origin of mitochondrial cristae [12, 156]. The MIC60 in humans as well as in α-proteobacteria shows a membrane bending activity and therefore helps with the formation of CJs [12, 155, 156]. Upon loss of MIC60 in yeast cells, concentric stacks of inner membrane in the mitochondrial matrix were observed with complete loss of CJ as well as increased levels of F_1F_0-ATP synthase. In contrast, the overexpression of MIC60 leads to branching of cristae and enlargement of CJ diameter as well as lower levels of F_1F_0-ATP synthase supercomplexes [116, 158]. Next to the function of MIC60 for CJ formation, it also plays a role in protein translocation by interacting with TOM and SAM as stated above. This interaction is independent of an intact MICOS, suggesting a dual role of MIC60 in both functions and the existence of two functionally different MIC60 pools [145, 154, 158]. This is supported by the fact, that MIC60 localizes in punctae across the mitochondrion, even upon loss of other MICOS components [75, 129, 147, 150]. These results state MIC60 is a primary factor for correct MICOS assembly and CJ formation [157]. In addition, MIC60 was shown to interact with OPA1, with OPA1 being epistatic to MIC60 in its function of defining the CJ diameter [104, 107]. These findings underline again the connection between inner membrane architecture and dynamics. MIC60 builds the core component of the bigger subcomplex with MIC19 and MIC25 attached to it. MIC19 and MIC25 are the only peripheral inner membrane proteins of MICOS and have an amino-terminal myristoylation motif that mediates their localization to the IMS site of the IM [159, 169]. MIC19 binds to the mitofilin domain of MIC60 and modulates its membrane shaping ability [170]. It is present in a reduced and oxidized form, that contains an intramolecular disulfide bond, which is involved in proper MICOS assembly [171]. The oxidative state of MIC19 thereby plays an important role in MICOS assembly and maintenance of the inner membrane morphology and MIC19 may act as a redox-sensitive regulator of MICOS [157].

The smaller MICOS subcomplex consists of MIC10 as its core component and the MICOS proteins MIC26, MIC27, and MIC13 [75, 110, 112]. MIC10 is a small hairpin-like protein with two transmembrane domains and both termini exposed to the IMS [145, 158, 172]. It has the ability of self-oligomerization with the help of a conserved glycine-rich motif (GxGxGxG), which was also found in the transmembrane segment of the ring-forming subunit c of the F_1F_0-ATP synthase [172]. This motif and the ability to self-oligomerize are crucial for the stability of CJ

[158, 172]. MIC10 oligomers promote the formation of CJ by their ability to change membrane morphology *in vivo* and *in vitro* [158, 172]. MIC26 and MIC27 were first identified by complexome profiling to be part of the MICOS and interact with MIC60, MIC10, and SAM50 [160, 161]. MIC26 in humans exists in three forms, a non-glycosylated form, a glycosylated form, and an ER/Golgi resident form. However, the function of the glycosylated form, which is secreted, is still unclear [135, 161, 173]. MIC27 was shown to bind CL *in vitro* and MIC26 is linked to the cardiolipin metabolism, therefore both are linked to correct mitochondrial ultrastructure [121, 160, 161]. MIC27 is a homologous protein to MIC26 and both regulate their levels in an antagonistic manner. Overexpression of MIC26 leads to the fragmentation of mitochondria, promotes ROS formation, and also impairs mitochondrial respiration. The downregulation of MIC26 on the other hand leads to a decrease in oxygen consumption and complete depletion leads to the alteration of mitochondrial ultrastructure and a significant decrease in CJs [161]. MIC26 and MIC27 were shown to be dispensable for the assembly of the remaining MICOS subunits. However, they are required for the integrity of the respiratory chain complexes as well as the F_1F_0-ATP synthase in humans [121]. In yeast MIC27 was shown to promote the stability of MIC10 oligomers, therefore it plays an important part in MICOS assembly and mitochondrial morphology [168].

MIC13/QIL1 being also one of the newly identified compounds of MICOS was identified as a part of MICOS in 2015 [110, 112]. This protein was later suggested to be the ortholog to yeast MIC12 [156]. Upon depletion of MIC13 in human cells, *Drosophila* muscle and neuronal cells a disrupted CJ structure could be observed with loss of the connection between CM and IBM and cristae as concentric stacks inside the mitochondria [110, 112]. In human cells, an impaired respiration and in *Drosophila* cells mitochondrial fragmentation, as well as MICOS disassembly and degradation of the MIC10-subcomplex, could be observed. Even upon overexpression of MIC10, the interaction with MICOS or SAM50 could not be restored [112]. In yeast, MIC12 was suggested to be required for the coupling of the two mitochondrial subcomplexes, and loss of MIC12 leads to loss of MIC10-subcomplex [168]. Therefore, the model of MIC13 acting as a bridge was established. Upon the loss of the bridge, the MIC10-subcomplex is destabilized and only the MIC60-subcomplex is left in the mitochondrial inner membrane [174]. The MIC60-subcomplex alone is not sufficient for building a correct mitochondrial cristae morphology. Right now, it is not known if the severe effects of loss of MIC13 are due to the function of MIC13 in general or are only due to the loss of the core component MIC10, which leads to the same effect if deleted (Figure 6). Nevertheless, MIC13 seems to play an important part in MICOS and mitochondrial morphology.

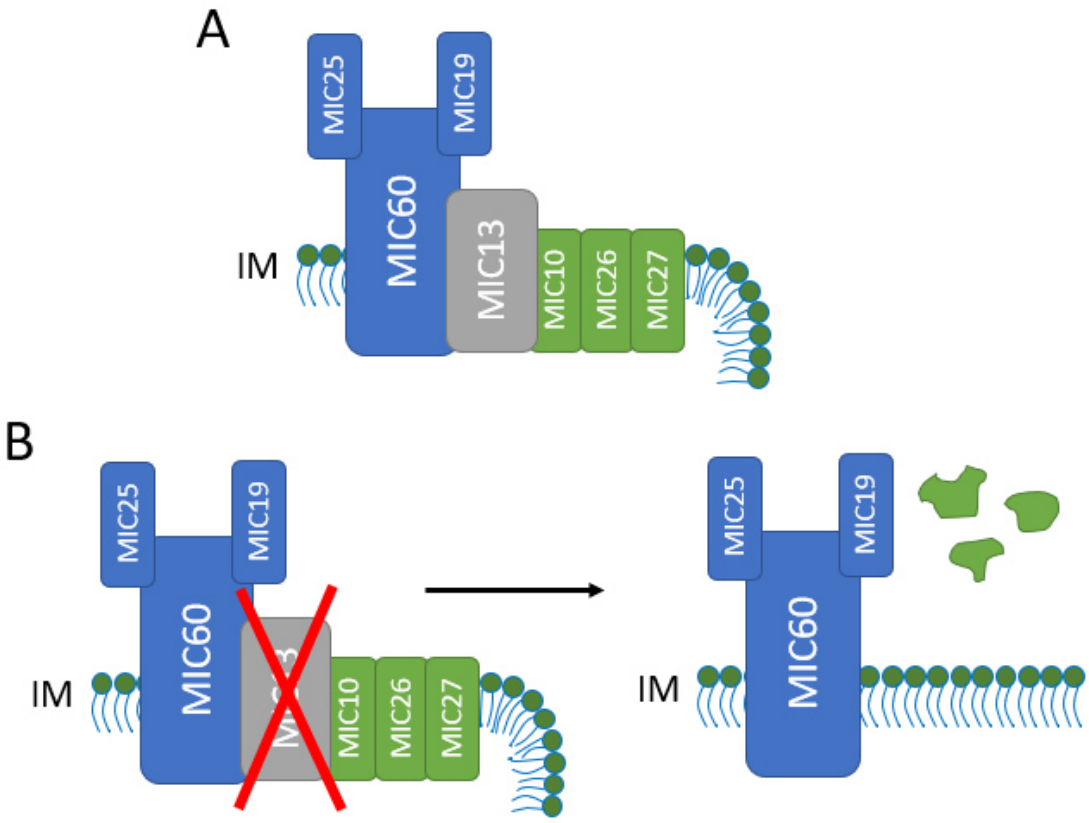

Figure 6. Model of MICOS with MIC13 functioning as a bridge. (A) MICOS consists of two subcomplexes, the MIC60-subcomplex with MIC60, MIC25, and MIC19 (blue) and the MIC10-subcomplex with MIC10, MIC26, and MIC27 (green). MIC13 (grey) is suggested to couple these two subcomplexes. (B) Upon loss of MIC13 in mitochondria the MIC10-subcomplex (green) is not assembled into the MICOS anymore and protein levels are decreased, suggesting degradation of these proteins.

1.3.3. Diseases Associated with MICOS

The neurodegenerative Parkinson's disease is also linked to the Ser/Thr kinase PINK1, with mutations in this protein causing autosomal recessive early-onset Parkinson's disease [175]. PINK1 was shown to be important for mitochondrial morphology by phosphorylating MIC60 to assure the maintenance of CJs [176]. The already described Barth syndrome is linked to MICOS by increased MICOS levels in patient cells [140]. Patients with mutations in CHCHD10, a protein that interacts with MIC60, present symptoms like isolated myopathy, frontotemporal dementia, amyotrophic lateral sclerosis type II, and spinal muscle atrophy [177-179]. Recently a mutation of MIC26 was associated with mitochondrial diseases due to impaired MICOS. This mutation shows X-linked recessive inheritance and shows the variable severity of the symptoms within the same family. Family members are presented with lactic acidosis, muscle weakness, and neurological problems [180].

Over the last years after the identification of MIC13 as part of MICOS, several studies were showing the severe effect of MIC13 deficiency in patients [136, 174, 181-183]. The common symptoms are lactic acidosis, hypoglycemia, 3-methylglutaconic aciduria, microcephaly, and liver disease. MIC13 was even linked to mitochondrial cardiomyopathy in Rhodesian ridgeback dogs [184]. The first human patients described having MIC13 deficiency showed neurodegenerative disorders accompanied by hyperlactatemia, 3-methylglutaconic aciduria, disturbed hepatocellular function with abnormal cristae morphology in the liver, as well as cerebellar and vermis atrophy [181]. In other studies, patients were shown to exhibit fatal mitochondrial encephalopathy with liver disease, lactate acidosis consistent with psychomotor retardation, and optic atrophy shown in Figure 7. In general, these patients can exhibit acute liver failure due to the hepato-encephalopathic phenotype [136, 174, 182, 183]. On a cellular level, the MIC13 deficiency in patients leads also to disassembly of the MIC10-subcomplex as well as aberrant cristae structures, impaired OXPHOS activity, and sensitivity to glucose withdrawal [136, 174]. These findings may be the cause of the symptoms, especially the reduced respiration. However, this may not be the only explanation, and it's more likely, that there are other molecular mechanisms involving MIC13 to cause these severe symptoms. The MIC13 deficiency leads to such severe phenotypes and often the death of the patients, which underlines the importance of understanding the molecular function of MIC13. MIC13 was only recently identified and the numbers of patients found with impaired MIC13 are likely to increase in the following years, which makes an understanding of this protein and its contribution to mitochondrial essential.

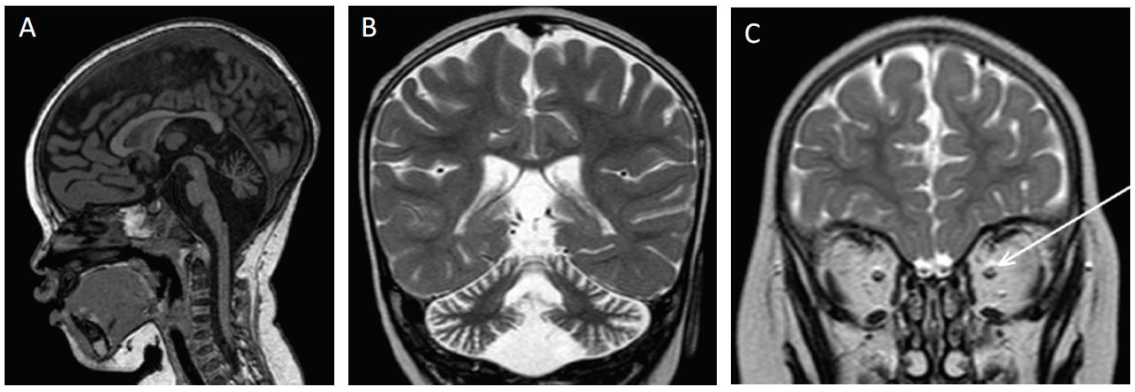

Figure 7. Brain MRI of a patient with MIC13 deficiency. (A) T1-weighted sagittal view. (B) and (C) T2-weighted coronal view. A shows cerebellar atrophy of the vermis and the brainstem, B shows cerebellar hemisphere atrophy and C shows optic atrophy (arrow) (image taken from Guarani et al. [174]).

2. Aim of the project

The function of mitochondria is highly dependent on its distinct ultrastructure, especially the existence of cristae and CJ. Alterations in the appearance of cristae or CJ and mitochondrial ultrastructure are associated with disrupted mitochondrial function and severe diseases in humans. Only recently a protein complex was identified, which actively takes part in the formation and maintenance of CJs, namely the MICOS complex. As part of the MIB, it is connected to the OM and takes part in the formation of contact sites of the two mitochondrial membranes. Notably, MICOS consists of two sub-complexes, that are supposed to be linked by MIC13, formerly known as QIL1, which was identified as a part of MICOS in 2015. Only a few studies describe MIC13 as a part of MICOS and it is already known that loss of MIC13 causes severe mitochondrial hepato-encephalopathy in patients. Till now there are no studies on the molecular role of MIC13 published. Therefore, this study investigates crucial key points to understand the molecular functions of MIC13:

1. To determine the role of MIC13 in mitochondrial function with respect to its bridging function in MICOS.
2. To systematically create and analyze the mutations of MIC13 to study the function of conserved amino acid residues of MIC13 sequence.
3. To determine the interaction partners and associated metabolic pathways of MIC13.

The results of the studies are presented in two published manuscripts (3.1. and 3.2.), followed by a manuscript in preparation (3.3.). Possible MIC13 interactors are found by proteomics and are shown here in an additional chapter with unpublished data, together with studies on the contribution of MIC13 to apoptosis (3.4.). The final discussion provides insight into the molecular function of MIC13 and shows a model of its possible role for MICOS and mitochondrial ultrastructure.

3. Results

3.1. Mic13 is essential for formation of crista junctions in mammalian cells

PLOS ONE

RESEARCH ARTICLE

Mic13 Is Essential for Formation of Crista Junctions in Mammalian Cells

Ruchika Anand[1], Valentina Strecker[2], Jennifer Urbach[1], Ilka Wittig[2,3,4], Andreas S. Reichert[1]*

1 Institute of Biochemistry and Molecular Biology I, Heinrich Heine University, Medical Faculty, Universitätsstr. 1, 40225, Düsseldorf, Germany, **2** Functional Proteomics, SFB 815 Core Unit, Faculty of Medicine, Goethe-University, Frankfurt am Main, Germany, **3** Cluster of Excellence "Macromolecular Complexes", Goethe University, Frankfurt am Main, Germany, **4** German Center of Cardiovascular Research (DZHK), Partner site RheinMain, Frankfurt, Germany

* reichert@hhu.de

Citation: Anand R, Strecker V, Urbach J, Wittig I, Reichert AS (2016) Mic13 Is Essential for Formation of Crista Junctions in Mammalian Cells. PLoS ONE 11(8): e0160258. doi:10.1371/journal.pone.0160258

Editor: Marc Liesa, University of California Los Angeles, UNITED STATES

Received: April 25, 2016

Accepted: July 15, 2016

Published: August 1, 2016

Data Availability Statement: All relevant data are within the paper and its Supporting Information files.

Funding: This work was supported by Deutsche Forschungsgemeinschaft, Sonderforschungsbereich 815, (www.dfg.de) and Heinrich Heine University, Medical Faculty, Forschungskommission, (http://www.medizin.hhu.de/forschung.html). The funders had no role in study design, data collection and analysis, decision to publish, or preparation of the manuscript.

Competing Interests: The authors have declared that no competing interests exist.

Contributions:

Conceptualization: RA AR.

Abstract

Mitochondrial cristae are connected to the inner boundary membrane via crista junctions which are implicated in the regulation of oxidative phosphorylation, apoptosis, and import of lipids and proteins. The MICOS complex determines formation of crista junctions. We performed complexome profiling and identified Mic13, also termed Qil1, as a subunit of the MICOS complex. We show that MIC13 is an inner membrane protein physically interacting with MIC60, a central subunit of the MICOS complex. Using the CRISPR/Cas method we generated the first cell line deleted for MIC13. These knockout cells show a complete loss of crista junctions demonstrating that MIC13 is strictly required for the formation of crista junctions. MIC13 is required for the assembly of MIC10, MIC26, and MIC27 into the MICOS complex. However, it is not needed for the formation of the MIC60/MIC19/MIC25 subcomplex suggesting that the latter is not sufficient for crista junction formation. MIC13 is also dispensable for assembly of respiratory chain complexes and for maintaining mitochondrial network morphology. Still, lack of MIC13 resulted in a moderate reduction of mitochondrial respiration. In summary, we show that MIC13 has a fundamental role in crista junction formation and that assembly of respiratory chain supercomplexes is independent of mitochondrial cristae shape.

Introduction

Mitochondria are double-membrane enclosed organelles which are essential for a number of cellular processes such as energy conversion, apoptosis, calcium buffering, lipid trafficking and heme biosynthesis. The inner mitochondrial membrane is characterized by membrane protrusions into the matrix termed cristae. Mitochondria show a dynamic remodeling of cristae length, density, and shape depending on the cell type and/or the physiological and developmental stage [1]. Indeed, aberrant changes in mitochondrial cristae are associated with numerous human diseases including Alzheimer's disease, Parkinson's disease, Wilson disease, and

Formal analysis: IW VS JU RA AR.
Funding acquisition: RA AR.
Investigation: IW VS JU RA.
Methodology: IW VS JU RA.
Validation: IW VS JU RA.
Writing - original draft: RA AR.
Writing - review & editing: RA AR.

hereditary mitochondrial hypertrophic cardiomyopathy. It is not understood whether mitochondrial cristae alteration is a cause or consequence of these diseases. Cristae divide the inner membrane (IM) into the cristae membrane (CM) and the inner boundary membrane (IBM) which runs parallel to the outer membrane. Cristae are physically connected to the IBM via crista junctions (CJs)—highly curved pore- or slit-like membrane structures with a diameter ranging from 12 to 40 nm [2–4]. CJs are proposed to play an important role in cristae remodeling during apoptosis and to act as a diffusion barrier between IBM and CM [1, 2, 5]. The IBM is rich in the proteins required for fusion/fission, protein import or signaling whereas the CM predominately contains proteins required for oxidative phosphorylation [6, 7]. This uneven, yet dynamic, distribution of various mitochondrial proteins between IBM and CM is likely mediated via CJs [1, 2, 5]. The presence of CJs also creates distinct aqueous compartments: the inter-membrane space between IBM the OM and the intracristal space. The diameter of CJs is proposed to be remodeled for example during apoptosis when cytochrome *c* is released from the intracristal space [8]. Also various metabolites such as protons, ADP and other apoptosis effectors reside in the intracristal space. Therefore, the shape and size of CJs was proposed to determine rates of ATP production and thus may be fundamental for regulation of bioenergetics [5, 9].

We have previously identified and characterized MIC60/Fcj1 in yeast cells as the first protein required for crista junction formation which was localized to CJs by immunoelectron microscopy [10]. Cells lacking MIC60/Fcj1 in baker's yeast have no CJs showing concentric stacks of membrane vesicles within the matrix. Independent studies have later identified a large heterooligomeric complex containing MIC60/Fcj1 as a core constituent playing a role to maintain cristae structure [11–13]. Following a uniform nomenclature, the complex is named as MICOS, "mitochondrial contact site and cristae organizing system" and its protein subunits MIC10 to MIC60 [14]. Thus, till date six subunits MIC60/Fcj1, MIC12/Aim5, MIC19/Aim13, MIC27/Aim37, MIC10/Mio10, and MIC26/Mio27, are reported in yeast. The MICOS complex is highly conserved from yeast to humans with the majority of the proteins also having mammalian homologs [15–17]

MIC60/Mitofilin is the mammalian homolog of MIC60/Fcj1. Apart from MIC60, the mammalian MICOS complex contains at least five other components, MIC10/Minos1, MIC19/CHCHD3, MIC25/CHCHD6, MIC26/APOO, and MIC27/APOOL [15–17]. CHCHD10 causative for frontotemporal dementia-amyotrophic lateral sclerosis was recently added to the growing list of subunits of MICOS [18]. The depletion of any of these subunits of the MICOS complex has been shown to alter cristae morphology. Reduced levels of MICOS components have deleterious effects on various cellular processes. For example, loss of MIC60/Mitofilin causes decreased cellular proliferation and increased sensitivity to induction of apoptosis [19]. Apparently, these cells are more prone to apoptosis due to the accelerated release of cytochrome *c* exemplifying the importance of CJs in regulating apoptosis [20]. MIC60/Mitofilin interacts with a variety of proteins such as MIC19/CHCHD3, DISC1, SAM50 linking the MICOS complex to cellular processes such as mitochondrial protein import and modulation of neuronal activity [11, 12, 17, 21]. Loss of MIC19/CHCHD3 leads to reduced cell proliferation and increased autophagy [21]. Depletion of MIC25/CHCHD6 causes alteration in cristae morphology and reduced cell growth, ATP production and oxygen consumption [22–24]. Moreover, altered levels or post-translational modifications of MICOS subunits are observed in a set of diverse human diseases such as epilepsy, Down syndrome, Parkinson's disease, diabetes, cardiomyopathy [17]. Overexpression of MIC60/Mitofilin in a transgenic mouse model protects against cardiac dysfunction normally observed after drug-induced diabetes mellitus indicating a protective role of MICOS in diabetes [25]. Altered levels of MIC19/CHCHD3 are found in disease models for familial amyotrophic lateral sclerosis and ischemia [26]. Downregulation

and overexpression of MIC25/CHCHD6 altered chemosensitivity of cancer cells to genotoxic anticancer drugs indicating its potential as a possible target for cancer therapeutics [22]. Overall, the physiological and pathophysiological importance of the MICOS complex is evident, however, the molecular understanding and the involved mechanisms are still unclear.

Recently, we have identified two apolipoproteins, MIC26/APOO and MIC27/APOOL, as subunits of the MICOS using a complexome profiling approach. [16, 27, 28]. Classically, apolipoproteins bind lipids in order to transport them within the lympathic and circulatory system. Recently, we have deciphered the role of MIC26/APOO and MIC27/APOOL in maintaining cristae morphology. Downregulation of MIC27/APOOL resulted in reduced numbers of cristae and appearance of small concentric structures which are partly branched and interconnected. Recombinant MIC27/APOOL can bind cardiolipin *in vitro* indicating that function of MIC27/APOOL is linked to its ability to bind the mitochondrial lipid cardiolipin. MIC26/APOO was previously known as a secreted glycosylated lipoprotein. MIC26/APOO levels are increased in diabetic heart tissue and in blood plasma of patients suffering from acute coronary syndrome [29–31]. We found that apart from the glycosylated form, MIC26 is also present in a non-glycosylated form which is localized to the inner mitochondrial membrane [27]. It physically interacts with components of the MICOS complex. Downregulation and overexpression of MIC26/APOO causes aberrant cristae morphology. Interestingly, both MIC26/APOO and MIC27/APOOL regulate each other's levels antagonistically and they positively regulate levels of MIC10 and tafazzin, an enzyme required for cardiolipin remodeling in mitochondria [27]. The binding of MIC27/APOOL to cardiolipin and the observed changes in tafazzin levels upon downregulation of MIC26/APOO and MIC27/APOOL point to a role of the MICOS complex in lipid homeostasis in mitochondria.

Here we applied 'complexome profiling' to identify novel MICOS components [32]. Apart from MIC26/APOO and MIC27/APOOL which we characterized previously, we have identified MIC13 as a novel MICOS component using this approach consistent with a recent study [33]. Here, we generated knockouts of MIC13 using CRISPR/Cas method and characterize the role of MIC13 in formation of crista junctions.

Results

Complexome profiling identifies MIC13 as a novel MICOS subunit

In order to identify novel subunits of the MICOS complex in mammalian systems we applied a proteomics method termed 'complexome profiling' [32]. Using this approach with bovine mitochondria we identified several mitochondrial complexes and their constituents including the MICOS complex and its known subunits MIC60/Mitofilin, MIC19/CHCHD3, and MIC10/MINOS1 [28]. Subsequently, we have identified and characterized MIC26/APOO and MIC27/APOOL as novel MICOS subunits [27, 28, 34]. Here we followed a similar strategy and solubilized mitochondria isolated from HEK293 cells using digitonin, separated native macromolecular protein complexes by large-pore blue native gel electrophoresis, and divided the gel lane in 60 equal gel slices. Quantitative mass spectrometry was performed for all gel slices and each identified protein was represented according to its relative abundance at the corresponding size. Hierarchical clustering was used to identify protein clusters with similar distribution profiles. We found that MIC13 also clustered with MICOS subunits in this complexome analysis compatible with the idea that MIC13 is a novel subunit of the MICOS complex (Fig 1A). We verified the interaction of MIC13 with MIC60 and MIC27 using coimmunoprecipitation experiments (Fig 1B). Human MIC13 is a small protein of 118 amino acids which is conserved from *C. elegans* to human (Fig 1C). We did not find any apparent homolog of MIC13 in

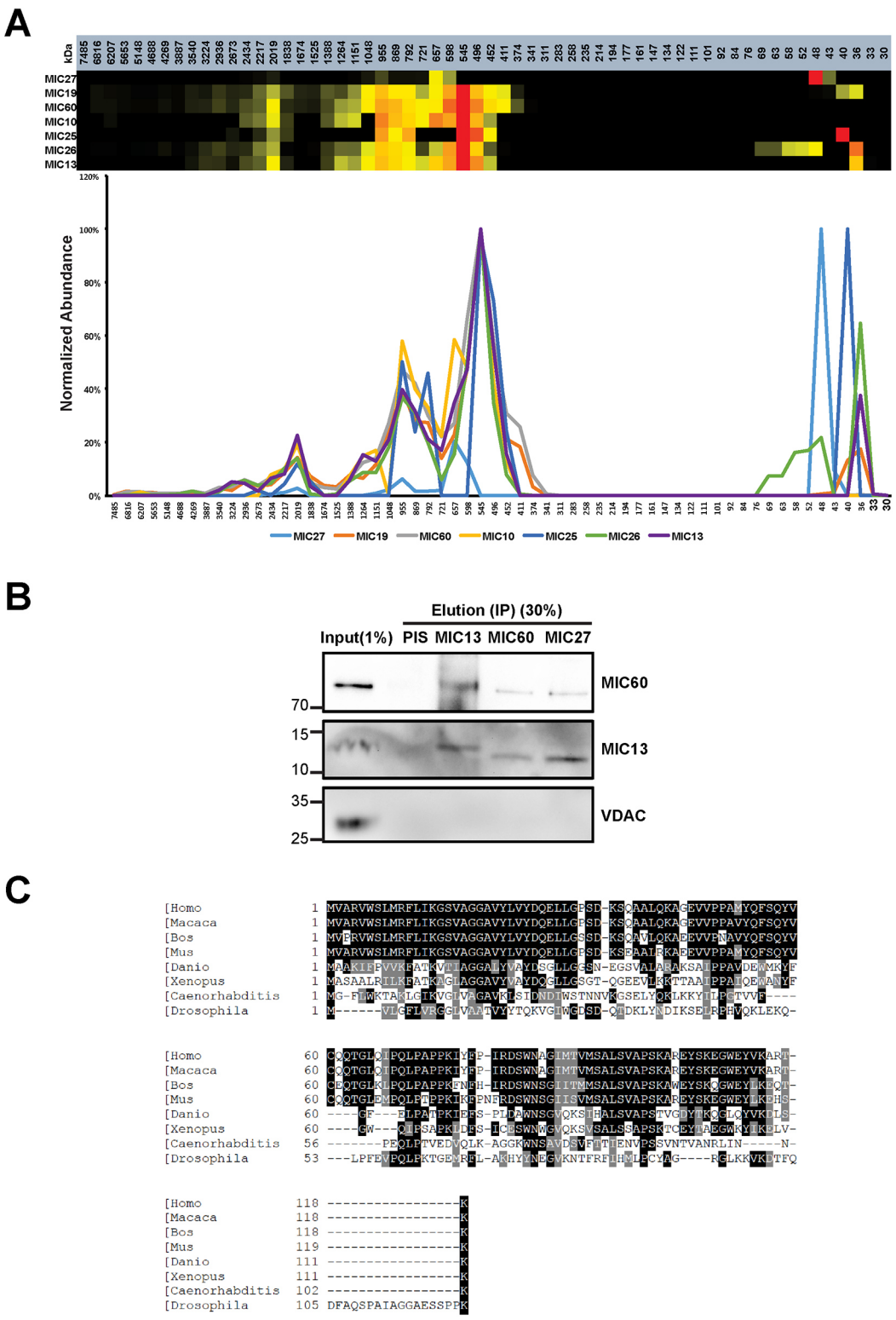

Fig 1. MIC13 is identified as MICOS subunit using complexome profiling. (A) The graph shows the normalized occurrence of the proteins which cocluster with the MIC60 and other MICOS components in control HEK293 cells. Using this complexome profile, MIC13 is identified as MICOS component. (B) Endogenous MIC13, MIC60 and MIC27 antibodies were used for coimmunoprecipitation. Preimmuneserum (PIS) was used as the control. Endogenous MIC13 could pull down MIC60 and reciprocally in control 143B cells, MIC60 and MIC27 can

pull down MIC13, indicating that MIC13 is the part of the MICOS complex. (C) Sequence alignment of MIC13 shows that it is conserved from *Caenorhabditis elegans* to higher eukaryotes.

doi:10.1371/journal.pone.0160258.g001

Saccharomyces cerevisiae. Overall, we conclude that MIC13 is a novel *bona fide* subunit of the MICOS complex consistent with a recent study [33].

MIC13 localized to mitochondrial inner membrane

We determined the subcellular localization of endogenous MIC13 using immunofluorescence microscopy. For that we immunostained human 143B cells using a MIC13-specific antibody. Mitochondria were visualized using a mitochondrially targeted GFP. We clearly observed a colocalization of MIC13 with mitochondrial structures demonstrating the mitochondrial localization of endogenous MIC13 (Fig 2A). MIC13 is uniformly distributed along the whole length of mitochondria. The antibody used was validated by western blot analysis showing a protein band at the expected size of approximately 10 kDa. Furthermore, we expressed MIC13 harboring a C-terminal FLAG-tag (MIC13-FLAG) in 143B cells. These cells were immunostained using an anti-FLAG antibody. The majority of MIC13-FLAG was present on mitochondria confirming the mitochondrial localization of MIC13 (Fig 2A).

We next investigated the submitochondrial localization of MIC13 using a standard protease protection assay. We found that MIC13 was susceptible to degradation after addition of proteinase K in mitoplasts behaving like the inner membrane protein TIM23 (Fig 2B, lanes 3 and 4). Outer membrane protein, TOM20 is degraded by proteinase K in the intact mitochondria (Fig 2B, lanes 1 and 2) The matrix protein TFAM is resistant to proteinase K treatment in mitochondria (Fig 2B, lanes 1 and 2) and in mitoplasts (Fig 2B, lanes 3 and 4) demonstrating that matrix proteins are protected from degradation by proteinase K. All proteins were degraded by Proteinase K after complete solubilization of membranes by Triton-X-100 (Fig 2B, lanes 5 and 6). Overall we conclude that MIC13 is an inner membrane protein consistent with its role as a novel subunit of the MICOS complex known to localize to the inner membrane.

MIC13 is essential for the formation of mitochondrial crista junctions

We generated MIC 13 knockout cells (MIC13 KO cells) using the CRISPR/Cas system. The double nickase Cas9 enzyme was targeted to specific sites of exon 2 of MIC13 to create deletions or insertions eventually resulting in cells lacking a functional MIC13 protein. The use of double nickase strategy drastically reduces the chances of non-specific targeting [35]. We first screened single clonal populations of cells that lack any visible immunoreactivity for the MIC13-specific antibody. We obtained several clonal cell populations lacking MIC13 which was validated in four cell lines by western blot analysis (Fig 3A). These are the first cell lines where MIC13 is knocked out serving as a valuable tool to study the function of MIC13 and the MICOS complex. These cell lines were viable and could be cultured in normal MEM media supplemented with bovine serum indicating that MIC13 is not essential for the viability of these cells. Apart from these MIC13 KO cells, we also depleted MIC13 in the HeLa cells using siRNA to obtain results using an independent approach. These cells also show considerably low levels of endogenous MIC13 protein (Fig 3C). With both cell systems we investigated the role of MIC13 in regulating mitochondrial cristae organization by electron microscopy. We observed complete loss of crista junctions in all the clones of MIC13 KO cells as in a total of 135 mitochondrial sections observed in three MIC13 KO cell lines no crista junction was observed (Fig 3B). The cristae were arranged in an onion-like fashion and lacked any visible connection to inner boundary membrane (IBM). HeLa cells depleted of MIC13 also showed a

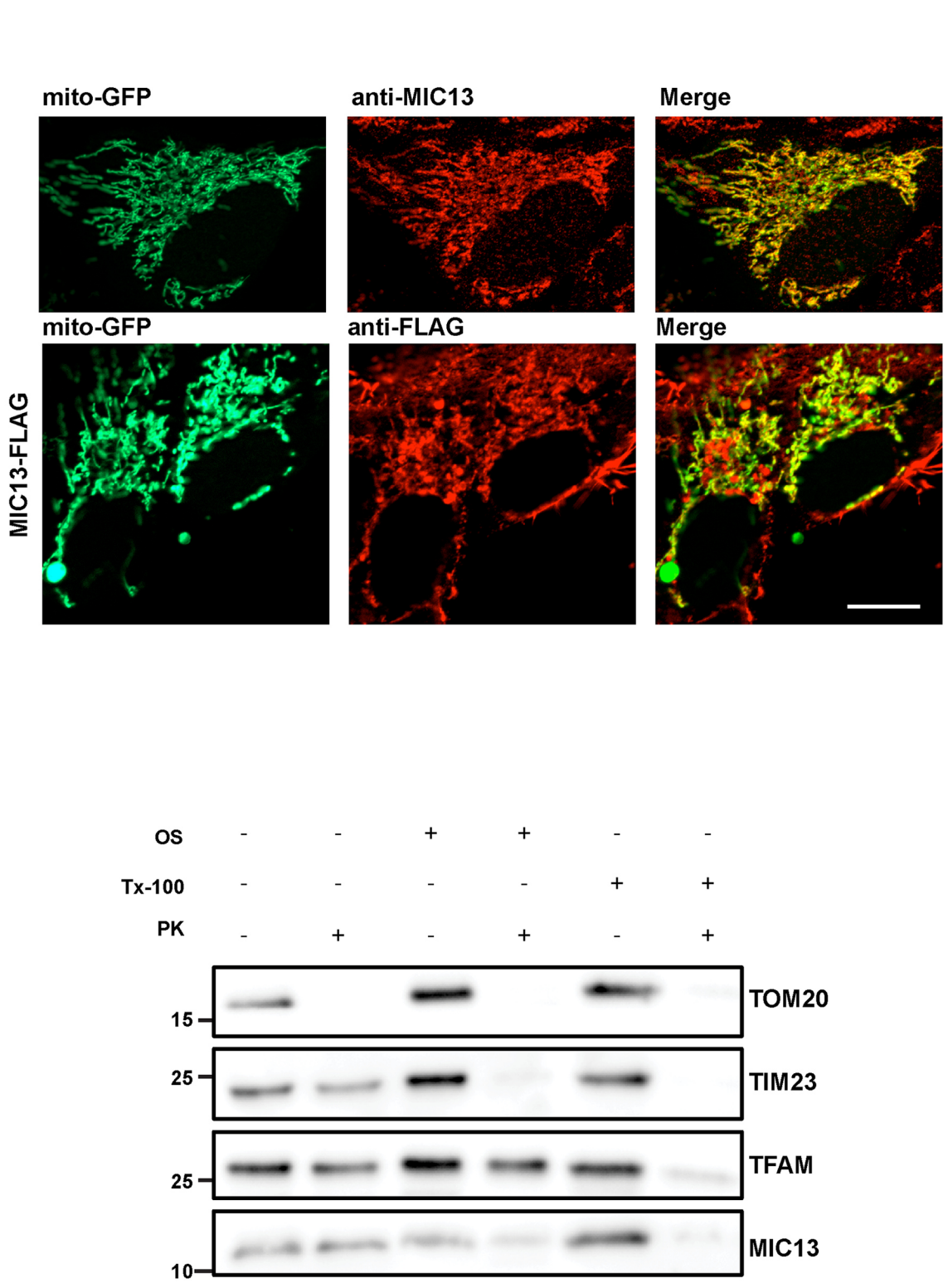

Fig 2. MIC13 localizes to inner mitochondrial membrane. (A) Representative images of mitochondria (marked by mito-GFP, green) and endogenous MIC13 (using MIC13 antibody, red) or MIC13-FLAG (marked by anti-FLAG) in control 143B cells. Merge shows the colocalization of mitochondria and MIC13. Scale bar 10μm. (B) Isolated mitochondria of control 143B cells were swelled by osmotic shock (OS) and then treated or untreated with Proteinase K (PK). Triton-x-100 (Tx100) was used to permeabilize all the membranes. TOM20, TIM23 and TFAM were used for outer membrane, inner membrane and matrix marker respectively.

doi:10.1371/journal.pone.0160258.g002

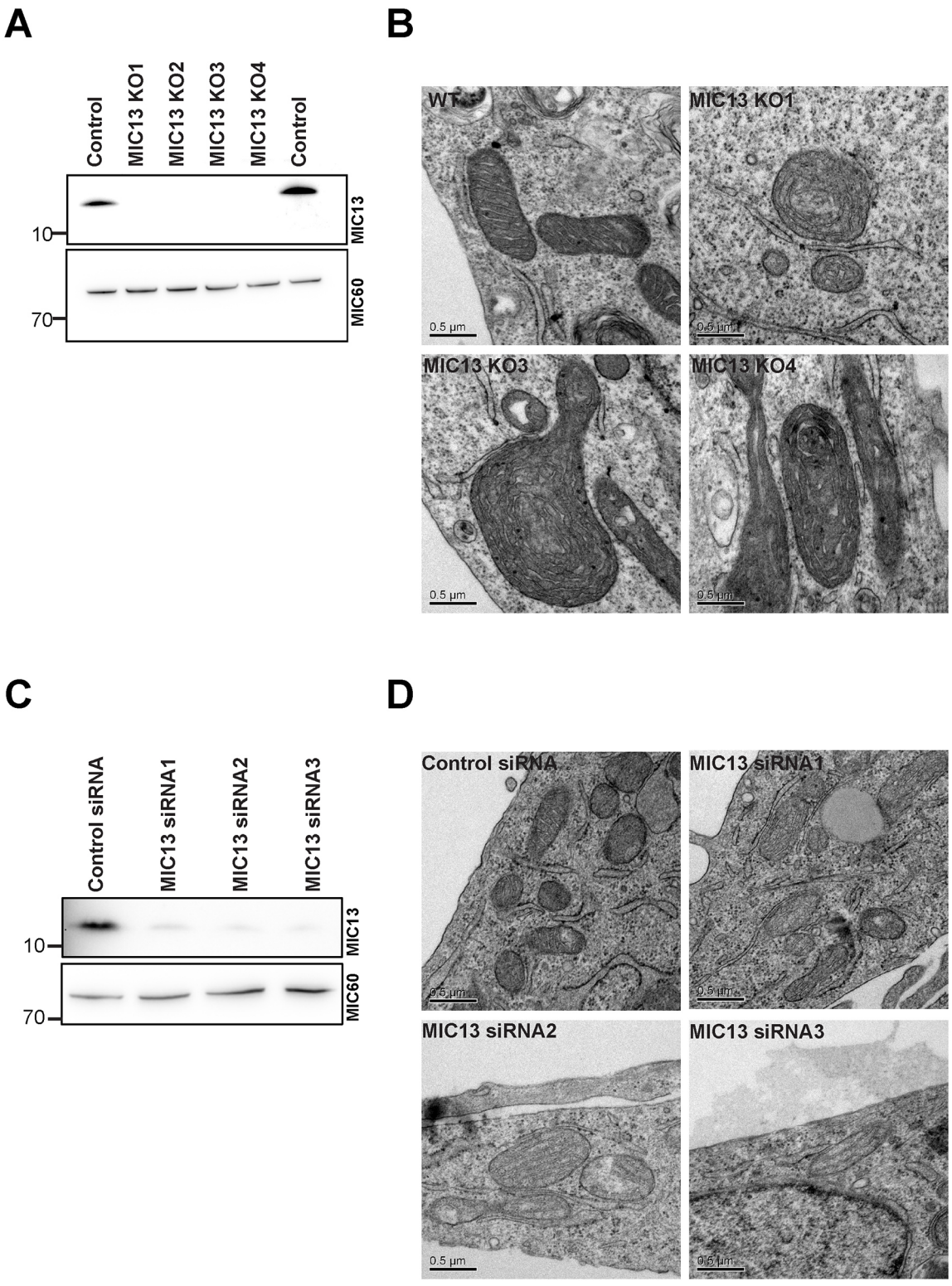

Fig 3. MIC13 KO cells have no crista junctions. (A) Immunoblot of MIC13 showing the complete loss of the protein in the knockout cell lines. (B) Representative EM images of control and MIC13 KO mitochondria (we analyzed approx. 40 to 50 mitochondria of each MIC13 KO cell line (N = 2). There is a complete loss of CJs in MIC13 KO cells whereas in control cells 1 to 5 CJs were observed in nearly all sections (40 to 50 mitochondria, N = 2). (C) Immunoblot of MIC13 in HeLa cells where MIC13 is depleted using SiRNA. (D) Representative EM images of control and MIC13 siRNA mitochondria.

doi:10.1371/journal.pone.0160258.g003

similar phenotype, yet occasionally crista junctions remained visible which we attribute to incomplete depletion of MIC13 (Fig 3D). Quantitative analysis of areas of mitochondrial sections in electron micrographs indicate that mitochondria in MIC13 KO cells are on average larger in size and show a larger range of observed values compared to wild type cells (S1A Fig). This increase in mitochondrial area is significant for two MIC13 KO cell lines whereas a third cell line only showed a slight tendency in the same direction which, however, was not significant. Given the fact that mitochondria appeared packed with onion-like stacks of cristae we decided to analyze whether the area of cristae is higher in MIC13 KO cells. For this we chose one of the KO cell line showing higher increase in mitochondrial area (MIC13 KO3). Our analysis revealed that area of cristae were markedly increased in the MIC13 KO3 cell line. This increase was not caused by swelling but by elongation of cristae stacks. This is compatible with the idea that an increase in mitochondrial size is caused by enlarged cristae stacks in KO cells (S1B Fig). Taken together, our data demonstrate that MIC13 is essential for crista junction formation in mammalian cells and determines mitochondrial size and ultrastructure. This is in accordance with MIC13 being an important subunit of MICOS complex.

MIC13 is required for efficient assembly of the MICOS complex

Next we aimed to check whether MIC13 is required for the stability and/or assembly of the MICOS complex. For this purpose, we studied MICOS complex using blue native electrophoresis in MIC13 KO cells and corresponding controls. In control cells the MICOS complex migrated at molecular weights of approximately 550 kDa, 950 kDa, and 2000 kDa (Figs 1A and 4A). In the absence of MIC13, the MICOS (sub)complex consistently showed a reduced molecular weight with values of approximately 400 kDa, 680 kDa, and 1800 kDa (Fig 4A and 4B). In order to study the composition of MICOS complex in the absence of MIC13 we subjected gel slices obtained from a blue native gel for quantitative mass spectrometry and complexome profiling. As expected from the blue native data, we observed a clear shift in the peak MICOS complex in MIC13 knockout cells (compare Figs 1A and 4B). The complexome profiles reveal that after deletion of MIC13 the MICOS complex predominantly consists of only MIC60, MIC19 and MIC25 while MIC26 and MIC27 appear as low molecular weight complexes (Fig 4B). Also MIC10 appears to form now separate complexes with approximate sizes of 1100 kDa, 720 kDa, and 500 kDa indicating that loss of MIC13 destabilizes the MICOS complex. We further investigated the steady state levels of other MICOS components in MIC13 KO cells and in MIC13 depleted cells. In both cell types we observed strongly reduced levels of MIC10, MIC26 and MIC27 compared to control cells, however, MIC60 levels remained unchanged (Fig 4C). MIC27 stability differs between the KO cells and transient siRNA, suggesting the differential effect on long term stability of some of the MICOS components. Steady state levels of MIC25 and MIC19 are unchanged upon MIC13 depletion (Fig 5A). Based on these observations we suggest that MIC13 is required for assembly of MIC10, 26 and 27 with the remaining subunits of the MICOS complex. However, the assembly of MIC60, MIC19 and MIC25 in the MICOS subcomplex is apparently independent of MIC13. We speculate hierarchical steps in the formation of MICOS complex wherein MIC60, MIC25 and MIC19 first form an intermediate complex and then bind to another intermediate subcomplex consisting of MIC13, MIC10, MIC26, and MIC27. If this is true we hypothesize that depletion of any of its constituents could make this subcomplex unstable and leads to subsequent degradation of its remaining constituents. This could explain the significant loss of MIC26, MIC27 and MIC10 in MIC13 KO cells. In order to verify this we decided to perform a reciprocal experiment and depleted MIC10 in HeLa cells using siRNA and probed for MIC13 protein levels. In line with our hypothesis, we observed a clear reduction of MIC13 in these

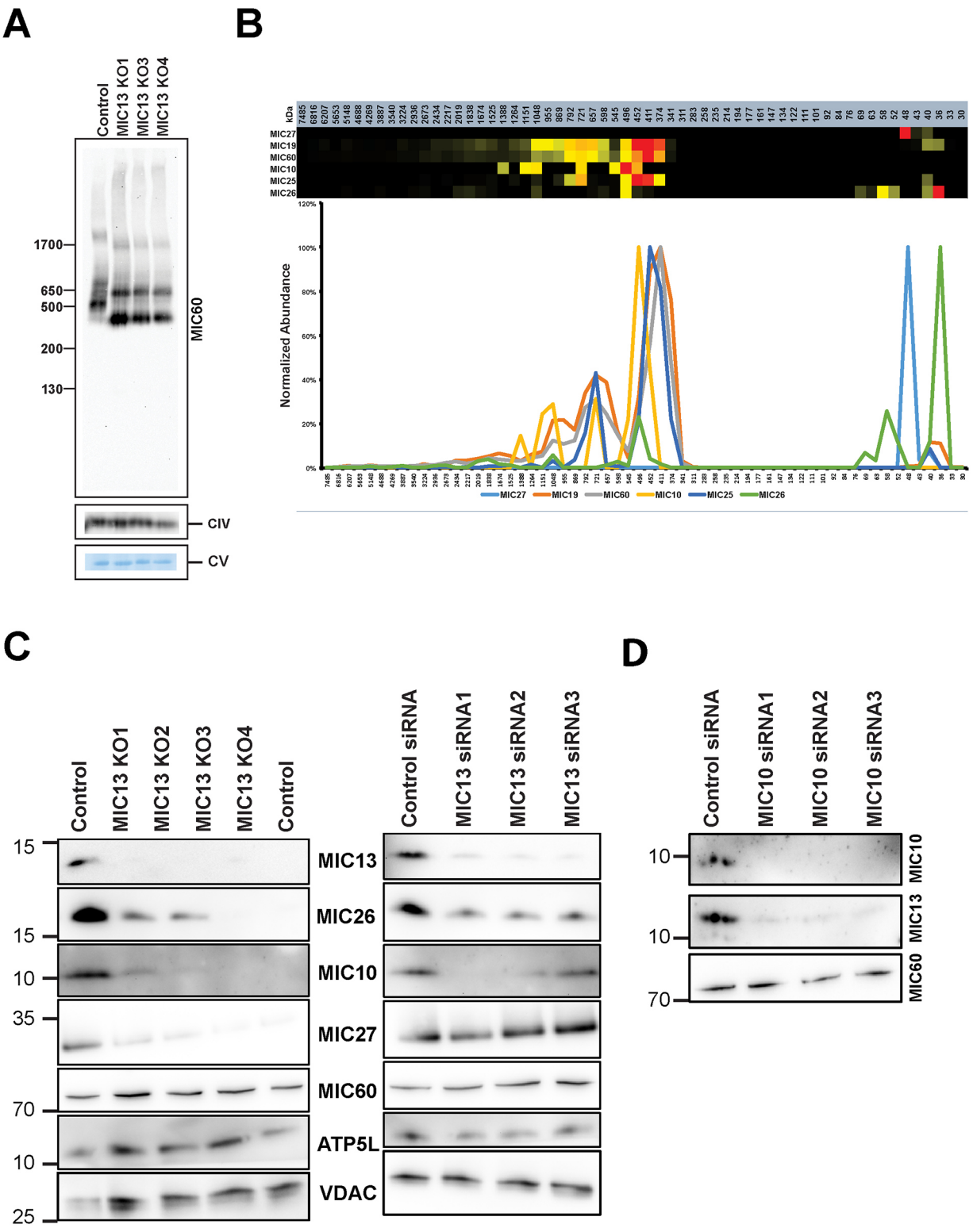

Fig 4. MIC13 knockout results in smaller but assembled MICOS complexes. (A) Protein complexes were isolated by blue-native electrophoresis (BNE) on 3 to 18% acrylamide gradient gels immuno-decorated against MIC60, subunit coxVIa/b of complex IV and ATP synthase was shown on blot to demonstrate equal loading of samples and no effect. In control HEK293 cells, MICOS is detected around 500 KDa. Deletion of MIC13 leads to smaller MICOS complex. (B) Complexome profiling of the MICOS complex in MIC13 KO cells demonstrate the smaller MICOS complex (subcomplex) comprises of MIC60, MIC19 and MIC25. (C) Immnuoblot showing the

steady state levels of various MICOS components in MIC13 KO cells as well as cells treated with MIC13 siRNA. There is reduction of MIC10, MIC27 and MIC26 upon deletion of MIC13. (D) Immunoblot from the cells depleted of MIC10 and probed for MIC13 and MIC60.

doi:10.1371/journal.pone.0160258.g004

cells (Fig 4D) indicating that MIC13 and MIC10 are reciprocally stabilized as they are the part of same MICOS subcomplex.

MIC13 is dispensable for OXPHOS complex formation but moderately affects respiration

It was proposed recently that cristae morphology is critical for proper assembly of respiratory chain supercomplexes [36]. Using the MIC13 KO cells we thus aimed to evaluate the role of crista junctions and cristae morphology on maintaining the structure and stability of OXPHOS complexes in mitochondria including respiratory chain supercomplexes. We initially examined the steady state levels of several subunits of complexes of the respiratory chain but we did not find any obvious and consistent differences between control and MIC13 KO cells (Fig 5A). To investigate this we analyzed respiratory chain complexes using BN-PAGE and subsequent complexome profiling in control and MIC13KO cells. Standard coomassie stain of major OXPHOS complexes in control and MIC13 Knockout cells does not reveal any obvious difference in the stability of any of the respiratory chain complexes (Fig 5B). We also compared the compositions of subunits of various OXPHOS complexes in control and MIC13 KO cells using complexome profiling. We did not find any major change in composition of any of the respiratory chain complex between control and MIC13 KO cells (S2 Fig). We further investigated the role of MIC13 in mitochondrial respiration. We observed a decrease in basal and maximal respiration of MIC13 KO cells compared to control cells (Fig 5C). We performed substrate inhibitor titration protocol to examine whether the activity of a specific respiratory complex is compromised in MIC13 KO cells. Consistent with our basal respiration experiment, we observed a significant decrease in basal respiration of MIC13 KO compared to control (Fig 5C and 5D). We observed only a slight decrease in Complex I (glutamate and malate) and Complex II/III (succinate) driven respiration of MIC13KO which was not statistically different compared to control. However, Complex IV (ascorbate/TMPD) driven respiration was significantly reduced in MIC13 KO (Fig 5D). From these results, we conclude that crista junctions are not required for the assembly and stability of major respiratory chain complexes and that basal respiration is only reduced moderately in the absence of crista junctions. This reduced basal respiration could be due to a combined modest reduction in the activity of all respiratory complexes. Overall we demonstrate a minor but significant influence of CJs on mitochondrial respiration.

We also checked mitochondrial morphology of MIC13 KO cells to observe any influence of crista junctions on mitochondrial tubulation. We stained mitochondria using cytochrome c in control and MIC13 KO cells (S3 Fig). We observed tubular mitochondria in both control and MIC13 KO cells, indicating that crista junctions are dispensable for mitochondrial tubular morphology.

Discussion

Mitochondrial crista junctions are crucial for mitochondrial structure and function. Using complexome profiling approach, we identified MIC13 as a novel subunit of MICOS complex. MIC13 was also reported as a subunit of MICOS complex in a recent publication [33]. Our data confirms the presence of MIC13 in MICOS complex. We have generated the first knock

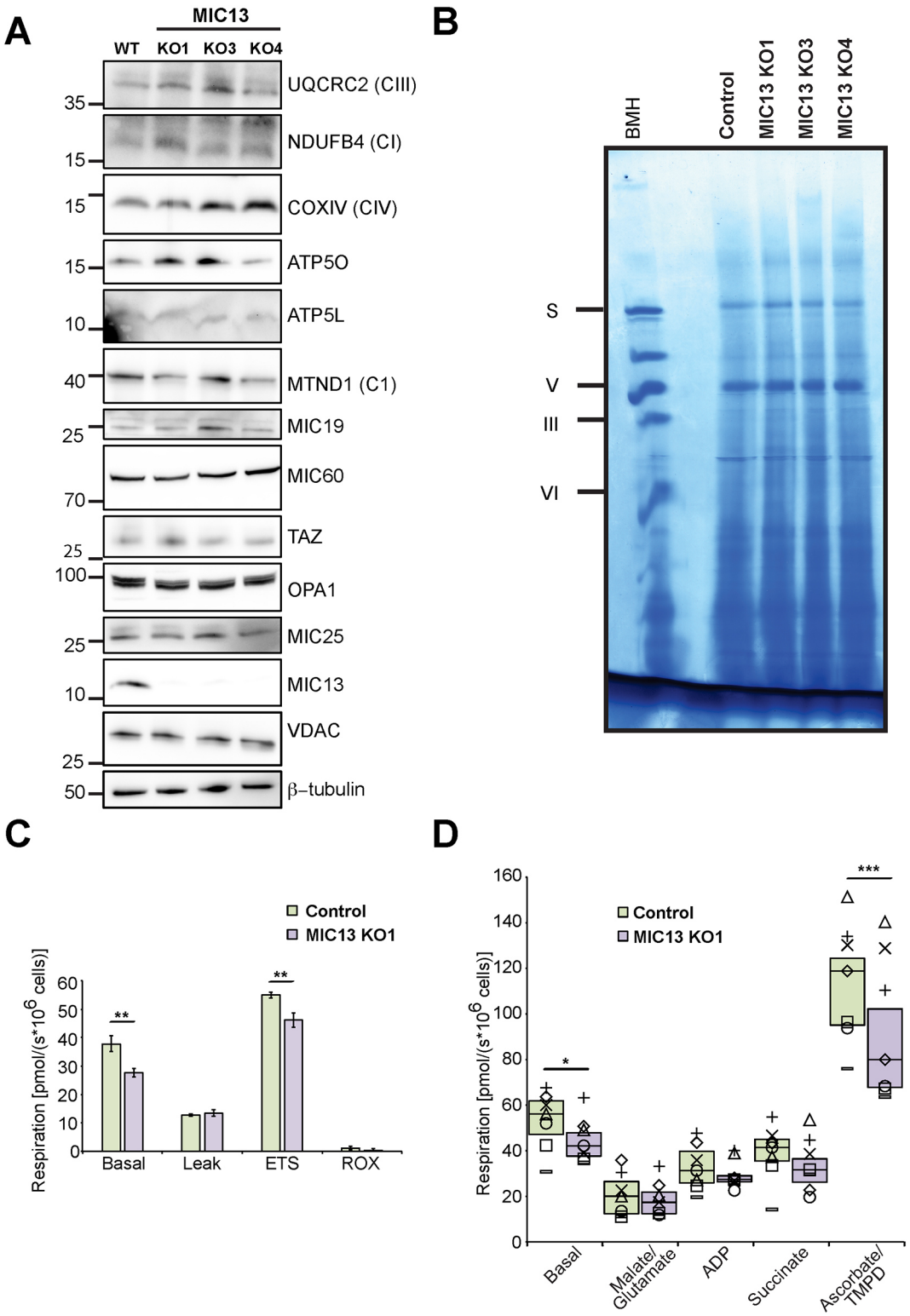

Fig 5. Stability and assembly of respiratory chain complexes are unchanged upon MIC13 depletion. (A) Immunoblot showing the steady state levels of various subunits of RC. (B) Blue-native electrophoresis of protein complexes stained with coomassie to detect major respiratory chain complexes in control and MIC13 KO cells. (C) Oxygen consumption rates of control and MIC13 KO1 cells are plotted as histogram (Mean±SE, N = 6). The basal, leak, ETS (electron transport system capacity or maximum respiration) and ROX (residual respiration) are shown

for control and MIC13 KO1 cells. **, p value < 0.01. (D) Oxygen consumption rates measured in digitonin permeabilized cells after addition of indicated respiratory substrates and inhibitors. Basal, malate/glutamate (Complex I), ADP, succinate (Complex II/III), and ascorbate/TMPD (Complex IV) respiration are represented as box plots on which the median and 75/25 percentiles is plotted. In addition, all data values from seven individual experiments are plotted (Δ = Exp.1, × = Exp. 2, ◊ = Exp. 3, – = Exp. 4, □ = Exp. 5, ○ = Exp. 6, + = Exp. 7). *, p value < 0.05; ***, p value < 0.001.

doi:10.1371/journal.pone.0160258.g005

out cell line of MIC13 using the CRISPR/Cas method. The knockout cell approach eliminates possible artefacts due to insufficient depletion of the protein of interest e.g. by a siRNA approach. MIC13 KO cells showed complete loss of crista junctions, hence proving an essential requirement of MIC13 in the formation of crista junctions. The cristae structure in MIC13 KO cells resembles the one that is observed upon deletion of certain MICOS subunits in yeast cells and mammalian cells with cristae arranged as an onion slices and devoid of any connection with IBM. We also observed a slight increase in area of mitochondria which correlates with the increased average area of cristae in the MIC13 KO cells suggesting the influence of CJs in determining the number and size of cristae per mitochondria. This strongly resembles the situation in Δ*MIC60/FCJ1* cells in baker's yeast [10]. Knockout cells of MIC25, which were generated using TALEN approach, did not show such drastic cristae phenotypes [23]. Contrary to earlier observations including ours [10, 19] knockdown cells of MIC60 showed circular cristae [23]. These differences in cristae phenotype of various subunits of MICOS indicate that they have different roles in the formation and maintenance of CJs. In this regard, the study of true knockout cell models might promote our understanding of the mechanisms mediating formation of cristae and crista junctions.

We observed that upon deletion of MIC13, the MICOS complex remains intact but is reduced in size. This smaller complex still contains the MIC60-MIC19-MIC25 subcomplex. MIC60 is the major component of MICOS complex. Despite the normal levels of MIC60 (and MIC60-MIC19-MIC25 subcomplex), crista junctions are completely absent in MIC13 KO cells implying that intact MIC60-MIC19-MIC25 subcomplex is not sufficient to maintain crista junctions. These results clearly show the importance of MIC13-MIC26-MIC27-MIC10 subcomplex for crista junction maintenance. Our study supports the hierarchical assembly of the MICOS complex which was also suggested earlier [37, 38]. It was suggested previously that MIC13 is required for the stability of MIC10 [33]. In a reciprocal experiment, we observed that MIC13 and MIC10 regulate each other´s stability. It is not understood that how this regulation is carried out. One possibility could be that during normal MICOS complex assembly MIC13 and MIC10 part of a transient MIC10-MIC13-MIC26-MIC27 subcomplex and depletion of one of the subunits of this subcomplex leads to degradation of the remaining subunits. Thus, we cannot conclude whether the loss of crista junctions is a direct or indirect consequence of MIC13 deletion. The crista junctions' phenotype in MIC13 KO cells could also be explained by a lack of MIC10. Mic10 forms large oligomers which are required for the formation of CJs [39, 40].

It was proposed that aberrant cristae structure could influence the assembly of the respiratory chain complexes [36]. We cannot support this as in our study loss of CJs in MIC13 KO cells does not influence assembly of major respiratory chain complexes. This is in accordance to the yeast phenotypes when Δ*mic60* and Δ*micos* cells were analyzed [41]. However, despite the normal assembly of the respiratory complexes, basal respiration was moderately reduced in the MIC13 KO cells. This indicates a functional role of crista junctions for proper functioning of respiratory chain complexes. Furthermore, we did not detect a role of CJs for allowing maintenance of tubular mitochondria. Overall, complete loss of CJs in the mammalian cells is apparently dispensable for viability of cells, OXPHOS complex assembly and mitochondrial morphology but affects basal respiration.

Using profile-profile comparison tools, a recent study indicated that Mic12/Aim5 from baker's yeast could be an ortholog of MIC13 [37]. However, the sequence similarity between these genes is very low and was not detected by us or a recent evolutionary analysis of the MICOS complex [38]. Mic12 was recently shown to be required for the coupling of two MICOS subcomplexes in baker's yeast [42] which support the idea that MIC13 and MIC12 have similar functions. Still, future studies are needed to test whether human MIC13 is a true orthologue of Mic12.

Material and Methods

Cell lines and cell culture

All the cells were cultured using Minimal Essential Media (M4655, sigma) with 1g/L of glucose supplemented with 10% Fetal Bovine Serum, 1mM Sodium Pyruvate (Gibco) and 1% Penicillin and streptomycin (Gibco), incubated at 37°C at 5% CO2 incubator. HEK (Flp-InTM T-RExTM 293) cells were obtained from Björn Stork from Institute of Molecular Medicine I, Düsseldorf, Germany.

Generation of MIC13KO cells using CRISPR/Cas method

For generation of knockouts of the MIC13, we selected the primers for targeting the Exon2 of MIC13 gene. We used website crispr.mit.edu for generation of primers using double nickase platform. We used these two sets of primers which have higher scores using this website. Pair 1: bottom strand `GCAGCTCCTGGTCGTACACCAGG` and top strand `GAGCCAGGCAGCCCTACAGAAGG`. Pair 2: bottom strand `CTGGTCGTACACCAGGTAGACGG` and top strand `AGGCAGCCCTACAGAAGGCTGGG`. Primers were generated and annealed to have overhangs of Bst1 restriction site, which were integrated in px335 (addgene) vector at Bst1 (NEB) site in its cloning site. The respective pair of plasmids for targeting the top and bottom strands respectively were transfected in HEK293 (Flp-InTM T-RExTM 293) cells using Effectene reagent (Qiagen) (transfection was done according to manufacturer's protocol). After two days of transfection, cells were trypsinized and sorted as single cells in a 96 well plates using FACS. These single cells were allowed to grow for 2–3 weeks until a visible colony could be found in the well. The single colony was trypsinized and further cultured. The cell lysate from these colonies was screened using western blotting for ones having no immunoreactivity to MIC13 antibody. The cells with no MIC13 protein were termed knockouts and used for further studies.

Transfections siRNA

HeLa cells were plated on a petri dish overnight for transfection of the siRNA of MIC13 and MIC10 (Invitrogen, shealth siRNA). Lipofectamine RNAiMax (Invitrogen) was used for the transfection of the siRNA using the manufacturer's protocol. We used 20nM final concentration for each of the siRNA. Scrambled siRNA provided by the manufacturers was used as control. The sample were collected after 72 h of transfection and prepared for western blotting or electron microscopy.

Electron microscopy

The cells were cultured on the petri dish with 80% confluency. The cells were chemically fixed using 3% glutaraldehyde buffered with 0.1M sodium cacodylate buffer, pH 7.2 on the petri dish. After fixation, cells were scraped using a cell scraper and collected as a pellet in a mini tube. The cell pellet is washed with 0.1M sodium cacodylate, pH 7.2 and subsequently embedded in 2% agarose. The staining was performed using 1% osmium tetroxide for 50min followed

by 1% uranyl acetate/ 1% phosphotungstic acid for 1h. These samples were dehydrated using the graded acetone series and specimens were embedded in spur epoxy resin for polymerization at 65°C for 24 h. The ultrathin sections were prepared using the microtome. Imaging was performed using Transmission electron microscope (Hitachi, H600) at 75V. Image were acquired using Bioscan model 792 (Gatan). Images were visualized and analyzed using ImageJ software. For measuring the size parameter of individual mitochondria, ImageJ Analyze Plugin was used.

Mitochondrial isolation and submitochondrial localization

The cells were scraped from the petri dish using a cell scarper and pelleted at 500 g for 5 min. This pellet was resuspended in an isotonic buffer (220 mM mannitol, 70 mM sucrose; 1 mM EDTA and 20 mM HEPES, pH 7.5 and 1x protease inhibitor cocktail (Roche)) for 5mins. Cells were lysed by mechanical rupture by repeatedly passing through a syringe needle of 20G cannula for 20 times. The suspension was centrifuged at 1000 g for 5 min to remove the cell debris and nuclei. The supernatant which contains heavy membrane was further centrifuged at 8000 g for 10 min to pellet crude mitochondria. This crude mitochondria were used for submitochondrial localization of MIC13 in mitochondria, where the swelling of the mitochondria was performed using 10mM HEPES, pH 7.5 for 10mins on ice. 1% TritonX-100 was used to solubilize all the membranes. Proteinase K was used at the final concentration of 50μg/ml for 10mins. The reaction was stopped using 2mM PMSF.

SDS electrophoresis and western blotting

The sample for the western blotting was prepared by scraping the cells in PBS. The protein extraction was done using RIPA lysis buffer. The amount of protein was determined using Bradford reagent and spectrophotometer for equal loading of a gel. The samples were prepared in Laemmli loading buffer. 10–20% precast Tricine gel (Invitrogen) was used (particularly for MIC13 as it is a small protein). The proteins were transferred onto nitrocellulose membrane and probed for various antibodies. Anti-HRP secondary antibodies were used. We used following antibodies for immunoblotting, MIC13 (Pineda, Berlin, polyclonal antibody raised in rabbit using following peptide CKAREYSKEGWEYVKARTK), MIC27/APOOL (Atlas Antibodies, HPA000612), MIC26/APOO (Thermo-Fisher, MA5-15493) MIC60/Mitofilin (Pineda, Berlin, polyclonal antibody raised in rabbit against human IMMT using the peptide CTDHPEIGEGKPTPALSEEAS), MIC10/MINOS1 (Pineda, Berlin, polyclonal antibody raised in rabbits against CQHDFQAPYL LHGKYVK), MIC25/CHCHD6 (cell signaling), VDAC (abcam), β-tubulin (Cell signaling), MIC19/CHCHD3 (abcam), ATP5L (proteintech), ATP5O (abcam), COXIV (abcam), NDUFB4 (abcam), UQCRC2 (abcam), MTND1 (abcam), TOM20 (Proteintech), TIM23 (BD biosciences), human TAZ1 (gift from Steve Claypool). Recording and visualization of chemiluminescent signals were done using VILBER LOURMAT Fusion SL (Peqlab).

Fluorescence microscopy

For colocalization of MIC13 with mitochondria, mitoGFP targeting into mitochondrial matrix was transfected into 143B cells using Effectene transfection reagent (protocol of manufacture was followed). For overexpression of MIC13, pxFLAG-MIC13 was cotransfected with mitoGFP. After 24h of transfection the cells were fixed with 4% paraformaldehyde, permeabilized with 0.15% Triton-X100 and blocked using 3%BSA. The anti-MIC13 or anti-FLAG were used respectively to visualize endogenous or over expressed MIC13. Imaging was done using Zeiss Apotome microscope. For mitochondrial morphology analysis, control and MIC13 KO cells were fixed and stained for Alexa-488 tagged cytochrome c antibody (BD bioscience). Images were

acquired using Zeiss LSM 710. Images were analyzed and prepared using Zeiss software using smooth filter.

Respirometry measurements

Respirometry experiments were performed with an Oxygraph-2k (Oroboros). To study the oxygen flux, oxygen consumption was observed according to Pesta and Gnaiger [43]. Basal respiration was measured in intact cells in complete growth media. The 'Leak' state was induced by addition of oligomycin (2 μg/ml) (Sigma). For maximal respiration (the electron transport system capacity (ETS)), CCCP (Sigma) was added in steps of 0.25 μM to a maximum final concentration of 4.5 μM. The residual oxygen consumption (ROX) was observed after addition of rotenone (0.5 μM) (Sigma) and antimycin A (2.5 μM) (Sigma).

To study respiratory chain complexes a protocol from Kuznetsov *et al.* [44] was used. Before the oxygen consumption measurements, the cells were pelleted and resuspended in MIR05 buffer (0.5 mM EGTA, 3 mM $MgCl_2$, 60 mM lactobionic acid, 20 mM taurine, 10 mM KH_2PO_4, 20 mM HEPES, 110 mM D-Sucrose, 1 g/l BSA, fatty acid free). Cells were permeabilized by addition of 10 μg digitonin (Sigma) per million cells in a total volume of 2 ml. Different substrates and inhibitors were consecutively added as follows: 10 mM glutamate (Sigma), 5 mM malate (Sigma), 5 mM ADP (Sigma), 0.5 μM rotenone (Sigma), 10 mM succinate (Sigma), 5 μM antimycin A (Sigma), 0.5 mM *N*,*N*,*N*′,*N*′-Tetramethyl-*p*-phenylenediamine dihydrochloride (TMPD) (Sigma), 2 mM ascorbate (Sigma) and 10 μM cytochrome C (Sigma).

Isolation of macromolecular complexes by blue native gels

Cells were homogenized in 1 ml buffer (83 mM sucrose, 7 mM sodiumphosphate, pH 7.5, 0.3 mM EDTA, 0.7 mM aminocaproic acid) by 30 strokes at 2,000 rpm using a motor-driven tightly fitting 0.5–1 ml glass/Teflon Potter-Elvehjem homogenizer. The homogenate was centrifuged 5 min at 500 g and 4°C. The resulting supernatant was aliquoted according to 20 mg cell wet weight and centrifuged 10 min at 22,000 xg. The pellet containing enriched mitochondrial membrane fraction were resuspended in 40 μl buffer A (50 mM NaCl, 50 mM imidazole pH 7, 1 mM EDTA, 2 mM aminocaproic acid). Membrane protein complexes were solubilized with 10 μl 20% digitonin (w/v in water) to obtain a detergent/protein ratio of 5 g/g. Samples were centrifuged for 10 min at 22,000 xg. 200 μg total protein were supplemented with 2.5 μl 5% Coomassie and 5 μl 50% glycerol and loaded equally onto two 3 to 18% gradient gels. For complexome profiling one BN-gel was stained with Coomassie and was scanned by an office scanner (Epson perfection 2400 PHOTO) for documentation. For identification, second BN-gel was blotted on PVDF membrane and decorated with antibodies against mitochondrial complexes. Chemiluminescence from blots was detected by ChemiDoc XRS system operated by Quantity One Software (Bio-Rad).

Sample preparation for complexome profiling

Coomassie stained gels were extensively washed with water. Each lane was cut into 60 equal slices and collected in 96 filter well plates (30–40μm PP/PE, Pall Corporation). The gel pieces were destained in 60% Methanol, 50 mM ammoniumbicarbonate (ABC). Solutions were removed by centrifugation for 2 min at 1500 rpm. Proteins were reduced in 10 mM DTT, 50 mM ABC for 1 hour at 56°C and alkylated for 45 min in 30 mM iodoacetamid. Samples were digested for 16 hours with trypsin (sequencing grade, Promega) at 37°C in 50 mM ABC, 0.01% Protease Max (Promega) and 1 mM $CaCl_2$. Peptides were eluted in 30% acetonitrile and 3% formic acid, centrifuged into a fresh 96 well plate, dried in speed vac and resolved in 1% acetonitrile and 0.5% formic acid.

Mass spectrometry

Liquid chromatography / mass spectrometry (LC/MS) was performed on Thermo Scientific™ Q Exactive mass spectrometer with an ultra-high performance liquid chromatography unit (Thermo Scientific Dionex Ultimate 3000) via a Nanospray Flex Ion-Source (Thermo Scientific) at the front end. Peptides were loaded on a C18 reversed-phase precolumn (Thermo Scientific) followed by separation on in-house packed 2.4 μm Reprosil C18 resin (Dr. Maisch GmbH) picotip emitter tip (diameter 100 μm, 15 cm long, New Objectives) using a gradient from 5% acetonitrile, 0.1% formic acid to 50% acetonitrile, 0.1% formic acid for 30 min with a flow rate of 400 nl/min. Each run was finished by washout with 80% acetonitrile, 0.1% formic acid and column equilibration in 5% acetonitrile, 0.1% formic acid. Mass spectrometry (MS) data were recorded by data dependent Top10 acquisition selecting the ten most abundant precursor ions in positive mode for fragmentation using dynamic exclusion of 30s. Full MS scan range was 300 to 2000 m/z with a resolution of 70000, and an automatic gain control (AGC) value of $3^{*}10^{6}$ total ion counts with a maximal ion injection time of 250 ms. Only higher charged ions (2+) were selected for MS/MS scans with a resolution of 17500, an isolation window of 2 m/z and an automatic gain control value set to $5^{*}10^{4}$ ions with a maximal ion injection time of 150 ms. Lock mass option for 445.120025 m/z (Olsen et al., 2005) and 371.10124 m/z was enabled to ensure high mass accuracy during many following runs.

Complexome profiling data analysis

X calibur Raw files were analysed by proteomics software Max Quant (1.5.2.8) [45]. The enzyme specificity was set to Trypsin, missed cleavages were limited to 2. Following variable modifications were selected: at N-terminus acetylation (+42.01), oxidation of methionine (+15.99), as fixed modification Carbamidomethylation (+57.02), on cysteines. Human reference proteome set from Uniprot (Download April 2015, 68506 entries) was used to identify peptides and proteins. False discovery rate (FDR) was set to 1%. MaxQuant output file includes peptide and protein identification, accession numbers, protein and gene names, sequence coverage of each sample or gel slice, posterior error probability (PEP) values and intensity-based absolute quantification (IBAQ) values for complexome profiling was prepared. Identifications from reverse decoy database, identified by site and known contaminants were excluded.

Abundance profiles were generated by NOVA software [46] using intensity-based absolute quantification (IBAQ) values from MaxQuant [45]. IBAQ values of proteins from gel lane fraction were normalized to maximum of the lane and hierarchical clustered using Pearson Correlation distance function and average linkage and displayed as heatmaps. For native mass calibration the slice number of the maximum appearance of mitochondrial complex II (123055 kDa), complex III dimer (483695 Da), Complex IV (210786 Da), complex V (618824Da) and respiratory supercomplex containing complex I, III dimer and one copy of complex IV (1654457Da) was used. The equation [$f(x) = 27240^{*}e\text{^}(0.0936x)$, $R^2 = 0.9918$] obtained by exponential regression was used to calculate the native masses of each slice.

Supporting Information

S1 Fig. Mitochondrial area and cristae density is more in MIC13 KO cells. (A) Box blot indicating the total mitochondrial area in control and MIC13 KO cells (*, p value < 0.05; **, p value < 0.01; $^{\#}$, p value = n.s.). (B) Box blot showing cristae area (per mitochondria) in control and MIC13 KO3 (****, p value < 0.0001).
(TIF)

S2 Fig. Complexome analysis of respiratory chain complexes in control and MIC13 KO1 cells.
(TIF)

S3 Fig. Mitochondrial morphology of MIC13 KO cells. Mitochondrial morphology of control and MIC13 KO cells analyzed by cytochrome *c* staining. The lower panel shows the zoomed image of the box in upper panel. Scale bar 10μm.
(TIF)

Acknowledgments

We thank Andrea Borchardt and Tania Portugall for excellent technical support and Jana Meisterknecht for excellent technical assistance generating the complexome profiling data. We are grateful to Klaus Zanger, Timm Filler, and Andreas Barbian from the Institute of Anatomy I, Heinrich Heine University, Düsseldorf, Germany, for assistance with EM imaging and to Stefanie Weidtkamp-Peters and the CAi imaging facility, Heinrich Heine University, Düsseldorf, Germany, for support with image acquisition.

References

1. Zick M, Rabl R, Reichert AS. Cristae formation-linking ultrastructure and function of mitochondria. Biochimica et biophysica acta. 2009; 1793(1):5–19. Epub 2008/07/16. doi: 10.1016/j.bbamcr.2008.06.013 PMID: 18620004.
2. Frey TG, Mannella CA. The internal structure of mitochondria. Trends in biochemical sciences. 2000; 25(7):319–24. Epub 2000/06/29. PMID: 10871882.
3. Frey TG, Renken CW, Perkins GA. Insight into mitochondrial structure and function from electron tomography. Biochimica et biophysica acta. 2002; 1555(1–3):196–203. Epub 2002/09/11. PMID: 12206915.
4. Reichert AS, Neupert W. Contact sites between the outer and inner membrane of mitochondria-role in protein transport. Biochimica et biophysica acta. 2002; 1592(1):41–9. Epub 2002/08/23. PMID: 12191767.
5. Mannella CA, Marko M, Penczek P, Barnard D, Frank J. The internal compartmentation of rat-liver mitochondria: tomographic study using the high-voltage transmission electron microscope. Microscopy research and technique. 1994; 27(4):278–83. Epub 1994/03/01. doi: 10.1002/jemt.1070270403 PMID: 8186446.
6. Vogel F, Bornhovd C, Neupert W, Reichert AS. Dynamic subcompartmentalization of the mitochondrial inner membrane. The Journal of cell biology. 2006; 175(2):237–47. Epub 2006/10/18. doi: 10.1083/jcb.200605138 PMID: 17043137; PubMed Central PMCID: PMCPmc2064565.
7. Wurm CA, Jakobs S. Differential protein distributions define two sub-compartments of the mitochondrial inner membrane in yeast. FEBS letters. 2006; 580(24):5628–34. Epub 2006/09/26. doi: 10.1016/j.febslet.2006.09.012 PMID: 16997298.
8. Scorrano L, Ashiya M, Buttle K, Weiler S, Oakes SA, Mannella CA, et al. A distinct pathway remodels mitochondrial cristae and mobilizes cytochrome c during apoptosis. Developmental cell. 2002; 2(1):55–67. Epub 2002/01/10. PMID: 11782314.
9. Mannella CA, Pfeiffer DR, Bradshaw PC, Moraru II, Slepchenko B, Loew LM, et al. Topology of the mitochondrial inner membrane: dynamics and bioenergetic implications. IUBMB life. 2001; 52(3–5):93–100. Epub 2002/01/19. doi: 10.1080/15216540152845885 PMID: 11798041.
10. Rabl R, Soubannier V, Scholz R, Vogel F, Mendl N, Vasiljev-Neumeyer A, et al. Formation of cristae and crista junctions in mitochondria depends on antagonism between Fcj1 and Su e/g. The Journal of cell biology. 2009; 185(6):1047–63. Epub 2009/06/17. doi: 10.1083/jcb.200811099 PMID: 19528297; PubMed Central PMCID: PMCPmc2711607.
11. von der Malsburg K, Muller JM, Bohnert M, Oeljeklaus S, Kwiatkowska P, Becker T, et al. Dual role of mitofilin in mitochondrial membrane organization and protein biogenesis. Developmental cell. 2011; 21(4):694–707. Epub 2011/09/29. doi: 10.1016/j.devcel.2011.08.026 PMID: 21944719.
12. Harner M, Korner C, Walther D, Mokranjac D, Kaesmacher J, Welsch U, et al. The mitochondrial contact site complex, a determinant of mitochondrial architecture. The EMBO journal. 2011; 30(21):4356–70. Epub 2011/10/20. doi: 10.1038/emboj.2011.379 PMID: 22009199; PubMed Central PMCID: PMC3230385.

13. Hoppins S, Collins SR, Cassidy-Stone A, Hummel E, Devay RM, Lackner LL, et al. A mitochondrial-focused genetic interaction map reveals a scaffold-like complex required for inner membrane organization in mitochondria. The Journal of cell biology. 2011; 195(2):323–40. Epub 2011/10/12. doi: 10.1083/jcb.201107053 PMID: 21987634; PubMed Central PMCID: PMC3198156.

14. Pfanner N, van der Laan M, Amati P, Capaldi RA, Caudy AA, Chacinska A, et al. Uniform nomenclature for the mitochondrial contact site and cristae organizing system. The Journal of cell biology. 2014; 204 (7):1083–6. Epub 2014/04/02. doi: 10.1083/jcb.201401006 PMID: 24687277; PubMed Central PMCID: PMCPmc3971754.

15. van der Laan M, Horvath SE, Pfanner N. Mitochondrial contact site and cristae organizing system. Current opinion in cell biology. 2016; 41:33–42. Epub 2016/04/12. doi: 10.1016/j.ceb.2016.03.013 PMID: 27062547.

16. Koob S, Reichert AS. Novel intracellular functions of apolipoproteins: the ApoO protein family as constituents of the Mitofilin/MINOS complex determines cristae morphology in mitochondria. Biological chemistry. 2014; 395(3):285–96. Epub 2014/01/07. doi: 10.1515/hsz-2013-0274 PMID: 24391192.

17. Zerbes RM, van der Klei IJ, Veenhuis M, Pfanner N, van der Laan M, Bohnert M. Mitofilin complexes: conserved organizers of mitochondrial membrane architecture. Biological chemistry. 2012; 393 (11):1247–61. Epub 2012/10/31. doi: 10.1515/hsz-2012-0239 PMID: 23109542.

18. Genin EC, Plutino M, Bannwarth S, Villa E, Cisneros-Barroso E, Roy M, et al. CHCHD10 mutations promote loss of mitochondrial cristae junctions with impaired mitochondrial genome maintenance and inhibition of apoptosis. EMBO molecular medicine. 2015; 8(1):58–72. Epub 2015/12/17. doi: 10.15252/emmm.201505496 PMID: 26666268.

19. John GB, Shang Y, Li L, Renken C, Mannella CA, Selker JM, et al. The mitochondrial inner membrane protein mitofilin controls cristae morphology. Molecular biology of the cell. 2005; 16(3):1543–54. Epub 2005/01/14. doi: 10.1091/mbc.E04-08-0697 PMID: 15647377; PubMed Central PMCID: PMCPmc551514.

20. Yang RF, Zhao GW, Liang ST, Zhang Y, Sun LH, Chen HZ, et al. Mitofilin regulates cytochrome c release during apoptosis by controlling mitochondrial cristae remodeling. Biochemical and biophysical research communications. 2012; 428(1):93–8. Epub 2012/10/13. doi: 10.1016/j.bbrc.2012.10.012 PMID: 23058921.

21. Darshi M, Mendiola VL, Mackey MR, Murphy AN, Koller A, Perkins GA, et al. ChChd3, an inner mitochondrial membrane protein, is essential for maintaining crista integrity and mitochondrial function. The Journal of biological chemistry. 2011; 286(4):2918–32. Epub 2010/11/18. doi: 10.1074/jbc.M110.171975 PMID: 21081504; PubMed Central PMCID: PMC3024787.

22. An J, Shi J, He Q, Lui K, Liu Y, Huang Y, et al. CHCM1/CHCHD6, novel mitochondrial protein linked to regulation of mitofilin and mitochondrial cristae morphology. The Journal of biological chemistry. 2012; 287(10):7411–26. Epub 2012/01/10. doi: 10.1074/jbc.M111.277103 PMID: 22228767; PubMed Central PMCID: PMCPmc3293568.

23. Ding C, Wu Z, Huang L, Wang Y, Xue J, Chen S, et al. Mitofilin and CHCHD6 physically interact with Sam50 to sustain cristae structure. Scientific reports. 2015; 5:16064. Epub 2015/11/05. doi: 10.1038/srep16064 PMID: 26530328; PubMed Central PMCID: PMCPmc4632003.

24. Xie J, Marusich MF, Souda P, Whitelegge J, Capaldi RA. The mitochondrial inner membrane protein mitofilin exists as a complex with SAM50, metaxins 1 and 2, coiled-coil-helix coiled-coil-helix domain-containing protein 3 and 6 and DnaJC11. FEBS letters. 2007; 581(18):3545–9. Epub 2007/07/13. doi: 10.1016/j.febslet.2007.06.052 PMID: 17624330.

25. Thapa D, Nichols CE, Lewis SE, Shepherd DL, Jagannathan R, Croston TL, et al. Transgenic overexpression of mitofilin attenuates diabetes mellitus-associated cardiac and mitochondria dysfunction. Journal of molecular and cellular cardiology. 2015; 79:212–23. Epub 2014/12/03. doi: 10.1016/j.yjmcc.2014.11.008 PMID: 25463274; PubMed Central PMCID: PMCPmc4302057.

26. Fukada K, Zhang F, Vien A, Cashman NR, Zhu H. Mitochondrial proteomic analysis of a cell line model of familial amyotrophic lateral sclerosis. Molecular & cellular proteomics: MCP. 2004; 3(12):1211–23. Epub 2004/10/27. doi: 10.1074/mcp.M400094-MCP200 PMID: 15501831; PubMed Central PMCID: PMCPmc1360176.

27. Koob S, Barrera M, Anand R, Reichert AS. The non-glycosylated isoform of MIC26 is a constituent of the mammalian MICOS complex and promotes formation of crista junctions. Biochimica et biophysica acta. 2015; 1853(7):1551–63. Epub 2015/03/15. doi: 10.1016/j.bbamcr.2015.03.004 PMID: 25764979.

28. Weber TA, Koob S, Heide H, Wittig I, Head B, van der Bliek A, et al. APOOL is a cardiolipin-binding constituent of the Mitofilin/MINOS protein complex determining cristae morphology in mammalian mitochondria. PloS one. 2013; 8(5):e63683. Epub 2013/05/25. doi: 10.1371/journal.pone.0063683 PMID: 23704930; PubMed Central PMCID: PMCPmc3660581.

29. Lamant M, Smih F, Harmancey R, Philip-Couderc P, Pathak A, Roncalli J, et al. ApoO, a novel apolipoprotein, is an original glycoprotein up-regulated by diabetes in human heart. The Journal of biological

chemistry. 2006; 281(47):36289–302. Epub 2006/09/08. doi: 10.1074/jbc.M510861200 PMID: 16956892.

30. Turkieh A, Caubere C, Barutaut M, Desmoulin F, Harmancey R, Galinier M, et al. Apolipoprotein O is mitochondrial and promotes lipotoxicity in heart. The Journal of clinical investigation. 2014; 124 (5):2277–86. Epub 2014/04/20. doi: 10.1172/jci74668 PMID: 24743151; PubMed Central PMCID: PMCPmc4001558.

31. Yu BL, Wu CL, Zhao SP. Plasma apolipoprotein O level increased in the patients with acute coronary syndrome. Journal of lipid research. 2012; 53(9):1952–7. Epub 2012/06/14. doi: 10.1194/jlr.P023028 PMID: 22693255; PubMed Central PMCID: PMCPmc3413234.

32. Heide H, Bleier L, Steger M, Ackermann J, Drose S, Schwamb B, et al. Complexome Profiling Identifies TMEM126B as a Component of the Mitochondrial Complex I Assembly Complex. Cell Metab. 2012; 16 (4):538–49. Epub 2012/09/18. S1550-4131(12)00332-4 [pii] doi: 10.1016/j.cmet.2012.08.009 PMID: 22982022.

33. Guarani V, McNeill EM, Paulo JA, Huttlin EL, Frohlich F, Gygi SP, et al. QIL1 is a novel mitochondrial protein required for MICOS complex stability and cristae morphology. eLife. 2015; 4. Epub 2015/05/23. doi: 10.7554/eLife.06265 PMID: 25997101; PubMed Central PMCID: PMCPmc4439739.

34. Koob S, Barrera M, Anand R, Reichert AS. Data supporting the role of the non-glycosylated isoform of MIC26 in determining cristae morphology. Data in brief. 2015; 4:135–9. Epub 2015/07/29. doi: 10.1016/j.dib.2015.04.014 PMID: 26217777; PubMed Central PMCID: PMCPmc4510393.

35. Ran FA, Hsu PD, Lin CY, Gootenberg JS, Konermann S, Trevino AE, et al. Double nicking by RNA-guided CRISPR Cas9 for enhanced genome editing specificity. Cell. 2013; 154(6):1380–9. Epub 2013/09/03. doi: 10.1016/j.cell.2013.08.021 PMID: 23992846; PubMed Central PMCID: PMCPmc3856256.

36. Cogliati S, Frezza C, Soriano ME, Varanita T, Quintana-Cabrera R, Corrado M, et al. Mitochondrial cristae shape determines respiratory chain supercomplexes assembly and respiratory efficiency. Cell. 2013; 155(1):160–71. Epub 2013/09/24. doi: 10.1016/j.cell.2013.08.032 PMID: 24055366; PubMed Central PMCID: PMC3790458.

37. Huynen MA, Muhlmeister M, Gotthardt K, Guerrero-Castillo S, Brandt U. Evolution and structural organization of the mitochondrial contact site (MICOS) complex and the mitochondrial intermembrane space bridging (MIB) complex. Biochimica et biophysica acta. 2016; 1863(1):91–101. Epub 2015/10/21. doi: 10.1016/j.bbamcr.2015.10.009 PMID: 26477565.

38. Munoz-Gomez SA, Slamovits CH, Dacks JB, Wideman JG. The evolution of MICOS: Ancestral and derived functions and interactions. Communicative & integrative biology. 2015; 8(6):e1094593. Epub 2016/04/12. doi: 10.1080/19420889.2015.1094593 PMID: 27065250; PubMed Central PMCID: PMCPmc4802753.

39. Barbot M, Jans DC, Schulz C, Denkert N, Kroppen B, Hoppert M, et al. Mic10 oligomerizes to bend mitochondrial inner membranes at cristae junctions. Cell metabolism. 2015; 21(5):756–63. Epub 2015/05/09. doi: 10.1016/j.cmet.2015.04.006 PMID: 25955211.

40. Bohnert M, Zerbes RM, Davies KM, Muhleip AW, Rampelt H, Horvath SE, et al. Central role of Mic10 in the mitochondrial contact site and cristae organizing system. Cell metabolism. 2015; 21(5):747–55. Epub 2015/05/09. doi: 10.1016/j.cmet.2015.04.007 PMID: 25955210.

41. Friedman JR, Mourier A, Yamada J, McCaffery JM, Nunnari J. MICOS coordinates with respiratory complexes and lipids to establish mitochondrial inner membrane architecture. eLife. 2015; 4. Epub 2015/04/29. doi: 10.7554/eLife.07739 PMID: 25918844; PubMed Central PMCID: PMCPmc4434539.

42. Zerbes RM, Hoss P, Pfanner N, van der Laan M, Bohnert M. Distinct Roles of Mic12 and Mic27 in the Mitochondrial Contact Site and Cristae Organizing System. Journal of molecular biology. 2016; 428 (8):1485–92. Epub 2016/03/13. doi: 10.1016/j.jmb.2016.02.031 PMID: 26968360.

43. Pesta D, Gnaiger E. High-resolution respirometry: OXPHOS protocols for human cells and permeabilized fibers from small biopsies of human muscle. Methods in molecular biology (Clifton, NJ). 2012; 810:25–58. doi: 10.1007/978-1-61779-382-0_3 PMID: 22057559.

44. Kuznetsov AV, Veksler V, Gellerich FN, Saks V, Margreiter R, Kunz WS. Analysis of mitochondrial function in situ in permeabilized muscle fibers, tissues and cells. Nature protocols. 2008; 3(6):965–76. Epub 2008/06/10. doi: 10.1038/nprot.2008.61 PMID: 18536644.

45. Cox J, Mann M. MaxQuant enables high peptide identification rates, individualized p.p.b.-range mass accuracies and proteome-wide protein quantification. Nature biotechnology. 2008; 26(12):1367–72. Epub 2008/11/26. doi: 10.1038/nbt.1511 PMID: 19029910.

46. Giese H, Ackermann J, Heide H, Bleier L, Drose S, Wittig I, et al. NOVA: a software to analyze complexome profiling data. Bioinformatics (Oxford, England). 2015; 31(3):440–1. Epub 2014/10/11. doi: 10.1093/bioinformatics/btu623 PMID: 25301849.

3.2. Cristae undergo continuous cycles of membrane remodelling in a MICOS-dependent manner

Article

TRANSPARENT PROCESS OPEN ACCESS

EMBO reports

Cristae undergo continuous cycles of membrane remodelling in a MICOS-dependent manner

Arun Kumar Kondadi[1,†], Ruchika Anand[1,†], Sebastian Hänsch[2], Jennifer Urbach[1], Thomas Zobel[2,§], Dane M Wolf[3,4,‡], Mayuko Segawa[4,‡], Marc Liesa[4,5], Orian S Shirihai[3,4], Stefanie Weidtkamp-Peters[2] & Andreas S Reichert[1,*]

Abstract

The mitochondrial inner membrane can reshape under different physiological conditions. How, at which frequency this occurs in living cells, and the molecular players involved are unknown. Here, we show using state-of-the-art live-cell stimulated emission depletion (STED) super-resolution nanoscopy that neighbouring crista junctions (CJs) dynamically appose and separate from each other in a reversible and balanced manner in human cells. Staining of cristae membranes (CM), using various protein markers or two lipophilic inner membrane-specific dyes, further revealed that cristae undergo continuous cycles of membrane remodelling. These events are accompanied by fluctuations of the membrane potential within distinct cristae over time. Both CJ and CM dynamics depended on MIC13 and occurred at similar timescales in the range of seconds. Our data further suggest that MIC60 acts as a docking platform promoting CJ and contact site formation. Overall, by employing advanced imaging techniques including fluorescence recovery after photobleaching (FRAP), single-particle tracking (SPT), live-cell STED and high-resolution Airyscan microscopy, we propose a model of CJ dynamics being mechanistically linked to CM remodelling representing cristae membrane fission and fusion events occurring within individual mitochondria.

Keywords crista junction; cristae; membrane dynamics; membrane potential; STED nanoscopy

Subject Categories Membranes & Trafficking; Organelles

DOI 10.15252/embr.201949776 | Received 28 November 2019 | Revised 13 January 2020 | Accepted 14 January 2020 | Published online 18 February 2020

EMBO Reports (2020) 21: e49776

Introduction

Mitochondria are vital organelles with key roles in energetics and metabolism of the cell. The ultrastructural morphology of this double-membrane-enclosed organelle is highly variable and altered in numerous human disorders [1,2]. The internal mitochondrial structure is characterized by invaginations of the inner membrane (IM) called cristae. The IM that closely remains apposed to the outer membrane (OM) is called the inner boundary membrane (IBM). The cristae membrane (CM) connects the IBM via a highly curved, circular or slit- or pore-like structures called crista junctions (CJs) [1,3–7]. CJs are structurally conserved with a diameter of 12–40 nm and were proposed to act as diffusion barriers for proteins or metabolites [8–11]. Thus, the presence of CJs could create distinct mitochondrial subcompartments by separating IBM from CM and intermembrane space (IMS) from intracristal space (ICS). Indeed, the CM is enriched in proteins involved in oxidative phosphorylation (OXPHOS), mitochondrial protein synthesis or iron–sulphur cluster biogenesis, whereas the IBM mainly contains proteins involved in mitochondrial fusion and protein import [12]. CJs could regulate bioenergetics by limiting the diffusion of ADP/ATP and affect the pH gradient across the IM [8–11]. As early as 1966, isolated mitochondria were known to occur in different morphological states, condensed (matrix condensed, high ADP, state III) or an orthodox (matrix expanded, low ADP, state IV) state, depending on the bioenergetic status [13–15]. Later, tomographic images of mitochondria undergoing this transition indicated that remodelling of the IM occurs in isolated mitochondria [10]. Cristae exist in different shapes and sizes depending on the physiological, bioenergetic or developmental cues [1,10,16]. Moreover, the general ability of cristae or CJs to dynamically remodel is well exemplified during apoptosis, where widening of CJs is observed, promoting cytochrome *c* release from the ICS into the cytosol [17,18]. However, molecular mechanisms for cristae

1 Institute of Biochemistry and Molecular Biology I, Medical Faculty, Heinrich Heine University Düsseldorf, Düsseldorf, Germany
2 Faculty of Mathematics and Natural Sciences, Center for Advanced Imaging, Heinrich Heine University Düsseldorf, Düsseldorf, Germany
3 Department of Medicine, Nutrition and Metabolism Section, Evans Biomedical Research Center, Boston University School of Medicine, Boston, MA, USA
4 Division of Endocrinology, Department of Medicine, Department of Molecular and Medical Pharmacology, David Geffen School of Medicine, University of California Los Angeles, Los Angeles, CA, USA
5 Molecular Biology Institute, University of California Los Angeles, Los Angeles, CA, USA
*Corresponding author. Tel: +49 211 81 12707; Fax: +49 211 81 13029; E-mail: reichert@hhu.de
†These first authors contributed equally to this work as first authors
‡These coauthors contributed equally to this work
§Present address: Münster Imaging Network, Cells in Motion Interfaculty Centre, Westfälische Wilhelms-Universität Münster, Münster, Germany

and CJs remodelling in response to metabolic and physiological adaptations are not known. Aberrant and altered cristae are associated with several human diseases including neurodegeneration, cancer, diabetes and cardiomyopathies [1,19], but their relevance to disease progression is unclear.

The formation of CJs is likely to require an intricate partnership between phospholipids and scaffolding proteins [20–22]. We identified that Fcj1 (*formation of crista junction protein 1*)/Mic60 resides preferentially at CJs in yeast, and its deletion leads to complete loss of CJs with cristae arranged as concentric stacks separate from the IBM. In addition, Fcj1/Mic60 and Su e/g (subunits of F_1F_o-ATP synthase) act antagonistically to control F_1F_o-ATP synthase oligomerization and thereby modulate formation of CJs and cristae tips [7]. Several groups have identified a large oligomeric complex termed mitochondrial contact site and cristae organizing system (MICOS) which is required for the formation and maintenance of CJs and contact sites between IM and OM [23–25]. The MICOS complex contains at least seven subunits in mammals: MIC10, MIC13, MIC19, MIC25, MIC26, MIC27 and MIC60 named after a uniform nomenclature [26]. Mic60 and Mic10 are considered to be the core components of the MICOS complex in baker's yeast as their deletion causes complete loss of CJs. MIC60 has a binding interface for a variety of proteins including TOM complex, OPA1, SAM/TOB, Ugo1 (mammalian homolog SLC25A46), DnaJC11, CHCHD10, DISC1 (disrupted-in-schizophrenia 1) and is proposed to provide the scaffold for MICOS as well as contact between IM and OM [27–34]. Mic10 contains conserved glycine motifs in its transmembrane domain that are crucial for MIC10 self-oligomerization and are required for the stability of CJs [35–37]. Mic10 additionally interacts with the dimeric F_1F_o-ATP synthase and promotes its oligomerization [38,39]. Both Mic60 and Mic10 have the capability to bend membranes [35,40,41]. Using complexome profiling, we identified MIC26/APOO and MIC27/APOOL as *bona fide* subunits of the MICOS complex [42,43]. Depletion or overexpression of MIC26 or MIC27 led to altered cristae morphology and reduced respiration. MIC27 binds to cardiolipin, the signature lipid in mitochondria [42]. The non-glycosylated form of MIC26 is a subunit of the MICOS complex, but not the glycosylated form [43]. Recently, we and another group have discovered that MIC13/QIL1 is an essential component of the MICOS complex responsible for the formation of CJs [44,45]. Loss of MIC13 resulted in reduced levels of MIC10, MIC26 and MIC27, accompanied by impaired OXPHOS. The protein levels of MIC60, MIC19 and MIC25 remain unaltered, suggesting that MICOS comprises two subcomplexes: MIC60/25/19 and MIC10/13/26/27 with MIC13 acting as a bridge between both subcomplexes [44,45]. Altered levels of MICOS components and their interactors are associated with many human diseases such as epilepsy, Down syndrome, frontotemporal dementia–amyotrophic lateral sclerosis, optic atrophy, Parkinson's disease, diabetes and cardiomyopathy [2,27,46]. Mutations in *MIC60* have been found in Parkinson's disease [47]. Mutations in *MIC13/QIL1* lead to mitochondrial encephalopathy and hepatic dysfunction [48–51].

Here, we studied cristae membrane remodelling in living cells and the role of MICOS complex in this context. To study systematically intramitochondrial dynamics of CJs and cristae, we devised a novel state-of-the-art method of live-cell STED super-resolution nanoscopy using the C-terminal SNAP-tagged versions of distinct mitochondrial proteins marking CJs and cristae. Within individual mitochondria MIC10- and MIC60-SNAP punctae marking CJs dynamically remodel to merge and split in a continuous and balanced manner. This occurred at a timescale of seconds and depends on the MICOS subunit MIC13. In conjunction, we observed that adjacent cristae marked by ATP5I-SNAP and COX8A-SNAP or by IM-specific dyes undergo repeated cycles of membrane remodelling in a similar timescale of seconds. Using different approaches, including live-cell STED after TMRM staining and photoactivation combined with high-resolution Airyscan fluorescence microscopy, we provide strong support that the spatial apposition between two adjacent cristae leads to an exchange of content and that cristae can transiently stay separated from other cristae or the IBM. Overall, by improved spatial (~60 nm) and temporal (~1.5–2.5 s) resolution using live-cell STED super-resolution nanoscopy in combination with the SNAP-tag technology and use of newly generated genetic cellular models lacking MICOS subunits, we resolved and characterized cristae membrane dynamics. Based on these findings, we propose a model linking CJ and CM dynamics and discuss the novel role of the MICOS complex and the physiological importance thereof.

Results

Mammalian MIC10 and MIC60 are required for cristae morphogenesis and cellular respiration

MIC60 and MIC10 are the core subunits of the MICOS complex that are also evolutionarily well conserved [52,53]. To better understand the role of these subunits in mammalian cells, we obtained human *MIC10* and *MIC60* knockout (KO) HAP1 cells. *MIC10* KO and *MIC60* KO have 29-bp deletion in exon 1 and 10-bp deletion in exon 8, respectively, leading to a frameshift and subsequent loss of the respective proteins (Fig 1A). Analysis of electron micrographs from these cells revealed that CJs are virtually absent in *MIC10* and *MIC60* KO cells (Fig 1B and C). The cristae membrane (CM) appears as concentric rings detached from the IBM (Fig 1B), consistent with earlier observations in baker's yeast and mammalian cells [7,23–25,54,55]. In addition, the abundance of cristae per mitochondrial section is reduced (Fig 1D). While the knockout of *MIC10* primarily causes a selective destabilization of the MICOS subcomplex comprising MIC13, MIC26 and MIC27, loss of MIC60 results in a clear destabilization of all subunits of the MICOS complex (Fig 1A), confirming its role as a main scaffolding subunit of MICOS. The basal and the maximal oxygen consumption rates of *MIC10* and *MIC60* KOs are significantly decreased compared to controls (Fig 1E and F), confirming the role of CJs in ensuring full bioenergetic capacity.

CJs are dispensable for the regular arrangement of MIC60 in the IBM

MICOS is a large oligomeric complex present at CJs. Using stimulated emission depletion (STED) super-resolution images of fixed WT HAP1 cells, we show a regularly spaced arrangement of MIC10 and MIC60 punctae along the IBM (Fig 2A) consistent with earlier reports [56,57]. We determined the median distance between consecutive punctae of MIC10 and MIC60 for each mitochondrion and called it interpunctae distance (IPD). The median mitochondrial

IPD was around 280 nm for both MIC10 and MIC60 in WT HAP1 cells under standard growth conditions (Fig 2B). Since *MIC60* deletion leads to reduction in all proteins of MICOS, while loss of *MIC10* still preserves MIC60 (Fig 1A), we asked whether MIC10 is required for the punctae-like appearance of MIC60. Deletion of MIC10, albeit leading to a loss of CJs, did not disturb the regular arrangement of MIC60 punctae along the mitochondrial length (Fig 2A). In line with this, the median IPD per mitochondrion of MIC60 in control and *MIC10 KO* cells was not significantly different (Fig 2B). Since lack of CJs together with loss of the MIC10/13/26/27 subcomplex did not alter the spatial arrangement of MIC60, we conclude that CJs are not necessary for regular spacing of MIC60 in the IBM (Fig 2C). We further analysed whether loss of MIC10 impairs formation of contact sites between the IM and OM marked by colocalization of MIC60 and TOMM70; two protein markers reported to be present at the contact sites in baker's yeast [23]. STED super-resolution nanoscopy

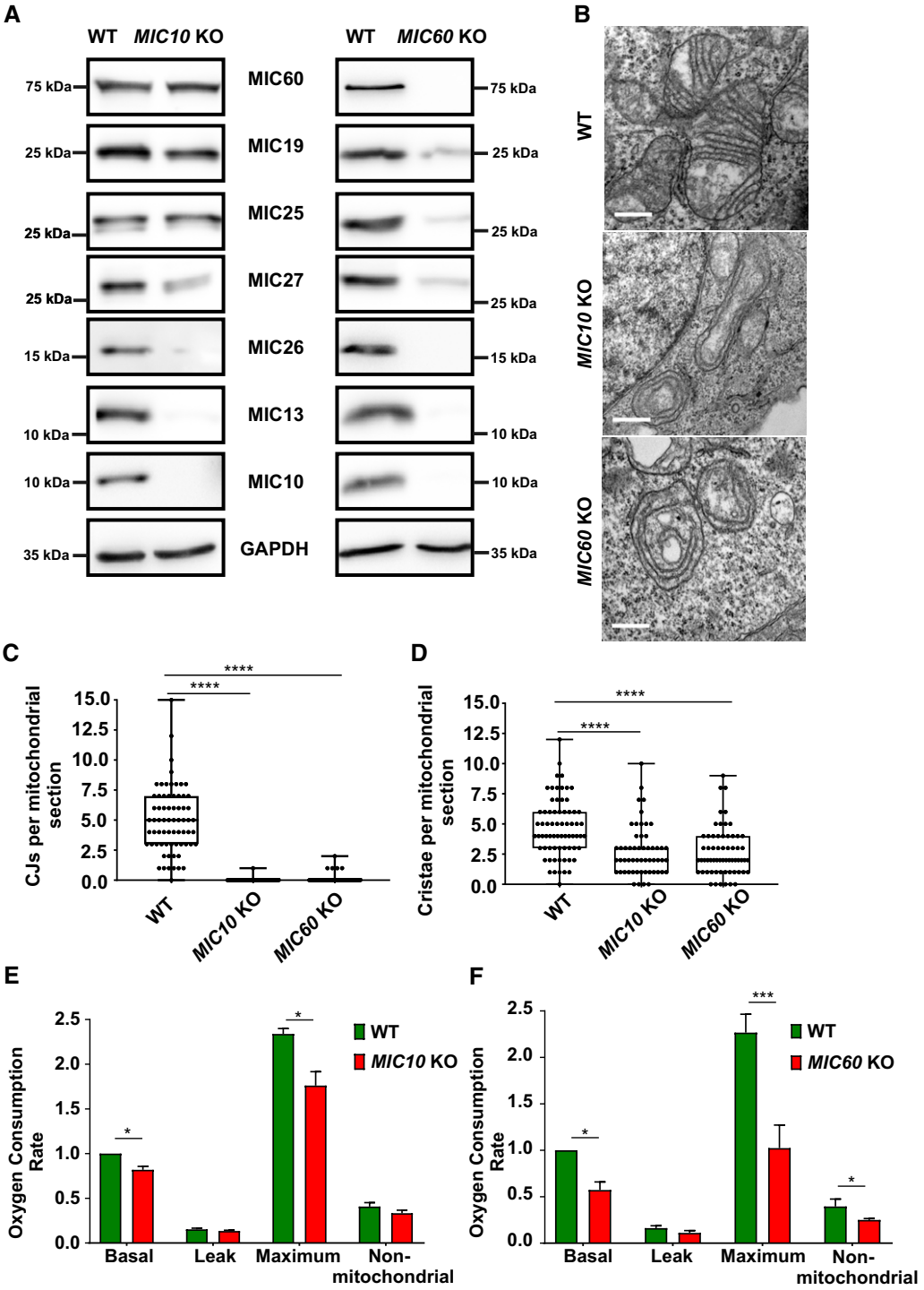

Figure 1.

Figure 1. *MIC10* and *MIC60* KO HAP1 cells show loss of crista junctions and impaired cellular respiration.

A Western blot analysis of lysates from WT and *MIC10* KO or *MIC60* KO HAP1 cells. *MIC10* KO cells show a drastic reduction in MIC13, MIC26 and MIC27 protein levels, while protein levels of other MICOS components remain unchanged. *MIC60* KO cells show a drastic reduction in protein levels of all MICOS components.

B Representative electron micrographs of WT, *MIC10* KO and *MIC60* KO HAP1 cells. Scale bar 500 nm.

C Quantification of CJs per mitochondrial section from different mitochondria in WT, *MIC10* and *MIC60* KO HAP1 cells using EM represented as boxplots. Boxplots show median and interquartile range from 25 to 75 percentile, and whiskers represent minimum and maximum value. Data from n = 55–69 mitochondria (from two independent experiments) are shown as data points in the boxplots. ****$P < 0.0001$ (using unpaired Student's t-test).

D Quantification of cristae per mitochondrial section from different mitochondria in WT, *MIC10* and *MIC60* KO HAP1 cells using EM represented as boxplots. Boxplots show median and interquartile range from 25 to 75 percentile, and whiskers represent minimum and maximum value. Data from n = 55–69 mitochondria (from two independent experiments) are shown as data points in the boxplots. ****$P < 0.0001$ (using unpaired Student's t-test).

E Comparison of oxygen consumption rates (pmol O_2/s, normalized for cell numbers by Hoechst staining) of basal, proton leak, maximum and non-mitochondrial respiration in WT and *MIC10* KO cells obtained from three independent experiments. The data are normalized to basal respiration from HAP1 WT. Bar and error bar represent mean ± SEM from 3 independent experiments. *$P = 0.034$ for basal (using one-sample t-test) and *$P = 0.018$ for maximum respiration (using unpaired Student's t-test).

F Comparison of oxygen consumption rates (pmol O_2/s, normalized for cell numbers by Hoechst staining) of basal, proton leak, maximum and non-mitochondrial respiration in WT and *MIC60* KO cells obtained from three independent experiments. The data are normalized to basal respiration from HAP1 WT. Bar and error bar represent mean ± SEM from three independent experiments. *$P = 0.01$ for basal (using one-sample t-test), ***$P = 0.0004$ for maximum respiration and *$P = 0.012$ for non-mitochondrial respiration (using unpaired Student's t-test).

after double immunostaining of HAP1 cells with antibodies against MIC60 and TOMM70 showed similar patterns of partial colocalization (Fig 2A, merge panel, arrowheads) in WT and *MIC10* KO cells, suggesting that MIC60/TOMM70-positive contact sites are still formed and maintained in *MIC10* KO cells. This supports the conclusion that MIC60 is positioned at uniform distances in the IBM,

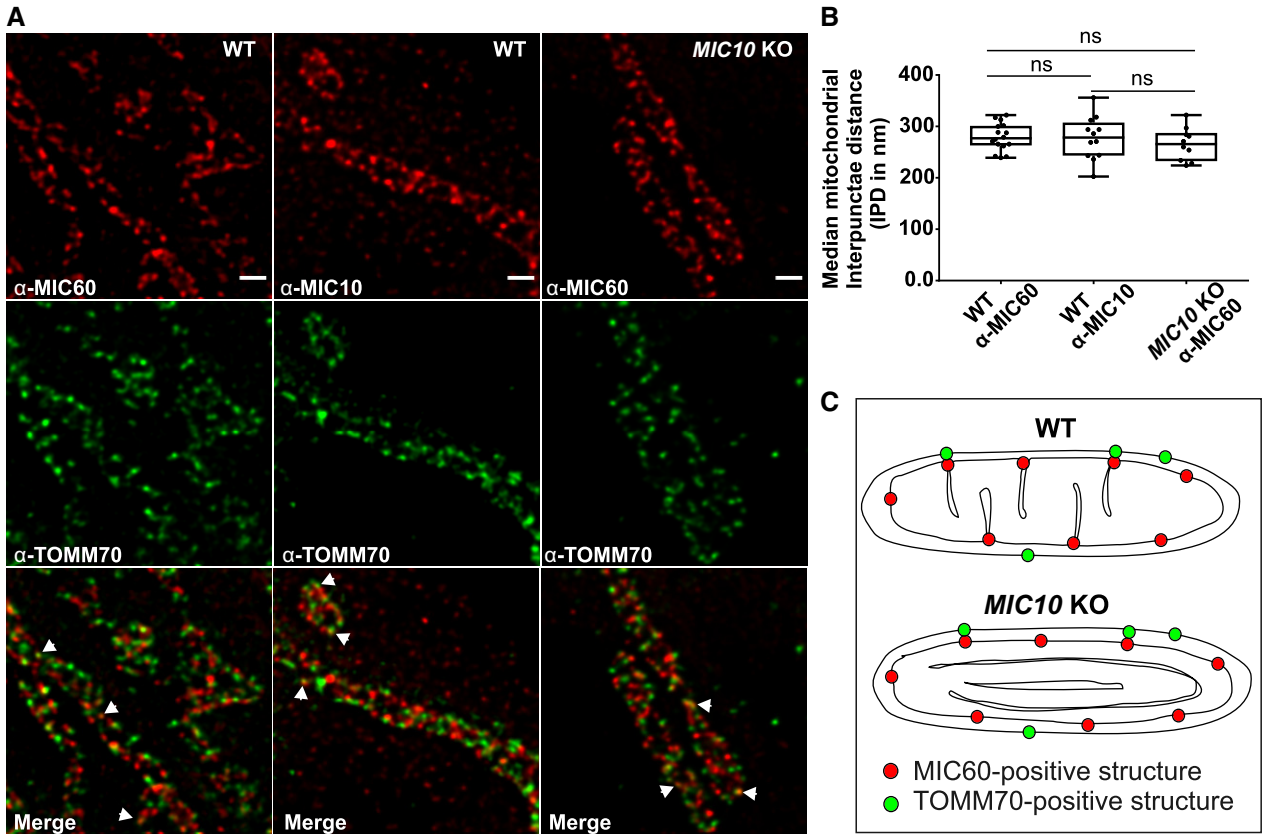

Figure 2. MIC60 assembles as regularly spaced punctae in the absence of CJs.

A Representative STED super-resolution images of WT and *MIC10* KO HAP1 cells immunostained with MIC60 or MIC10 antibodies (top panel) and TOMM70 (middle panel). Bottom panel shows merged images. Arrowheads show colocalization of MIC60 and TOMM70 punctae. Scale bar 500 nm.

B Quantification of median interpunctae distance (IPD) per mitochondrion between MIC60 and MIC10 punctae in indicated cell lines represented by boxplots. Boxplots show median and interquartile range from 25 to 75 percentile, and whiskers represent minimum and maximum value. Median IPD from n = 10–16 mitochondria (from two independent experiments) is shown as data points in the boxplots. ns, not significant, unpaired Student's t-test.

C Scheme shows MIC60 marking the nascent sites of CJ formation independent of MIC10 and presence of contact sites in WT and *MIC10* KO HAP1 cells shown by colocalization of MIC60 and TOMM70.

which are partially linked to the OM at contact sites, and that MIC60 represents a docking and scaffolding platform for other MICOS subunits (Fig 2C) such as MIC10 for CJ formation. This is consistent with an earlier report using confocal fluorescence microscopy in baker's yeast [58].

Crista junction proteins show a markedly reduced mobility in the inner membrane, and loss of *MIC13* affects the mobility of distinct inner membrane proteins

We asked how mobile the two core MICOS subunits, MIC60 and MIC10, are compared to other membrane proteins localized to different mitochondrial subcompartments. We constructed GFP-tagged versions of MIC60/MIC10, TOMM20, TIMM23 and ATP5I, established markers of CJs, OM, IBM and CM, respectively (Fig 3A), and performed fluorescence recovery after photobleaching (FRAP) experiments. For TOMM20, TIMM23 and ATP5I, we observed substantially shorter $T^{1/2}$ recovery times, higher diffusion coefficients and higher mobile fractions than for MIC10 and MIC60, demonstrating that CJ proteins are more restricted in movement compared to membrane proteins of other mitochondrial complexes present in various subcompartments (Fig 3B, D and E, Appendix Fig S1F). In line with this, MIC60 was reported to show restricted diffusion in the IM compared to OM proteins in another study [59]. To know whether the mobility of these proteins depends on the presence of a fully assembled MICOS complex, which is essential for formation of CJs, we generated *MIC13* KO HeLa cells that are well suited for microscopy of mitochondria. Consistent with prior reports [44,45], we observed a loss of MIC10, MIC26, MIC27, altered cristae morphology and loss of CJs in *MIC13* KO HeLa cells (Fig EV1A–D). Upon deletion of *MIC13*, in particular the diffusion coefficients of TIMM23 and MIC10 were altered to a major extent but less for MIC60 (Fig 3C–E, Appendix Fig S1A, B, D and F). The latter is consistent with our finding that MIC60 can arrange in regularly spaced punctae in the absence of other MICOS subunits (Fig 2). Interestingly, the loss of MIC13 decreases the mobile fraction of TIMM23 considerably. As in baker's yeast, Tim23 was shown to dynamically redistribute between the CM and the IBM in a manner dependent on mitochondrial protein import [12], we propose that the decreased TIMM23 mobile fraction in cells lacking CJs is due to trapping of a fraction of TIMM23 in the CM providing experimental support for the role of CJs as "gates" between the CM and the IBM and acting as diffusion barriers. This view is also supported by a very recent study showing that cristae behave as independent units within a single mitochondrion and can even adopt distinct levels of membrane potential [60]. Moreover, the mobility of MIC10 increases drastically in *MIC13* KO HeLa cells compared to WT cells, in line with the view that MIC13 is required for specifically stabilizing MIC10 at the MICOS complex [44,45].

To study the mobility of MIC10 and MIC60 by a different approach, we used single-particle tracking (SPT) technique (Fig 4). For this, we constructed the SNAP-tagged versions of MIC60 and MIC10 and confirmed their functionality as revealed by coimmunoprecipitation using anti-MIC13 antibodies (Fig EV2A and B), BN-PAGE analysis (Fig EV2C) and restoration of MIC13 levels upon MIC10 expression (Fig EV2D). This confirmed that the tagging of MIC10 and MIC60 with SNAP or GFP does not interfere with their function and proper incorporation into MICOS complex. Using SPT data, we observed that on average, MIC60-SNAP showed a smaller instantaneous diffusion coefficient (insD) compared to MIC10-SNAP (Fig 4A, B and E), consistent with the view that MIC60 represents regularly arranged nascent sites priming CJ and contact site formation which has to be steadily positioned. Deletion of *MIC13* led to a significant shift of tracks towards long-range movements (increased instantaneous diffusion coefficient; insD) of both MIC10 and MIC60 suggesting an increased mobility in both cases (Fig 4C–E). This is fully in line with the FRAP data and the interpretation that the MICOS complex is not fully assembled in *MIC13* KO cells. Further, in order to obtain a better understanding of the dynamic behaviour of individual single particles, each track was further subdivided into subtracks based on confinement in increasing order of directionality as confined diffusion, subdiffusion, normal diffusion or directed motion (Fig 4F, Appendix Fig S2E–L). The percentage of subtracks showing directed motion is significantly higher for MIC10 than for MIC60 in WT HeLa cells, suggesting a considerably higher directionality for MIC10 (Fig 4F and Appendix Fig S2E). Additionally, directed motion of both MIC10 and MIC60 is significantly higher in *MIC13* KO cells compared to WT (Fig 4F and Appendix Fig S2E), indicating that both subunits, when present in the fully assembled MICOS complex, have lower directed motion compared to when the MICOS complex exists in separate subcomplexes. Intriguingly, MIC10-directed motion in *MIC60* KOs is significantly reduced compared to control cells, indicating that the presence of MIC60 is specifically required for the enhanced directed motion of MIC10 (Fig 4F and Appendix Fig S2A–D). This suggests that MIC10 is recruited to the MICOS complex via MIC60. We propose that MIC60 acts as a docking platform pioneering CJ formation, consistent with our findings in this study (Fig 2).

Crista junctions dynamically move within the inner membrane in a reversible and balanced manner

FRAP and SPT data provided insights about the mobility of MIC10 and MIC60 as a group of molecules and individual MIC10 and MIC60 molecules within the IBM, respectively. As immunostaining of MIC10 and MIC60 revealed regularly arranged CJ punctae using STED nanoscopy (Fig 2A), we further asked if CJs are dynamic and if so at what timescale individual CJs move. For this, we devised a novel method to perform live-cell STED super-resolution nanoscopy using MIC60-SNAP and MIC10-SNAP as markers of CJs. SNAP-tag, a well-characterized protein tag, binds covalently to silicon rhodamine [61,62] and allows high-resolution imaging with minimal fluorophore bleaching [63]. The functionality and the proper incorporation of MIC10- and MIC60-SNAP into the MICOS complex were verified as described before (Fig EV2). The MIC10-SNAP and MIC60-SNAP fusion proteins were arranged in a regularly spaced punctae-like pattern across the IBM (Figs 5A and EV3A) as shown for the endogenous proteins using immunostaining (Fig 2A), providing further evidence for proper localization of the tagged constructs. We were able to image MIC10- and MIC60-SNAP for ~15 s at least every 2.6 s. While mitochondria as a whole stay relatively static during this observation time, we observed rapid movements of MIC10/MIC60-SNAP punctae during this short time period (Movies EV1 and EV2), demonstrating that CJs show an unexpectedly pronounced dynamic behaviour at a timescale of seconds. We repeatedly visualized these movies, by going back and forth between consecutive frames, to

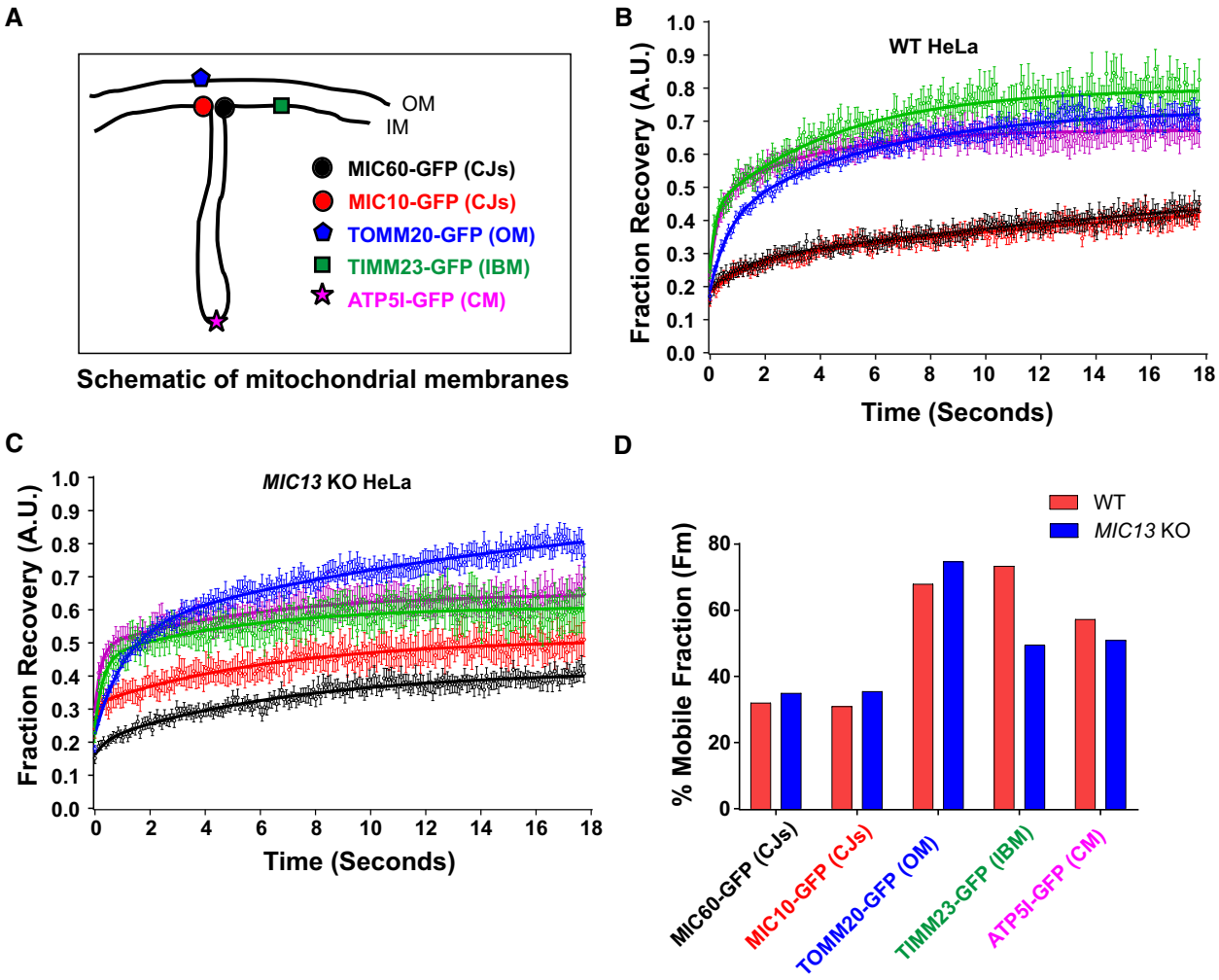

E Diffusion coefficient (μm²/second) of different molecules

	Mitochondrial Compartment	Molecule	WT (Fast)	*Mic13* KO (Fast)	WT (Slow)	*Mic13* KO (Slow)
1	**CJs**	MIC60-GFP	0.048	0.139	0.002	0.008
2	**CJs**	MIC10-GFP	0.041	0.453	0.002	0.008
3	**OM**	TOMM20-GFP	0.088	0.052	0.010	0.003
4	**IBM**	TIMM23-GFP	0.325	0.195	0.012	0.010
5	**Cristae**	ATP5I-GFP	0.185	0.278	0.015	0.010

Figure 3. Mobility of crista junction proteins is restricted compared to proteins of other mitochondrial subcompartments, and loss of MIC13 affects the mobility of distinct IM proteins.

A Scheme of investigated marker proteins, subjected to FRAP, located at different mitochondrial subcompartments.

B, C FRAP curves (curve fitted) of WT (B) and *MIC13* KO HeLa cells (C) expressing GFP-tagged fusion proteins of MIC60 (CJs), MIC10 (CJs), TOMM20 (OM), TIMM23 (IBM) and ATP5I (CM). Average FRAP curves (intensities in arbitrary units) for each marker were obtained (three independent experiments, 6–10 mitochondria for each experiment). Error bars for each time point representing SEM are shown.

D Histogram showing average percentage of mobile fractions, obtained from curve fits of all mitochondria expressing GFP-tagged versions of MIC60 (CJs), MIC10 (CJs), TOMM20 (OM), TIMM23 (IBM) and ATP5I (CM) in WT and *MIC13* KO HeLa cells (data calculated from FRAP curves shown in B and C that are obtained from three independent experiments, 6–10 mitochondria from each experiment).

E Diffusion coefficients of the above-mentioned proteins are shown in the table.

check for a possible regular pattern of MIC10 or MIC60 movement within a mitochondrion. Firstly, we focused on MIC10-SNAP and manually tracked the individual punctae of MIC10 in subsequent frames (Fig 5A and B, Movie EV3). We observed numerous instances where two MIC10-SNAP punctae rapidly merged into one visible puncta, split and re-merged at a timescale of seconds (Fig 5B, Movie

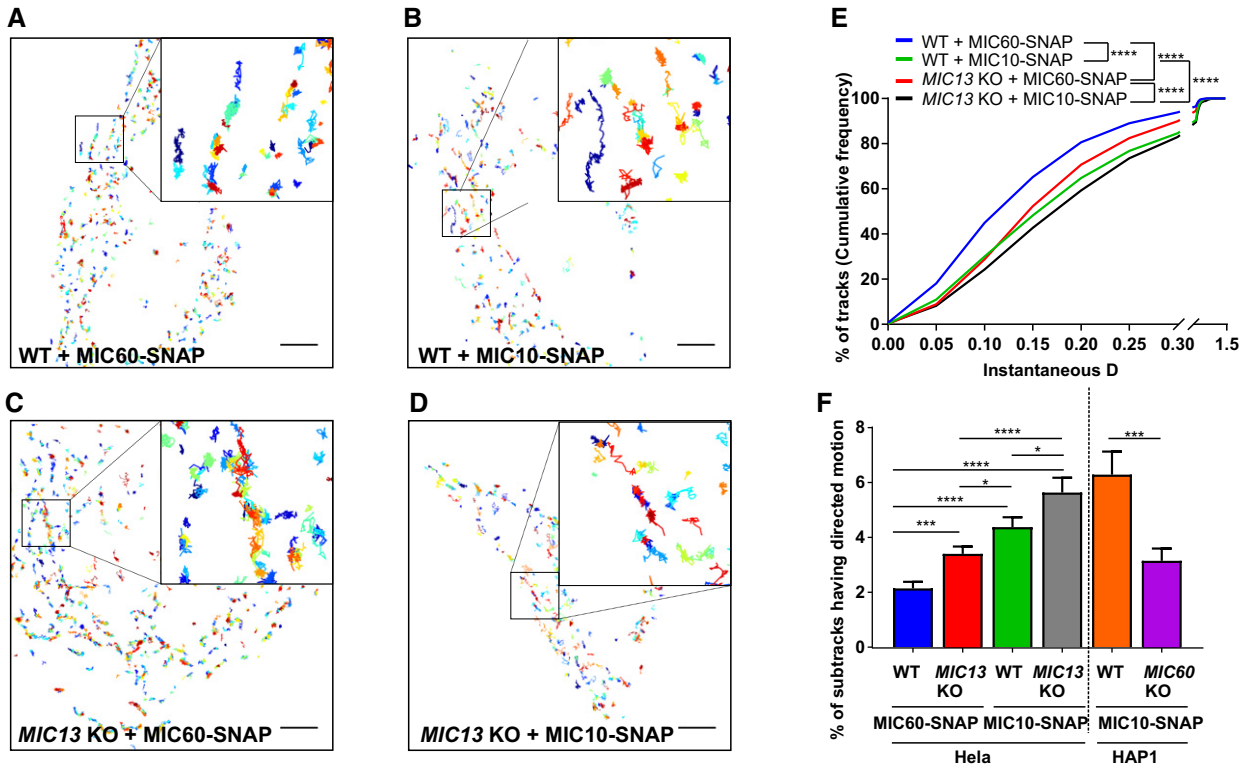

Figure 4. Single-particle tracking reveals requirement of MIC60 for high directionality of MIC10 motion.

A–D Representative single-particle tracks of cells expressing MIC60- (A) and MIC10-SNAP (B) in WT HeLa cells and MIC60- (C) and MIC10-SNAP (D) in *MIC13* KO HeLa cells, stained with silicon rhodamine dye and imaged at a rate of 33 ms/frame. Single tracks were colour-coded according to temporal appearance. Scale Bar 5 µm. Insets in each image show zoomed-in images of few representative tracks.

E Cumulative frequency of tracks having corresponding values of instantaneous diffusion coefficients (insD) in WT and *MIC13* KO HeLa cells expressing MIC60- and MIC10-SNAP stained with silicon rhodamine. Number of tracks analysed (obtained from two independent experiments): n = 2,541, 2,540, 3,560 and 1,441 in WT HeLa cells expressing MIC60-SNAP and MIC10-SNAP, *MIC13* KO HeLa cells expressing MIC60-SNAP and MIC10-SNAP, respectively. (****$P \leq 0.0001$ for all possible comparisons, unpaired Student's t-test).

F Percentage of subtracks having directed motion in WT and *MIC13* KO HeLa cells expressing MIC60- and MIC10-SNAP and in WT and *MIC60* KO HAP1 cells expressing MIC10-SNAP. Number of corresponding subtracks analysed (obtained from two independent experiments): n = 2,561, 2,443, 3,402, 1,360, 561 and 1,110. Data are mean ± SEM. *$P \leq 0.05$, ***$P \leq 0.001$, ****$P \leq 0.0001$, unpaired Student's t-test.

EV3). The term "merging" of two fluorescent MIC10/MIC60-positive punctae implies a proximity of ~60 nm or less due to the given spatial resolution of 50–60 nm using STED nanoscopy. We blindly quantified the occurrence of merging/splitting events of visible puncta per unit length of mitochondria and found that the numbers for merging and splitting events per time were similar, indicating that these events are balanced and possibly coupled (Fig 5E). MIC60-SNAP showed a very similar pattern of merging and splitting of adjacent punctae (Fig EV3A, B and E, Movie EV4) which also occurred at a similar temporal frequency compared to MIC10-SNAP punctae. We conclude that CJs marked by MICOS subunits in WT cells dynamically merge and split in a reversible and balanced manner at a timescale of seconds.

CJ dynamics occur in a MIC13-dependent manner

To test whether the dynamic behaviour of MIC60-SNAP punctae depends on the presence of a fully assembled MICOS complex, we analysed dynamics of MIC60-SNAP in *MIC13* KO cells. We again observed the regular arrangement of MIC60-SNAP punctae in the IBM of mitochondria in *MIC13* KO cells (Fig EV3C) consistent with our observation that MIC60 forms regularly arranged punctae also in the absence of MIC10 (Fig 2). MIC60-SNAP punctae showed dynamic movements in *MIC13* KO cells (Fig EV3D, Movie EV5); however, this occurred at a markedly reduced frequency when compared to WT HeLa cells (Fig EV3C and E, Movie EV5). This indicates that, although the regular arrangement of MIC60 in principle is unaltered, the movement of MIC60-positive punctae, reflected normally by balanced merging and splitting events, is drastically impaired in the absence of CJs in *MIC13* KO cells. We also expressed MIC10-SNAP in *MIC13* KOs and found that MIC10-positive punctae are dynamic, yet the merging and splitting events of these punctae were markedly reduced compared to WT cells (Fig 5C–E). These observations indicate that the extent of CJ dynamics depends on a functional MIC13-containing MICOS complex, which would be needed for cristae to be connected to the IBM via CJs (Fig 5F).

To further corroborate our findings on CJ dynamics, we decided to analyse the movement of MIC13-SNAP, another marker for CJs, in WT HeLa cells. Different from MIC60 or MIC10, we observed that the staining pattern of MIC13-SNAP not only marked regularly

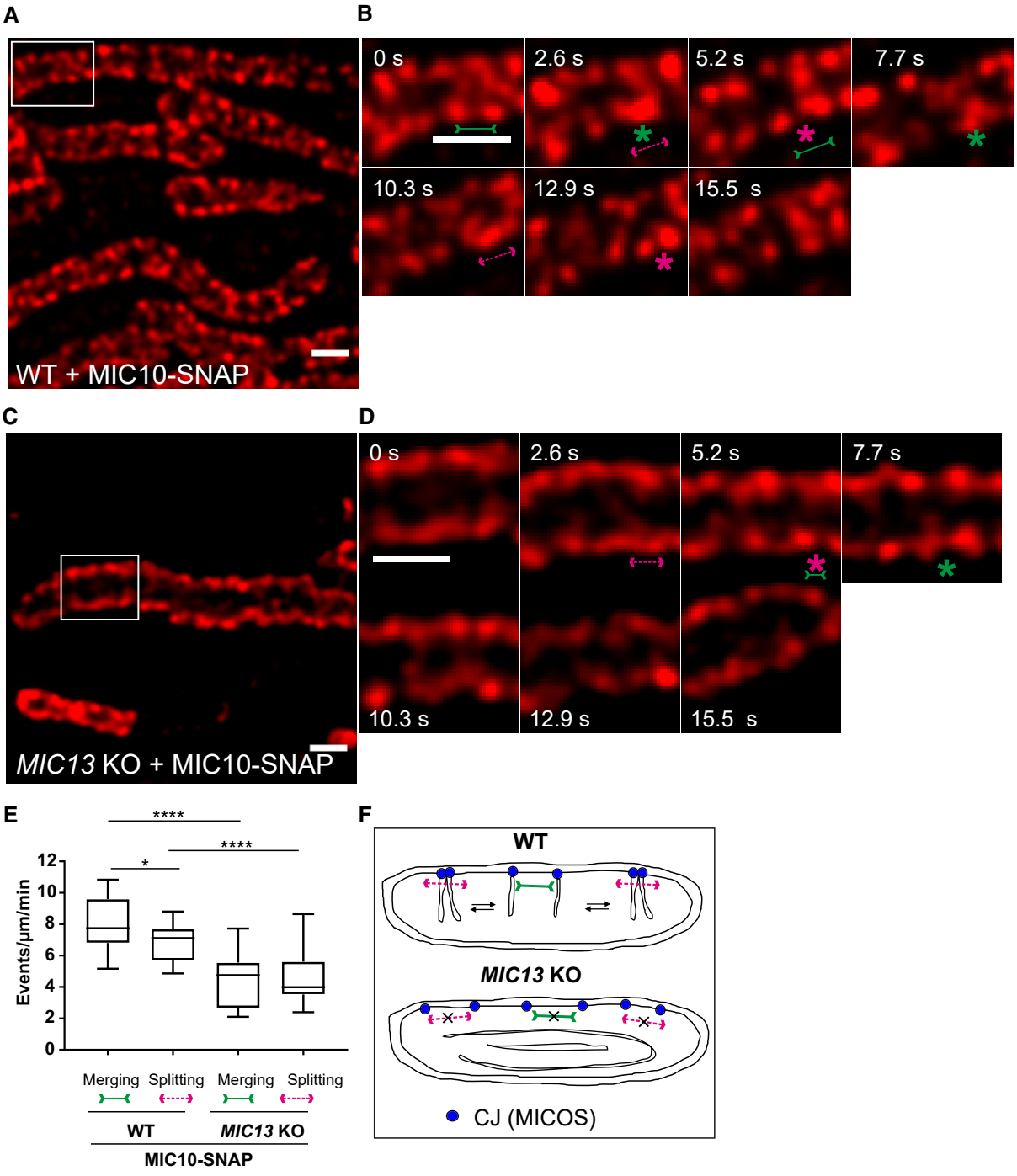

Figure 5. Crista junctions marked by MIC10-SNAP dynamically merge and split within a mitochondrion in a MIC13-dependent manner.

A–D Representative live-cell STED super-resolution images (t = 0 s) showing WT (A) and *MIC13* KO (C) HeLa cells expressing MIC10-SNAP stained with silicon rhodamine. Box in (A and C) mark selection shown as a zoom in panel (B and D), respectively. Scale bar 500 nm. Time-lapse image series of a mitochondrion expressing MIC10-SNAP in WT (B) and *MIC13* KO (D) HeLa cells (2.6 s/frame). Green and magenta asterisks show merging and splitting events of MIC10-SNAP, respectively. Green arrows pointing inward connected by solid line and magenta arrows pointing outward connected by dotted line show sites of imminent merging and splitting events, respectively. Scale bar 500 nm.

E Blind quantification of merging and splitting events of CJs in WT and *MIC13* KO HeLa cells expressing MIC10-SNAP (three independent experiments, 5–8 mitochondria for each experiment) represented as boxplots. Boxplots show median and interquartile range from 25 to 75 percentile, and whiskers represent minimum and maximum value. *P = 0.026 (merging and splitting events in WT cells) and ****P < 0.0001 (merging and splitting events of WT versus *MIC13* KO), unpaired Student's t-test.

F Scheme representing the dynamic nature of CJs in WT and *MIC13* KO cells.

arranged punctae in the IBM but also labelled transverse bridges across mitochondria resembling cristae membranes (Figs 6A–D and EV4A–D (raw data)). This dual distribution of MIC13-SNAP with maximal intensity at the IBM region is illustrated using line scans of fluorescence intensities along three cristae (Fig 6E and F), suggesting that MIC13-SNAP is dually localized to both CJs and cristae. As endogenous MIC13 in WT HeLa cells is mostly found as punctae in the IBM region (Fig EV2E), we attribute the partial localization of MIC13 to cristae to excess of MIC13-SNAP in the IM. Earlier studies have shown the partial occurrence of MICOS subunits in the CM and at cristae tips as well [7,23,28,56]. Nevertheless, in this context this is even beneficial as it allows us to visualize cristae and CJs at the same time. We analysed the movement of MIC13-SNAP in live-cell STED nanoscopy and observed dynamics of both CJs and CMs at a timescale of seconds (Movie EV6). We not only observed merging and splitting events of CJs as shown by MIC10-SNAP and MIC60-SNAP, but also dynamic movement of cristae attached to these CJs (Fig 6B and D). Upon careful analysis, we observed several instances showing that, when two CJs move towards each other, reaching a proximity of ~60 nm or less based on the spatial resolution of STED nanoscopy, they also bring along adjoining cristae close to each other generating the appearance that two cristae originate from one region in the IBM resembling the letter "V" (Figs 6B and EV4B (raw data), from 0 to 2.5 s, Movie EV7). Moreover, we observe other occasions where the fluorescence staining of cristae rather appeared to merge internally, along the length of other cristae, sometimes forming structures resembling the letters "X" and "Y" (Figs 6B and EV4B (raw data) at 5 and 14.9 s, respectively). In many instances, such events are directly followed by a crista splitting event at or near the site of the prior merging event (Figs 6B and EV4B (raw data), arrows pointing outward). To better visualize these events, we acquired images every 1.3 s and also found numerous examples of apparently linked merging and splitting events of cristae (Figs 6C and D, and EV4C and D (raw data), Movies EV8 and EV9). We propose that cristae undergo dynamic and continuous events of membrane remodelling, in a way resembling the cycles of merging and splitting observed for CJs.

Cristae membrane dynamics depends on the MICOS complex

To substantiate our initial observation of cristae membrane dynamics using MIC13-SNAP, we obtained SNAP-tagged versions of *bona fide* cristae markers, ATP5I and COX8A of F_1F_O ATP synthase and complex IV, respectively. HeLa cells expressing ATP5I-SNAP and COX8A-SNAP were imaged by live-cell STED super-resolution nanoscopy. The STED images of both ATP5I and COX8A showed transversely spanning bridges across the mitochondria (Fig 7A, Appendix Fig S3A), consistent with electron micrographs of cristae in HeLa cells. ATP5I-SNAP shows maximum fluorescence intensities in the centre of cristae in exemplary line scans (Fig 7E and F) in accordance with ATP5I, a subunit of F_1F_O ATP synthase complex, primarily located within the cristae and less at the IBM. Further, intensity profiles of line scans perpendicular to cristae (Figs 7A and EV5A) show that we can resolve adjacent cristae that are only ~50–60 nm apart (Fig EV5B) using live-cell STED imaging. Cristae were rapidly changing their position in consecutive timeframes confirming that cristae visualized with ATP5I-SNAP and COX8A-SNAP are dynamic within mitochondria at a timescale of seconds (Fig 7B, Appendix Fig S3B and Movie EV10). We observed several instances where the fluorescence signals of ATP5I-/COX8A-SNAP-positive cristae merged either across the IBM (transverse-type mergence) or along their length (X- or Y-type mergence) (Fig 7B, Appendix Fig S3B, Movies EV11 and EV12), consistent with our observations using MIC13-SNAP (Fig 6). Again, most of the instances of merging events were accompanied by a subsequent splitting event (Figs 7B, and EV4E and F (raw data), Appendix Fig S3B). We also observed merging and splitting events of fluorescence signals when we acquired images in XZ dimension (Z-axis, diffraction-limited confocal imaging; *X*-axis STED super-resolution (Fig EV5C and D). This strongly suggests that parallel oriented cristae sheets shown here in the *z*-axis do not simply overlap in different planes along the *z*-axis but indeed appose each other as close as ~60 nm or less in a reversible manner within a single mitochondrion. Next, we performed a blind quantification of the rate of merging and splitting events of respective fluorescence signals per unit length of mitochondria (μm) and found that they occur in a balanced manner with 4–12 events per μm per min using both ATP5I-SNAP and COX8A-SNAP (Fig 7G, Appendix Fig S3E). As opposed to the classical view of static cristae invaginating from the IBM, our results demonstrate that in addition to CJs, cristae constantly change their shape in a way that involves close apposition and subsequent splitting from each other. This challenges the prevailing view that cristae are constantly attached to CJs and represent rather static structures. Moreover, our observations are consistent with another possibility, namely that cristae may even pinch-off transiently and subsequently reconnect to the IBM or with other cristae.

Next, we checked whether the presence of a fully assembled MICOS complex is required for the dynamic behaviour of cristae using *MIC13* KO cells. We overexpressed ATP5I-SNAP and COX8A-SNAP in *MIC13* KO cells and performed blind quantification of the rate of merging and splitting events of respective fluorescence signals per unit length of mitochondria. This revealed that CM remodelling is significantly reduced in cells lacking MIC13 (Fig 7C, D and G, Appendix Fig S3C–E, Movies EV13 and EV14). Hence, a functional MICOS complex is required for CM dynamics, further supporting the view that CJ formation and dynamics are linked to CM dynamics.

Cristae membrane dynamics is accompanied by redistribution of membrane potential from distinct cristae to other regions of the inner membrane

The timescales of intramitochondrial membrane dynamics, the balanced occurrence of these events and the morphological features observed were very similar despite using a variety of protein markers (MIC10-, MIC60-, MIC13-, ATP5I- and COX8A-SNAP) for both CJs and cristae. This makes it unlikely that the observed cristae remodelling events are merely due to diffusion of different membrane protein complexes within a rather static IM. Still, we decided to use mitochondria-specific membrane dyes not labelling specific protein complexes. We further asked whether cristae merging events may result in an immediate change in the membrane potential $\Delta\Psi$ between distinct cristae, similar to the situation previously described for fusion between two mitochondria [64]. Thus, we used TMRM, a dye labelling the IM in a membrane potential manner. Performing STED with TMRM, as opposed to SNAP-tagged proteins, is challenging due to its high sensitivity to photobleaching. Nevertheless, we could record movies for a similar time period as

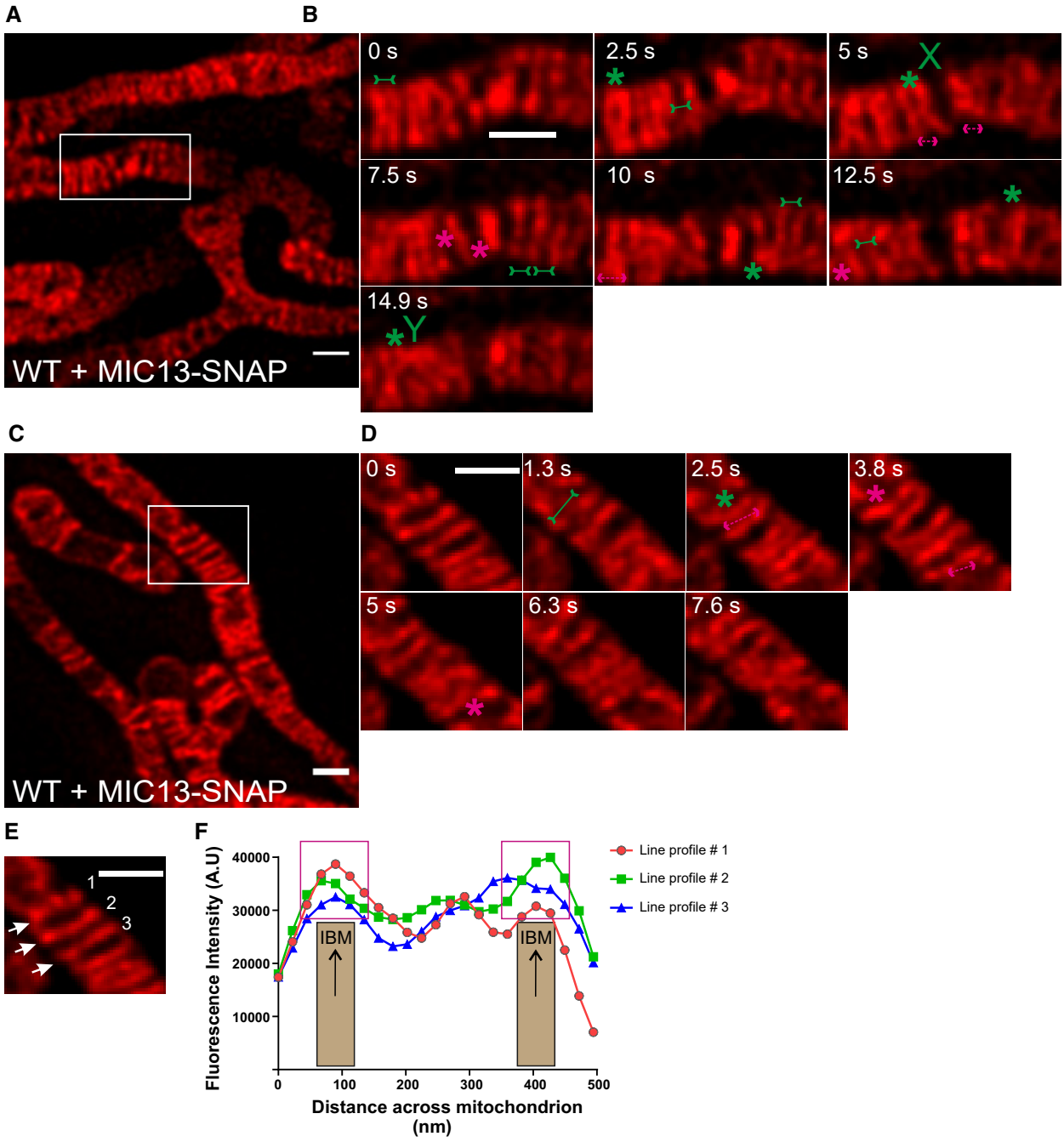

Figure 6. MIC13-SNAP shows that CJs and cristae undergo remodelling at a timescale of seconds.

A Representative live-cell STED super-resolution images (t = 0 s), showing WT HeLa cells expressing MIC13-SNAP, from a time-series of images acquired at a time interval of 2.5 s stained with silicon rhodamine. Box in (A) marks selection shown as a zoom in panel (B). Scale bar 500 nm.

B Time-lapse image series of a mitochondrion expressing MIC13-SNAP imaged at a time interval of 2.5 s/frame. Green and magenta asterisks show cycles of cristae merging and splitting marked by MIC13-SNAP. Green arrows pointing inward connected by solid line and magenta arrows pointing outward connected by dotted line show sites of imminent merging and splitting events, respectively. Cristae mergence events that form structure resembling letter "X" or "Y" are marked at 5 or 14.9 s, respectively. Scale bar 500 nm.

C Representative live-cell STED super-resolution images (t=0 s), showing WT HeLa cells expressing MIC13-SNAP, from a time-series of images acquired at a time interval of 1.3 s stained with silicon rhodamine. Box in (C) marks selection shown as a zoom in panel (D). Scale bar 500 nm.

D Time-lapse image series of a mitochondrion expressing MIC13-SNAP imaged at a time interval of 1.3 s/frame. Green and magenta asterisks show cycles of cristae merging and splitting marked by MIC13-SNAP. Green arrows pointing inward connected by solid line and magenta arrows pointing outward connected by dotted line show sites of imminent merging and splitting events, respectively. Scale bar 500 nm.

E First image from (D) was used for showing the intensity profiles along the length of three cristae (numbered 1–3 and marked with white arrows) in (F).

F Intensity profiles of lines drawn across the length of cristae show increased intensities at the edges of the line scans representing the IBM. Magenta boxes depict intensity maxima at IBM.

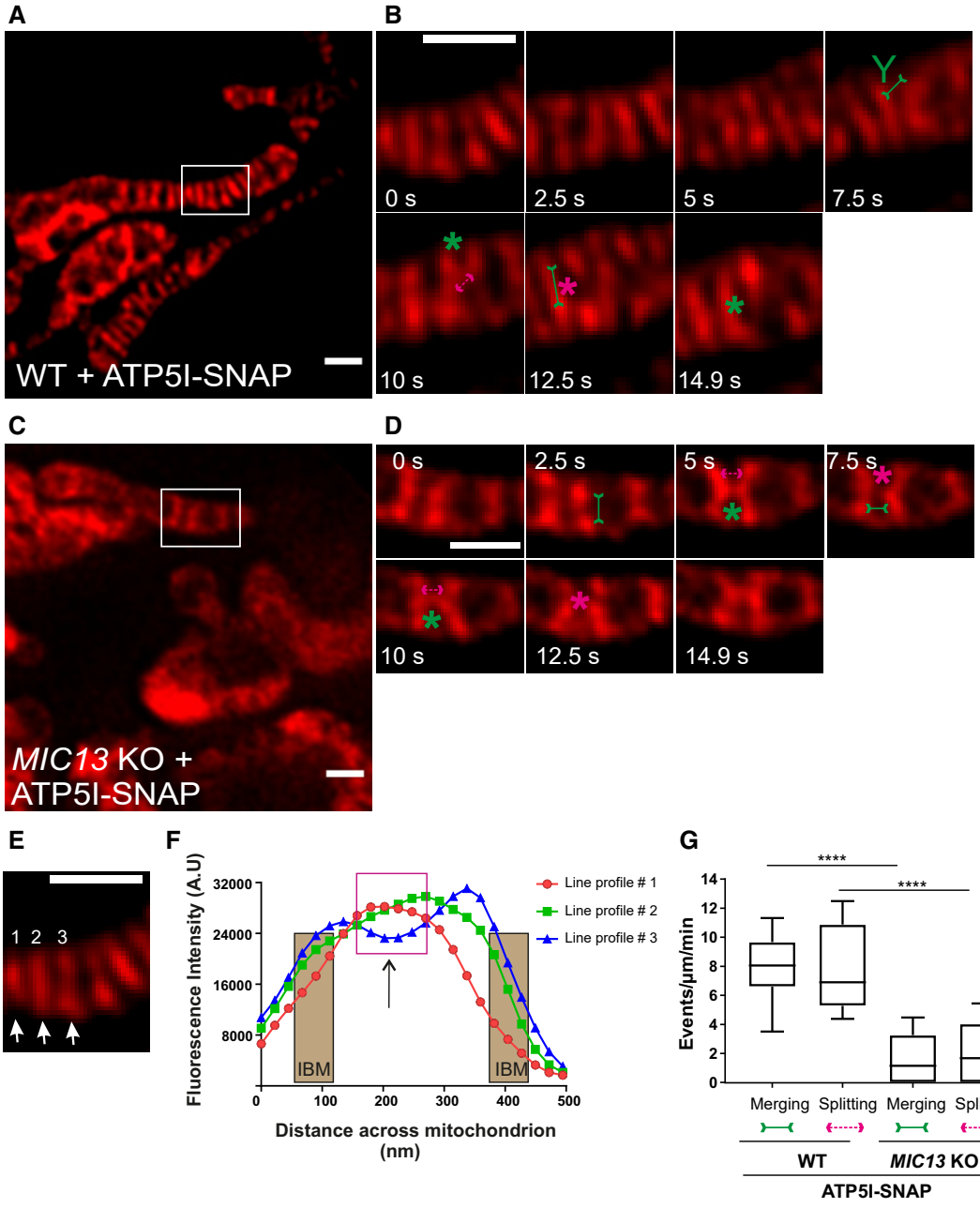

Figure 7. Cristae undergo balanced merging and splitting events in a MICOS-dependent manner.

A Representative live-cell STED super-resolution images (t = 0 s) showing WT HeLa cells expressing ATP5I-SNAP stained with silicon rhodamine. Box in (A) marks selection shown as a zoom in panel (B). Scale bar 500 nm.

B Time-lapse image series of a mitochondrion expressing ATP5I-SNAP in WT HeLa cells (2.5 s/frame). Green and magenta asterisks show merging and splitting events of cristae marked by ATP5I-SNAP, respectively. Green arrows pointing inward connected by solid line and magenta arrows pointing outward connected by dotted line show sites of imminent merging and splitting events, respectively. Green "Y" represents Y-type imminent mergence event. Scale bar 500 nm.

C Representative live-cell STED super-resolution images (t = 0 s) showing *MIC13* KO HeLa cells expressing ATP5I-SNAP stained with silicon rhodamine. Box in (C) marks selection shown as a zoom in panel (D). Scale bar 500 nm.

D Time-lapse image series of a mitochondrion expressing ATP5I-SNAP in *MIC13* KO HeLa cells (2.5 s/frame). Green and magenta asterisks show merging and splitting events of cristae marked by ATP5I-SNAP, respectively. Green arrows pointing inward connected by solid line and magenta arrows pointing outward connected by dotted line show sites of imminent merging and splitting events, respectively. Scale bar 500 nm.

E First image from (B) was used for showing the intensity profiles along the length of three cristae (numbered 1–3 and marked with white arrows) in (F).

F Intensity profiles of lines drawn across the length of cristae show increased intensities in the middle of the line scans representing the CM. The represented IBM area is superimposed from intensities of MIC13-SNAP from Fig 6F. Magenta box depicts intensity maxima at cristae membrane apart from IBM.

G Blind quantification of cristae merging and splitting events in WT and *MIC13* KO HeLa cells expressing ATP5I-SNAP (three independent experiments, 3–7 mitochondria for each experiment) represented as boxplots. Boxplots show median and interquartile range from 25 to 75 percentile, and whiskers represent minimum and maximum value. ****$P < 0.0001$, unpaired Student's t-test.

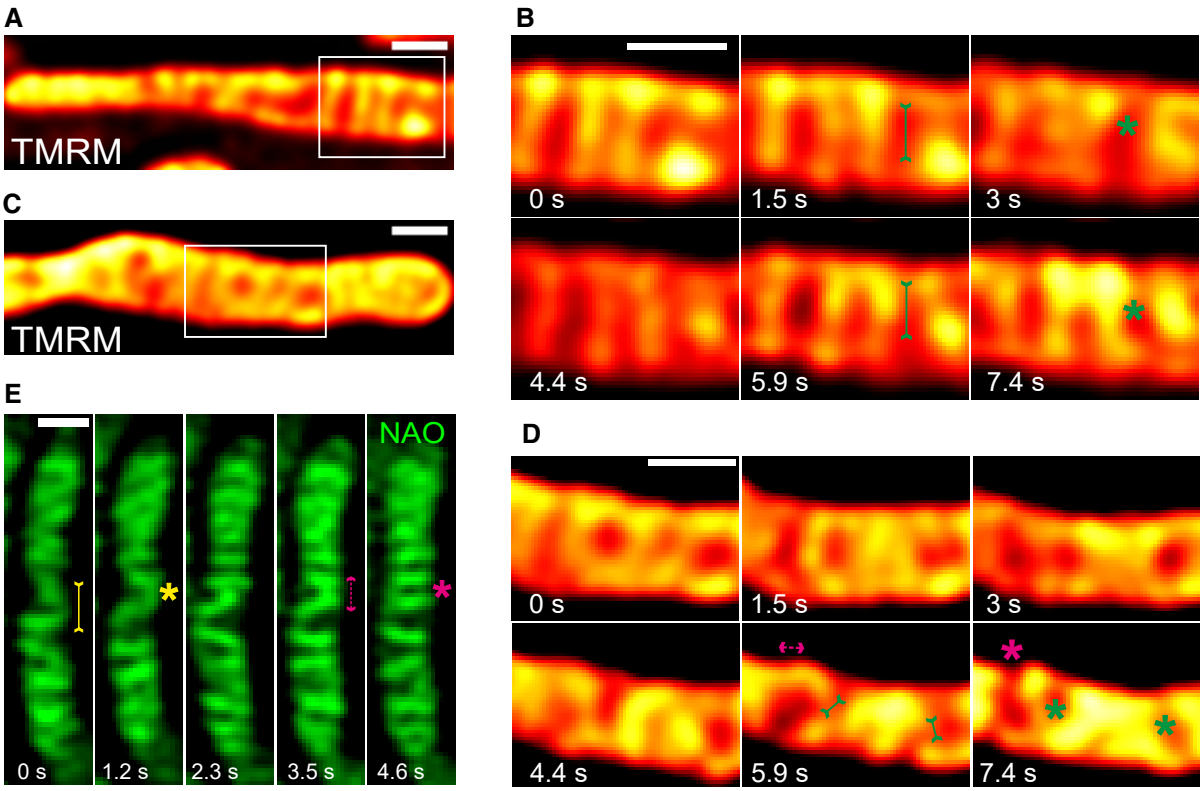

Figure 8. Cristae spatial remodelling is corroborated using mitochondrial inner membrane-specific dyes.

A Representative live-cell STED super-resolution images (t = 0 s) showing WT HeLa cells stained with TMRM. Box in (A) marks selection shown as a zoom in panel (B) (red hot LUT). Scale bar 500 nm.

B Time-lapse image series of two mitochondria stained with TMRM (1.5 s/frame). Green asterisks show merging events and redistribution of TMRM intensity from a high-intensity crista to a low-intensity crista (two such instances are shown at 3 and 7.4 s). Green arrows pointing inward connected by solid line at 1.5 and 5.9 s indicate imminent merging events. Scale bar 500 nm.

C Representative live-cell STED super-resolution images (t = 0 s) showing WT HeLa cells stained with TMRM. Box in (C) marks selection shown as a zoom in panel (D) (red hot LUT). Scale bar 500 nm.

D Time-lapse image series of two mitochondria stained with TMRM (1.5 s/frame). Green and magenta asterisks show cristae merging and splitting cycles (shown at 5.9 s and 7.4 s). Green arrows pointing inward connected by solid line and magenta arrows pointing outward connected by dotted line show sites of imminent merging and splitting events, respectively. Scale bar 500 nm.

E Representative time-lapse images of WT HeLa cells stained with NAO, and imaged using Airyscan microscope, indicate cristae merging and splitting dynamics. Yellow and magenta asterisks show merging and splitting events of cristae, respectively. Yellow arrows pointing inward connected by solid line and magenta arrows pointing outward connected by dotted line show sites of imminent merging and splitting events, respectively. Scale bar 500 nm.

we did with SNAP-tagged protein markers using STED nanoscopy. TMRM labelling showed transversely arranged cristae that were highly dynamic, consistent with our results for SNAP-tagged IM proteins (Fig 8A–D). Moreover, we observed instances of immediate distribution of a TMRM signal from one crista (e.g. high-intensity signal at 1.5 s in Fig 8B) to another crista and the IBM (lower-intensity signal at 3 s in Fig 8B) (Movie EV15), coinciding with the time of a cristae mergence event. Subsequent to this event, the respective cristae are spatially separated again showing a low membrane potential increasing with time. Interestingly, here and in several more instances we observed that the membrane potential is increasing overtime suggesting that the membrane potential can fluctuate within single cristae over time and that this is spatially linked to changes in cristae membrane shape and position within a mitochondrion. This is in line with a physical separation and/or insulation of the cristae from the IBM. Another instance of instantaneous redistribution of TMRM staining is shown (Fig 8C and D). Our observations showing that the location of the TMRM label within one crista can redistribute upon close apposition to the IBM could point to a membrane fusion event accompanied with content mixing. We also stained mitochondria with a non-potential specific dye, nonyl acridine orange (NAO), and employed another high-resolution microscopy technique, namely using a Zeiss Airyscan module. We observed that the CM was stained as transverse bridges in mitochondria and found instances of cristae dynamics at similar timescales (Fig 8E). We thus confirmed by two dyes and by a different imaging technique that cristae and CJs are highly dynamic and that these membrane remodelling events are balanced and reversible.

Mixing of cristae membrane proteins is linked to cristae membrane dynamics

In order to test whether cristae could undergo *bona fide* fusion events with other cristae or with the IBM, we devised techniques

that are based on the principles classically used to monitor membrane fusion between mitochondria and adapted them to study fusion between cristae. Firstly, we constructed ATP5I-PAGFP (photoactivatable GFP targeted to cristae) and performed photoactivation experiments using the high-resolution fast Airyscan module (Fig 9A). We rationalized that immediately after photoactivation of ATP5I-PAGFP, we label those cristae that are in continuity along the IM but barring instances where cristae are transiently isolated from the IBM and exist as cristae vesicles. Initially, putative cristae vesicles would remain in a non-fluorescent state (dark cristae), while cristae more distant from the site of photoactivation, which are in continuity with the IBM, would show fluorescence earlier. When such dark cristae would undergo fusion with already fluorescing cristae, we could instantaneously observe a previously non-fluorescent crista that becomes fluorescent. In fact, we found several such instances in mitochondria. An illustration is shown where immediately after photoactivation a dark crista (Fig 9A, red arrowhead in white box at 0.38, 0.59 and 0.78 s) subsequently gained fluorescence (Fig 9A, red arrow in white box at 0.98 s), but this was delayed compared to other cristae that were located more distant from the site of photoactivation. These observations demonstrate that at a certain time, a limited set of cristae are efficiently insulated from the IBM by a physical diffusion barrier preventing membrane protein distribution but that this insulation is dynamically changing over time. This could point to the possibility that transiently isolated cristae vesicles exist and undergo fusion with the IBM or with adjacent cristae. An alternative explanation we cannot exclude at this stage is that the MICOS complex can dynamically regulate the efficiency of such a diffusion barrier at CJs.

Next, we used a cell fusion assay to test these possibilities further. We labelled cristae in two different cell populations either with ATP5I-SNAP or with ATP5I-GFP and fused the cells using polyethylene glycol (PEG). We reasoned that if cells with mitochondria expressing differently labelled cristae were fused using PEG, in the presence of cycloheximide which inhibits protein synthesis, cristae fission and fusion would help in the formation of mixed cristae labelled with both ATP5I-SNAP and ATP5I-GFP. In light of our results, we would further predict that the extent of mixed cristae after a certain time of cell fusion is dependent on MIC13. Using dual-colour STED super-resolution nanoscopy, we observed the majority of individual cristae labelled with both colours, namely silicon rhodamine dye (labelling ATP5I-SNAP) and anti-GFP antibody (labelling ATP5I-GFP) (Fig 9B, left panel) in WT HeLa cells corroborating that cristae have efficiently mixed within the time frame of a few hours. Blind quantification of the number of colocalization events per unit length of mitochondria revealed 1–5 events per μm of mitochondrion in WT HeLa cells. In *MIC13* KO cells, we often observed cristae labelled with either ATP5I-SNAP or ATP5I-GFP next to each other within single mitochondrion in these cells (Fig 9B, right panel). There was a significant decrease in the number of colocalization events per unit length (μm) of mitochondria in *MIC13* KO cells (Fig 9B right panel and 9C). Only mitochondria that contained both colours, and therefore have undergone mitochondrial fusion, were analysed here, and there is no apparent effect of MIC13 deletion on "classical" mitochondrial fusion. Thus, we can exclude that this MIC13-dependent effect on content mixing is due to a possible effect of MIC13 on "classical" mitochondrial fusion. We rather conclude that MIC13 promotes mixing of CM proteins at an intramitochondrial level.

Discussion

The idea that cristae must be able to undergo remodelling under certain physiological conditions has been around for half a century, yet studying the dynamic behaviour of cristae membranes in real time was technically challenging due to limitations in optical resolution of diffraction-limited conventional light microscopy and due to the fact that electron microscopy can only capture fixed samples. In addition, the majority of studies using super-resolution techniques to study mitochondria have used fixed samples [56,57,65]. STED super-resolution microscopy of living cells has been utilized so far to visualize other cellular organelles, such as ER or Golgi [66,67]. To date, one study illustrated the power of Hessian structured illumination microscopy by giving an example in a single mitochondrion indicating cristae dynamics [68]. While this manuscript was under review, further two studies reported on technical advances in determining cristae dynamics using STED nanoscopy: one using MitoPB Yellow, a novel fluorescent dye [69], and another using a single protein marker of cristae, namely COX8A-SNAP in WT HeLa cells [70]. Here, we provide several lines of evidence demonstrating for the first time that spatial remodelling of CJs as well as of cristae is balanced and reversible process that occurs at a timescale of seconds. We further identified the first molecular player that is required for CJ and CM dynamics: the MICOS complex. These findings are based on the application of different advanced imaging techniques such as live-cell STED, SPT, FRAP and high-resolution Airyscan microscopy, which were applied to a wide variety of protein markers to visualize distinct mitochondrial substructures (MIC60-SNAP, MIC10-SNAP, MIC13-SNAP, ATP5I-SNAP,

Figure 9. Demonstration of content mixing in mitochondria using intramitochondrial cristae photoactivation and PEG fusion experiments.

A Mitochondrion in WT HeLa cells expressing ATP5I-PAGFP was photoactivated, in the area shown by a blue box, at 0 s. Inset of white box at 0.98 s clearly shows fluorescent crista (red arrow), absent at 0.38, 0.59 and 0.78 s (red arrowhead showing the area enclosed by white dotted lines), confirming merging of non-fluorescent cristae vesicle with the IBM. Threshold images of insets are shown above the whole images. Scale bar 500 nm.

B Dual-colour STED super-resolution images of fused mitochondrion in WT HeLa cells (left panel) showing colocalization of cristae marked with ATP5I-GFP (using anti-GFP antibody) and ATP5I-SNAP (stained with silicon rhodamine). (Right panel) Fused mitochondrion in *MIC13* KO HeLa cells showing cristae marked with either ATP5I-GFP (using anti-GFP antibody) or ATP5I-SNAP (stained with silicon rhodamine). Arrowheads show merged cristae, while arrows show cristae that maintain their individual identity. Scale bar 500 nm.

C Boxplot showing quantification of colocalization events per μm of mitochondria in WT and *MIC13* KO HeLa cells. Boxplots show median and interquartile range from 25 to 75 percentile, and whiskers represent minimum and maximum value (15 mitochondria were taken from WT and MIC13 KO cells from four and two independent experiments, respectively, $*P = 0.03$, unpaired Student's *t*-test).

D Schematic illustration of the proposed "Cristae fission and fusion" (CriFF) as a working model and its link to CJ dynamics.

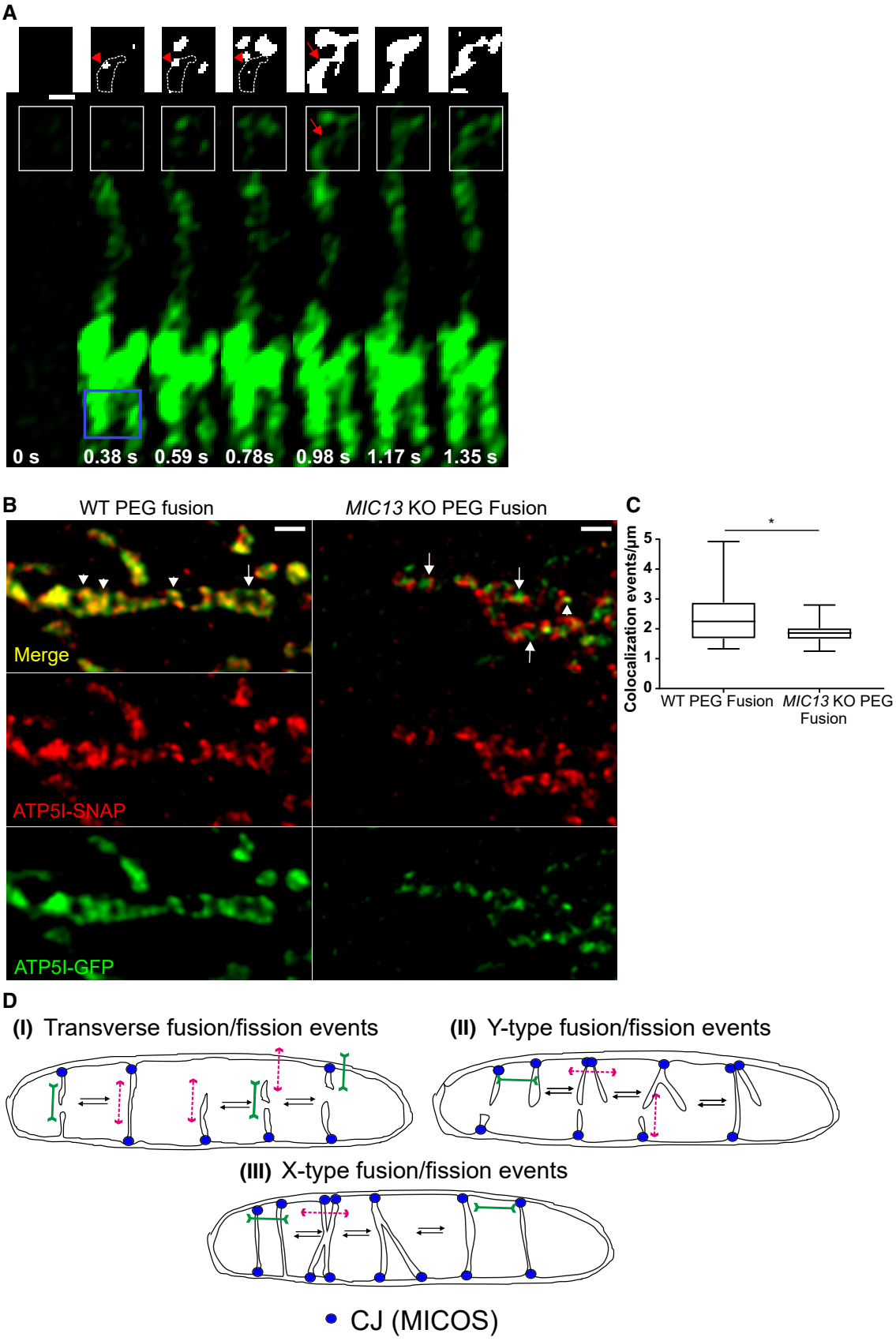

Figure 9.

COX8A-SNAP), as well as two dyes labelling the IM. We obtained three mammalian knockout cell lines lacking *MIC10*, *MIC60* and *MIC13*, respectively, and expressed the various constructs of SNAP- and GFP-tagged mitochondrial IM proteins in those and wild-type cells to reveal the functional role of the MICOS complex in this regard. Our improved tagging and imaging conditions allowed us to achieve a time resolution of up to 1.3–2.6 s per frame revealing that CJs and cristae dynamics occur at very similar timescales (seconds) and both depend on the MICOS complex. The idea of MIC60 as a central initiator of the MICOS complex was proposed earlier from confocal experiments in baker's yeast as reintroducing MIC60-GFP into a strain lacking all MICOS subunits and showed MIC60-GFP to be assembled into discrete spots [58]. Hence, improved spatial resolution obtained by STED imaging, FRAP, and SPT experiments in combination corroborates that MIC60 is the pioneering subunit of the MICOS complex positioning MICOS assembly and CJ formation in mammalian cells. The careful and extensive characterization of this novel MICOS-dependent process of continuous cycles of cristae membrane remodelling in living human cells revealed another highly interesting aspect, namely the possibility that cristae can actually be physically insulated or connected to each other and/or the IBM in a dynamic and regulated manner. In principle, there are two possibilities explaining this: (i) the MICOS complex stably forms CJs acting as diffusion barriers and dynamically regulates the permeability of CJs for proteins and lipids. (ii) The MICOS complex dynamically forms CJs and allows transient formation of isolated cristae vesicles by membrane fission and re-fusion of these transient vesicles with the IBM or with adjacent cristae. Both explanations do not exclude each other, yet based on our findings and the following arguments, we propose a model that is more in line with the second explanation. We term it "*Cris*tae *F*ission–*F*usion" (CriFF) model. The possibility of CMs to actually undergo membrane fission and fusion upon changing between condensed and orthodox states *in vitro* was proposed earlier using EM tomography under different conditions of isolated mitochondria [11]. Here, we now show for the first time, by following the fluctuations of membrane potential in time and space, using photoactivation at the resolution of individual cristae, and performing PEG fusion assays, that cristae might undergo *bona fide* membrane fusion in living cells and that this occurs in a MICOS-dependent manner. Overall, the CriFF model integrates our observations as follows (Fig 9D): (i) MIC60 serves as a docking site for the formation of CJs via recruitment of other subunits of the MICOS complex; (ii) once the MICOS complex is fully assembled, CJs are the sites for cristae to grow and emerge from the IBM. This does not exclude that the MICOS complex can dynamically change its composition or assembly state; (iii) CJs can dynamically merge and split; (iv) cristae are mainly, but not necessarily always, attached to CJs; and (v) cristae can undergo transient pinching-off from CJs and re-merge at the same CJ or another one (transverse or neighbouring CJ; Fig 9Di). The formation of separated cristae subcompartments is consistent with another study showing that, within the same mitochondrion, individual cristae can maintain a stable membrane potential over time and that neighbouring cristae can maintain disparate $\Delta\Psi$ [60]. This is also consistent with our FRAP data showing that TIMM23-GFP shows a reduced mobility upon loss of CJs, presumably by enhanced trapping in the CM. (vi) Formation of Y-type cristae fusion may be preceded by CJ merging and subsequent cristae membrane remodelling (Fig 9Dii). This would represent one possibility to link CJ dynamics and cristae remodelling. (vii) X-type cristae fusion could represent preceding/following CJ splitting/merging from a Y-type like cristae morphology or cristae fusion between cristae distant from CJs (Fig 9Diii). This clearly is a working model and will require further testing in future studies.

What could be the physiological advantage for cristae to undergo fusion and fission and why could impairment thereof lead to severe human diseases including mitochondrial encephalopathy with liver dysfunction as reported for mutations in *MIC13* [48–51]? Although future experiments will have to provide the answer to these questions, from the results shown here and in other studies, it is very clear that OXPHOS is impaired in cells lacking MICOS subunits such as MIC10, MIC60, MIC26, MIC27 or MIC13 [42–45]. How can we explain this and what could comprise possible functions of highly dynamic CMs? To answer this, on one hand it is worth considering that cristae fission would result in transient cristae subcompartments, which are physically isolated from the rest of the IM. This goes along with a reduced surface of the IM that is directly accessible to the cytosol via passing the intermembrane space and the outer membrane. On the other hand, cristae fusion reverts this and leads to an increase in accessible IM surface. The former situation is expected to favour trapping of metabolites and protons within the intracristal space, whereas the latter would increase the accessible surface, which is expected to favour metabolite exchange. As both processes, decreasing versus increasing IM surface, are critical for mitochondrial function, we propose that cristae dynamics is a way to adapt between these opposing necessities. Moreover, CriFF may help to distribute and mix proteins, lipids and important metabolites in the mitochondrion. In summary, we propose that CriFF has major implications for the following processes: (i) proton trapping; fission of cristae at CJs, resulting in transient intramitochondrial vesicles, could prevent proton leakage from the intracristal space to the cytosol, thereby promoting ATP synthesis. This does not exclude other ways of proton trapping proposed earlier, including proton buffering via cardiolipin [71] and preferential electrostatic local concentration at highly curved cristae tips [72]. Interestingly, pH differences within the intermembrane space have been reported, as the pH near ATP5I-SEcGFP (Superecliptic GFP, pH-sensitive version of GFP), residing at cristae tips, was shown to be 0.3 higher compared to COX8A-SEcGFP [73] located in the cristae. This was proposed to reflect a concentration gradient of protons, which dilutes at the cristae tips, which appear to act as a sink. Furthermore, we have recently shown that cristae behave as independent, bioenergetic units within a single mitochondrion which is fully in line with the transient formation of separated subcompartments that can adopt discrete levels of membrane potential [60]. (ii) Content mixing; CriFF may promote metabolite exchange including ADP, which was proposed to be limiting under certain conditions for OXPHOS [9]. (iii) Intramitochondrial quality control by protein content mixing; ongoing cristae fission and fusion dynamics may serve to mix partially damaged protein complexes, such as ETC complexes, in the CM to allow intramitochondrial complementation and protein quality control by proteases. (iv) Biogenesis of membrane protein complexes; continuous mixing of newly imported protein subunits (nuclear as well as mtDNA encoded) may promote efficient assembly of membrane protein complexes, in particular when considering that the cristae membrane is very densely packed with proteins. This view is consistent with hybrid cristae, which were reported to

be formed upon mitochondrial fusion, following PEG fusion of cells expressing mitochondria with different tags to respiratory chain complexes [74] and supported by our PEG fusion experiment as well (Fig 9B and C). (v) Lipid remodelling, mixing and exchange; cristae dynamics could promote exchange of lipids between organelles and OM and IM and optimize cardiolipin synthesis. Contact sites between the IM and the OM, defined by the MICOS complex, were shown to coordinate the synthesis of phosphatidylethanolamine by Psd1 to dictate lipid remodelling in mitochondrial membranes [75]. (vi) Other processes likely to be affected by altered cristae dynamics could include redox homeostasis, thermogenesis, Ca^{2+} buffering and iron–sulphur biogenesis.

What are the molecular machineries required for these processes? We show that these processes are dependent on fully assembled MICOS complex in a MIC13-dependent manner. This and the fact that both CJs and cristae dynamics occur at the similar timescales in a balanced manner strongly suggest that they are mechanistically linked. Indeed, the MIC13-SNAP live-cell STED movies allow the simultaneous visualization of CJs and cristae supporting this view. Still, we cannot fully exclude that the MICOS complex has two independent functions explaining our observation equally well. Further experiments will provide insights into the bioenergetic parameters and the molecular mechanisms of these fascinatingly fast and continuously occurring dynamics of CJs and cristae.

In conclusion, live-cell STED super-resolution nanoscopy in combination with biochemical and genetic methods has expanded our view on the dynamics of IM remodelling at a nanoscopic level in real time. Future research will provide further insights into the regulation, physiology and pathophysiology of these newly revealed dynamic processes occurring within mitochondria.

Materials and Methods

Cell culture, transfection and generation of knockout cell lines

HeLa and HEK293 cells were maintained in DMEM (Sigma-Aldrich) supplemented with 10% foetal bovine serum (PAN Biotech), 2 mM glutaMAX (Gibco), 1 mM sodium pyruvate (Gibco) and penstrep (Sigma-Aldrich, penicillin 100 units/ml and streptomycin 100 μg/ml), whereas HAP1 cells were cultured using Iscove's modified DMEM media (IMDM) supplemented with 20% foetal bovine serum (PAN Biotech), 2 mM glutaMAX (Gibco) and penstrep (Sigma-Aldrich, penicillin 100 units/ml and streptomycin 100 μg/ml). Cells were grown in incubator with 37°C and 5% CO_2. All cell lines were tested negative for possible mycoplasma contamination. HeLa and HAP1 cells were transfected with 1 μg of corresponding plasmid using GeneJuice® (Novagen) according to the manufacturer's instructions. In case of SNAP-tag constructs, 0.2 μg of MitoGFP (matrix-targeted) and 1 μg of corresponding SNAP-tag were co-transfected. HEK293 cells were grown on a large scale in 10 cm dishes and transfected with 10 μg of respective plasmids that were used for biochemical experiments. *MIC13* KO HeLa cells were generated using CRISPR/Cas method as described before [44]. *MIC10* and *MIC60* KO HAP1 cells along with WT cells were custom-made upon our request by Horizon (UK). For TMRM imaging, HeLa cells were stained with 50 nM TMRM dye (Invitrogen) for 30 min followed by three washes with complete medium.

Molecular cloning

Human MIC60, MIC10, MIC13, ATP5I and TOMM20 were cloned into pSNAPf vector (NEB) using Gibson Assembly Cloning Kit (NEB). COX8A-SNAP vector was obtained from NEB. MIC60 and MIC10 were cloned into pEGFPN1 using restriction digestion by *Xho*I and *Bam*H1 followed by ligation. Human TOMM20, TIMM23 and ATP5I were cloned into pEGFPN1 vector, and human ATP5I was cloned into pPAGFPN1 vector using Gibson Assembly Cloning Kit (NEB) to acquire their respective GFP- or PAGFP-tagged versions.

SDS electrophoresis and Western blotting

For preparing samples for Western blotting, corresponding cells were collected and proteins were extracted using RIPA lysis buffer. The amount of solubilized proteins in all the samples were determined using the Lowry method (Bio-Rad). 15% SDS–PAGE was performed, and separated proteins were subsequently blotted onto a PVDF membrane, and probed with indicated antibodies: MIC10 from Abcam (84969), MIC13 (custom-made by Pineda (Berlin) against human MIC13 peptide CKAREYSKEGWEYVKARTK), MIC19 (Proteintech, 25625-1-AP), MIC25 (Proteintech, 20639-1-AP), MIC26 (Thermo Fisher, MA5-15493), MIC27 (Atlas Antibodies, HPA000612), MIC60 (custom-made, Pineda (Berlin)) against human IMMT using the peptide CTDHPEIGEGKPTPALSEEAS), SNAP-tag (P9310S, NEB) and β-tubulin (Abcam, ab6046). Goat anti-mouse IgG HRP-conjugated antibody (ab97023) and goat anti-rabbit IgG HRP-conjugated antibody (Dianova, 111-035-144) were used as secondary antibodies. Chemiluminescence was captured using a VILBER LOURMAT Fusion SL (PEQLAB).

Coimmunoprecipitation

For coimmunoprecipitation, isolated mitochondria from HEK293 cells overexpressing either MIC10-SNAP, MIC10-GFP, MIC60-SNAP or MIC60-GFP were used. Mitochondrial isolation was done as described before [44]. The coimmunoprecipiation experiment was performed using the protocol described in Ref. [28] with the following modification. The beads were incubated with 4 μg of MIC13 antibody (custom-made by Pineda (Berlin)) against human MIC13 peptide CKAREYSKEGWEYVKARTK). During lysis of the mitochondria, a detergent/protein ratio of 2 g/g was used.

Isolation of macromolecular complexes by blue native gels

Mitochondria from HEK293 cells overexpressing MIC60-SNAP or MIC60-GFP were isolated and BN-PAGE experiment was performed as shown by Ref. [44] with the use of a detergent/protein ration of 2 g/g during solubilization.

Electron microscopy

HAP1 WT, *MIC10* KO and *MIC60* KO cells were grown on petri dishes, and cells were washed with PBS and fixed using 3% glutaraldehyde in 0.1 M sodium cacodylate buffer, pH 7.2. After fixation, cells were collected in a small tube using a cell scraper and pelleted. These cell pellets were washed with 0.1 M sodium

cacodylate, pH 7.2 and subsequently embedded in 2% agarose. The pellets were stained using 1% osmium tetroxide for 50 min and 1% uranyl acetate/1% phosphotungstic acid for 1 h. The samples were dehydrated using graded acetone series and embedded in spur epoxy resin for polymerization at 65°C for 24 h. The ultrathin sections were prepared using microtome, and the images were acquired using transmission electron microscope (Hitachi, H600) at 75V equipped with Bioscan model 792 camera (Gatan) and analysed with ImageJ software.

Cellular respiration measurements

All respiration measurements were performed using Seahorse XFe96 Analyzer (Agilent). The HAP1 cells were seeded into Seahorse XF96 cell culture plate (Agilent) at a density of 30,000 cells per well overnight. Next day, cells were washed and incubated in basic DMEM media (Sigma, D5030) supplemented with glucose, glutamine and pyruvate at 37°C in non-CO_2 incubator 1 h prior to the assay. Mitochondrial respiration function was measured using Seahorse XF Cell Mito Stress Test Kit (Agilent) according to the manufacturer's instructions. Briefly, the delivery chambers of the sensor cartridge were loaded with oligomycin (F_1F_O-ATPase synthase inhibitor) or FCCP (uncoupler) or rotenone and antimycin (complex I and complex III inhibitors, respectively) to measure basal, proton leak, maximum and residual respiration. Cell number was normalized after the run using Hoechst staining. Data were analysed using wave software (Agilent).

Immunofluorescence staining

HAP1 cells were fixed with pre-warmed (37°C) 3.7% paraformaldehyde for 15 min. After fixation, cells were washed three times with PBS, permeabilized with 0.15% Triton X-100 for 15 min and blocked using 10% goat serum for 15 min followed by incubation with appropriate dilution of primary antibodies for 3 h at room temperature or overnight at 4°C. After washing thrice with PBS, samples were incubated at room temperature with appropriate secondary antibody for 1 h and washed three times with PBS before proceeding for microscopy. For STED super-resolution imaging, primary antibodies used were against MIC60 (custom-made, Pineda (Berlin)), MIC10 (Abcam, 84969) and TOMM70 (Santa Cruz Biotechnology, sc-390545). Goat anti-rabbit Abberior STAR 635P (Abberior) and goat anti-mouse Abberior STAR 580 (Abberior) were used as secondary antibodies.

Quantification of mitochondrial interpunctae distance (IPD)

The longitudinal distance along the mitochondrial length between two successive MIC60 or MIC10 punctae is termed as interpunctae distance (IPD). The IPD between MIC60 and MIC10 punctae was calculated using the ImageJ software by manually drawing lines between two spots from the centre of the punctae and measured using the "Analyze" function to calculate the length of that particular line. In order to avoid repetition of measuring the IPD, the length between the punctae was measured in a clockwise direction. If the edges of mitochondria containing the MIC60 or MIC10 spots were curved, a segmented line tool was used to measure the IPD. In rare cases where MIC60 spots were replaced by longitudinal bridges, the centre of the line was taken into consideration for defining the spot. The distance between MIC60 or MIC10 punctae per mitochondrion was calculated (from an average of 36–55 spots/mitochondrion), and a median interpunctae distance was obtained for that individual mitochondrion. Data were represented in a boxplot where a single value represented IPD value for each mitochondrion.

FRAP and associated quantification

FRAP experiments were performed on Leica SP8 using the FRAP module with Fly mode function switched on. Images were acquired with 40× water objective (N.A = 1.1) using 25x zoom. In order to avoid acquisition photobleaching, only 1–1.5% laser power of the Argon laser line at 488 nm was used to acquire the images using a PMT in green emission range. A square region of 0.7 × 0.7 μm was bleached using 100% laser power at 488 nm. Ten pre-bleach images were acquired, while 10 images were acquired during bleaching. 200 post-bleach images were acquired at a maximal possible frame rate of 88–89 ms/frame to monitor the recovery of fluorescence. After the images were acquired, quantification of the FRAP experiment was done in the following way: three different regions of interest (ROIs) were taken into consideration: (i) ROI^1, an area where no mitochondria were found in the image, was used to perform background subtraction. (ii) ROI^2 was the area of mitochondria where the photobleaching was performed. (iii) ROI^3, another region of a separate mitochondria not subjected to FRAP, was used to obtain correction factor for acquisition photobleaching. $ROI^2(P)$ was the average of 10 pre-bleach measurements of ROI^2, whereas $ROI^3(P)$ was the average of 10 pre-bleach measurements of ROI^3. Hence, photobleach correction was performed by using the formula: ROI^2-ROI^1/ROI^3-ROI^1 and normalization were performed by using the formula: ROI^2-ROI^1/ROI^3-ROI^1 X $ROI^3(P)$-ROI^1/$ROI^2(P)$-ROI^1. All the mitochondria belonging to a particular condition from independent experiments were pooled and averaged for their FRAP curves. Standard error of mean (SEM) was plotted for all the pooled mitochondria for each condition.

Once the FRAP recovery values were obtained, they were fitted, using GraphPad Prism 7.04, by nonlinear regression two-phase association model for all molecules. First and second phase association $T^{1/2}$ recovery values were obtained for each condition when the curves were fitted by nonlinear regression two-phase association model. Mobile fraction was calculated by using the formula: $F_m = F_p\text{-}F_0/F_{initial}\text{-}F_0$, where F_m denotes the mobile fraction, F_p denotes the fraction of fluorescence when the plateau is reached, $F_{initial}$ is 1 and F_0 is the fraction of initial fluorescence after the last pulse of photobleaching for all cases except MIC60-GFP, MIC10-GFP and TOMM20-GFP (in *MIC13* KO cells), where the Fp was calculated from the average of last 5 intensity values. Diffusion coefficients (D) were calculated using the formula $D = 0.25 \times r^2/T^{1/2}$, where r is the radius of the bleached ROI and $T^{1/2}$ is the recovery time in seconds, as suggested before [76]. We bleached a square ROI region of 0.49 μm^2 in the mitochondria for our experiments. Hence, we used 0.49 μm^2 as the area of the circle to calculate the radius.

Single-particle tracking imaging and quantification

Cells transfected with the SNAP-tag and stained with low concentrations of SNAP-cell 647-SiR (NEB) (15 nM for MIC60-SNAP and

0.225 nM for MIC10-SNAP) were imaged in fluoroBrite DMEM media supplemented with 10% foetal bovine serum (PAN Biotech), 2 mM glutaMAX (Gibco), 1 mM sodium pyruvate (Gibco) and penstrep (Sigma-Aldrich, penicillin 100 units/ml and streptomycin 100 μg/ml). Lower concentrations of silicon rhodamine were used here compared to STED super-resolution imaging to allow for selective labelling of only few molecules in a mitochondrion. Movies were acquired on a Zeiss Elyra PS.1 microscope equipped with a 63× (NA = 1.46) objective lens in total internal reflection fluorescence (TIRF) mode, where highly inclined and laminated optical sheet (HILO) illumination was used, at a frame rate of 33 ms/frame for 1,000 frames. The angle of the illuminating laser, EMCCD gain and laser intensity was manually adjusted to acquire the best signal-to-noise ratio (SNR). The first 50–100 frames of every movie were not used for analyses so that acquisition bleaching will additionally provide a sufficiently low concentration of single particles. For analyses of movies, a ROI was set around each cell and single-particle tracking (SPT) was performed using the Fiji/ImageJ [77] plugin TrackMate [78] where the following TrackMate settings were used: Detector: Laplacian of Gaussian, Estimated blob diameter: 0.5 μm, Do sub-pixel localization: Yes, Initial thresholding: No, Filter on spots: SNR above 0.4. For tracking spots, the linear assignment problem (LAP) tracker with following settings worked well: Frame to frame linking: 0.3 μm, Gap-closing maximal distance: 0.5 μm, Gap-closing maximal frame gap: 5 frames. The filter on tracks function was used to only analyse tracks with more than 20 spots within a track. After analysis, the calculated mean square displacement (MSDs) and instantaneous diffusion coefficients (insDs) of all tracks were loaded into the Fiji plugin "Trajectory Classifier" [79]. MSD analysis allows to determine the mode of displacement of particles over time. For the calculation of the MSD for every track and time point, the MATLAB class @msdanalyzer was used [80]. Additionally, the insDs were calculated using insD = mean MSD/4*dt [81] where mean MSDs were calculated using the first 4 MSD points of every track. Besides the calculation of the MSD and insD, tracks were analysed using the Fiji plugin Trajectory classifier [79]. The plugin classifies tracks generated with TrackMate into confined diffusion, subdiffusion, normal diffusion and directed motion in increasing order of directionality. As most tracks were relatively short, following settings for the classification were used: Minimal track length: 20, Window size: 10, Minimal segment length: 10. SPT data were obtained for each condition in two independent experiments from 2 to 5 cells in each experiment.

2D STED (stimulated emission depletion) super-resolution nanoscopy

Cells transfected with corresponding SNAP tags and stained with silicon rhodamine dye (SNAP-cell 647-SiR (NEB) (3 μM)) were imaged at 37°C and 5% CO_2 mimicking cell culture incubator conditions in fluoroBrite DMEM media supplemented with 10% foetal bovine serum (PAN Biotech), 2 mM glutaMAX (Gibco), 1 mM sodium pyruvate (Gibco) and penstrep (Sigma-Aldrich, penicillin 100 units/ml and streptomycin 100 μg/ml). Live-cell STED super-resolution nanoscopy was performed on Leica SP8 laser scanning confocal microscope fitted with a STED module. Before imaging, the alignment of excitation and depletion laser was checked in reflection mode using colloidal 80-nm gold particles (BBI Solutions). Cells expressing the SNAP-tag and stained with SNAP-cell 647-SiR (NEB) were excited with a white light laser at an excitation wavelength of 633 nm. Images were collected using a hybrid detector (HyD) at an emission range from 640 to 730 nm using a 93× glycerol (N.A = 1.3) or 100× oil objective (N.A = 1.4) while using a pulsed STED depletion laser beam at 775-nm emission wavelength. The images were obtained at a zoom to acquire 9.7 × 9.7 μm area (12× magnification for 100× or 12.9× magnification for 93× objective). Movies were obtained at a frame rate of ~2.5 s/frame or ~ 1.25 s/frame (pixel size was 22.5 nm for live-cell STED imaging). Gating STED was used from 0.8 to 1 ns onwards in order to increase the specificity of the fluorescence signal.

For dual-colour STED, we used pulsed STED depletion laser at 775-nm emission wavelength. Images were collected in sequential mode using a hybrid detector while exciting at 633 and 561 nm to acquire images at emission wavelengths of 660–730 nm and 570–610 nm, respectively. Care was taken to avoid any crosstalk between the channels by performing a sequential scan and reducing the range of emission wavelengths for both the channels mentioned. Additionally, we confirmed that there was no chromatic aberration between both the channels by using an antibody against nuclear pore complex emitting in both channels. Anti-NUP1 153 (ab 24700) is an antibody, ideally suited to check samples for chromatic aberration during STED imaging, staining the nuclear pores. For imaging of fixed samples in this study, the pixel size was 17 nm. Image processing post-image acquisition of live-cell SNAP movies was performed with Huygens Deconvolution software. The raw data images are provided. Due to the strong depletion and the drastic decrease in emitting fluorophores in STED microscopy, the resulting images tend to have a lower signal-to-noise ratio. The increase in axial resolution, and by that reduction in out of focus blur, is not the only benefit of deconvolution. The other major advantages are increase in signal-to-noise ratio and resolution, which enhance image quality for 2D datasets as well, as shown before [82].

Quantification of crista junction and cristae dynamics

Blind quantification of intramitochondrial merging and splitting events in case of MIC10- and MIC60-SNAP marking CJs and ATP5I-SNAP, COX8A-SNAP and MIC13-SNAP marking cristae was done manually by observing the corresponding live-cell STED movies for a time span of ~15 s obtained at a frame rate of ~2.5 s/frame. The number of merging/splitting events was divided by the mitochondrial length to yield corresponding number of events/unit length (μm) of mitochondrion. Events/μm/min of mitochondria was subsequently calculated. All quantifications were performed from three independent experiments using 3–10 mitochondria from each experiment, which were all chosen from separate cells.

Airyscan microscopy

HeLa cells were stained with 100 nM nonyl acridine orange for 1 h and imaged using Plan-Apochromat 100×/1.46 Oil DIC M27 objective on the Zeiss LSM 880 with Airyscan. Raw.czi files were processed into deconvoluted images using the Zen software automatically. HeLa cells expressing ATP5I-PAGFP and mitocherry were used for photoactivation experiments. Images were acquired by exciting at

488 nm using Plan-Apochromat 63×/1.4 Oil DIC M27 objective on the Zeiss LSM 880 with Airyscan. We photoactivated a 1 × 1 μm area of the mitochondria by using a 405-nm laser followed by acquisition of the images in fast mode every 0.2 s after photoactivation.

PEG fusion assay

PEG fusion assay was adapted from Ref. [83]. Cells expressing ATP5I-SNAP and ATP5I-GFP were co-plated (1:1 ratio) in such a way that they were 100% confluent and adhering to each other on the day of PEG fusion. Cells were treated with cycloheximide (20 μg/ml) 30 min prior to PEG fusion till the time they were fixed in PFA. After PEG (suitable for hybridoma, Merck) fusion for 60 s, mitochondria from cells expressing ATP5I-SNAP and ATP5I-GFP were allowed to fuse for 3 h. In the last 30 min, silicon rhodamine was added to bind to those cells expressing ATP5I-SNAP followed by three washes in serum-free medium with cycloheximide (20 μg/ml). Cells were then fixed in pre-warmed (37°C) 3.7% paraformaldehyde for 15 min. The paraformaldehyde also contained cycloheximide (20 μg/ml). After fixation, cells underwent immunofluorescence staining as described in the section before. Mouse Anti-GFP (Merck, 11814460001) primary and goat anti-mouse Abberior STAR 580 (Abberior) secondary antibodies were used.

Statistics

Statistical analysis for different experiments was done in GraphPad Prism 7.04 using unpaired Student's *t*-test except for comparison in Seahorse experiments where differences in basal oxygen consumption were compared by one-sample *t*-test. Mean ± SEM was used for different experiments, and sample size was not predetermined using any statistical methods.

Expanded View for this article is available online.

Acknowledgements
We thank T. Portugall and A. Borchardt for technical assistance in constructing the plasmids used in this study and in electron microscopy experiments, respectively. STED, FRAP, SPT and cristae photoactivation experiments were performed at the Centre for Advanced Imaging (CAi) facility at HHU, Düsseldorf. We are also grateful to Prof. Wilhelm Stahl, Prof. Peter Brenneisen and Dr. Marcel Zimmermann for helpful and stimulating discussions. This work was supported by Deutsche Forschungsgemeinschaft (DFG) grant RE 1575/2-1 (ASR), Project-ID 267205415—SFB 1208 project B12 (ASR), SFB 974 Project B09 (ASR), Research Committee of the Medical faculty of Heinrich Heine University Düsseldorf FoKo-37/2015 (AKK) and Foko-02/2015 (RA & ASR), SFB 1208 Project Z02 (SWP) and grant WE 5343/1-1 (SWP).

Author contributions
AKK, RA and ASR developed the underlying concept of the study, designed the experiments and wrote the manuscript with comments from all other authors. AKK performed all experiments of STED super-resolution imaging and FRAP with help from SH and SWP. TZ and AKK performed the SPT experiments, while TZ performed quantification of SPT data using ImageJ with a MATLAB interface. RA performed all the biochemical experiments, electron microscopy and blind quantification. AKK and RA performed cristae photoactivation experiments with help from SH and SWP. JU characterized the *MIC13* KO cells and performed co-IP and BN-PAGE experiments. DMW and MS performed the NAO staining using Zeiss Airyscan imaging and analysis. ML and OSS contributed with scientific and critical inputs to the manuscript.

Conflict of interest
The authors declare that they have no conflict of interest.

References

1. Zick M, Rabl R, Reichert AS (2009) Cristae formation-linking ultrastructure and function of mitochondria. *Biochem Biophys Acta* 1793: 5 – 19
2. Zerbes RM, van der Klei IJ, Veenhuis M, Pfanner N, van der Laan M, Bohnert M (2012) Mitofilin complexes: conserved organizers of mitochondrial membrane architecture. *Biol Chem* 393: 1247 – 1261
3. Acehan D, Xu Y, Stokes DL, Schlame M (2007) Comparison of lymphoblast mitochondria from normal subjects and patients with Barth syndrome using electron microscopic tomography. *Lab Invest* 87: 40 – 48
4. Perkins G, Renken C, Martone ME, Young SJ, Ellisman M, Frey T (1997) Electron tomography of neuronal mitochondria: three-dimensional structure and organization of cristae and membrane contacts. *J Struct Biol* 119: 260 – 272
5. Perkins GA, Ellisman MH, Fox DA (2003) Three-dimensional analysis of mouse rod and cone mitochondrial cristae architecture: bioenergetic and functional implications. *Mol Vis* 9: 60 – 73
6. Perkins GA, Tjong J, Brown JM, Poquiz PH, Scott RT, Kolson DR, Ellisman MH, Spirou GA (2010) The micro-architecture of mitochondria at active zones: electron tomography reveals novel anchoring scaffolds and cristae structured for high-rate metabolism. *J Neurosci* 30: 1015 – 1026
7. Rabl R, Soubannier V, Scholz R, Vogel F, Mendl N, Vasiljev-Neumeyer A, Körner C, Jagasia R, Keil T, Baumeister W *et al* (2009) Formation of cristae and crista junctions in mitochondria depends on antagonism between Fcj1 and Su e/g. *J Cell Biol* 185: 1047 – 1063
8. Frey TG, Renken CW, Perkins GA (2002) Insight into mitochondrial structure and function from electron tomography. *Biochem Biophys Acta* 1555: 196 – 203
9. Mannella CA, Lederer WJ, Jafri MS (2013) The connection between inner membrane topology and mitochondrial function. *J Mol Cell Cardiol* 62: 51 – 57
10. Mannella CA, Marko M, Penczek P, Barnard D, Frank J (1994) The internal compartmentation of rat-liver mitochondria: tomographic study using the high-voltage transmission electron microscope. *Microsc Res Tech* 27: 278 – 283
11. Mannella CA, Pfeiffer DR, Bradshaw PC, Moraru II, Slepchenko B, Loew LM, Hsieh CE, Buttle K, Marko M (2001) Topology of the mitochondrial inner membrane: dynamics and bioenergetic implications. *IUBMB Life* 52: 93 – 100
12. Vogel F, Börnhovd C, Neupert W, Reichert AS (2006) Dynamic subcompartmentalization of the mitochondrial inner membrane. *J Cell Biol* 175: 237 – 247
13. Hackenbrock CR (1966) Ultrastructural bases for metabolically linked mechanical activity in mitochondria. I. Reversible ultrastructural changes with change in metabolic steady state in isolated liver mitochondria. *J Cell Biol* 30: 269 – 297
14. Hackenbrock CR (1968) Chemical and physical fixation of isolated mitochondria in low-energy and high-energy states. *Proc Natl Acad Sci USA* 61: 598 – 605
15. Hackenbrock CR (1972) Energy-linked ultrastructural transformations in isolated liver mitochondria and mitoplasts. Preservation of

configurations by freeze-cleaving compared to chemical fixation. *J Cell Biol* 53: 450 – 465

16. Nicastro D, Frangakis AS, Typke D, Baumeister W (2000) Cryo-electron tomography of neurospora mitochondria. *J Struct Biol* 129: 48 – 56
17. Frezza C, Cipolat S, Martins de Brito O, Micaroni M, Beznoussenko GV, Rudka T, Bartoli D, Polishuck RS, Danial NN, De Strooper B *et al* (2006) OPA1 controls apoptotic cristae remodeling independently from mitochondrial fusion. *Cell* 126: 177 – 189
18. Scorrano L, Ashiya M, Buttle K, Weiler S, Oakes SA, Mannella CA, Korsmeyer SJ (2002) A distinct pathway remodels mitochondrial cristae and mobilizes cytochrome c during apoptosis. *Dev Cell* 2: 55 – 67
19. Vincent AE, Ng YS, White K, Davey T, Mannella C, Falkous G, Feeney C, Schaefer AM, McFarland R, Gorman GS *et al* (2016) The spectrum of mitochondrial ultrastructural defects in mitochondrial myopathy. *Sci Rep* 6: 30610
20. Koob S, Reichert AS (2014) Novel intracellular functions of apolipoproteins: the ApoO protein family as constituents of the Mitofilin/MINOS complex determines cristae morphology in mitochondria. *Biol Chem* 395: 285 – 296
21. Quintana-Cabrera R, Mehrotra A, Rigoni G, Soriano ME (2017) Who and how in the regulation of mitochondrial cristae shape and function. *Biochem Biophys Res Comm* 500: 94 – 101
22. Rampelt H, Zerbes RM, van der Laan M, Pfanner N (2016) Role of the mitochondrial contact site and cristae organizing system in membrane architecture and dynamics. *Biochem Biophys Acta* 1864: 737 – 746
23. Harner M, Korner C, Walther D, Mokranjac D, Kaesmacher J, Welsch U, Griffith J, Mann M, Reggiori F, Neupert W (2011) The mitochondrial contact site complex, a determinant of mitochondrial architecture. *EMBO J* 30: 4356 – 4370
24. Hoppins S, Collins SR, Cassidy-Stone A, Hummel E, Devay RM, Lackner LL, Westermann B, Schuldiner M, Weissman JS, Nunnari J (2011) A mitochondrial-focused genetic interaction map reveals a scaffold-like complex required for inner membrane organization in mitochondria. *J Cell Biol* 195: 323 – 340
25. von der Malsburg K, Muller JM, Bohnert M, Oeljeklaus S, Kwiatkowska P, Becker T, Loniewska-Lwowska A, Wiese S, Rao S, Milenkovic D *et al* (2011) Dual role of mitofilin in mitochondrial membrane organization and protein biogenesis. *Dev Cell* 21: 694 – 707
26. Pfanner N, van der Laan M, Amati P, Capaldi RA, Caudy AA, Chacinska A, Darshi M, Deckers M, Hoppins S, Icho T *et al* (2014) Uniform nomenclature for the mitochondrial contact site and cristae organizing system. *J Cell Biol* 204: 1083 – 1086
27. Abrams AJ, Hufnagel RB, Rebelo A, Zanna C, Patel N, Gonzalez MA, Campeanu IJ, Griffin LB, Groenewald S, Strickland AV *et al* (2015) Mutations in SLC25A46, encoding a UGO1-like protein, cause an optic atrophy spectrum disorder. *Nat Genet* 47: 926 – 932
28. Barrera M, Koob S, Dikov D, Vogel F, Reichert AS (2016) OPA1 functionally interacts with MIC60 but is dispensable for crista junction formation. *FEBS Lett* 590: 3309 – 3322
29. Genin EC, Plutino M, Bannwarth S, Villa E, Cisneros-Barroso E, Roy M, Ortega-Vila B, Fragaki K, Lespinasse F, Pinero-Martos E *et al* (2015) CHCHD10 mutations promote loss of mitochondrial cristae junctions with impaired mitochondrial genome maintenance and inhibition of apoptosis. *EMBO Mol Med* 8: 58 – 72
30. Glytsou C, Calvo E, Cogliati S, Mehrotra A, Anastasia I, Rigoni G, Raimondi A, Shintani N, Loureiro M, Vazquez J *et al* (2016) Optic atrophy 1 is epistatic to the core MICOS component MIC60 in mitochondrial cristae shape control. *Cell Rep* 17: 3024 – 3034
31. Körner C, Barrera M, Dukanovic J, Eydt K, Harner M, Rabl R, Vogel F, Rapaport D, Neupert W, Reichert AS (2012) The C-terminal domain of Fcj1 is required for formation of crista junctions and interacts with the TOB/SAM complex in mitochondria. *Mol Biol Cell* 23: 2143 – 2155
32. Ott C, Ross K, Straub S, Thiede B, Gotz M, Goosmann C, Krischke M, Mueller MJ, Krohne G, Rudel T *et al* (2012) Sam50 functions in mitochondrial intermembrane space bridging and biogenesis of respiratory complexes. *Mol Cell Biol* 32: 1173 – 1188
33. Pinero-Martos E, Ortega-Vila B, Pol-Fuster J, Cisneros-Barroso E, Ruiz-Guerra L, Medina-Dols A, Heine-Suner D, Llado J, Olmos G, Vives-Bauza C (2016) Disrupted in Schizophrenia 1 (DISC1) is a constituent of the mammalian Mitochondrial contact site and Cristae Organizing System (MICOS) complex, and is essential for oxidative phosphorylation. *Hum Mol Genet* 25: 4157 – 4169
34. Xie J, Marusich MF, Souda P, Whitelegge J, Capaldi RA (2007) The mitochondrial inner membrane protein mitofilin exists as a complex with SAM50, metaxins 1 and 2, coiled-coil-helix coiled-coil-helix domain-containing protein 3 and 6 and DnaJC11. *FEBS Lett* 581: 3545 – 3549
35. Barbot M, Jans DC, Schulz C, Denkert N, Kroppen B, Hoppert M, Jakobs S, Meinecke M (2015) Mic10 oligomerizes to bend mitochondrial inner membranes at cristae junctions. *Cell Metab* 21: 756 – 763
36. Bohnert M, Zerbes RM, Davies KM, Muhleip AW, Rampelt H, Horvath SE, Boenke T, Kram A, Perschil I, Veenhuis M *et al* (2015) Central role of Mic10 in the mitochondrial contact site and cristae organizing system. *Cell Metab* 21: 747 – 755
37. Milenkovic D, Larsson NG (2015) Mic10 oligomerization pinches off mitochondrial cristae. *Cell Metab* 21: 660 – 661
38. Eydt K, Davies KM, Behrendt C, Wittig I, Reichert AS (2017) Cristae architecture is determined by an interplay of the MICOS complex and the F1FO ATP synthase via Mic27 and Mic10. *Microbial Cell* 4: 259 – 272
39. Rampelt H, Bohnert M, Zerbes RM, Horvath SE, Warscheid B, Pfanner N, van der Laan M (2017) Mic10, a core subunit of the mitochondrial contact site and cristae organizing system, interacts with the dimeric F1Fo-ATP synthase. *J Mol Biol* 429: 1162 – 1170
40. Hessenberger M, Zerbes RM, Rampelt H, Kunz S, Xavier AH, Purfurst B, Lilie H, Pfanner N, van der Laan M, Daumke O (2017) Regulated membrane remodeling by Mic60 controls formation of mitochondrial crista junctions. *Nat Commun* 8: 15258
41. Tarasenko D, Barbot M, Jans DC, Kroppen B, Sadowski B, Heim G, Mobius W, Jakobs S, Meinecke M (2017) The MICOS component Mic60 displays a conserved membrane-bending activity that is necessary for normal cristae morphology. *J Cell Biol* 216: 889 – 899
42. Weber TA, Koob S, Heide H, Wittig I, Head B, van der Bliek A, Brandt U, Mittelbronn M, Reichert AS (2013) APOOL is a cardiolipin-binding constituent of the Mitofilin/MINOS protein complex determining cristae morphology in mammalian mitochondria. *PLoS ONE* 8: e63683
43. Koob S, Barrera M, Anand R, Reichert AS (2015) The non-glycosylated isoform of MIC26 is a constituent of the mammalian MICOS complex and promotes formation of crista junctions. *Biochem Biophys Acta* 1853: 1551 – 1563
44. Anand R, Strecker V, Urbach J, Wittig I, Reichert AS (2016) Mic13 is essential for formation of crista junctions in mammalian cells. *PLoS ONE* 11: e0160258
45. Guarani V, McNeill EM, Paulo JA, Huttlin EL, Frohlich F, Gygi SP, Van Vactor D, Harper JW (2015) QIL1 is a novel mitochondrial protein required for MICOS complex stability and cristae morphology. *Elife* 4: 06265

46. Penttila S, Jokela M, Bouquin H, Saukkonen AM, Toivanen J, Udd B (2015) Late onset spinal motor neuronopathy is caused by mutation in CHCHD10. *Ann Neurol* 77: 163 – 172
47. Tsai PI, Lin CH, Hsieh CH, Papakyrikos AM, Kim MJ, Napolioni V, Schoor C, Couthouis J, Wu RM, Wszolek ZK *et al* (2018) PINK1 phosphorylates MIC60/mitofilin to control structural plasticity of mitochondrial crista junctions. *Mol Cell* 69: 744 – 756.e6
48. Godiker J, Gruneberg M, DuChesne I, Reunert J, Rust S, Westermann C, Wada Y, Classen G, Langhans CD, Schlingmann KP *et al* (2018) QIL1-dependent assembly of MICOS complex-lethal mutation in C19ORF70 resulting in liver disease and severe neurological retardation. *J Hum Genet* 63: 707 – 716
49. Guarani V, Jardel C, Chretien D, Lombes A, Benit P, Labasse C, Lacene E, Bourillon A, Imbard A, Benoist JF *et al* (2016) QIL1 mutation causes MICOS disassembly and early onset fatal mitochondrial encephalopathy with liver disease. *Elife* 5: e17163
50. Russell BE, Whaley KG, Bove KE, Labilloy A, Lombardo RC, Hopkin RJ, Leslie ND, Prada C, Assouline Z, Barcia G *et al* (2019) Expanding and underscoring the hepato-encephalopathic phenotype of QIL1/MIC13. *Hepatology* 70: 1066 – 1070
51. Zeharia A, Friedman JR, Tobar A, Saada A, Konen O, Fellig Y, Shaag A, Nunnari J, Elpeleg O (2016) Mitochondrial hepato-encephalopathy due to deficiency of QIL1/MIC13 (C19orf70), a MICOS complex subunit. *Eur J Hum Genet* 24: 1778 – 1782
52. Huynen MA, Muhlmeister M, Gotthardt K, Guerrero-Castillo S, Brandt U (2016) Evolution and structural organization of the mitochondrial contact site (MICOS) complex and the mitochondrial intermembrane space bridging (MIB) complex. *Biochem Biophys Acta* 1863: 91 – 101
53. Munoz-Gomez SA, Slamovits CH, Dacks JB, Baier KA, Spencer KD, Wideman JG (2015) Ancient homology of the mitochondrial contact site and cristae organizing system points to an endosymbiotic origin of mitochondrial cristae. *Curr Biol* 25: 1489 – 1495
54. Callegari S, Muller T, Schulz C, Lenz C, Jans DC, Wissel M, Opazo F, Rizzoli SO, Jakobs S, Urlaub H *et al* (2019) A MICOS-TIM22 association promotes carrier import into human mitochondria. *J Mol Biol* 431: 2835 – 2851
55. John GB, Shang Y, Li L, Renken C, Mannella CA, Selker JM, Rangell L, Bennett MJ, Zha J (2005) The mitochondrial inner membrane protein mitofilin controls cristae morphology. *Mol Biol Cell* 16: 1543 – 1554
56. Jans DC, Wurm CA, Riedel D, Wenzel D, Stagge F, Deckers M, Rehling P, Jakobs S (2013) STED super-resolution microscopy reveals an array of MINOS clusters along human mitochondria. *Proc Natl Acad Sci USA* 110: 8936 – 8941
57. Stoldt S, Stephan T, Jans DC, Bruser C, Lange F, Keller-Findeisen J, Riedel D, Hell SW, Jakobs S (2019) Mic60 exhibits a coordinated clustered distribution along and across yeast and mammalian mitochondria. *Proc Natl Acad Sci USA* 116: 9853 – 9858
58. Friedman JR, Mourier A, Yamada J, McCaffery JM, Nunnari J (2015) MICOS coordinates with respiratory complexes and lipids to establish mitochondrial inner membrane architecture. *Elife* 4: 07739
59. Appelhans T, Busch KB (2017) Dynamic imaging of mitochondrial membrane proteins in specific sub-organelle membrane locations. *Biophys Rev* 9: 345 – 352
60. Wolf DM, Segawa M, Kondadi AK, Anand R, Bailey ST, Reichert AS, van der Bliek AM, Shackelford DB, Liesa M, Shirihai OS (2019) Individual cristae within the same mitochondrion display different membrane potentials and are functionally independent. *EMBO J* 38: e101056
61. Gautier A, Juillerat A, Heinis C, Correa IR Jr, Kindermann M, Beaufils F, Johnsson K (2008) An engineered protein tag for multiprotein labeling in living cells. *Chem Biol* 15: 128 – 136
62. Keppler A, Gendreizig S, Gronemeyer T, Pick H, Vogel H, Johnsson K (2003) A general method for the covalent labeling of fusion proteins with small molecules *in vivo*. *Nat Biotechnol* 21: 86 – 89
63. Lukinavicius G, Umezawa K, Olivier N, Honigmann A, Yang G, Plass T, Mueller V, Reymond L, Correa IR Jr, Luo ZG *et al* (2013) A near-infrared fluorophore for live-cell super-resolution microscopy of cellular proteins. *Nat Chem* 5: 132 – 139
64. Twig G, Elorza A, Molina AJA, Mohamed H, Wikstrom JD, Walzer G, Stiles L, Haigh SE, Katz S, Las G *et al* (2008) Fission and selective fusion govern mitochondrial segregation and elimination by autophagy. *EMBO J* 27: 433 – 446
65. Kukat C, Davies KM, Wurm CA, Spahr H, Bonekamp NA, Kuhl I, Joos F, Polosa PL, Park CB, Posse V *et al* (2015) Cross-strand binding of TFAM to a single mtDNA molecule forms the mitochondrial nucleoid. *Proc Natl Acad Sci USA* 112: 11288 – 11293
66. Schroeder LK, Barentine AES, Merta H, Schweighofer S, Zhang Y, Baddeley D, Bewersdorf J, Bahmanyar S (2018) Dynamic nanoscale morphology of the ER surveyed by STED microscopy. *J Cell Biol* 218: 83 – 96
67. Shin W, Ge L, Arpino G, Villarreal SA, Hamid E, Liu H, Zhao WD, Wen PJ, Chiang HC, Wu LG (2018) Visualization of membrane pore in live cells reveals a dynamic-pore theory governing fusion and endocytosis. *Cell* 173: 934 – 945.e12
68. Huang X, Fan J, Li L, Liu H, Wu R, Wu Y, Wei L, Mao H, Lal A, Xi P *et al* (2018) Fast, long-term, super-resolution imaging with Hessian structured illumination microscopy. *Nat Biotechnol* 36: 451 – 459
69. Wang C, Taki M, Sato Y, Tamura Y, Yaginuma H, Okada Y, Yamaguchi S (2019) A photostable fluorescent marker for the superresolution live imaging of the dynamic structure of the mitochondrial cristae. *Proc Natl Acad Sci USA* 116: 15817 – 15822
70. Stephan T, Roesch A, Riedel D, Jakobs S (2019) Live-cell STED nanoscopy of mitochondrial cristae. *Sci Rep* 9: 12419
71. Kates M, Syz JY, Gosser D, Haines TH (1993) pH-dissociation characteristics of cardiolipin and its 2'-deoxy analogue. *Lipids* 28: 877 – 882
72. Strauss M, Hofhaus G, Schroder RR, Kuhlbrandt W (2008) Dimer ribbons of ATP synthase shape the inner mitochondrial membrane. *EMBO J* 27: 1154 – 1160
73. Rieger B, Junge W, Busch KB (2014) Lateral pH gradient between OXPHOS complex IV and F(0)F(1) ATP-synthase in folded mitochondrial membranes. *Nat Commun* 5: 3103
74. Wilkens V, Kohl W, Busch K (2013) Restricted diffusion of OXPHOS complexes in dynamic mitochondria delays their exchange between cristae and engenders a transitory mosaic distribution. *J Cell Sci* 126: 103 – 116
75. Aaltonen MJ, Friedman JR, Osman C, Salin B, di Rago JP, Nunnari J, Langer T, Tatsuta T (2016) MICOS and phospholipid transfer by Ups2-Mdm35 organize membrane lipid synthesis in mitochondria. *J Cell Biol* 213: 525 – 534
76. Kang M, Day CA, Kenworthy AK, DiBenedetto E (2012) Simplified equation to extract diffusion coefficients from confocal FRAP data. *Traffic* 13: 1589 – 1600
77. Schindelin J, Arganda-Carreras I, Frise E, Kaynig V, Longair M, Pietzsch T, Preibisch S, Rueden C, Saalfeld S, Schmid B *et al* (2012) Fiji: an open-source platform for biological-image analysis. *Nat Methods* 9: 676 – 682
78. Tinevez JY, Perry N, Schindelin J, Hoopes GM, Reynolds GD, Laplantine E, Bednarek SY, Shorte SL, Eliceiri KW (2017) TrackMate: an

open and extensible platform for single-particle tracking. *Methods* 115: 80 – 90

79. Wagner T, Kroll A, Haramagatti CR, Lipinski HG, Wiemann M (2017) Classification and segmentation of nanoparticle diffusion trajectories in cellular micro environments. *PLoS ONE* 12: e0170165
80. Tarantino N, Tinevez JY, Crowell EF, Boisson B, Henriques R, Mhlanga M, Agou F, Israel A, Laplantine E (2014) TNF and IL-1 exhibit distinct ubiquitin requirements for inducing NEMO-IKK supramolecular structures. *J Cell Biol* 204: 231 – 245
81. Giannone G, Hosy E, Levet F, Constals A, Schulze K, Sobolevsky AI, Rosconi MP, Gouaux E, Tampe R, Choquet D *et al* (2010) Dynamic superresolution imaging of endogenous proteins on living cells at ultra-high density. *Biophys J* 99: 1303 – 1310
82. Schoonderwoert V, Dijkstra R, Luckinavicius G, Kobler O, Voort HVD (2013) Huygens STED deconvolution increases signal-to-noise and image resolution towards 22 nm. *Microsc Today* 21: 38 – 44
83. Cipolat S, Martins de Brito O, Dal Zilio B, Scorrano L (2004) OPA1 requires mitofusin 1 to promote mitochondrial fusion. *Proc Natl Acad Sci USA* 101: 15927 – 15932

3.3. Conserved residues of the MICOS subunit MIC13 are important for its function to bridge MICOS subcomplexes

Jennifer Urbach[1], Arun Kumar Kondadi[1], Céline David[1], Kim Deinert[1], Andreas S Reichert[1], Ruchika Anand[1*]

[1]Institute of Biochemistry and Molecular Biology I, Heinrich Heine University Düsseldorf, Medical Faculty, Universitätsstr. 1, 40225, Düsseldorf, Germany

ABSTRACT

Mitochondria own a distinct ultrastructure with a double membrane and characteristic invaginations, called cristae. MICOS is an important protein complex to maintain and form cristae junctions (CJs) between cristae and inner membrane. MIC13 was recently identified to be part of this complex and suggested to act as a bridge between the two subcomplexes of MICOS. Defects of MIC13 are associated with mitochondrial hepato-encephalopathy. In this study, we could show, that expression of FLAG-tagged MIC13 in *MIC13* KO cells can restore morphology of cristae and MICOS levels and assembly. Further, we could show, that large parts of MIC13 are dispensable for its function in MICOS assembly. We found the N-terminal region and the region between amino acids 84 and 103 to be most important for MIC13 function. In these regions a conserved GxxxG motif, as well the conserved amino acid residues WN are located, which we proofed to be essential for the interaction of MIC13 and other MICOS components, as well as for maintenance of cristae morphology. We could further confirm MIC13 functioning as a bridge between the two MICOS subcomplexes and the conserved regions to be important for this function.

INTRODUCTION

Mitochondria are key organelles that are required for many important cellular processes including energy conversion and metabolic processes. The internal structure of the mitochondrial is versatile and undergoes dynamic alteration upon changing cellular and energetic cues. The most important feature of this double membrane enclosed organelle is the invaginations of the inner membrane (IM) that are termed cristae. The protein and lipid composition of the cristae membrane is different from the remaining IM that is parallel to the outer membrane (OM) and is called inner boundary membrane (IBM) (Huynen et al., 2016; Vogel et al., 2006; Wurm and Jakobs, 2006). This could be mainly due to the presence of crista junctions (CJs) that have a very small opening at the neck of the cristae and could act as a diffusion barrier for proteins or metabolites (Mannella, 2006; Mannella et al., 2013; Mannella et al., 2001). Individual crista in a mitochondrion can maintain distinctive membrane potential possibly due to the diffusion barrier created by CJ (Wolf et al., 2019). Moreover, the cytochrome c that resides in the cristae lumen only comes out during the apoptotic signaling that causes subsequent opening of the crista junctions so that to initiate the apoptotic cascade (Scorrano et al., 2002). Very recently our long-standing perception of the static cristae was changed due to the advent of diffraction-unlimited super-resolution techniques such as STED where the IM structures imaged at unprecedented details showed the dynamic nature of cristae membranes (Huang et al., 2018; Kondadi et al., 2020; Stephan et al., 2019; Wang et al., 2019). Using Live-STED super-resolution nanoscopy, we found that CJs and cristae undergo constant dynamic remodeling comprising reversible and balanced events of merging and splitting of CJs and cristae at the timescales of seconds (Kondadi et al., 2020). We devised novel cristae fusion assays that suggested that cristae merging could lead to content mixing between cristae and therefore proposed a model of Cristae Fusion and Fission (CriFF). Cristae (and CJs) remodeling depends on the presence of the fully assembled MICOS complex (Kondadi et al., 2020). MICOS (Mitochondrial Contact Site and Cristae Organizing System) is a conserved heterooligomeric complex that is enriched at the CJs and is required for the formation of CJs and contact between IM and OM (Harner et al., 2011; Hoppins et al., 2011; Rabl et al., 2009;

von der Malsburg et al., 2011). Seven bonafide subunits of MICOS have been identified in mammalian MICOS that are named as MIC 'X' (MIC10 to MIC60) according to a uniform nomenclature regime (Pfanner et al., 2014). Apart from their role in CJs and contact site formation, various subunits of MICOS are required for cellular respiration, protein import, mtDNA organization, mitochondrial translation, apoptosis, autophagy, and phospholipid biogenesis. Changes in steady state levels or protein modification of MICOS subunits are associated with several human diseases including diabetic cardiomyopathy, Down syndrome, Parkinson's disease, diabetes, and epilepsy (Colina-Tenorio et al., 2020; Eramo et al., 2020; Zerbes et al., 2012). Direct mutations in two subunits of MICOS, namely *MIC60* and *MIC13* are found in Parkinson's disease (PD) (Tsai et al., 2018) and infantile fatal mitochondrial encephalopathy with liver dysfunction respectively (Godiker et al., 2018; Guarani et al., 2016; Russell et al., 2019; Zeharia et al., 2016).

At molecular level, the MICOS complex is composed of two subcomplexes, MIC60-containing complex (MIC60-MIC25-MIC19) for contact between IM and OM and MIC10-containing membrane sculpting subcomplex (MIC10-MIC13-MIC26-MIC27) (Khosravi and Harner, 2020; Rampelt et al., 2016). MIC60 subcomplex interacts with several OM proteins including SAM and TOM complexes to form a bigger complex termed MIB, mitochondrial intermembrane space bridging complex (Huynen et al., 2016; Ott et al., 2012; von der Malsburg et al., 2011; Xie et al., 2007). MIC60 and MIC10 are the key subunits of MICOS that also possess membrane-bending abilities (Barbot et al., 2015; Bohnert et al., 2015; Hessenberger et al., 2017; Tarasenko et al., 2017). MIC13 is proposed to act as a bridge between the two subcomplexes of MICOS. In mammalian cells, the deletion of MIC13 leads to nearly complete loss of CJs with the concomitant accumulation of cristae that are arranged in concentric rings, the phenotype reminiscing of loss of MICOS subunits (Anand et al., 2016; Guarani et al., 2015). Additionally, MIC13 is required for the assembly of the MIC10-containing subcomplex as loss of MIC13 causes degradation of this complex with reduced steady state levels of its components namely MIC10, MIC26, and MIC27. MIC60-subcomplex remains intact in the

MIC13 KO cells albeit has reduced size compared to control cells. Likewise, MIC12, a MIC13 homolog of baker yeast, was shown to participate in coupling between the MIC60- and MIC10-subcomplexes (Zerbes et al., 2016). The importance of MIC13 for human health and survival is undoubtedly evident because mutations in *MIC13/Qil1* cause severe neonatal mitochondrial encephalopathy associated with liver dysfunction (Godiker et al., 2018; Guarani et al., 2016; Russell et al., 2019; Zeharia et al., 2016). Patients die at an early age ranging from a few months old to 5 years. Pleiotropic symptoms include neurodegeneration with cerebellar and vermis atrophy, acquired microcephaly, and optic atrophy accompanied by liver disease that could lead to acute liver failure (ALF) in several patients. Kidney stones and cardiac hypertrophy were also observed in some patients. Patients showed excessive secretion of 3-methylglutaconic acids that indicated mitochondrial dysfunction. Moreover, increased plasma levels of lactic acid, methionine, tyrosine, and Krebs cycle intermediates were found. In all the reported cases, the MIC13 protein was completely lost and the patient tissues showed swollen cristae that were arranged in concentric rings similar to what has been observed in the *MIC13* KO cell lines, indicating that altered cristae structure could be the main trigger that leads to mitochondrial defects and progression of pathological symptoms. In line with many mitochondrial diseases, the same mutation of MIC13 could lead to different onset of the disease (Russell et al., 2019). Furthermore, a point mutation (Gly to Ser) at the C-terminal region of *MIC13* in Rhodesian Ridgeback Dog was found to be associated with cardiac ventricular arrhythmias and sudden cardiac arrest (Meurs et al., 2019).

MIC13 is a small protein with no structural or functional domains identified yet. As loss of MIC13 causes a concomitant loss of MIC10, MIC26, and MIC27, it is difficult to assign the defects observed in *MIC13* KO cell lines exclusively to the function of MIC13. Overexpression of MIC10 or MIC26 in the patient cell lines could only partially rescue the MIC13 defects (Guarani et al., 2016). To determine the exact molecular role of MIC13 and identify its functional domains, we took an unbiased systemic approach to generate deletion variants of MIC13 across its length. We found that large parts of the MIC13 sequence are dispensable for

its function. Nevertheless, there are two conserved regions, namely a GxxxG motif and a WN, which play an important role in interaction with other MICOS components and assembly of the MICOS, therefore affecting mitochondrial ultrastructure. Our findings emphasize the role of MIC13 as a bridge between the two subcomplexes, but also show, that there might be another molecular function of this protein.

RESULTS

Generation and expression of MIC13 deletion variants in *MIC13* KO

MIC13 is a small protein with 118 aa and no structural or functional homology has been associated with any other known proteins so far. Additionally, loss of MIC13 leads to degradation of MIC10-subcomplex containing MIC10, MIC26, and MIC27 accompanied by impaired assembly of MICOS complex that makes it tricky to determine the specific function of MIC13. To determine the molecular role of MIC13, we decided to systematically generate deletion variants of MIC13 across its length. For these experiments, we first generated MIC13-FLAG constructs where FLAG moiety was attached to the C-terminus of MIC13. To verify that this construct was fully functional, we overexpressed MIC13-FLAG or MIC13 (untagged) in *MIC13* KO. Both the constructs were equally able to restore the loss of the subunits of MIC10-subcomplex *MIC13* KO **(Fig 1A)** as well as their integration into the MICOS complex **(Fig 1B)**. *MIC13* KO causes loss of CJ and shows cristae that are arranged as concentric rings. Overexpression of MIC13 or MIC13-FLAG in *MIC13* KO could fully rescue the cristae morphology defects of the *MIC13* KO **(Fig 1C)**. This implies that the expression of MIC13-Flag in *MIC13* KO rescues its defects and the FLAG-tag does not impact the assembly and function of the MICOS complex. We used the MIC13-FLAG construct to systematically generate approximately 20 aa deletion across the length of MIC13 using site-directed, ligase-independent mutagenesis (SLIM) as depicted in **Fig 2A** and made stable cell lines that express individual deletion variants or MIC13-FLAG or empty vector (pMSCVpuro) in *MIC13* KO cells using retroviral transduction methods. We analyzed the expression levels of each deletion variants in *MIC13* KO and found that most of them were significantly expressed in stable cell

lines except MIC13$^{\Delta 2\text{-}26}$ and MIC13$^{\Delta 84\text{-}103}$ that hardly show any expression and MIC13$^{\Delta 46\text{-}63}$ show slightly lower expression compared to MIC13-FLAG **(Fig 2B).** MIC13 antibody used in this study binds to the C-terminus of MIC13 and therefore could not recognize the C-terminal deletion variant MIC13$^{\Delta 104\text{-}118}$ that was subsequently detected using FLAG antibody in the western blots **(Fig 2B).** *MIC13* KO (with ev) shows highly reduced levels of MIC10, MIC26, and MIC27 and a slight shift in the molecular weight of MIC27 compared to Hek-293T WT (with ev), which is consistent with earlier findings (Anand et al., 2016; Guarani et al., 2015). Next, we checked whether the expression of deletion variants of MIC13 in *MIC13* KO could restore the steady state levels of MIC10 and MIC26 and MIC27 using western blots analysis **(Fig 2B).** We found that expression of most of the deletion variants that include MIC13$^{\Delta 27\text{-}45}$, MIC13$^{\Delta 64\text{-}83}$ and MIC13$^{\Delta 104\text{-}118}$ in *MIC13* KO could restore the levels of MIC10, MIC26, and MIC27. MIC13$^{\Delta 46\text{-}63}$ that has lower expression was still able to restore MIC10, MIC26, and MIC27 levels almost comparable to MIC13-FLAG. However, N-terminal deletion MIC13$^{\Delta 2\text{-}26}$ and MIC13$^{\Delta 84\text{-}103}$ were unable to restore the steady state levels of MIC10 and MIC26. Interestingly, while MIC13-FLAG was able to restore the steady state levels as well as the shift in molecular weight of MIC27, most of the other deletion variants (MIC13$^{\Delta 27\text{-}45}$, MIC13$^{\Delta 46\text{-}63}$, MIC13$^{\Delta 64\text{-}83}$ and MIC13$^{\Delta 104\text{-}118}$) show the presence of both the forms of MIC27. Expression of both MIC13$^{\Delta 2\text{-}26}$ and MIC13$^{\Delta 84\text{-}103}$ contained only the lower molecular weight form of MIC27, among which MIC13$^{\Delta 84\text{-}103}$ show a slight rescue in steady state levels compared to *MIC13* KO (with ev). Overall, we conclude that most of the truncated versions of MIC13 could restore the steady state levels of MIC10 and MIC26 except for two regions, the first 26 amino acids at the N-terminal region and a middle region between 84 to 103 amino acids. This observation is in line with the expression levels of these mutants as they fail to express properly in the stable cell lines. Therefore, we conclude that residues 2 to 26 and 84 to 103 of MIC13 are critical for the stability of MIC13 and consequently fail to restore the levels MIC10-subcomplex when expressed in *MIC13* KO.

N-terminus domain (2-26aa) and middle domain (84-103aa) of MIC13 are required for the interaction with MICOS subunits

To determine how these deletion variants of MIC13 affect the distribution of MIC13 within mitochondria and its integration into the MICOS complex, we stained cells expressing the individual deletion variants using FLAG and MIC60 antibody and analyzed the staining pattern using STED nanoscopy. *MIC13* KO had normal localization of MIC60 arranged in a rail-like punctate pattern that is consistent with our earlier finding that MIC60 acts as a primer for CJ formation (Kondadi et al., 2020). MIC13-FLAG shows characteristic punctate-like staining across the mitochondria that colocalizes with MIC60-specific puncta **(Fig 3)**. Deletion variants MIC13$^{\Delta 27\text{-}45}$, MIC13$^{\Delta 64\text{-}83}$ and MIC13$^{\Delta 104\text{-}118}$ show the staining pattern similar to MIC13-FLAG suggesting these residues do not interfere in the formation of MIC13-specific puncta and their colocalization to MIC60 in the mitochondria. MIC13$^{\Delta 46\text{-}63}$ shows a weaker signal of FLAG antibody due to lower expression level albeit marking the MIC13-specific puncta that are arranged similar to MIC13-FLAG and show comparable colocalization to MIC60. For MIC13$^{\Delta 2\text{-}26}$ and MIC13$^{\Delta 84\text{-}103}$ a very sparsely localized, disturbed pattern of FLAG staining was observed with little or no colocalization with MIC60, which could be due to their lower expression or lack of integration into MICOS. We further analyzed whether the deletion variants of MIC13 can restore the stability and integrity of the MICOS complex using blue-native gel electrophoresis (BN-PAGE). Loss of MIC13 leads to degradation of MIC10-subcomplex and a consequent shift in size of the remaining MICOS complex (MIC60-subcomplex) is observed in BN-PAGE (Anand et al., 2016) **(Fig 4A, Fig 4B)**. MIC13-FLAG rescues the assembly and stability of MICOS complex in *MIC13* KO as shown by incorporation of MIC10 and MIC27 into the complex and the restoration of the shift in molecular size of MICOS marked by MIC60 and MIC25 **(Fig 4A, Fig 4B)**. *MIC13* KO expressing MIC13$^{\Delta 2\text{-}26}$ show no restoration of MICOS complex assembly or any incorporation of MIC10 and MIC27 in MICOS complex, which is consistent with the steady state levels of these proteins **(Fig 2B).** Expression of MIC13$^{\Delta 27\text{-}45}$, MIC13$^{\Delta 46\text{-}63}$, MIC13$^{\Delta 64\text{-}83,}$ and MIC13$^{\Delta 104\text{-}118}$

in *MIC13* KO show the restoration in size shift of MIC60-subcomplex but only partial incorporation of MIC10 and MIC27 in the MICOS complex. The levels of MIC10 or MIC27 that is incorporated in the MICOS complex is lower compared to the MIC13-FLAG despite the comparable restoration in the steady state levels of these subunits **(Fig 2B),** suggesting perhaps these residues might have additional roles in the assembly of MIC10 and MIC27 in the MICOS complex. Deletion variant MIC13$^{\Delta 84\text{-}103}$ fail to restore the shift of the MIC60-subcomplex as well as the incorporation of MIC10 in the MICOS complex, but could partially restore the MIC27 incorporation that is in line with the steady state levels of MIC27. Interestingly in *MIC13* KO expressing MIC13$^{\Delta 2\text{-}26}$, MIC13$^{\Delta 27\text{-}45}$ and MIC13$^{104\text{-}118}$, an increase in a lower molecular weight complex marked by MIC27 which could be a MIC26-MIC27 complex was observed.

Next, we wanted to determine which residues of MIC13 are required for its interaction with the other subunits of the MICOS complex using co-immunoprecipitation (co-IP) experiments with FLAG-antibody. Firstly, we compared the input and elution fractions between the expression of ev or MIC13-FLAG in *MIC13 KO* for MICOS subunits. MIC13-FLAG could successfully elute all the MICOS subunits but they were absent in elution from the expression of ev in *MIC13* KO, confirming the specificity of the co-IP experiments **(Fig 4C)**. Prohibitin was used as a negative control and does not any show interaction with MIC13-FLAG. Deletion variants MIC13$^{\Delta 2\text{-}26}$ and MIC13$^{\Delta 84\text{-}103}$ show loss in interaction with MIC10, MIC26, MIC25, and MIC60 and considerably decrease interaction with MIC27 compared to MIC13-FLAG. Despite the lower expression of MIC13$^{\Delta 2\text{-}26}$ and MIC13$^{\Delta 84\text{-}103}$ in *MIC13* KO, we could compare them with other deletion variants (or MIC13-FLAG) by choosing the blots with the visibly similar levels of input fractions that were generated by varying the exposure times for developing western blots among different conditions. Both MIC13$^{\Delta 2\text{-}26}$ and MIC13$^{\Delta 84\text{-}103}$ show self-interaction marked by MIC13 in the elution fraction that was comparable to MIC13-FLAG, indicating no problems with the co-IP experiments **(Fig 4C)**. The interaction of the other deletion variants of MIC13 MIC13$^{\Delta 27\text{-}45}$, MIC13$^{\Delta 46\text{-}63}$, MIC13$^{\Delta 64\text{-}83,}$ and MIC13$^{\Delta 104\text{-}118}$ with subunits of MICOS were largely similar to

MIC13-FLAG **(Fig 4C)**. Therefore, we conclude that the N-terminal region (2 to 26 aa) and a middle domain (84 to 103 aa) of MIC13 are required for its interaction with other MICOS subunits and hence are crucial for the stability and assembly of the MICOS complex. It has been proposed that MIC13 acts as a bridging protein between MIC60 and MIC10 for the maturation and assembly of the MICOS complex. We performed co-IP using MIC60 antibody to probe the interaction of MIC60 with other subunits of MICOS in cells expressing deletion variants of MIC13 and confirmed that residues 2 to 26 aa and 84 to 103 aa are important for the bridging function of MIC13 between MIC60 and MIC10 **(Fig S1A)**.

Effect of expression of deletion variants of MIC13 on cristae morphology in *MIC13* KO

Loss of MIC13 causes cristae defects with absence of CJs and arrangement of cristae in the form of concentric rings that resembles onion slices in cell lines as well as patient samples (Anand et al., 2016; Guarani et al., 2016; Guarani et al., 2015; Zeharia et al., 2016). To methodically determine the role of various domains of MIC13 in maintaining the cristae structure, we analyzed the mitochondrial ultrastructure of stable cells expressing various deletion variants using TEM analysis. Firstly, we confirm that overexpression of MIC13-FLAG fully rescues the mitochondrial morphology as described earlier **(Fig 1C)**. At the first glance, we noticed that the deletion variants of MIC13 differ in their ability to rescue cristae structure despite being able to restore the steady state levels of MIC10-subcomplex **(Fig 5A).** We performed in detail quantification to find the extent of rescue among different deletion variants and determined the percentage of mitochondria that contained normal/abnormal cristae in each condition **(Fig 5C)**. We also determine the number of cristae and CJs per mitochondrial section in each cell line **(Fig 5B)**. Expression of MIC13$^{\Delta 2\text{-}26}$ and MIC13$^{\Delta 84\text{-}103}$ in *MIC13* KO shows the least amount of rescue among all the deletion variants, which was expected considering their lower expression levels and loss of MIC10-subcomplex. While *MIC13* KO expression MIC13$^{\Delta 46\text{-}63}$ and MIC13$^{\Delta 104\text{-}118}$ show an overall normal cristae morphology that was comparable to MIC13-FLAG, MIC13$^{\Delta 64\text{-}83}$ and MIC13$^{\Delta 27\text{-}45}$ show a partial rescue of the cristae morphology with prevalence of some abnormal cristae. Some instances of interconnected

cristae were found in *MIC13* KO expressing MIC13$^{\Delta 64\text{-}83}$. Considering that expression of MIC13$^{\Delta 64\text{-}83}$ and MIC13$^{\Delta 27\text{-}45}$ in *MIC13* KO restore the levels of MIC10, MIC26, and MIC27, the presence of abnormal cristae structure indicates that these residues of MIC13 might have a direct molecular role in manifesting these defects independent of levels of MIC10-subcomplex.

Conserved GxxxG and WN motif of MIC13 are required for its bridging role in MICOS assembly

We found that the N-terminal domain (2-26aa) and middle region (84-103aa) of MIC13 are crucial for the stability of MIC13 and its interaction with other MICOS subunits. To pinpoint the smaller motifs in these residues that are important for the interaction with MICOS subunits, we searched for conserved domains in these regions. N-terminal region has the putative transmembrane domain and sequence alignment of MIC13 from different species show conserved ^{15}GxxxG^{19} motif in this region (Anand et al., 2016). Previously, a highly conserved ^{81}RDSWN^{85} motif was also found by sequence alignment in MIC13 (Huynen et al., 2016), which falls between deletion variants MIC13$^{\Delta 64\text{-}83}$ and MIC13$^{\Delta 84\text{-}103}$. We mutated the ^{15}GxxxG^{19} region of MIC13 to either one (G15L) or two (G15L, G19L) amino acid substitutions of glycine to leucine. As the residues RDSWN lay in between the deletion variants MIC13$^{\Delta 64\text{-}83}$ and MIC13$^{\Delta 84\text{-}103}$, we decided to generate separate deletion (or substitution to alanine) mutants for RD and WN along with the deletion of whole RDSWN in MIC13 **(Fig 6A)**. Recently a point mutation (glycine to serine) in the C-terminal region of MIC13 was found to be associated with cardiac death in Rhodesian ridgeback dogs (Meurs et al., 2019). We also generated a MIC13 variant with G to S substitution at 109 aa position to determine how this pathological mutation affects the stability or integrity of MICOS subunits in human cell lines. We stably expressed all these MIC13 mutation variants **(Fig 6A)** in *MIC13* KO cells using viral transduction and analyzed the steady state levels for all the MICOS subunits **(Fig 6B)**. For GxxxG substitution mutations, we found that while expression of the MIC13^{G15L} in *MIC13* KO does not affect the steady state levels of MIC13 or other MICOS subunits, MIC13^{G15L,G19L} causes destabilization of MIC13 and loss of the components of MIC10-subcomplexes, underlining the importance of

GxxxG motif for the stability and integrity of MIC13 and MIC10-subcomplex. Among cells expressing MIC13$^{\Delta RD}$ or MIC13$^{\Delta WN}$ in *MIC13* KO, MIC13$^{\Delta RD}$ show no obvious change steady state levels of MIC13 or other MICOS component but MIC13$^{\Delta WN}$ shows a reduced expression and loss of MIC10 and reduced levels of MIC26 compared to the expression of MIC13-FLAG. MIC13$^{\Delta RDSWN}$ shows a similar extent of decrease in levels of MIC13, MIC10, and MIC26 as found for MIC13$^{\Delta WN}$ indicating the importance WN motif in the whole RDSWN motif. The substitution of WN to AA shows slightly lower defects compared to the deletion variant. We also analyzed the ability of these mutant variants to interact with the other MICOS subunits using co-immunoprecipitation **(Fig 6C)**. Expression of single substitution mutation MIC13^{G15L} in *MIC13* KO show normal interaction comparable to MIC13-FLAG expression, but double substitution MIC13^{G15L,G19L} shows a drastic decrease in its ability to interact with MICOS subunits, indicating a central role of GxxxG motif of MIC13 in interaction with other MICOS components. Both MIC13$^{\Delta WN}$ and MIC13$^{\Delta RDSWN}$ also show reduced ability to interact with other MICOS subunits, while MIC13$^{\Delta RD}$ show no defect in the efficiency of interaction compared to MIC13-FLAG, implying the necessary role of WN motif in regulating the stability and the interaction with MICOS subunits. Interestingly the substitution of WN to alanine residues has normal ability to interact with MIC10, MIC26, and MIC27 but slightly reduced ability to interact with MIC60, MIC19, and MIC25 showing the differential effect of the substitution compared to deletion variant of WN motif. GxxxG is a known motif of transmembrane domains and therefore we wanted to check whether the mutated version affects the association with the mitochondrial membrane using alkaline extraction assay **(Fig 6D)**. In a western blot, MIC13^{G15L,G19L} shows two forms, one similar to the size of MIC13-FLAG and another at slightly higher molecular weight. The lower form was more soluble compared to MIC13-FLAG but the higher form is more resistant to alkaline extraction and shows more stringent association with membrane almost similar to membrane protein TOM20. In summary, we find that two conserved motifs, GxxxG and WN, of MIC13 are required for the interaction of MIC13 with other MICOS components and maintaining the stability of the MIC10-subcomplex.

Conserved GxxxG and WN of MIC13 are necessary for the formation of crista junction

We further checked how does the expression of mutated versions of GxxxG and WN motif in *MIC13* KO affect the cristae morphology using EM. We found that while expression of $MIC13^{G15L}$ in *MIC13* KO was able to completely rescue the defective cristae morphology in *MIC13* KO, the expression of $MIC13^{G15L,G19L}$ show more drastic defects with complete loss of CJ, widening of cristae, and accumulation of interconnected cristae, emphasizing on a very crucial and necessary role of GxxxG motif for the formation of CJs and maintenance of proper cristae morphology **(Fig 7A)**. Expression of $MIC13^{\Delta WN}$ or $MIC13^{\Delta RDSWN}$ in *MIC13* KO could not rescue cristae morphology, but expression of $MIC13^{\Delta RD}$ shows normal cristae structure again highlighting the vital role of WN motif in regulating the formation of CJs. Expression of WN substitution shows only partial rescue which is consistent with the previous observation that this could partially recover the MIC10-subcomplex. The loss of crista junctions was observed upon deletion of *MIC13* and could also be observed in cells expressing the mutated proteins $MIC13^{G15L,G19L}$, $MIC13^{\Delta WN}$, $MIC13^{WN84,85AA,}$ and $MIC13^{\Delta RDSWN}$. This observation correlates with the overall appearance of mitochondria, as well as the results from co-immunoprecipitation **(Fig 6C)** and the steady state levels of MICOS proteins **(Fig 6B)**. Overall, we find that GxxxG and WN motifs of MIC13 are essential for maintaining the stability of MIC10-subcomplex, interaction with MICOS subunits, and maintenance of cristae morphology. Taken together these data show a clear relevance of the GxxxG motif of the transmembrane domain of MIC13, as well as the conserved WN at amino acid residues 84 and 85. These conserved regions seem to be important for the correct insertion of MIC13 into the membrane, as well as for the interaction with both of the MICOS subcomplexes, underlining the function of MIC13 as a bridge of the two MICOS subcomplexes **(Fig 7D)**.

DISCUSSION

MIC13 was identified before as a part of the MICOS complex by complexome profiling and interaction proteomics. It was shown to play an essential role in the formation of CJ (Anand et al., 2016; Guarani et al., 2015). Mutations in MIC13 lead to severe childhood mitochondrial

hepato-encephalopathy, which is mostly lethal at a young age (Godiker et al., 2018; Guarani et al., 2016; Kishita et al., 2020; Russell et al., 2019; Zeharia et al., 2016). Till now, there are no studies on the molecular role of this small protein. In this study, we wanted to decipher the molecular role of MIC13 function by mapping functional residues in the MIC13 amino acid sequence. For this, we used an experimental approach, where we created systematic deletions and mutations across the MIC13 sequence. We prepared stable cell lines, expressing the different MIC13 in *MIC13* KO cells with help of viral transduction.

Upon expression of MIC13-FLAG in *MIC13* KO cells, the protein levels of other MICOS components, as well as the MICOS assembly and mitochondrial ultrastructure was restored. Interestingly some of the MIC13 variants were able to restore this phenotype as well, indicating that large parts of MIC13 sequence are dispensable for MICOS assembly. However, we observed, that MIC13$^{\Delta 2\text{-}27}$ and MIC13$^{\Delta 84\text{-}103}$ showed less MIC13 protein levels. This leads to the conclusion, that these residues are required for the stability of MIC13. As a consequence, MIC13$^{\Delta 2\text{-}27}$ and MIC13$^{\Delta 84\text{-}103}$ were also not able to restore the levels of MIC10, MIC26, and MIC27 and the MICOS assembly, as shown by BN-PAGE. With help of co-immunoprecipitation experiments, we showed that these residues are important for the interaction between MIC13 and other MICOS components. Despite the lower protein levels, we found a pulldown of MIC13$^{\Delta 2\text{-}27}$ and MIC13$^{\Delta 84\text{-}103}$ with the FLAG antibody. Other MIC13 variants were able to pulldown all tested MICOS components, suggesting the missing regions in MIC13$^{\Delta 2\text{-}27}$ and MIC13$^{\Delta 84\text{-}103}$ are important for the interaction of MIC13 and MICOS proteins. These findings are supported by crosslink experiments performed with transient transfected MIC13 variants, that could show a loss of a characteristic MIC13-MIC10 band for MIC13$^{\Delta 2\text{-}26}$ and MIC13$^{\Delta 84\text{-}103}$ **(Figure S1B)**. This shows that the N-terminal region and the region between aa 84 and aa 103 are important for the stability of the MIC10-subcomplex and also for the interaction of MIC13 with other MICOS components. To pinpoint the important residues in these regions, we checked alignments of MIC13 to find conserved amino acids and found a GxxxG motif in the N-terminal region and the amino acids RDSWN (81-85aa) in the latter region to be highly

conserved in the sequence (Anand et al., 2016; Huynen et al., 2016). We mutated these residues as well and again created stable cell lines expressing the MIC13 variants in *MIC13* KO cells. For MIC13^{G15L,G19L,} and MIC13$^{\Delta RDSWN}$ no pulldown of other MICOS proteins was observed anymore. MIC13$^{\Delta WN}$ was also not able to pulldown MICOS proteins, whereas MIC13$^{\Delta RD}$ could do that, indicating that only WN (8 –85aa) is needed to pull down other MICOS proteins. These results show, that these two conserved regions, GxxxG and WN are important for the interaction of MIC13 and MICOS. This ultimately supports the role of MIC13 as a bridge between the two MICOS subcomplexes and indicated these conserved residues to be important for the bridging function.

Interestingly the mutation of a single glycine in the GxxxG motif in MIC13^{G19L} shows the same level of restoration as MIC13-FLAG. Also, the mutation of the conserved amino acid residues to alanine in MIC13^{W84A,N85A} did not show a drastic effect on the interaction of MIC13 with other MICOS components. We observed that the coimmunoprecipitation with MIC13^{W84A,N85A} shows a better pulldown of MIC60, than MIC10, suggesting, that this mutation disrupts only the interaction with MIC10 and not with MIC60. It is possible, that the mutation to alanine is not a drastic change for the structure and function of the protein, but the deletion of these residues is much more severe for the protein. There is no 3D-structure model for MIC13 available yet, but a possible 3D-structure model could provide important information and, together with results from this study, further explain the mechanism of how the conserved residues may support MIC13 bridging function. We show here that these conserved residues are important for the interaction of MIC13 to the other MICOS component and MIC13 acts as a bridge between the two MICOS subcomplexes, as proposed earlier (Anand et al., 2016; Guarani et al., 2015; Zeharia et al., 2016).

The GxxxG motif in the suggested transmembrane domain of MIC13 is a well-known motif of transmembrane domains, with ~ 12% of transmembrane helices presenting this motif (Senes et al., 2000; Unterreitmeier et al., 2007). Here we found that motif to be important for the stability of MIC13, as well as for the interaction with other MICOS components as explained

earlier. It directly plays a role in interaction with other MICOS components, especially MIC60 and MIC10. This glycine-rich motif is known to promote protein-protein interaction between helical transmembrane structures (Russ and Engelman, 2000; Senes et al., 2004). Furthermore, mutations of the conserved glycine to leucine in this motif in subunit e of the yeast F_1F_0-ATP synthase leads to a defect in oligomerization of this protein (Arselin et al., 2003). The MICOS component MIC10 is also known to harbor a conserved glycine rich sequence in the transmembrane domain. The GxGxGxG motif in MIC10 was shown to play a crucial role for MIC10 oligomerization, which contributes to its membrane shaping ability and ultimately to a proper mitochondrial ultrastructure (Bohnert et al., 2015). In many cases, the presence of GxxxG motifs hints at dimerization of the protein due to the interaction of two transmembrane domains and this has been shown for more than 20 different proteins (Teese and Langosch, 2015). The GxxxG motif can also be important for interactions between transmembrane domains of different proteins, even if this motif is only present in one of the two interacting helices (Lau et al., 2009). We showed with alkaline extraction, that MIC13^{G15L,G19L} is less associated to the membrane than MIC13-FLAG. This shows the importance of the GxxxG motif for the insertion of MIC13 into the membrane. This is in line with the literature that also postulates other roles of the GxxxG motif than in protein interaction. It can also be involved in functions like lipid interactions, correct orientation of the soluble domain, and also cell localization (Cosson et al., 2013; Monk et al., 2014; Stangl and Schneider, 2015). Interestingly MIC13^{G15L,G19L} shows a second band upon western blot analysis, which has a stronger association to the membrane and migrates at a higher kDa weight than MIC13. It is possible, that the mutation in the GxxxG motifs prevents partly from cleaving off a precursor sequence for mitochondrial inner membrane localization and enhances the hydrophobicity. Another possibility would be a posttranslational modification of the protein or alternative folding of the mutated MIC13.

A conserved glycine in the MIC13 sequence was found before to be mutated in Rhodesian ridgeback dogs diagnosed with cardiac arrhythmia (Meurs et al., 2019). We created the same mutation and introduced it into *MIC13* KO cells. Interestingly, our studies do not show any

effect of this mutation on mitochondrial ultrastructure or levels of MICOS **(Fig S2)**. We suggest, that the effect of this mutation is specific to the organism, so only affects the MIC13 function in dogs and not in human. Also, it is possible, that the effect of this mutation is tissue dependant. Muscle cells have a very high energy demand, therefore a MICOS defect might lead to a much more severe phenotype than in other cell types. It is furthermore possible, that this mutation might affect some unknown function of MIC13. This can be an unidentified interaction of MIC13 with protein or metabolic pathway that contributes to the energy metabolism.

In a previous study, we found that loss of MIC13 leads to loss of CJ and decreased respiration, accompanied by decreased levels of MIC10, Mic26, and MIC27 (Anand et al., 2016). This raises the question if the phenotype is caused by loss of MIC13 directly or by loss of some of the other MICOS components. Loss of MIC10 also leads to a decrease of respiration and disrupted mitochondrial morphology with loss of CJs (Bohnert et al., 2015; Callegari et al., 2019; Kondadi et al., 2020; Tarasenko et al., 2017). The mitochondrial cristae morphology is highly important for proper mitochondrial function and related to apoptosis and respiratory defects (Anand et al., 2020; Kondadi et al., 2020; Scorrano et al., 2002; Wurm and Jakobs, 2006). We wanted to know if MIC13 has a function independent of other MICOS components. Therefore, we looked for a MIC13 variant, which can restore the MICOS assembly but shows an effect on other mitochondrial functions or morphology. Here we show, that the MIC13 variants MIC13$^{\Delta 64\text{-}83}$ and MIC13$^{\Delta 27\text{-}45}$ can restore the interaction with other MICOS components and the assembly of MICOS but do not completely restore the mitochondrial ultrastructure. MIC13$^{\Delta RD}$ can also not completely restore the mitochondrial morphology, despite proper interaction with other MICOS components. We concluded that the conserved amino acid residues RD (81-82aa) from the deleted region in MIC13$^{\Delta 64\text{-}83}$ are important for normal cristae morphology. This suggests that MIC13 could have another role in maintaining mitochondrial cristae morphology that is independent of MIC10-subcomplex and MICOS assembly. It is also possible that these conserved residues mediate interactions with other proteins, which are required for a proper formation of mitochondrial ultrastructure. The interaction of MIC13 with outer membrane proteins like SAMM50, MTX1, and MTX2, but also with matrix proteins GK,

DNAJC1, and TMEM11 was shown before (Guarani et al., 2015). This hints at the involvement of MIC13 to other mitochondrial functions besides its bridging function for the MICOS.

Overall, we found that distinct conserved residues in MIC13 play an important role in the assembly of the MICOS. These results lead to the postulation of a model with MIC13 as a bridge between the MIC60-subcomplex and MIC10-subcomplex and the conserved GxxxG and WN motif as interaction sites to the other MICOS components **(Fig 7D)**. Also, a function of MIC13, besides this bridging function and independent of other MICOS proteins is strongly suggested, but still has to be deciphered. The complete role and the molecular function of MIC13 are not completely unraveled but are an interesting field of research due to the rising numbers of patients presented with MIC13 deficiency (Godiker et al., 2018; Guarani et al., 2016; Kishita et al., 2020; Russell et al., 2019; Zeharia et al., 2016). With the introduction of mutated versions into a *MIC13* KO cell line we found a powerful tool for further studies of this small, yet important MICOS component.

Figure 1

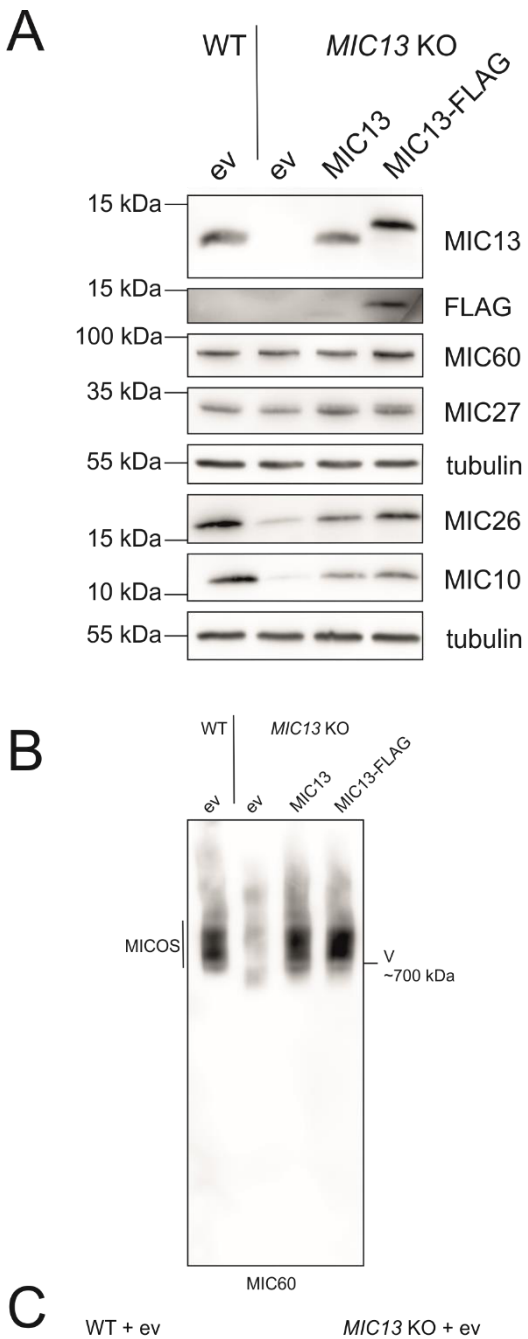
A
WT
MIC13 KO
ev
ev
MIC13
MIC13-FLAG
15 kDa
MIC13
15 kDa
FLAG
100 kDa
MIC60
35 kDa
MIC27
55 kDa
tubulin
15 kDa
MIC26
10 kDa
MIC10
55 kDa
tubulin
B
WT
MIC13 KO
ev
ev
MIC13
MIC13-FLAG
MICOS
V
~700 kDa
MIC60
C
WT + ev
MIC13 KO + ev
MIC13 KO + MIC13
MIC13 KO + MIC13-FLAG

Figure 2

A

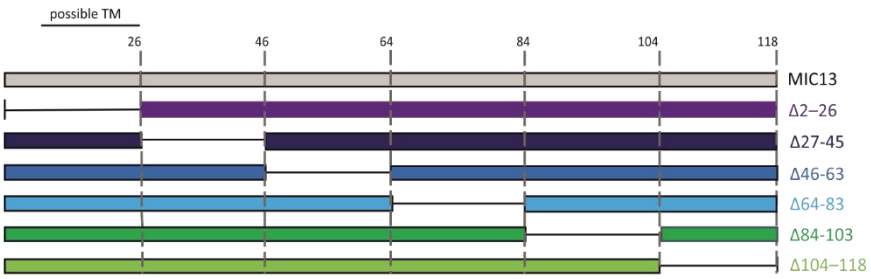
possible TM
26
46
64
84
104
118
MIC13
Δ2–26
Δ27-45
Δ46-63
Δ64-83
Δ84-103
Δ104–118

B

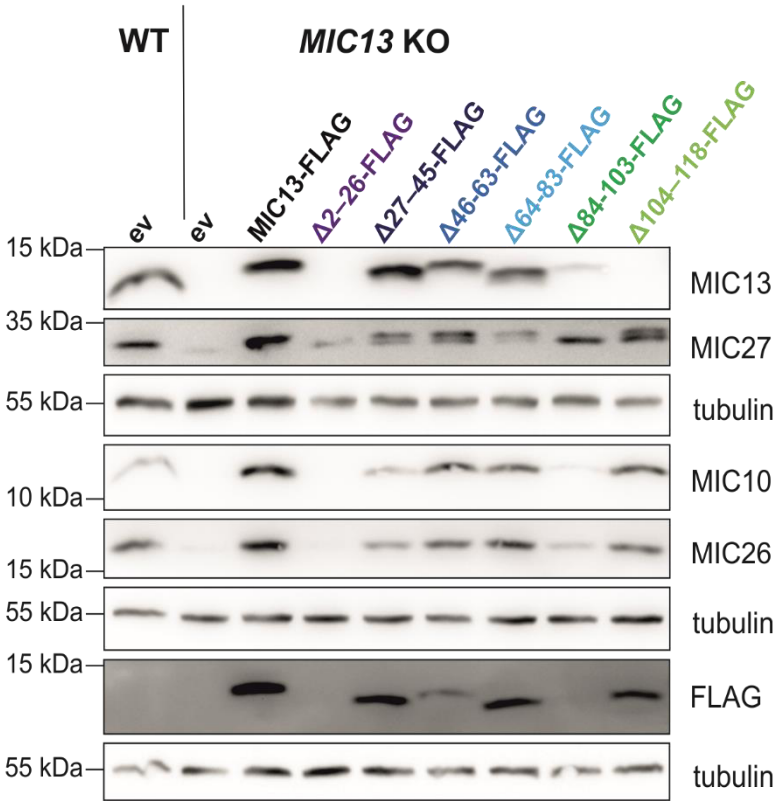
WT
MIC13 KO
ev
ev
MIC13-FLAG
Δ2–26-FLAG
Δ27–45-FLAG
Δ46-63-FLAG
Δ64-83-FLAG
Δ84-103-FLAG
Δ104–118-FLAG
15 kDa
MIC13
35 kDa
MIC27
55 kDa
tubulin
10 kDa
MIC10
15 kDa
MIC26
55 kDa
tubulin
15 kDa
FLAG
55 kDa
tubulin

Figure 3

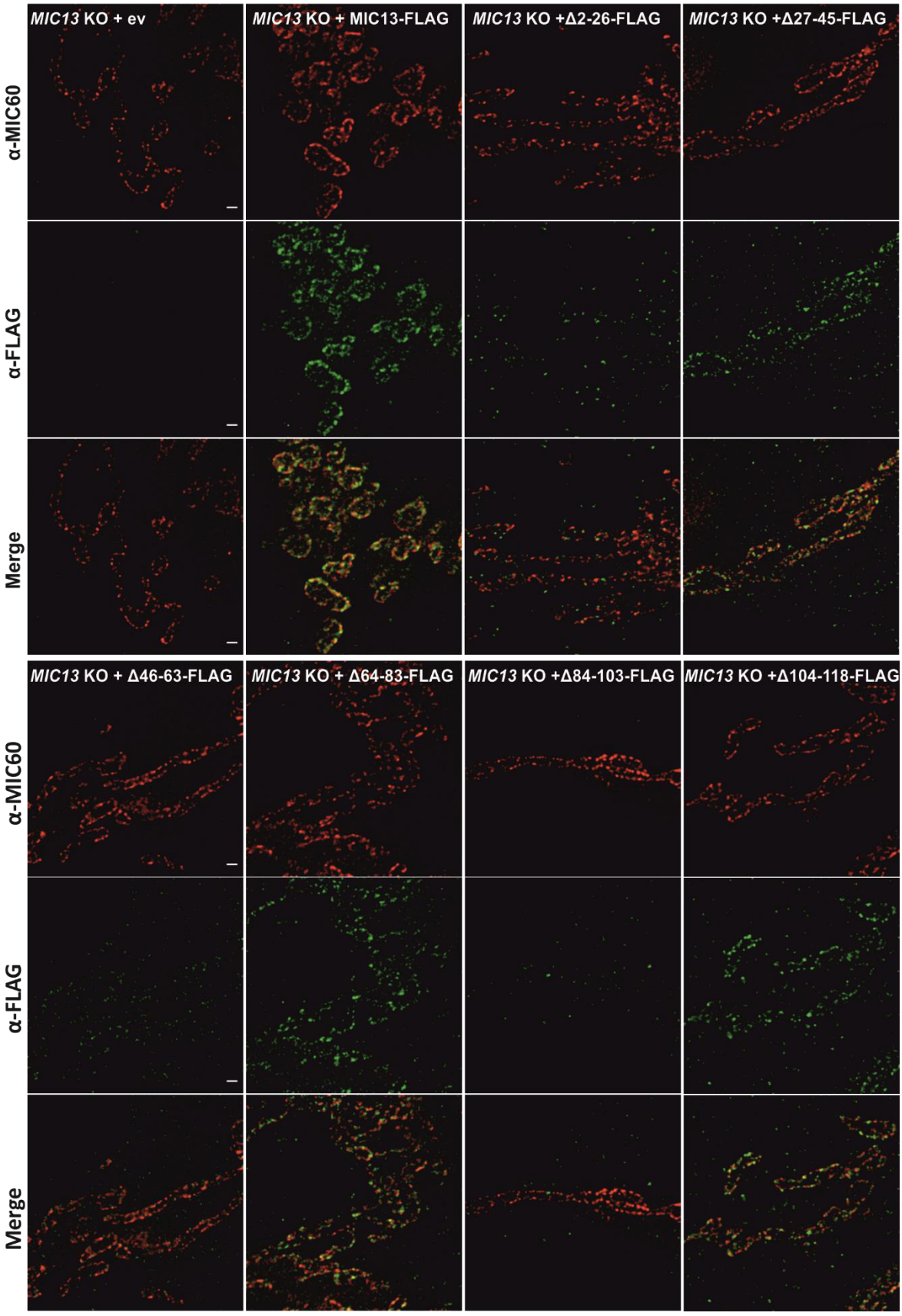
MIC13 KO + ev
MIC13 KO + MIC13-FLAG
MIC13 KO +Δ2-26-FLAG
MIC13 KO +Δ27-45-FLAG
α-MIC60
α-FLAG
Merge
MIC13 KO + Δ46-63-FLAG
MIC13 KO + Δ64-83-FLAG
MIC13 KO +Δ84-103-FLAG
MIC13 KO +Δ104-118-FLAG
α-MIC60
α-FLAG
Merge

Figure 4

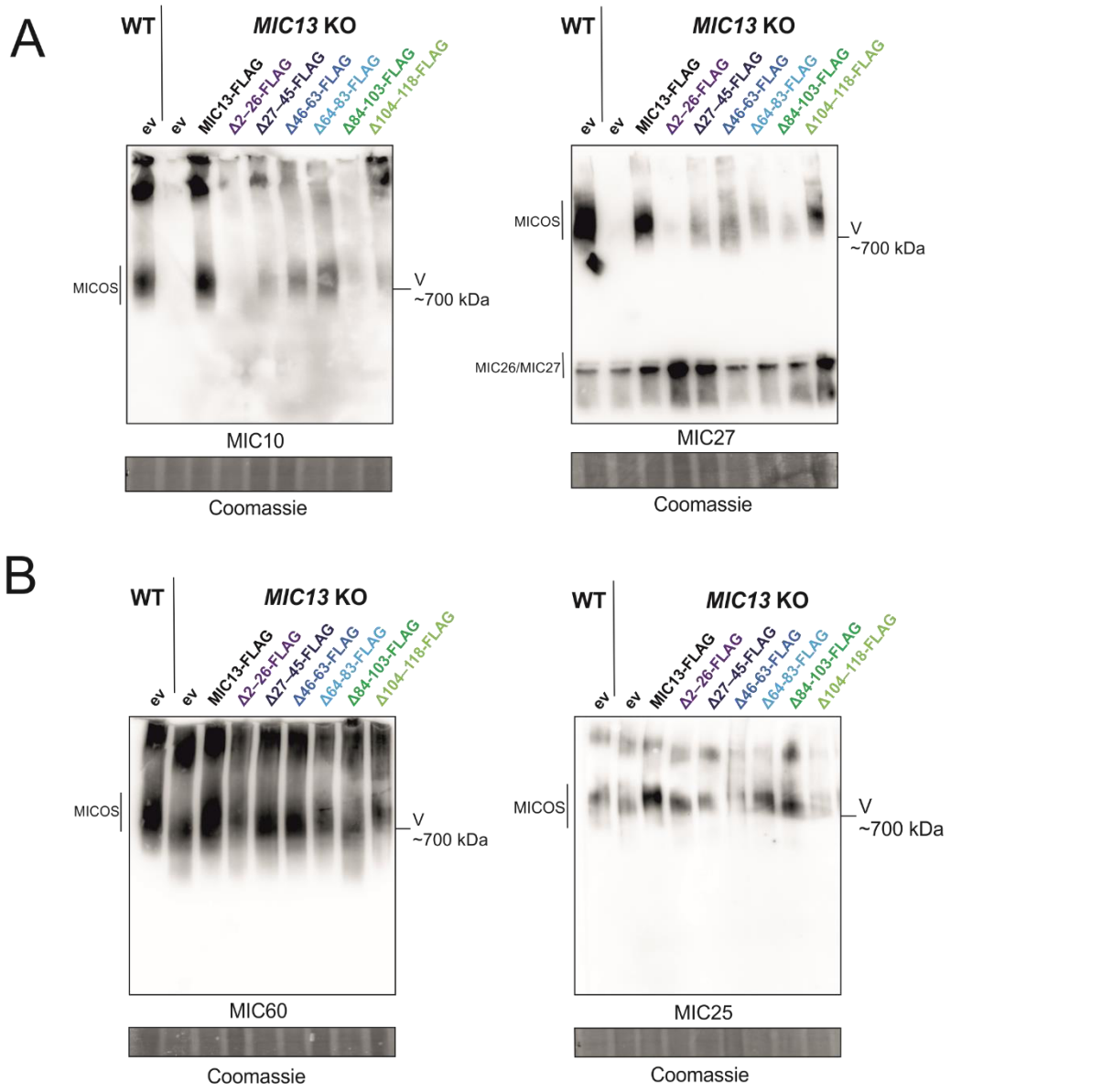
A
WT
MIC13 KO
ev
ev
MIC13-FLAG
Δ2–26-FLAG
Δ27–45-FLAG
Δ46-63-FLAG
Δ64-83-FLAG
Δ84-103-FLAG
Δ104–118-FLAG
MICOS
V
~700 kDa
MIC26/MIC27
MIC10
MIC27
Coomassie
B
MIC60
MIC25
C
IP:
FLAG
I
E
15 kDa
10 kDa
15 kDa
35 kDa
35 kDa
100 kDa
70 kDa
MIC13/FLAG
MIC10
MIC26
MIC27
MIC25
MIC60
Prohibitin

Figure 5

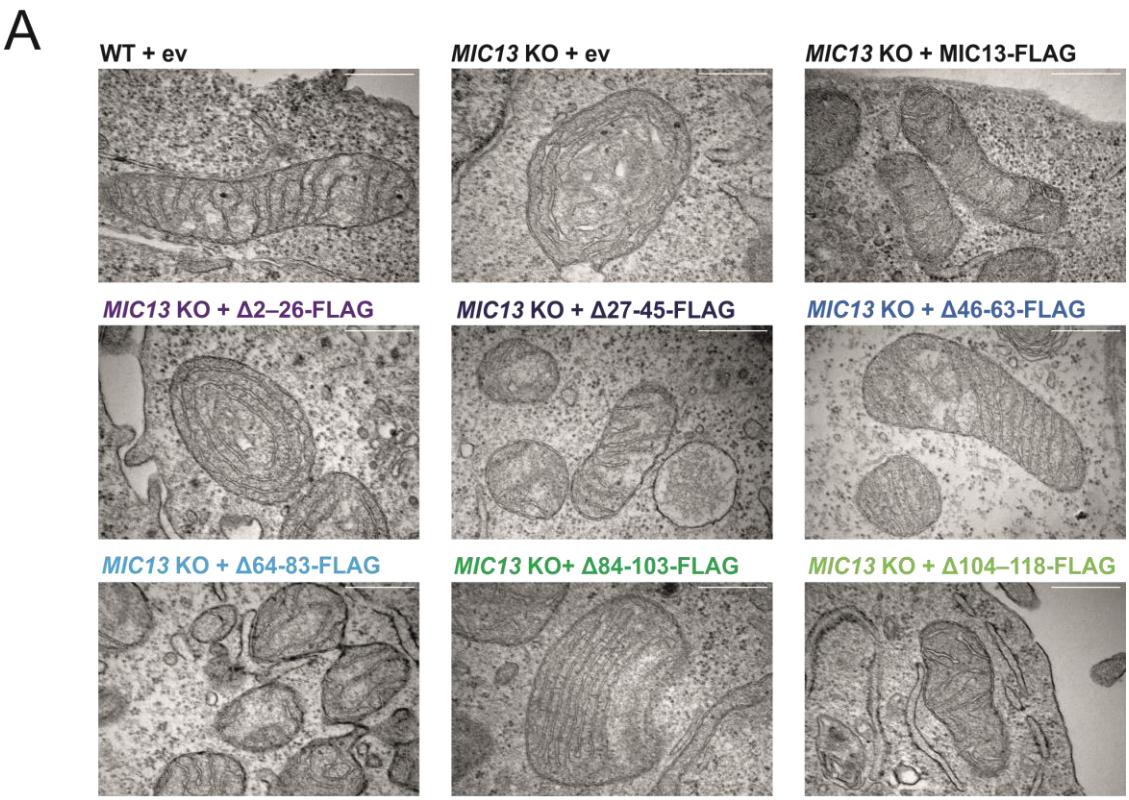
A
WT + ev
MIC13 KO + ev
MIC13 KO + MIC13-FLAG
MIC13 KO + Δ2–26-FLAG
MIC13 KO + Δ27-45-FLAG
MIC13 KO + Δ46-63-FLAG
MIC13 KO + Δ64-83-FLAG
MIC13 KO+ Δ84-103-FLAG
MIC13 KO + Δ104–118-FLAG

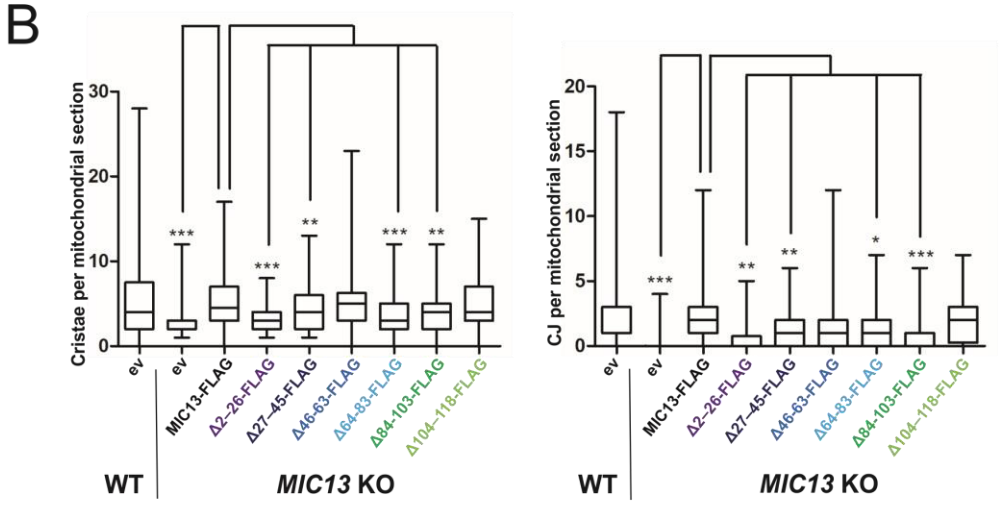
B
Cristae per mitochondrial section
CJ per mitochondrial section
ev
ev
MIC13-FLAG
Δ2–26-FLAG
Δ27–45-FLAG
Δ46-63-FLAG
Δ64-83-FLAG
Δ84-103-FLAG
Δ104–118-FLAG
WT
MIC13 KO

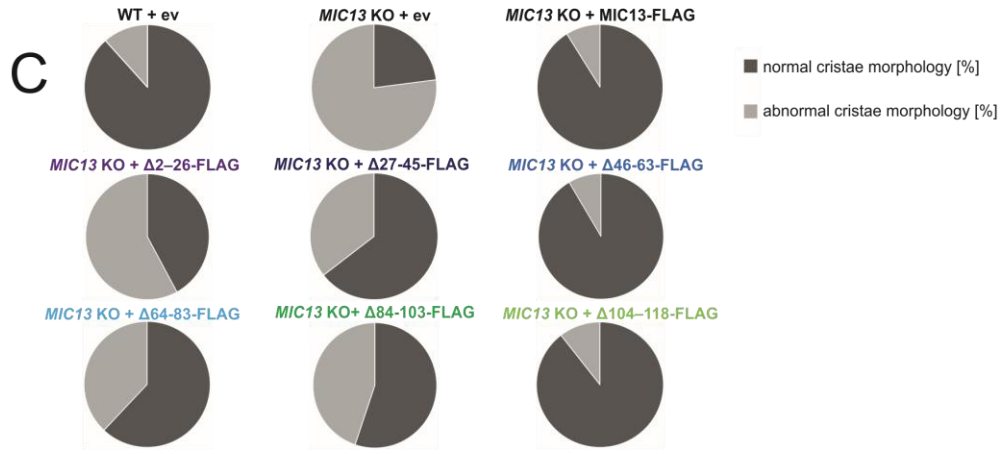
C
WT + ev
MIC13 KO + ev
MIC13 KO + MIC13-FLAG
MIC13 KO + Δ2–26-FLAG
MIC13 KO + Δ27-45-FLAG
MIC13 KO + Δ46-63-FLAG
MIC13 KO + Δ64-83-FLAG
MIC13 KO+ Δ84-103-FLAG
MIC13 KO + Δ104–118-FLAG
normal cristae morphology [%]
abnormal cristae morphology [%]

Figure 6

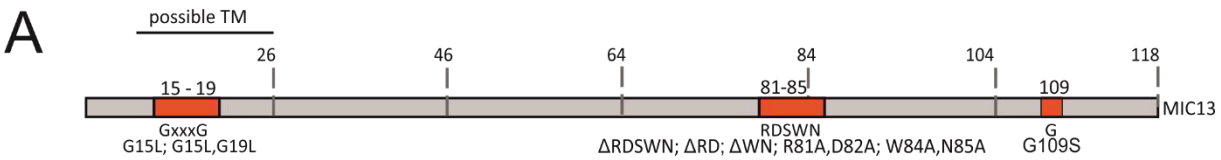
A
possible TM
26
46
64
84
104
118
15 - 19
81-85
109
MIC13
GxxxG
G15L; G15L,G19L
RDSWN
ΔRDSWN; ΔRD; ΔWN; R81A,D82A; W84A,N85A
G
G109S

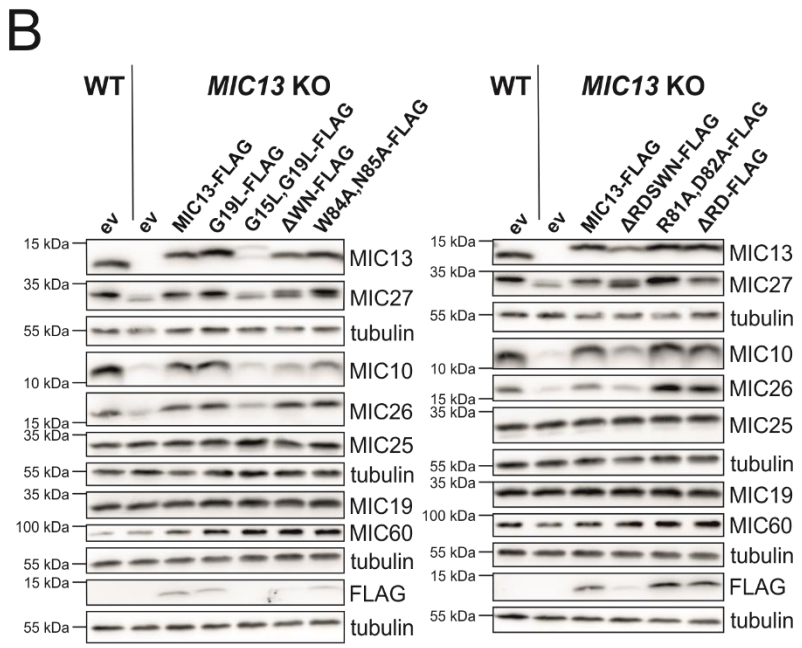
B
WT
MIC13 KO
ev
MIC13-FLAG
G19L-FLAG
G15L,G19L-FLAG
ΔWN-FLAG
W84A,N85A-FLAG
ΔRDSWN-FLAG
R81A,D82A-FLAG
ΔRD-FLAG
MIC13
MIC27
tubulin
MIC10
MIC26
MIC25
MIC19
MIC60
FLAG
15 kDa
35 kDa
55 kDa
10 kDa
100 kDa

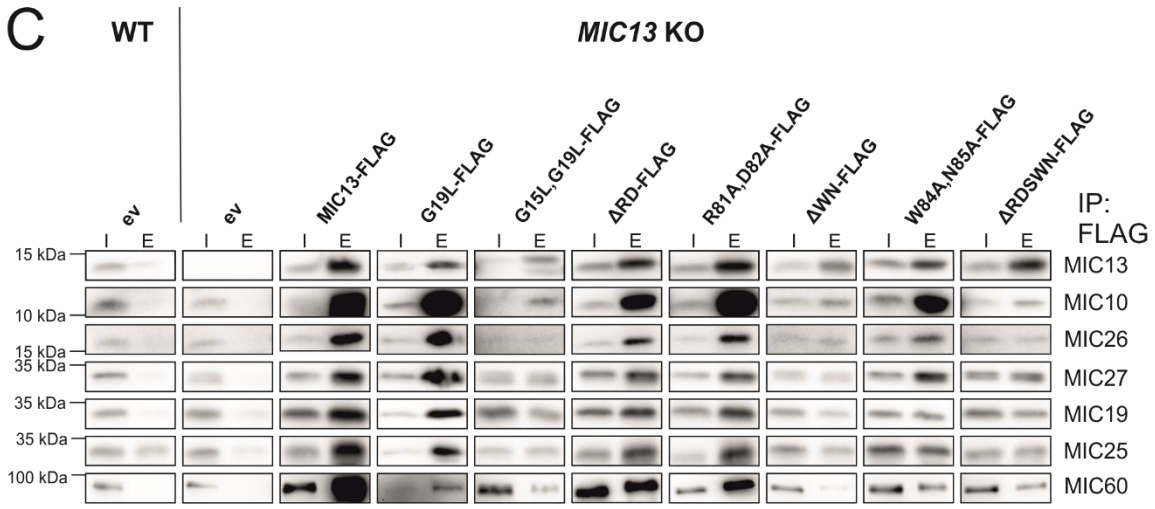
C
WT
MIC13 KO
ev
MIC13-FLAG
G19L-FLAG
G15L,G19L-FLAG
ΔRD-FLAG
R81A,D82A-FLAG
ΔWN-FLAG
W84A,N85A-FLAG
ΔRDSWN-FLAG
I
E
IP: FLAG
MIC13
MIC10
MIC26
MIC27
MIC19
MIC25
MIC60
15 kDa
10 kDa
35 kDa
100 kDa

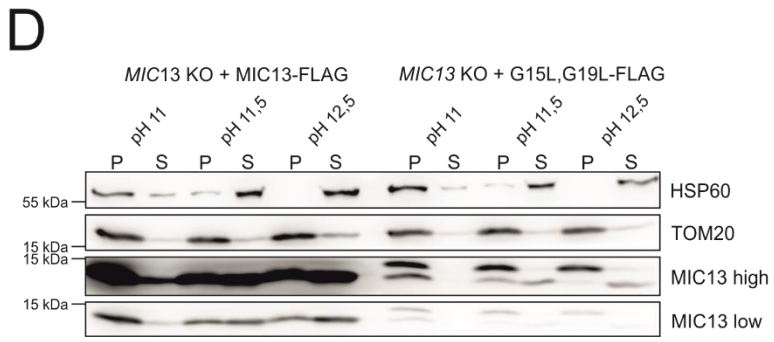
D
MIC13 KO + MIC13-FLAG
MIC13 KO + G15L,G19L-FLAG
pH 11
pH 11,5
pH 12,5
P
S
HSP60
TOM20
MIC13 high
MIC13 low
55 kDa
15 kDa

Figure 7

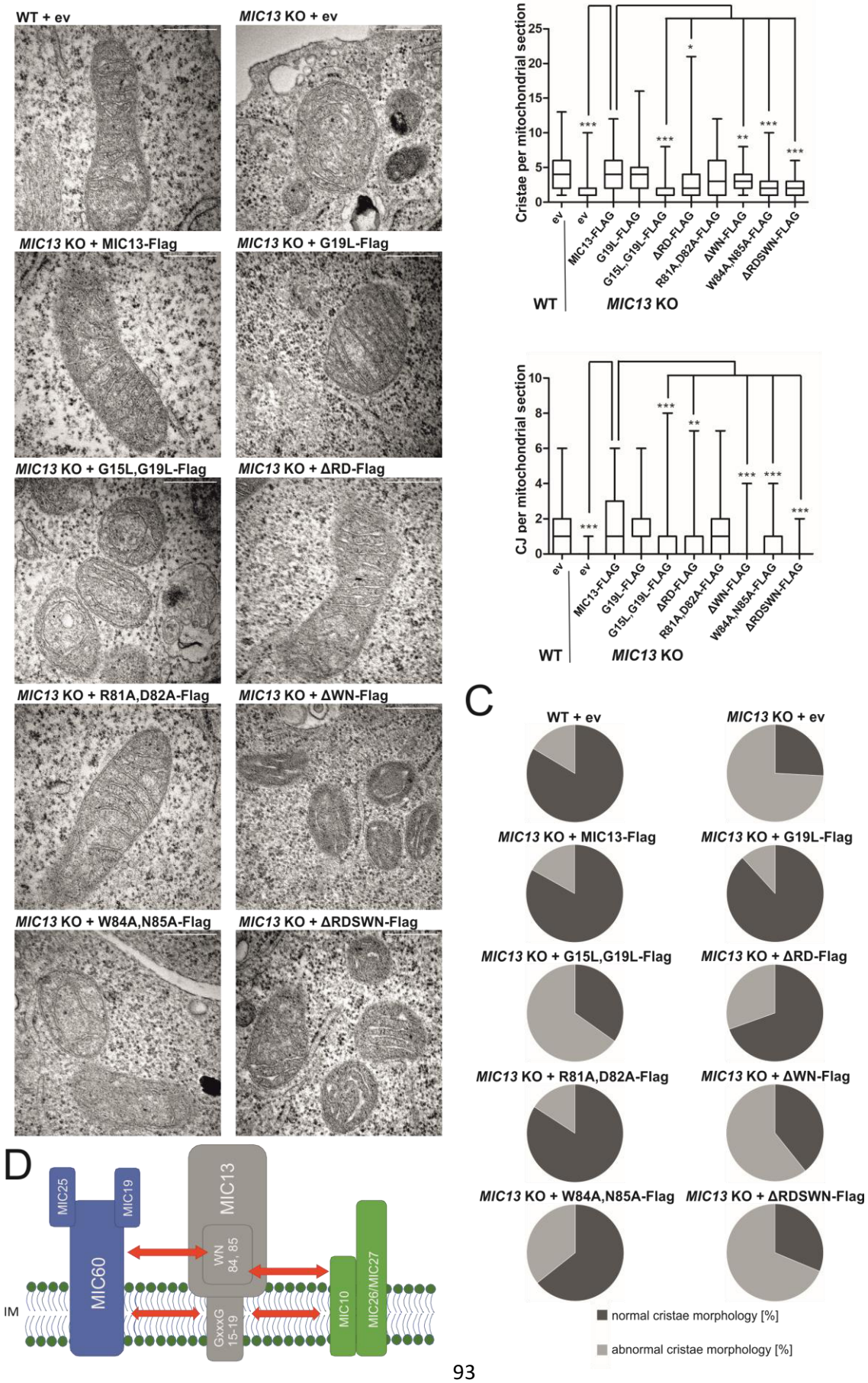
A
WT + ev
MIC13 KO + ev
MIC13 KO + MIC13-Flag
MIC13 KO + G19L-Flag
MIC13 KO + G15L,G19L-Flag
MIC13 KO + ΔRD-Flag
MIC13 KO + R81A,D82A-Flag
MIC13 KO + ΔWN-Flag
MIC13 KO + W84A,N85A-Flag
MIC13 KO + ΔRDSWN-Flag
B
Cristae per mitochondrial section
CJ per mitochondrial section
ev
MIC13-FLAG
G19L-FLAG
G15L,G19L-FLAG
ΔRD-FLAG
R81A,D82A-FLAG
ΔWN-FLAG
W84A,N85A-FLAG
ΔRDSWN-FLAG
WT
MIC13 KO
C
normal cristae morphology [%]
abnormal cristae morphology [%]
D
MIC25
MIC19
MIC60
MIC13
WN 84, 85
GxxxG 15-19
MIC10
MIC26/MIC27
IM

Figure S1

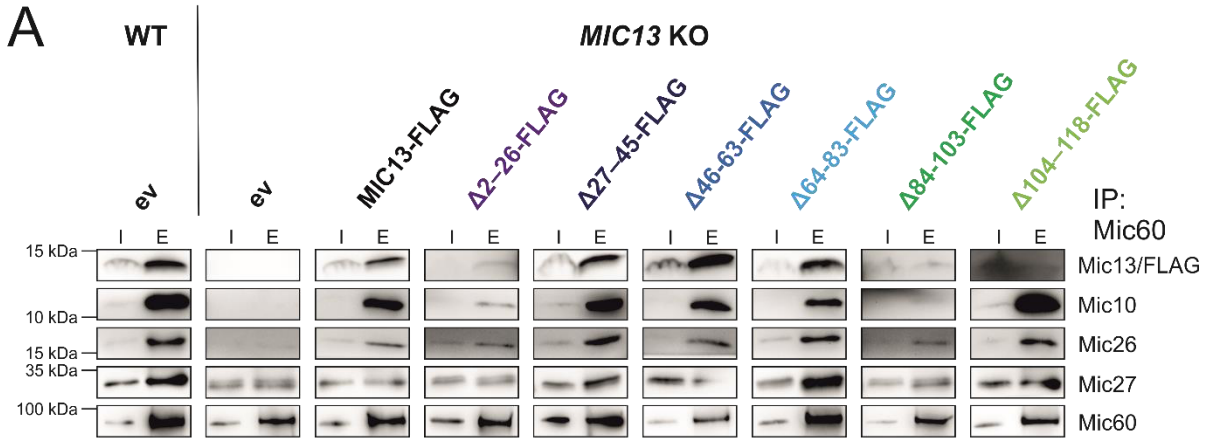
A
WT
MIC13 KO
ev
ev
MIC13-FLAG
Δ2–26-FLAG
Δ27–45-FLAG
Δ46-63-FLAG
Δ64-83-FLAG
Δ84-103-FLAG
Δ104–118-FLAG
IP: Mic60
I E
15 kDa
10 kDa
15 kDa
35 kDa
100 kDa
Mic13/FLAG
Mic10
Mic26
Mic27
Mic60

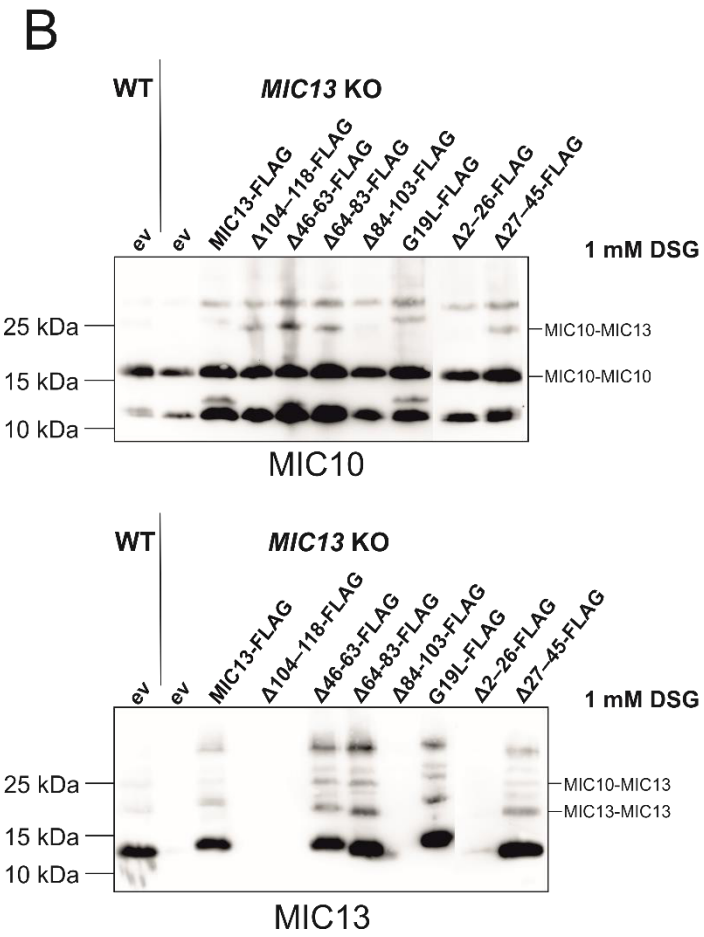
B
WT
MIC13 KO
ev
ev
MIC13-FLAG
Δ104–118-FLAG
Δ46-63-FLAG
Δ64-83-FLAG
Δ84-103-FLAG
G19L-FLAG
Δ2–26-FLAG
Δ27–45-FLAG
1 mM DSG
25 kDa
15 kDa
10 kDa
MIC10-MIC13
MIC10-MIC10
MIC10
WT
MIC13 KO
ev
ev
MIC13-FLAG
Δ104–118-FLAG
Δ46-63-FLAG
Δ64-83-FLAG
Δ84-103-FLAG
G19L-FLAG
Δ2–26-FLAG
Δ27–45-FLAG
1 mM DSG
25 kDa
15 kDa
10 kDa
MIC10-MIC13
MIC13-MIC13
MIC13

Figure S2

A

B

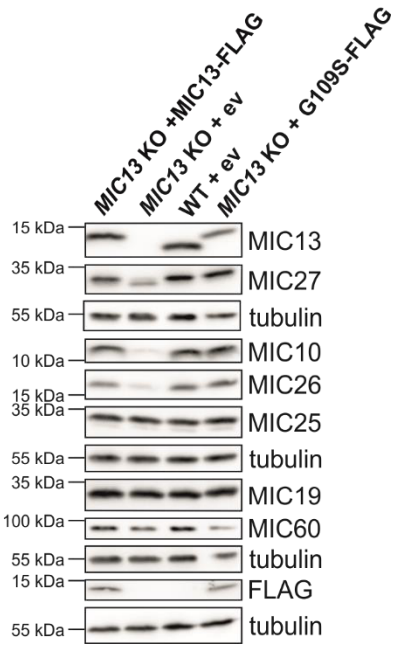

C

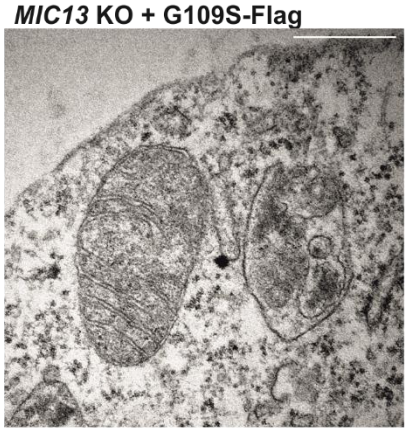

MATERIALS AND METHODS

Cell lines, cell culture, and transfection

All the cells were cultured using Dulbecco's Modifies Eagle's Medium (DMEM, D5546, Sigma) with 1 g/L of glucose supplemented with 10% fetal bovine serum (PAN biotech), 2 mM glutaMAX (Gibco), 1 mM sodium pyruvate (Gibco) and 1% penicillin and streptomycin (Gibco), incubated at 37 °C at 5% CO_2. *MIC13* KO Hek-293T and *MIC13* KO HeLa cells were described before (Anand et al., 2016; Kondadi et al., 2020). Cells were transfected with 1 µg of corresponding plasmid using GeneJuice (Novagen) according to the manufacturer's instruction.

Electron microscopy

Cells were grown on petri dishes until they reached 80% confluency. Chemical fixation using 3% glutaraldehyde buffered with 0.1 M sodium cacodylate buffer, pH 7.2 was performed on the petri dish, followed by scraping the cells using a cell scraper and collecting them as a pellet. The pellet was washed with 0.1 M sodium cacodylate, pH 7.2, and subsequently embedded in 2% agarose. The cells were stained with 1% osmium tetroxide for 50 min followed by 1% uranyl acetate/ 1% phosphotungstic acid for 1 h. For dehydration graded acetone series was used and the samples were embedded in spur epoxy resin for polymerization at 65 °C for 24 h. The ultrathin sections were prepared using microtome and images were acquired using transmission electron microscope (Hitachi, H600) at 75 V equipped with Bioscan model 792 camera (Gatan) and analyzed with ImageJ software. The data was analyzed by Graph Pad Prism 7 and outliers were removed.

Mitochondrial isolation and carbonate extraction

Cells were cultured in petri dishes, scraped with a cell scraper in PBS (Sigma), and pelleted at 500 g for 5 min. The pellet was resuspended in an isotonic buffer (220 mM mannitol, 70 mM sucrose, 1 mM EDTA, 20 mM HEPES (pH 7.5) and 1 x protease inhibitor cocktail (Roche)) with 0.1% BSA (Roth) and incubated on ice for 10 min. Cells were homogenized by mechanical

rupture using a syringe with a 21 G cannula and repeatedly soaking the suspension in and releasing it in a stroke for 20 times. Lysed cells were centrifuged at 1000 g and 4 °C for 10 min. The supernatant was then centrifuged at 10000 g and 4 °C for 15 min and the pellet was resuspended in the isotonic buffer to obtain crude mitochondria. Mitochondria were divided into aliquots and frozen using freezing buffer (300 M trehalose, 10 mM KCl, 1 mM EDTA, 10 mM HEPES and 0.1% BSA). For carbonate extraction 50 µg mitochondria were used directly after isolation and centrifuged at 10000 g and 4 °C for 10 min. The pellet was resuspended in 100 mM freshly prepared sodium carbonate at different pH and incubated on ice for 30 min. After centrifugation at 21000 g and 4 °C for 20 min, supernatant and pellet were collected and subjected to SDS electrophoresis.

SDS electrophoresis and western blotting

Samples for SDS electrophoresis were scraped in PBS and proteins were extracted with RIPA lysis buffer. Protein concentration was determined by Lowry method (Bio-Rad) and samples were prepared with Laemmli loading buffer. For protein separation, 10% SDS-PAGE, 15% SDS-PAGE, and 4% – 20% gradient SDS-PAGE (BioRad) were performed. The proteins were subsequently transferred on a nitrocellulose membrane and probed with following antibodies: MIC10 (Abcam, 84969), MIC13 (custom made by Pineda (Berlin) against human MIC13 peptide CKAREYSKEGWEYVKARTK), MIC19 (Proteintech, 25625-1-AP), MIC25 (Proteintech, 20639-1-AP), MIC26 (Thermofisher Scientific, MA5-15493 or custom made by Pineda (Berlin) against human MIC26 peptide CQETYSQTKPKMQ), MIC27 (Atlas Antibodies, HPA000612), MIC60 (custom made by Pineda (Berlin) against human MIC60 peptide CTDHPEIGEGKPTPALSEEAS), FLAG (Sigma, F3165), TOM20 (Santa Cruz Biotechnology, sc-114115), beta-tubulin (Cell Signalling Technology, 2128S), HSP60 (sigma, SAB4501464), Prohibitin (LSBio, LS-B2316-50). Chemiluminescent signal was recorded with VILBER LOURMAT Fusion SL (Peqlab) and quantification was performed with Image Studio Lite Ver 5.2.

Isolation of macromolecular complexes by blue native gels

Mitochondrial aliquots of 150 µg were pelleted and resuspended in 15 µL isotonic buffer (50 mM NaCl, 2 mM aminohexanoic acid, 50 mM imidazole/HCl pH 7, 1 mM EDTA, protease inhibitor cocktail). 3 µL 10% Digitonin (Serva) was added to reach a detergent to protein ratio of 2 g/g and incubated on ice for 10 min. After centrifugation at 21000 g and 4 °C for 20 min, 4 µL of 50% glycerol and 1.5 µL of 1% Coomassie brilliant blue G-250 with 10% glycerol was added and samples were loaded on a 3% – 18% gradient gel. Protein complexes were transferred to a PVDF membrane and probed with following antibodies: MIC10 (Abcam, 84969), MIC25 (Proteintech, 20639-1-AP), MIC27 (Atlas Antibodies, HPA000612), MIC60 (custom made by Pineda (Berlin) against human MIC60 peptide CTDHPEIGEGKPTPALSEEAS). Chemiluminescent signal was recorded with VILBER LOURMAT Fusion SL (Peqlab).

STED nanoscopy

For imaging with stimulated emission depletion super resolution nanoscopy stable transfected Hek-293T cells were fixed in 4% paraformaldehyde, permeabilized with 0.15% Triton-X100 and blocked using 10% goat serum, followed by incubation with antibodies against MIC60 (custom made by Pineda (Berlin) against human MIC60 peptide CTDHPEIGEGKPTPALSEEAS) and FLAG (Sigma, F3165) over night at 4 °C. Cells were washed three times with PBS and incubated with secondary antibody goat anti-rabbit Abberior STAR 635P (Abberior, ST635P-1001) and goat anti-mouse Abberior STAR 580 (Abberior, ST580-1001) for 1 h at room temperature. Cells were imaged as described before (Kondadi et al., 2020).

Molecular cloning

Human *MIC13-FLAG* was cloned into pMSCV vector (Anand et al., 2020) using Gibson Assembly Cloning Kit (NEB). Deletions across the whole sequence of *MIC13-FLAG* were obtained with Site-directed, Ligase-Independent Mutagenesis (SLIM) (Chiu et al., 2008). Point

mutations and other deletions were obtained with the Q5 mutagenesis kit (NEB) using manufacturer protocols.

Co-immunoprecipitation

For co-immunoprecipitation mitochondrial aliquots of 250 µg were pelleted and resuspended in an isotonic buffer (150 mM NaCl, 10 mM Tris/HCl (pH 7.5), 5 mM EDTA, protease inhibitor cocktail). 5 µL 10% Digitonin (Serva) was added to reach a detergent to protein ratio of 2 g/g and incubated on ice for 10 min. After centrifugation at 21000 g and 4 °C for 20 min, the input was subjected to the respective beads. For co-IP with Flag anti-Flag M2 affinity beads (Sigma) were used, for Co-IP with MIC60, protein A sepharose beads (Thermofisher Scientific, 101041) were incubated over night with MIC60 (custom made by Pineda (Berlin) against human MIC60 peptide CTDHPEIGEGKPTPALSEEAS). Before addition of the input on the beads, the beads were washed with PBS and with the isotonic buffer with the same concentration of digitonin. Beads were incubated with the sample for at least 4 h at 4 °C and washed with the isotonic buffer with 0.01% digitonin. Proteins were eluted with Laemmli buffer without beta-mercaptoethanol at 65 °C for 10 min. After separating the elution from the beads 1 µL beta-mercaptoethanol was added to the elution and samples were subjected to SDS electrophoresis and western blotting.

Crosslink

Isolated mitochondria were resuspended in 2 mM DSG (Thermofisher Scientific) in PBS and were incubated for 1 h at room temperature. Crosslink was stopped with the addition of TRIS (pH 7.5) to a total concentration of 50 mM and 15 min of incubation. Samples were centrifuged for 10 min at 4 °C and 10.000 g and the pellet was dissolved in Laemmli buffer and subjected to SDS PAGE and western blot analysis.

Generating stable cells with viral transduction

For viral transduction, Plat-E cells were transfected with 1.9 µg of the respective pMSCVpuro-based plasmid and 1 µg pVSV-G (Anand et al., 2020) using FuGENE6

transfection reagent (Promega) according to the manufacturer's instruction. After 48 h the supernatant of these cells was added to Hek-293T WT and *MIC13* KO cells and incubated for at least 24 h before addition of selection medium with 1 µg/mL puromycin.

FIGURE LEGENDS:

Figure 1. Transient expression of MIC13 or MIC13-FLAG can restore the defects associated with *MIC13* KO. Hek-293T WT and *MIC13* KO cells were transfected with pMSCV empty vector (ev), pMSCV-MIC13, or pMSCV-MIC13-FLAG. (A) RIPA lysates, decorated with antibodies against MIC13, FLAG, MIC60, MIC27, tubulin, MIC26, and MIC10. (B) BN-PAGE with isolated mitochondria. Complex V was detected by coomassie. MICOS complex was stained with antibody against MIC60. (C) Representative EM pictures. Scale bar 0.5 µm.

Figure 2. Expression of the deletion variants of MIC13 in MIC13 KO variably restores MIC10-subcomplex. (A) Schematic overview of the created MIC13 deletion mutants. All deletion mutants were created with a FLAG tag. (B) RIPA lysates of Hek-293T stable cell lines expressing pMSCV empty vector (ev) or respective MIC13-FLAG variant. Western blot was decorated with antibodies against MIC13, MIC27, tubulin, MIC10, MIC26, and FLAG.

Figure 3. Staining pattern of deletion variants of MIC13 using STED nanoscopy. Representative STED super-resolution images of Hek-293T stable cell lines expressing pMSCV empty vector (ev) or respective MIC13-FLAG variant. Cells were immunostained with MIC60 (red) and FLAG (green) antibodies. Bottom image shows merged image, colocalization is seen in yellow. Scale bar 0.5 µm.

Figure 4. MICOS assembly and interaction with other MICOS components in different deletion mutants. (A) BN-PAGE with isolated mitochondria of Hek-293T stable cell lines expressing pMSCV empty vector (ev) or respective MIC13-FLAG variant. Complex V was detected by coomassie. Coomassie was used to show possible loading differences. Samples were stained with antibodies against MIC10 or MIC27 to visualize MIC10-subcomplex. (B) BN-PAGE with isolated mitochondria of Hek-293T stable cell lines expressing pMSCV empty

vector (ev) or respective MIC13-FLAG variant. Complex V was detected by coomassie. Coomassie was used to show possible loading differences. Samples were stained with antibodies against MIC60 or MIC25 to visualize MIC60-subcomplex. (C) Co-immunoprecipitation with mitochondria isolated from Hek-293T stable cell lines expressing pMSCV empty vector (ev) or respective MIC13-FLAG variant. Pulldown was performed with FLAG antibody. The MIC13 construct could be pulled down to different extents as well as other tested MICOS components MIC10, MIC26, MIC27, MIC25, and MIC60. Prohibitin was used as a negative control. I: Input (5%); E: Elution (50%).

Figure 5. Expression of deletion variants of MIC13 in MIC13 KO variably affect cristae morphology. (A) Representative EM pictures of Hek-293T stable cell lines expressing pMSCV empty vector (ev) or respective MIC13-FLAG variant. Scale bar 0.5 µm. (B) Quantification of cristae and CJ per mitochondrial section from different mitochondria in Hek-293T stable cell lines expressing pMSCV empty vector (ev) or respective MIC13-FLAG variant using EM represented as boxplots. Boxplots show median and interquartile range from 25 to 75 percentile, and whiskers represent minimum and maximum value. Data from n = 69 to 121 mitochondria. (C) Quantification of normal versus abnormal cristae morphology in percent from all imaged mitochondria in Hek-293T stable cell lines expressing pMSCV empty vector (ev) or respective MIC13-FLAG variant using EM.

Figure 6. MIC13 has a conserved region that affects MICOS levels and interactions. (A) Schematic overview of the conserved motifs in MIC13 and created mutations. All mutants were created with a FLAG tag. (B) RIPA lysates of Hek-293T stable cell lines expressing pMSCV empty vector (ev) or respective MIC13-FLAG variant. Western blot was decorated with antibodies against MIC13, MIC27, tubulin, MIC10, MIC26, MIC25, MIC19, MIC60, and FLAG. (C) Co-immunoprecipitation with mitochondria isolated from Hek-293T stable cell lines expressing pMSCV empty vector (ev) or respective MIC13-FLAG variant. Pulldown was performed with FLAG antibody. The MIC13 construct could be pulled down to different extents as well as other tested MICOS components MIC10, MIC26, MIC27, MIC19, MIC25, and

MIC60. (D) Alkaline extraction of freshly isolated mitochondria from Hek-293T stable cell lines expressing MIC13-FLAG and the variant with mutated G15L, G19L. Alkaline extraction was performed at pH 11, pH 11.5, and pH 12 and after centrifugation supernatant (S) and pellet fraction (P) were subjected to western blot. Proteins were visualized with antibodies against HSP60, TOM20, and MIC13 (two different exposure times shown here).

Figure 7. Conserved regions of MIC13 are important for mitochondrial ultrastructure. (A) Representative EM pictures of Hek-293T stable cell lines expressing pMSCV empty vector (ev) or respective MIC13-FLAG variant. Scale bar 0.5 µm. (B) Quantification of cristae and CJ per mitochondrial section from different mitochondria in Hek-293T stable cell lines expressing pMSCV empty vector (ev) or respective MIC13-FLAG variant using EM represented as boxplots. Boxplots show median and interquartile range from 25 to 75 percentile, and whiskers represent minimum and maximum value. Data from n = 56 to 102 mitochondria. (C) Quantification of normal versus abnormal cristae morphology in percent from all imaged mitochondria in Hek-293T stable cell lines expressing pMSCV empty vector (ev) or respective MIC13-FLAG variant using EM. (D) Model of MIC13 role in MICOS assembly.

Figure S1. (A) Co-immunoprecipitation with mitochondria isolated from Hek-293T stable cell lines expressing pMSCV empty vector (ev) or respective MIC13-FLAG variant. Pulldown was performed with MIC60 antibody. The MIC13 construct could be pulled down to different extents as well as other tested MICOS components MIC10, MIC26, MIC27, and MIC60. I: Input (5%); E: Elution (50%). (B) Western blot of mitochondria from Hek 293 WT and *MIC13* KO with transient expression of different MIC13 variants treated with PBS or 1 mM DSG for 1 h. Blots are stained with antibodies against MIC10 and MIC13. Self-oligomerization was detected as well as a crosslink between MIC10 and MIC13.

Figure S2. (A) Alignment of human and dog MIC13 sequence. (B) RIPA lysates of Hek-293T stable cell lines expressing pMSCV empty vector (ev) MIC13-FLAG or the variant with mutated G109S. Western blot was decorated with antibodies against MIC13, MIC27, tubulin, MIC10,

MIC26, MIC25, MIC19, MIC60, and FLAG. (C) Representative EM picture of Hek-293T stable cell lines expressing MIC13-FLAG with mutated G109S. Scale bar 0.5 µm.

REFERENCES:

Anand, R., Kondadi, A.K., Meisterknecht, J., Golombek, M., Nortmann, O., Riedel, J., Peifer-Weiss, L., Brocke-Ahmadinejad, N., Schlutermann, D., Stork, B.*, et al.* (2020). MIC26 and MIC27 cooperate to regulate cardiolipin levels and the landscape of OXPHOS complexes. Life Sci Alliance *3*.

Anand, R., Strecker, V., Urbach, J., Wittig, I., and Reichert, A.S. (2016). Mic13 Is Essential for Formation of Crista Junctions in Mammalian Cells. PLoS One *11*, e0160258.

Arselin, G., Giraud, M.F., Dautant, A., Vaillier, J., Brethes, D., Coulary-Salin, B., Schaeffer, J., and Velours, J. (2003). The GxxxG motif of the transmembrane domain of subunit e is involved in the dimerization/oligomerization of the yeast ATP synthase complex in the mitochondrial membrane. Eur J Biochem *270*, 1875-1884.

Barbot, M., Jans, D.C., Schulz, C., Denkert, N., Kroppen, B., Hoppert, M., Jakobs, S., and Meinecke, M. (2015). Mic10 oligomerizes to bend mitochondrial inner membranes at cristae junctions. Cell Metab *21*, 756-763.

Bohnert, M., Zerbes, R.M., Davies, K.M., Muhleip, A.W., Rampelt, H., Horvath, S.E., Boenke, T., Kram, A., Perschil, I., Veenhuis, M.*, et al.* (2015). Central role of Mic10 in the mitochondrial contact site and cristae organizing system. Cell Metab *21*, 747-755.

Callegari, S., Muller, T., Schulz, C., Lenz, C., Jans, D.C., Wissel, M., Opazo, F., Rizzoli, S.O., Jakobs, S., Urlaub, H.*, et al.* (2019). A MICOS-TIM22 Association Promotes Carrier Import into Human Mitochondria. J Mol Biol *431*, 2835-2851.

Chiu, J., Tillett, D., Dawes, I.W., and March, P.E. (2008). Site-directed, Ligase-Independent Mutagenesis (SLIM) for highly efficient mutagenesis of plasmids greater than 8kb. Journal of microbiological methods *73*, 195-198.

Colina-Tenorio, L., Horten, P., Pfanner, N., and Rampelt, H. (2020). Shaping the mitochondrial inner membrane in health and disease. J Intern Med.

Cosson, P., Perrin, J., and Bonifacino, J.S. (2013). Anchors aweigh: protein localization and transport mediated by transmembrane domains. Trends Cell Biol *23*, 511-517.

Eramo, M.J., Lisnyak, V., Formosa, L.E., and Ryan, M.T. (2020). The 'mitochondrial contact site and cristae organising system' (MICOS) in health and human disease. J Biochem *167*, 243-255.

Godiker, J., Gruneberg, M., DuChesne, I., Reunert, J., Rust, S., Westermann, C., Wada, Y., Classen, G., Langhans, C.D., Schlingmann, K.P.*, et al.* (2018). QIL1-dependent assembly of MICOS complex-lethal mutation in C19ORF70 resulting in liver disease and severe neurological retardation. J Hum Genet *63*, 707-716.

Guarani, V., Jardel, C., Chretien, D., Lombes, A., Benit, P., Labasse, C., Lacene, E., Bourillon, A., Imbard, A., Benoist, J.F.*, et al.* (2016). QIL1 mutation causes MICOS disassembly and early onset fatal mitochondrial encephalopathy with liver disease. Elife *5*.

Guarani, V., McNeill, E.M., Paulo, J.A., Huttlin, E.L., Frohlich, F., Gygi, S.P., Van Vactor, D., and Harper, J.W. (2015). QIL1 is a novel mitochondrial protein required for MICOS complex stability and cristae morphology. Elife *4*.

Harner, M., Korner, C., Walther, D., Mokranjac, D., Kaesmacher, J., Welsch, U., Griffith, J., Mann, M., Reggiori, F., and Neupert, W. (2011). The mitochondrial contact site complex, a determinant of mitochondrial architecture. EMBO J *30*, 4356-4370.

Hessenberger, M., Zerbes, R.M., Rampelt, H., Kunz, S., Xavier, A.H., Purfurst, B., Lilie, H., Pfanner, N., van der Laan, M., and Daumke, O. (2017). Regulated membrane remodeling by Mic60 controls formation of mitochondrial crista junctions. Nat Commun *8*, 15258.

Hoppins, S., Collins, S.R., Cassidy-Stone, A., Hummel, E., Devay, R.M., Lackner, L.L., Westermann, B., Schuldiner, M., Weissman, J.S., and Nunnari, J. (2011). A mitochondrial-focused genetic interaction map reveals a scaffold-like complex required for inner membrane organization in mitochondria. J Cell Biol *195*, 323-340.

Huang, X., Fan, J., Li, L., Liu, H., Wu, R., Wu, Y., Wei, L., Mao, H., Lal, A., Xi, P.*, et al.* (2018). Fast, long-term, super-resolution imaging with Hessian structured illumination microscopy. Nature biotechnology.

Huynen, M.A., Muhlmeister, M., Gotthardt, K., Guerrero-Castillo, S., and Brandt, U. (2016). Evolution and structural organization of the mitochondrial contact site (MICOS) complex and the mitochondrial intermembrane space bridging (MIB) complex. Biochim Biophys Acta *1863*, 91-101.

Khosravi, S., and Harner, M.E. (2020). The MICOS complex, a structural element of mitochondria with versatile functions. Biological chemistry.

Kishita, Y., Shimura, M., Kohda, M., Akita, M., Imai-Okazaki, A., Yatsuka, Y., Nakajima, Y., Ito, T., Ohtake, A., Murayama, K.*, et al.* (2020). A novel homozygous variant in MICOS13/QIL1 causes hepato-encephalopathy with mitochondrial DNA depletion syndrome. Mol Genet Genomic Med, e1427.

Kondadi, A.K., Anand, R., Hansch, S., Urbach, J., Zobel, T., Wolf, D.M., Segawa, M., Liesa, M., Shirihai, O.S., Weidtkamp-Peters, S.*, et al.* (2020). Cristae undergo continuous cycles of membrane remodelling in a MICOS-dependent manner. EMBO Rep *21*, e49776.

Lau, T.L., Kim, C., Ginsberg, M.H., and Ulmer, T.S. (2009). The structure of the integrin alphaIIbbeta3 transmembrane complex explains integrin transmembrane signalling. EMBO J *28*, 1351-1361.

Mannella, C.A. (2006). The relevance of mitochondrial membrane topology to mitochondrial function. Biochim Biophys Acta *1762*, 140-147.

Mannella, C.A., Lederer, W.J., and Jafri, M.S. (2013). The connection between inner membrane topology and mitochondrial function. J Mol Cell Cardiol *62*, 51-57.

Mannella, C.A., Pfeiffer, D.R., Bradshaw, P.C., Moraru, II, Slepchenko, B., Loew, L.M., Hsieh, C.E., Buttle, K., and Marko, M. (2001). Topology of the mitochondrial inner membrane: dynamics and bioenergetic implications. IUBMB Life *52*, 93-100.

Meurs, K.M., Friedenberg, S.G., Olby, N.J., Condit, J., Weidman, J., Rosenthal, S., and Shelton, G.D. (2019). A QIL1 Variant Associated with Ventricular Arrhythmias and Sudden Cardiac Death in the Juvenile Rhodesian Ridgeback Dog. Genes (Basel) *10*.

Monk, B.C., Tomasiak, T.M., Keniya, M.V., Huschmann, F.U., Tyndall, J.D., O'Connell, J.D., 3rd, Cannon, R.D., McDonald, J.G., Rodriguez, A., Finer-Moore, J.S.*, et al.* (2014). Architecture of a single membrane spanning cytochrome P450 suggests constraints that orient the catalytic domain relative to a bilayer. Proc Natl Acad Sci U S A *111*, 3865-3870.

Ott, C., Ross, K., Straub, S., Thiede, B., Gotz, M., Goosmann, C., Krischke, M., Mueller, M.J., Krohne, G., Rudel, T.*, et al.* (2012). Sam50 functions in mitochondrial intermembrane space bridging and biogenesis of respiratory complexes. Mol Cell Biol *32*, 1173-1188.

Pfanner, N., van der Laan, M., Amati, P., Capaldi, R.A., Caudy, A.A., Chacinska, A., Darshi, M., Deckers, M., Hoppins, S., Icho, T.*, et al.* (2014). Uniform nomenclature for the mitochondrial contact site and cristae organizing system. J Cell Biol *204*, 1083-1086.

Rabl, R., Soubannier, V., Scholz, R., Vogel, F., Mendl, N., Vasiljev-Neumeyer, A., Korner, C., Jagasia, R., Keil, T., Baumeister, W.*, et al.* (2009). Formation of cristae and crista junctions in mitochondria depends on antagonism between Fcj1 and Su e/g. J Cell Biol *185*, 1047-1063.

Rampelt, H., Zerbes, R.M., van der Laan, M., and Pfanner, N. (2016). Role of the mitochondrial contact site and cristae organizing system in membrane architecture and dynamics. Biochimica et biophysica acta.

Russ, W.P., and Engelman, D.M. (2000). The GxxxG motif: a framework for transmembrane helix-helix association. J Mol Biol *296*, 911-919.

Russell, B.E., Whaley, K.G., Bove, K.E., Labilloy, A., Lombardo, R.C., Hopkin, R.J., Leslie, N.D., Prada, C., Assouline, Z., Barcia, G.*, et al.* (2019). Expanding and Underscoring the Hepato-Encephalopathic Phenotype of QIL1/MIC13. Hepatology *70*, 1066-1070.

Scorrano, L., Ashiya, M., Buttle, K., Weiler, S., Oakes, S.A., Mannella, C.A., and Korsmeyer, S.J. (2002). A distinct pathway remodels mitochondrial cristae and mobilizes cytochrome c during apoptosis. Dev Cell *2*, 55-67.

Senes, A., Engel, D.E., and DeGrado, W.F. (2004). Folding of helical membrane proteins: the role of polar, GxxxG-like and proline motifs. Curr Opin Struct Biol *14*, 465-479.

Senes, A., Gerstein, M., and Engelman, D.M. (2000). Statistical analysis of amino acid patterns in transmembrane helices: the GxxxG motif occurs frequently and in association with beta-branched residues at neighboring positions. J Mol Biol *296*, 921-936.

Stangl, M., and Schneider, D. (2015). Functional competition within a membrane: Lipid recognition vs. transmembrane helix oligomerization. Biochim Biophys Acta *1848*, 1886-1896.

Stephan, T., Roesch, A., Riedel, D., and Jakobs, S. (2019). Live-cell STED microscopy of mitochondrial cristae. bioRxiv, 640920.

Tarasenko, D., Barbot, M., Jans, D.C., Kroppen, B., Sadowski, B., Heim, G., Mobius, W., Jakobs, S., and Meinecke, M. (2017). The MICOS component Mic60 displays a conserved membrane-bending activity that is necessary for normal cristae morphology. J Cell Biol *216*, 889-899.

Teese, M.G., and Langosch, D. (2015). Role of GxxxG Motifs in Transmembrane Domain Interactions. Biochemistry *54*, 5125-5135.

Tsai, P.I., Lin, C.H., Hsieh, C.H., Papakyrikos, A.M., Kim, M.J., Napolioni, V., Schoor, C., Couthouis, J., Wu, R.M., Wszolek, Z.K.*, et al.* (2018). PINK1 Phosphorylates MIC60/Mitofilin to Control Structural Plasticity of Mitochondrial Crista Junctions. Mol Cell *69*, 744-756 e746.

Unterreitmeier, S., Fuchs, A., Schaffler, T., Heym, R.G., Frishman, D., and Langosch, D. (2007). Phenylalanine promotes interaction of transmembrane domains via GxxxG motifs. J Mol Biol *374*, 705-718.

Vogel, F., Bornhovd, C., Neupert, W., and Reichert, A.S. (2006). Dynamic subcompartmentalization of the mitochondrial inner membrane. J Cell Biol *175*, 237-247.

von der Malsburg, K., Muller, J.M., Bohnert, M., Oeljeklaus, S., Kwiatkowska, P., Becker, T., Loniewska-Lwowska, A., Wiese, S., Rao, S., Milenkovic, D.*, et al.* (2011). Dual role of mitofilin in mitochondrial membrane organization and protein biogenesis. Dev Cell *21*, 694-707.

Wang, C., Taki, M., Sato, Y., Tamura, Y., Yaginuma, H., Okada, Y., and Yamaguchi, S. (2019). A photostable fluorescent marker for the superresolution live imaging of the dynamic structure of the mitochondrial cristae. Proceedings of the National Academy of Sciences of the United States of America.

Wolf, D.M., Segawa, M., Kondadi, A.K., Anand, R., Bailey, S.T., Reichert, A.S., van der Bliek, A.M., Shackelford, D.B., Liesa, M., and Shirihai, O.S. (2019). Individual cristae within the same mitochondrion display different membrane potentials and are functionally independent. The EMBO journal, e101056.

Wurm, C.A., and Jakobs, S. (2006). Differential protein distributions define two sub-compartments of the mitochondrial inner membrane in yeast. FEBS Lett *580*, 5628-5634.

Xie, J., Marusich, M.F., Souda, P., Whitelegge, J., and Capaldi, R.A. (2007). The mitochondrial inner membrane protein mitofilin exists as a complex with SAM50, metaxins 1 and 2, coiled-coil-helix coiled-coil-helix domain-containing protein 3 and 6 and DnaJC11. FEBS Lett *581*, 3545-3549.

Zeharia, A., Friedman, J.R., Tobar, A., Saada, A., Konen, O., Fellig, Y., Shaag, A., Nunnari, J., and Elpeleg, O. (2016). Mitochondrial hepato-encephalopathy due to deficiency of QIL1/MIC13 (C19orf70), a MICOS complex subunit. Eur J Hum Genet *24*, 1778-1782.

Zerbes, R.M., Hoss, P., Pfanner, N., van der Laan, M., and Bohnert, M. (2016). Distinct Roles of Mic12 and Mic27 in the Mitochondrial Contact Site and Cristae Organizing System. J Mol Biol *428*, 1485-1492.

Zerbes, R.M., van der Klei, I.J., Veenhuis, M., Pfanner, N., van der Laan, M., and Bohnert, M. (2012). Mitofilin complexes: conserved organizers of mitochondrial membrane architecture. Biol Chem *393*, 1247-1261.

3.4. MIC13 affects apoptosis and different protein levels

3.4.1. Loss of MIC13 affects cytochrome *c* release upon apoptosis induction

Loss of MIC13 leads to a disrupted mitochondrial ultrastructure with a loss of CJs [110, 112]. During apoptosis cytochrome *c* is released through outer membrane permeabilization and widening of CJ [26, 39]. Since about 85% of cytochrome *c* resides in the cristae lumen, CJ widening is an important step for sufficient cytochrome *c* release upon apoptosis induction [39, 103]. A role of MICOS in this mechanism was proposed earlier because loss of MIC60 leads to a faster cytochrome *c* release [108]. This raises the question if MIC13 associated loss of CJs affects cytochrome *c* release upon induction of apoptosis. To address this question, cytochrome *c* release was monitored by immunofluorescence microscopy. For this HeLa WT and *MIC13* KO cells were seeded on microscopy dishes and apoptosis was induced with 1 µM of staurosporine (STS). This treatment was performed over a time course of 3, 4.5, and 6 hours to obtain different stages of cytochrome *c* release. To exclude effects on cytochrome *c* release by the solvent, one set of each cell type was incubated with DMSO for 6 hours and was used as a negative control. To visualize cytochrome *c*, immunofluorescence staining was performed against cytochrome *c* and also against the outer membrane protein TOM20 to visualize mitochondria. This helps to see the colocalization of cytochrome *c* and mitochondria before apoptotic cytochrome *c* release. Cells were then subjected to fluorescence microscopy (Figure 9).

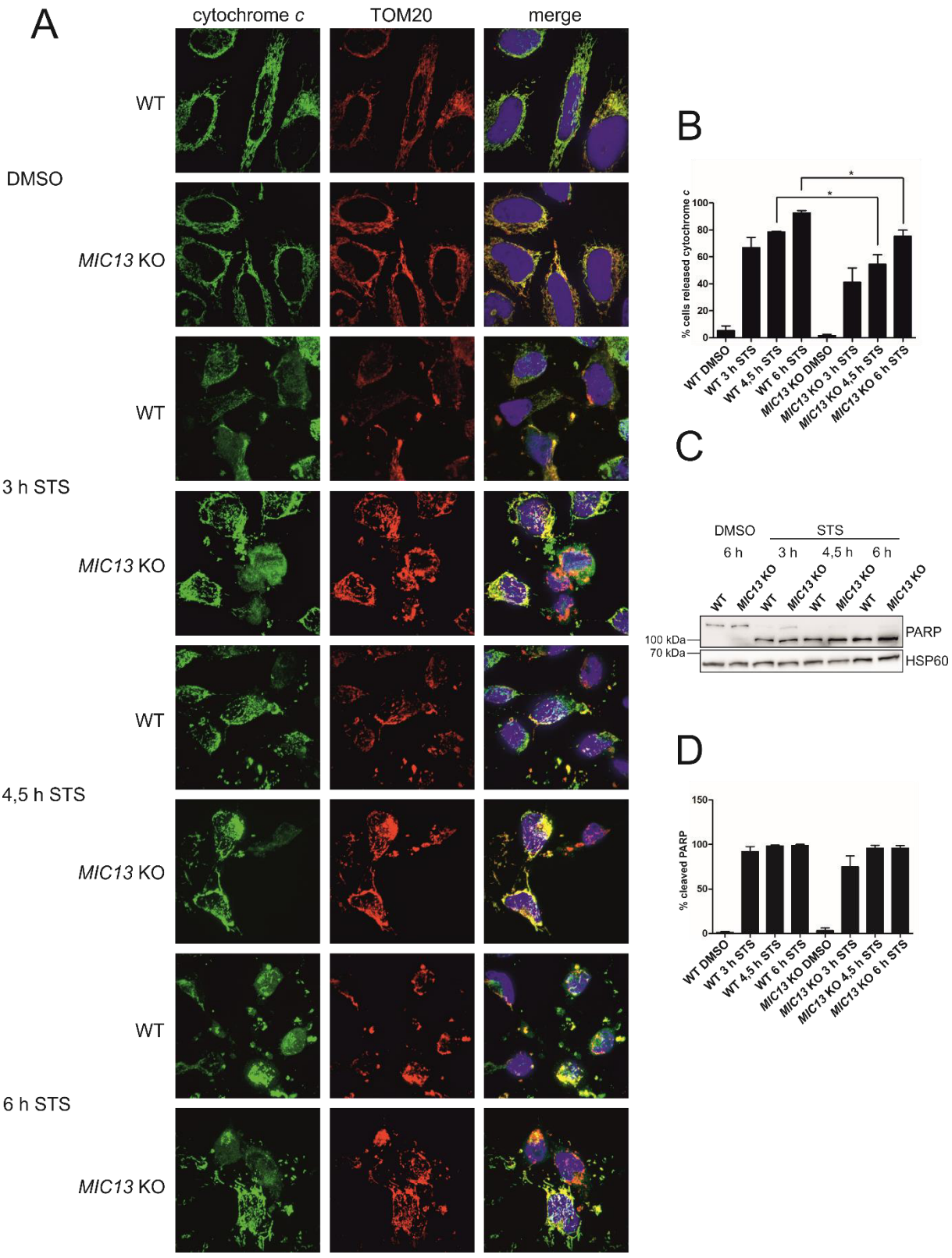

Figure 9. Cytochrome *c* release and PARP cleavage are delayed in *MIC13* KO cell lines after induction of apoptosis. (A) Representative images of HeLa WT and *MIC13* KO cells treated with 1 µM staurosporine (STS) for 3, 4.5, or 6 h or DMSO for 6 h. Cytochrome *c* was imaged by immunostaining (green), mitochondria were marked by immunostaining of TOM20 (red). Merged image shows colocalization in yellow and nucleus stained by DAPI (blue). (B) Quantification of cytochrome *c* releasing

cells (HeLa WT and *MIC13* KO) after treatment with 1 µM staurosporine (STS) for 3, 4.5, or 6 h or DMSO for 6 h. *, p value < 0.05. (C) PARP cleavage in HeLa WT and *MIC13* KO cells after treatment with 1 µM staurosporine (STS) for 3, 4.5, or 6 h or DMSO for 6 h shown on a western blot. (D) Quantification of PARP cleavage in HeLa WT and *MIC13* KO cells after treatment with 1 µM staurosporine (STS) for 3, 4.5, or 6 h or DMSO for 6 h from western blot analysis.

Cells treated with DMSO show colocalization of TOM20 and cytochrome *c*, as well as no fragmentation of the mitochondrial network. Upon treatment with staurosporine, the mitochondrial network structure gets more fragmented and the distribution of cytochrome *c* becomes more uniform inside the cells, indicating a cytochrome *c* release from the mitochondria. The number of cells releasing cytochrome *c* and showing fragmented mitochondria increase with longer staurosporine treatment. *MIC13* KO cells also show fragmented mitochondria and cytochrome *c* release upon apoptosis induction, despite the loss of CJ in these cells. To further investigate if the cytochrome *c* release is impaired, a quantification of the microscopy pictures was performed and the number of cells releasing cytochrome *c* relative to all imaged cells was shown in percent (Figure 9B). Quantification shows, that after 4.5 h and 6 h of staurosporine treatment there is significantly less cytochrome *c* release upon loss of MIC13. These results state, that there still is cytochrome *c* release in MIC13 deficient cells, but it is slightly delayed with significantly fewer cells releasing cytochrome *c* in a distinct time. To further investigate the question if apoptosis is affected upon this slower cytochrome *c* release, the cleavage of poly(ADP-ribose) polymerase (PARP) was observed. PARP is a 116 kDa protein, which is cleaved during apoptosis by the effector caspase 3 to an 89 kDa cleavage product. With a PARP antibody, both forms are visualized on western blot (Figure 9C). In both WT and *MIC13* KO cells PARP cleavage could be observed after 3 hours of staurosporine treatment. In WT almost all PARP is visible as the cleaved product and after 4.5 or 6 hours also in *MIC13* KO cells, all PARP is present in its cleaved form. The higher amount of cleaved PARP after 3 hours in WT cells suggests a delay of apoptosis upon loss of MIC13. To confirm the findings on the western blot, quantification of three independent experiments was performed and the amount of cleaved PARP is shown relative to the complete PARP signal in percent (Figure 9D). The quantification shows that after 4.5 hours all PARP is cleaved in both cell lines, which proofs that apoptosis is still functional upon loss of MIC13. However, after 3 h there is a slight reduction of cleaved PARP in *MIC13* KO, compared to WT. This reduction is not significant but it is in line with the observation of significantly less cytochrome *c* release (Figure 9B). Taken together, the loss of MIC13 leads to a slower release of cytochrome *c* and a slower PARP cleavage upon apoptosis induction with staurosporine. Therefore, in *MIC13* KO cells there is a delayed or slower apoptosis, likely due to the loss of crista junctions.

3.4.2. Loss of MIC13 affects levels of other proteins

In collaboration with Prof. Dr. Kai Stühler from the Institute of Molecular Medicine I a proteomics approach in Hek-293T cells was performed to study the whole proteome of *MIC13* KO cells and earn a better insight into possible metabolic pathways affected by MIC13. WT proteome, as well as *MIC13* KO proteome, were analyzed using liquid chromatography coupled with mass spectrometry. Changes in the proteome between WT and *MIC13* KO were plotted as a volcano plot (Figure 10A). On this plot proteins with a false discovery rate (FDR) of 5% are shown in red and proteins, whose levels are decreased to 50% and less or increased to 200% and more in *MIC13* KO compared to wildtype are also named. These proteins, their respective gene name, and the amount in *MIC13* KO compared to WT are also shown in a table (Figure 10B). The protein most affected by the loss of MIC13 is Plastin-2, encoded by the gene *LCP1*, whose levels are reduced to only 4% upon loss of MIC13. This protein localizes to the cytoskeleton and no connections to mitochondria are known so far [185]. Plastins are primarily involved in the regulation of the cytoskeleton, but also involvement in other functions such as cell migration, neutrophil function, DNA repair, and endocytosis is reported [186]. Plastin-2 is known to bind actin and additionally plays a role in the activation of T-cells [185, 187]. The link between MIC13 and Plastin-2 however is not clear, but the reduction of Plastin-2 may hint at a function of MIC13 outside MICOS and mitochondria. Most interesting in the list of affected proteins are those, which are already associated with mitochondria or mitochondrial function. These are the glycerol kinases, glutathione S-transferase P (GTSP1), adrenodoxin reductase, and MICU1 (Figure 10B). The glycerol kinases are reduced to approximately 30% (GK, GK3P) and 38% (GK), GTSP1 is reduced to about 32% and adrenodoxin reductase is reduced to roughly 42% upon loss of MIC13. The glutathione S-transferase P, encoded by the gene *GSTP1* belongs to the glutathione S-transferases (GSTs), a family of proteins, that are involved in detoxifying endogenous reactions with reduced glutathione and thus protect cellular macromolecules from damage caused by cytotoxic agents [188]. GSTs are also involved in protection against oxidative stress and *GSTP1* is associated with neurodegeneration in Alzheimer's disease [189, 190]. Adrenodoxin reductase is a mitochondrial protein encoded by the gene *FDXR* and takes part in electron transfer in the mitochondrial cytochrome P450 systems by reducing adrenodoxin [191]. The enzyme carries FAD as a cofactor and transfers two electrons from NADPH to the electron transfer protein adrenodoxin [192]. Mutations in *FDXR* are associated with sensorial neuropathies [193]. The mitochondrial protein, which levels are increased upon loss of MIC13 is MICU1, which increased to about 211% compared to WT levels. MICU1 stands for mitochondrial calcium uptake 1 and this protein is associated with the mitochondrial inner membrane, with a role in calcium sensing [194]. An upregulation of MICU1 upon loss of MIC13 suggests a link of MIC13 to calcium homeostasis. The group of glycerol kinases is reduced in *MIC13* KO to about one third of the WT amount. Glycerol kinase

1, 2, and 3 (GK, GK2, GK3P) are all key enzymes in glycerol degradation and are localized to mitochondria. Glycerol kinases catalyze the reaction of glycerol to glycerol-3-phosphate with the help of ATP. Glycerol-3-phosphate can be metabolized by the glycerol dehydrogenase and this plays a role in the TCA cycle [195]. Therefore, a link to MIC13 or the MICOS related to energy production seems possible. To check a possible interaction, the levels of this protein upon loss of MIC13 were checked again on western blot (Figure 10C). In Hek-293T cells, there is a clear reduction of glycerol kinase upon loss of MIC13. However, in HeLa and Hap1 cells the levels of glycerol kinase are unchanged upon loss of MIC13 and also upon loss of MIC10. MIC10 protein levels are drastically decreased upon loss of MIC13, therefore the correlation of MIC10 and GK levels was investigated. The reduction of glycerol kinase seems to be specific to Hek-293T *MIC13* KO cells. Taken together these results show, that there are a variety of proteins, which are affected by the loss of MIC13 and a lot of interesting candidates for further investigation about the involvement of MIC13 in different metabolic pathways or diseases.

A

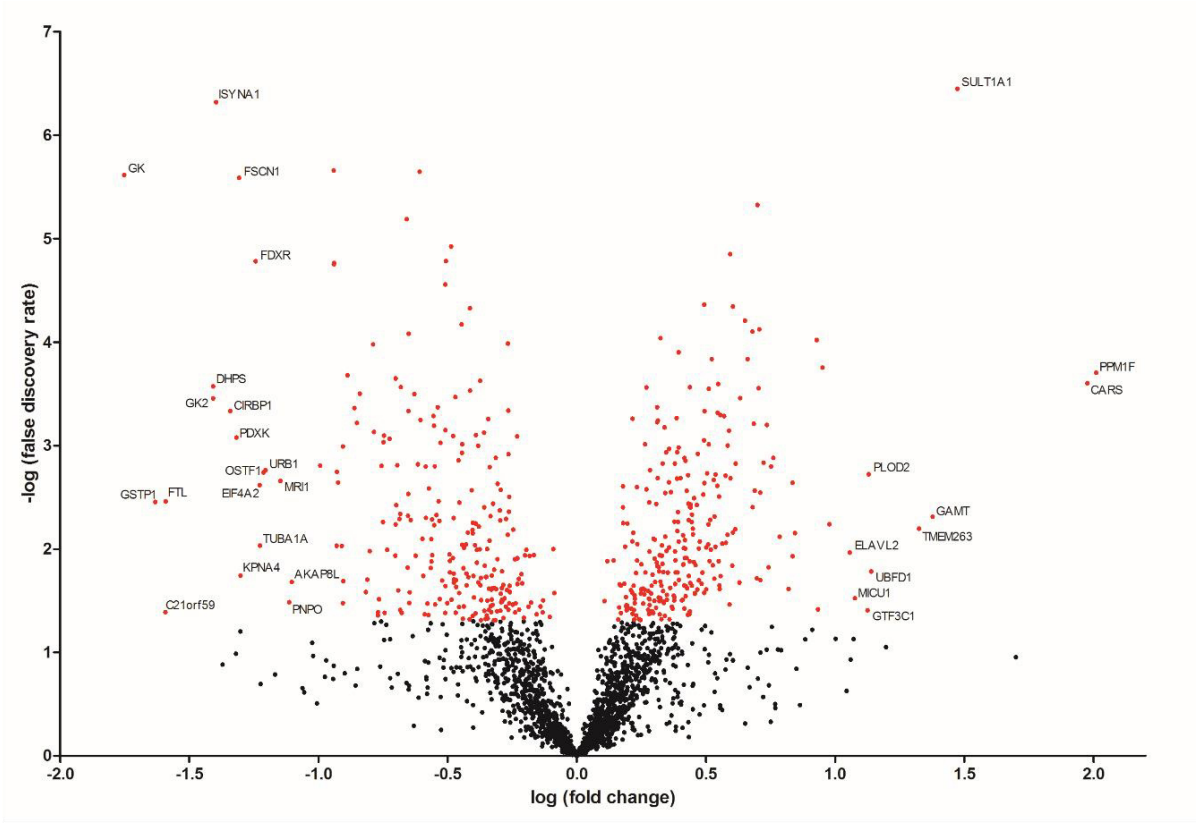

B

Protein name	Gene name	amount in *MIC13* KO compared to WT in %
Plastin-2	LCP1	4,08
Glycerol kinase	GK;GK3P	29,68
Glutathione S-transferase P	GSTP1	32,26
UPF0769 protein C21orf59	C21orf59	33,15
Ferritin light chain	FTL	33,18
Glycerol kinase 2	GK2	37,69
Deoxyhypusine synthase	DHPS	37,69
Inositol-3-phosphate synthase 1	ISYNA1	37,98
Cold-inducible RNA-binding protein	CIRBP	39,46
Pyridoxal kinase	PDXK	40,12
Fascin	FSCN1	40,40
Importin subunit alpha-3	KPNA4	40,55
NADPH:adrenodoxin oxidoreductase, mitochondrial	FDXR	42,22
Eukaryotic initiation factor 4A-II	EIF4A2	42,70
Tubulin alpha-1A chain; Tubulin alpha-3C/D chain	TUBA1A;TUBA3C	42,74
Osteoclast-stimulating factor 1	OSTF1	43,13
Nucleolar pre-ribosomal-associated protein 1	URB1	43,37
Methylthioribose-1-phosphate isomerase	MRI1	45,13
Pyridoxine-5-phosphate oxidase	PNPO	46,22
A-kinase anchor protein 8-like	AKAP8L	46,54

Protein name	Gene name	amount in *MIC13* KO compared to WT in %
ELAV-like protein	ELAVL2;ELAVL4	207,87
Calcium uptake protein 1	MICU1	210,82
General transcription factor 3C polypeptide 1	GTF3C1	218,05
Procollagen-lysine, 2-oxoglutarate 5-dioxygenase 2	PLOD2	218,73
Ubiquitin domain-containing protein UBFD1	UBFD1	220,25
Transmembrane protein 263	TMEM263	250,40
Guanidinoacetate N-methyltransferase	GAMT	259,64
Sulfotransferase	SULT1A1;SULT1A2	277,58
Cysteine--tRNA ligase	CARS	393,25
Protein phosphatase 1F	PPM1F	402,73

C

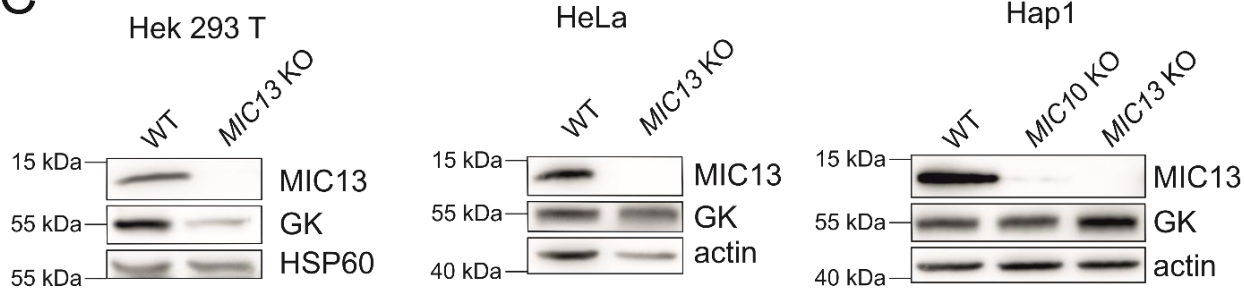

Figure 10. Proteomics approach of WT compared to *MIC13* KO cells show alteration of different protein levels upon loss of MIC13. (A) Volcano plot of proteomics data from Hek-293T WT and *MIC13* KO cells. Proteins with an FDR of 5% are depicted in red and proteins, whose levels are reduced to

50% and less or 200%, and more in upon loss of MIC13 are named on the plot. (B) Interesting candidates from proteomic screening, which levels were reduced to 50% and less or 200%, and more upon loss of MIC13. Protein levels in *MIC13* KO relative to WT are shown in percent. (C) Western blot of Hek-293T WT and *MIC13* KO cells decorated against MIC13, glycerol kinase (GK), and HSP60 as a loading control.

3.4.3. Material and Methods

3.4.3.1. Cell lines, cell culture, and transfection

All cells were cultured using Dulbecco's Modified Eagle's Medium (Sigma, D5546) with 1 g/L of glucose supplemented with 10% Fetal Bovine Serum (PAN biotech), 2 mM GlutaMAX (Invitrogen, 35050-8-087), 1 mM Sodium Pyruvate (Gibco, 11360070) and 1% penicillin and streptomycin (Sigma, P4333), incubated at 37 °C at 5% CO_2 incubator. *MIC10* KO Hap1, *MIC13* KO Hek-293T, and *MIC13* KO HeLa cells were described before [110, 111], as well as Hek-293T cells stable expressing MIC13 variants [196]. *MIC13* Hap1 cells were custom made by Horizon (UK) using the CRISP/R-Cas method. Cells were transfected with 1 µg of corresponding plasmid using GeneJuice (Novagen) according to the manufacturer's instruction.

3.4.3.2. SDS electrophoresis and western blotting

Samples for SDS electrophoresis were scraped in PBS and proteins were extracted with RIPA lysis buffer (50 mM TRIS-HCl, 150 mM NaCl, 1% Triton X-100, 1% sodium deoxycholate, 0,1% SDS, 5 mM EDTA, pH 7.4). Protein concentration was determined by Lowry method (Bio-Rad, DC™ Protein Assay Kit I, 5000111) and samples were prepared with Laemmli loading buffer (250 mM TRIS-HCl pH 6.8, 2% SDS, 10% Glycerol, 2% β-mercaptoethanol, 0.01% bromphenol blue). For protein separation, 10% SDS-PAGE, 15% SDS-PAGE, and 7.5% SDS-PAGE (BioRAD, 4561025) were performed. The proteins were subsequently transferred on a nitrocellulose membrane and probed with the following antibodies: MIC10 (Abcam, 84969), MIC13 (custom made by Pineda (Berlin) against human MIC13 peptide CKAREYSKEGWEYVKARTK), MIC26 (Thermofisher Scientific, MA5-15493), MIC27 (Atlas Antibodies, HPA000612), MIC60 (custom made by Pineda (Berlin) against human MIC60 peptide CTDHPEIGEGKPTPALSEEAS), HSP60 (sigma, SAB4501464), PARP (Cell Signaling, 9542), GK (Thermofisher Scientific, PA5-49825), actin (Abcam, ab1801), STOML2 (Abcam, ab102051), GPD2 (Sigma, HPA008012), NME1 (Thermofisher Scientific, HPA008467). Chemiluminescent signal was recorded with VILBER LOURMAT Fusion SL (Peqlab) and quantification was performed with Image Studio Lite Ver 5.2.

3.4.3.3. Apoptosis induction

For analysis of PARP cleavage and cytochrome *c* release cells were treated with 1 µM staurosporine (Sigma, 11055682001) for 3 h, 4.5 h, or 6 h. Control samples were treated for 6 h with DMSO. Caspase activity was blocked with 20 µM zVAD-(OMe)-FMK (Santa Cruz, sc-311561A). Samples were then subjected to SDS electrophoresis and western blotting (3.4.3.2) or immunofluorescence staining und fluorescence microscopy (3.4.3.4).

3.4.3.4. Immunofluorescence staining and fluorescence microscopy

Cells were fixed with 4% paraformaldehyde, permeabilized with 0.15% Triton-X100 (Sigma, T8787), and blocked using 3% BSA (Roth, 8076). The cells were incubated with the primary antibodies AlexaFluor 488 Mouse anti-cytochrome *c* (BD Biosciences, 560263) and TOM20 (Santa Cruz Biotechnology, sc-114115). Then the secondary antibody goat anti-rabbit Alexa Fluor 568 (Thermofisher Scientific, A11011) was added and the cells were stained with 5 µg/mL DAPI to stain the nucleus (Sigma). Samples were imaged on a ZEISS Axiovert Observer D1 microscope using the AxioVision software (ZEISS).

3.4.3.5. Mitochondrial isolation

Cells were cultured in petri dishes, scraped with a cell scraper in PBS (Sigma), and pelleted at 500 g for 5 min. The pellet was resuspended in an isotonic buffer (220 mM mannitol, 70 mM sucrose, 1 mM EDTA, 20 mM HEPES (pH 7.5) and 1 x protease inhibitor cocktail (Roche)) with 0.1% BSA (Roth) and incubated on ice for 10 min. Cells were homogenized by mechanical rupture using a syringe with a 21 G cannula and repeatedly soaking the suspension in and releasing it in a stroke for 20 times. Lysed cells were centrifuged at 1000 g and 4 °C for 10 min. The supernatant was then centrifuged at 10000 g and 4 °C for 15 min and the pellet was resuspended in the isotonic buffer. Mitochondria were divided into aliquots and frozen in 300 M trehalose, 10 mM KCl, 1 mM EDTA, 10 mM HEPES and 0.1% BSA for further experiments.

3.4.3.6. Proteomics

Samples were prepared as described before [197]. Measurements and analytics were performed with the help of Dr. Gereon Poschmann, AG Stühler, Institute of Molecular Medicine I, Uniklinikum Düsseldorf.

4. Discussion

In 2015 MIC13 was first described to be a part of the MICOS complex [112]. Since then more and more studies showed a link between mutated MIC13 and severe diseases. MIC13 deficiency leads to mitochondrial hepato-encephalopathy in patients and is linked to lactic acidosis, hypoglycemia, 3-methylglutaconic aciduria, and cardiac arrhythmia [136, 174, 181-183]. The studies shown here help to decipher the molecular role of MIC13 and lead to a better understanding of the associated diseases. We showed that loss of MIC13 is accompanied by the loss of the MIC10-subcomplex and an impaired assembly of MICOS. It is also accompanied by a distinct mitochondrial ultrastructure, with elongated cristae in concentric stacks and loss of CJ. The assembly of respiratory chain complexes was not affected, but the respiration is mildly affected upon loss of MIC13 [110]. Our studies on cristae dynamics showed that CJs are dynamic and merge in a reversible and balanced manner at a timescale of seconds. This dynamic is dependent on MIC13 and therefore a functional MICOS. Depletion of MIC13 leads to a decreased mobility of TIM23 in the inner membrane, as well as increased mobility of MIC10 in the inner membrane. We show, that cristae pinch off transiently and reconnect to the IBM or with other cristae, building 'X' and 'Y' structures [111]. In an unpublished study, we show that MIC13 functions as a bridge between the two MICOS subcomplex. We furthermore supported that this bridging function is dependent on conserved residues in the MIC13 sequence, namely a GxxxG motif in the N-terminal region and WN (84-85aa). Interestingly, there was a function of MIC13 for mitochondrial morphology independent of MICOS assembly [196]. In additional unpublished results, I proved that loss of MIC13 leads to delayed cytochrome *c* release upon apoptosis induction and also leads to changes in other proteins levels, indicating MIC13 interaction in other mitochondrial pathways. Since there are no studies on the molecular functions, the studies presented here help to unravel the molecular role of MIC13 not only for MICOS but for the whole mitochondria. The role of MIC13 for MICOS, but also cristae dynamics, apoptosis, and respiration become clearer upon linking the results from these different studies and will be explained to some extent in the following chapters.

4.1. Molecular function of MIC13

Our findings show a reduction of protein levels of the MIC10-subcomplex upon loss of MIC13. In cells lacking MIC13, there is a shift of the MICOS complex on the BN-PAGE. The MICOS usually migrates at weights of approximately 550 kDa, 950 kDa, and 2000 kDa. In *MIC13* KO cells the MICOS migration shifts to 400 kDa, 680 kDa, and 1800 kDa [110]. This shift can be explained by the loss of the MICOS proteins MIC13, MIC10, MIC26, and MIC27. These proteins or at least some must be present in oligomers to cause a shift of approximately 150 to 200 kDa. This is already known for MIC10, but not shown for MIC13 so far [172]. The

disassembly of the smaller subcomplex was also confirmed by testing the BN-PAGE for the MICOS proteins MIC10 and MIC27. Upon loss of MIC13, there is no signal at a higher molecular weight detected, which indicates that the MIC10-subcomplex is not abundant and therefore not integrated into the complex. MIC27 however is still abundant to some extent as shown by western blot analysis, but upon depletion of MIC13 it only migrates at a very low molecular weight, which is very likely oligomerizes MIC27 or a complex of MIC26-MIC27 [196]. Our findings, that loss of MIC13 leads to a loss of the smaller subcomplex is also supported by other studies, where the same effect was shown in cell lines, as well as in patient cells [112, 174, 181]. The idea is, that MIC13 acts as a bridge between the two MICOS subcomplexes, and upon loss of this link the smaller subcomplex, containing MIC10, MIC26, and MIC27 does not assemble into the MICOS anymore and therefore degrades. This is supported by the finding, that mRNA levels of these proteins are not significantly changed in patient cells with a MIC13 deficiency [174]. The bridging function of MIC13 is also supported by the role of the yeast homolog MIC12 [156]. MIC12 in yeast is important for the connection of the two MICOS complex subunits and also suggested to have a bridging function [168].

In this study, we also show that large parts of the MIC13 sequence are dispensable for this bridging function. Upon deletion of about one-sixth of the sequence of the protein, it still shows interaction with other MICOS components as shown by co-immunoprecipitation. Also, the integration into the MICOS is not affected, as shown by BN-PAGE. Nevertheless, there are regions, which are important for not only MICOS expression and stability, but also for its interaction with other MICOS proteins, as shown by western blot and co-immunoprecipitation [196]. Here we identified two distinct regions, that are important for the MIC13 bridging function, a GxxxG motif in the N-terminal region and WN (84-85aa). These residues are highly conserved, especially WN, which is even conserved in MIC12 [156]. This indicates that also the bridging function of MIC13 is highly conserved and these two residues are important for the interaction with the other MICOS components and therefore the correct assembly of MICOS. The GxxxG motif is known for its ability to provide a basis for protein-protein interactions between transmembrane helices and therefore lead to dimerization [198]. In summary, this motif in MIC13 can possibly be important for dimerization of the protein or interaction with other transmembrane proteins.

MIC60 levels, as well as the assembly into a higher molecular weight complex, does not depend on MIC13 levels [110, 112]. In addition to that, we showed here that the distribution of MIC60 along the inner membrane is also not affected by the loss of MIC13 [111]. This distribution is not dependent on the presence of CJs as they are nearly lost upon deletion of MIC13. MIC60 is the oldest and most conserved part of the MICOS with orthologues even found in α-proteobacteria [12]. It plays a major role in the formation of contact sites with the

OM via interaction with the SAM and TOM complex in the OM [157]. This function of MIC60 seems to be independent of MIC13 and the MIC10-subcomplex. The assembly of MICOS most likely happens hierarchically. The MIC60-subcomplex is present at the IBM and builds the CS together with MIB proteins in the OM. MIC13 links the MIC10-subcomplex to MIC60 and therefore facilitates the complete MICOS assembly. Upon complete MICOS assembly CJ can be formed and stabilized properly. Without MIC60, as a platform for docking of the other subcomplex, or upon loss of MIC10, which promotes membrane binding by oligomerization, CJs are lost [116, 158, 172]. Taken together, all presented studies support the function of MIC13 as a bridge especially when the identified conserved residues and binding motives are taken into account (Figure 11).

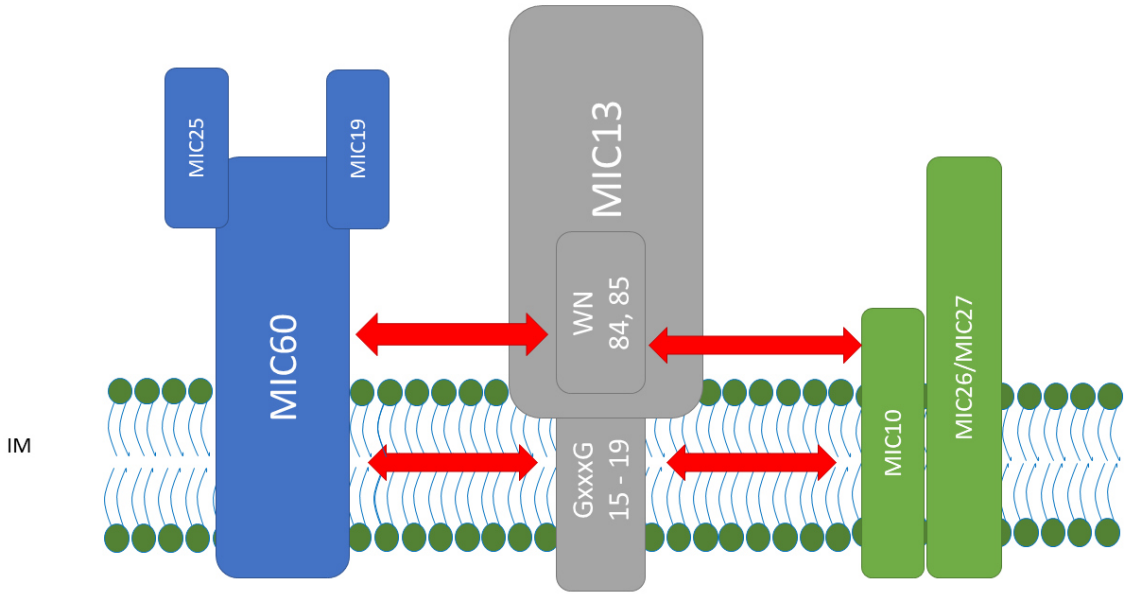

Figure 11. Model of MIC13 interaction and function. MIC13 (grey) interacts with known MICOS components MIC60-subcomplex (blue) and MIC10-subcomplex (green) via the conserved residues GxxxG (15-19aa) and WN (84-85aa). Residues RD (81-81aa) are linked to proper cristae morphology. Experiments indicate involvement in other pathways and interactions with other proteins, which are not studied yet (image taken from Urbach et al. [196]).

Besides the bridging function, no other functions of MIC13 were described so far. Here we show for the first time that variants of MIC13 can restore the bridging function and interaction with the other MICOS components. However, for the variant MIC13$^{\Delta 64\text{-}83}$ and more specifically MIC13$^{\Delta RD}$ the interaction to other MICOS proteins could be restored, but the normal cristae morphology is not completely restored [196]. Upon loss of MIC10, the mitochondrial morphology is affected and CJs are lost [158]. If MIC13 function is limited to the bridging function the aberrant mitochondrial morphology in *MIC13* KO cells is caused by loss of MIC10. In the stated MIC13 variants the levels of MIC10 are restored and the MICOS assembles, but

the mitochondrial morphology is still affected. This indicates either a direct function of MIC13 in shaping the mitochondrial membrane or a function of MIC13 in another pathway or interaction with other proteins responsible for mitochondrial morphology. I showed that loss of MIC13 affects levels of other proteins (Figure 10A-B). Levels of the mitochondrial proteins GK, GSPT1, and adrenodoxin reductase are less in *MIC13* KO, and levels of mitochondrial protein MICU1 increase upon loss of MIC13. These proteins are involved in mitochondrial processes and are also linked to several diseases. GSTP1 is important for protection against oxidative stress and is involved in Alzheimer's disease [189, 190]. In Alzheimer's disease cristae morphology is disrupted and concentric and parallel stacks of cristae membranes appear [199]. This links the disease to both, mitochondrial ultrastructure and oxidative stress. Therefore, the involvement of MIC13 or MICOS, in general, is possible. This can be mediated via the disrupted mitochondrial ultrastructure or because of increased oxidative stress upon loss of GSTP1 levels. In this study, the loss of GK levels is only visible in Hek-293T cells. GK is involved in glycerol degradation to glycerol-3-phosphate which can be dehydrogenated to dihydroxyacetone phosphate (DHAP). DHAP can be converted into glyceraldehyde 3-phosphate, which is part of the glycolysis and fuels into the TCA-cycle [195]. Glycerol-3-phosphate can also directly fuel into the electron transport chain by the glycerol-3-phosphate shuttle, where glycerol-3-phosphate is oxidized to glycerone phosphate, which leads to electron transfer to the mitochondrial quinone pool [200]. A loss of GK could therefore explain the respiration defect in *MIC13* KO cells. However, Hap1 and HeLa cells show no loss of GK protein levels upon loss of MIC13 (Figure 10C). These cell lines are derived from different tissue types. Hap1 cells are derived from myeloid tissue, HeLa from cervix tissue and Hek-293T from embryonal kidney tissue. It is possible, that the importance of glycerol-3-phosphate for the energy metabolism or other pathways differs in these cell types. Another explanation would be, that the loss of GK levels is an artefact caused by CRISPR/Cas. The levels of MICU1 are increased upon loss of MIC13. MICU1 can regulate calcium uptake by regulation of the mitochondrial calcium uniporter MCU. It can act both as an activator or inhibitor of mitochondrial calcium uptake [201]. MIC13 is therefore linked to calcium homeostasis. One possible explanation is, that loss of MIC13 disrupts normal calcium homeostasis and more MICU1 is needed to keep calcium levels and assure cell survival. Overall, the data suggest, that there is a link of MIC13 and MICOS in general to several different mitochondrial pathways besides the mitochondrial ultrastructure. Research on possible interaction partners and involvement of MIC13 in several mitochondrial pathways is an interesting topic for future studies.

4.2. Role of MIC13 in Cristae Dynamics

Loss of MIC10 and MIC60 leads to loss of CJ and reduced number of cristae, similar to the loss of MIC13 [110, 111]. This was already shown in yeast for MIC60. The membrane shaping

abilities of these proteins are already known and our findings support these former results [12, 116, 158, 172]. There is a loss of MIC10 levels upon loss of MIC13. However, as shown before this is not the only reason for the loss of CJs in *MIC13* KO cells. MIC13 has an independent function in CJ formation or stabilization. The MICOS in general plays an important role in the mitochondrial ultrastructure. Here we show, that this ultrastructure is highly dynamic and CJ merge and split in a reversible and balanced manner in a timescale of seconds [111]. This led to the 'Cristae Fission and Fusion' (CriFF) model with transient subcompartmentalization and physically isolated cristae. Thinking of the importance of fission and fusion of mitochondria for mitochondrial quality control [84]], the CriFF model is a probate explanation for the building of independent cristae as well as assuring an optimal cristae quality and therefore optimal mitochondrial function. This dynamic is highly dependent on functional MICOS and MIC13 levels. Upon loss of MIC13 the dynamic movement of MIC60 and MIC10 punctae, indicating sites of CJs is markedly reduced. In addition, the mobility of the IBM protein TIM23 is also reduced [111]. It was shown before, that TIM23 can be redistributed between the IBM and CM, adapting to the physiological state [46]. The role of CJs as 'gates' for a prober redistribution is therefore supported as well as the role of MIC13 in CJ maintenance. The mobility of single MIC60 and MIC10 proteins is reduced upon loss of MIC13, but the directed motion of both proteins is significantly higher, indicating a lower directed motion in the fully assembled subcomplex compared to the two subcomplexes. The distribution of MIC60 was also not affected by the loss of MIC13 [111]. These findings support the role of MIC13 as a bridge between the two subcomplexes. The MIC60-subcomplex acts in this model as a docking station in the IBM and the MIC10-subcomplex can merge to it with the help of MIC13. The fully assembled MICOS is then able to maintain the CJs and their dynamic fusion and fission. One idea is, that the fusion and fission of CJs depend on MIC13 in a way, that MIC13 can merge the two subcomplexes, present on two membranes, and therefore facilitate fusion of these membranes. We showed, that this fusion leads to 'X' and 'Y' structures of the cristae [111]. In our study of MIC13 function, we found in the variant MIC13$^{\Delta 64\text{-}83}$ structures of interconnected cristae. In the same mutant, we also found restoration of the MICOS, but not of the mitochondrial morphology [196]. Taken together, these two findings strongly support a function of MIC13 in merging and splitting of CM, which is independent of other MICOS components. So MIC13 cannot only build a bridge to induce membrane fusion but has also a role in fission of these membranes, which might be independent of the other MICOS proteins and is impaired in MIC13$^{\Delta 64\text{-}83}$.

In our first study on MIC13, we showed a complete loss of CJs upon loss of MIC13 in Hek-293T cells [110]. This was confirmed in the studies on cristae dynamics to be true in HeLa cells as well [111]. However, in our recent study on MIC13 function we show, that upon loss of MIC13 in Hek-293T cells, there is not a complete loss of CJ. Quantification of EM data suggests, that

there are only very few CJs, but they could be observed. Still, the number of cristae is decreased, and the counted CJs are a very rare phenomenon in *MIC13* KO cells [196]. The appearance of CJs can be explained by the dynamic as well as by the formation of the cristae itself. Other proteins are also involved in membrane shaping of mitochondria, for example F_1F_0-ATP synthase dimers [57]. Since cristae appear, even upon loss off MICOS, there is a mechanism that forms these isolated membrane compartments. Therefore, it is possible, that upon loss of MIC13, another mechanism, probably F_1F_0-ATP synthase dimers build invaginations in the IBM to form cristae, that pinch of, for there is no MICOS to stabilize the CJs. This cristae formation might look like CJs on EM pictures and this explains the appearance of few CJs upon loss of MIC13. Another theory could be, that MIC60 alone can facilitate CJ formation, but these CJs are not stable without the MIC10-subcomplex. This leads to very few and transient CJ. The mechanism of CJs formation, maintenance, and dynamics was only developed recently and is far from being completely understood, making this a very interesting topic for future studies.

4.3. Role of MIC13 in Apoptosis

Mitochondrial ultrastructure is closely linked to functional apoptosis via the intrinsic pathway. The remodeling of CJs to facilitate cytochrome *c* release was shown before to be dependent on OPA1 and MIC60 [107]. About 85% of cytochrome *c* is located at the cristae and only a minor part resides in the IMS [39]. Therefore, the remodeling of CJs plays a crucial part in cytochrome *c* release and is important for functional apoptosis via the intrinsic pathway. This raises the question if cytochrome *c* release is possible upon loss of CJs in *MIC13* KO cell lines. In this study, I showed, that the loss of MIC13 leads to a slower cytochrome *c* release upon apoptosis induction with staurosporine (Figure 9B). Cytochrome *c* release is possible in cells lacking CJs, but how is it mediated? The effect of MIC13 on cristae dynamics was already discussed (chapter 4.2.). This may also contribute to cytochrome *c* release upon apoptosis. The cristae dynamic can assure a proper distribution of cytochrome *c* across cristae lumen and IMS. Upon loss of this dynamic, the fate of cytochrome *c* is unknown. It is possible, that even upon disrupted cristae dynamic there are very few occasions of cristae merging with the IBM, which was also shown in our study on MIC13 function [196]. These rare appearances of CJ can be the reason why there is cytochrome *c* release in *MIC13* KO cells, but this release is delayed. Another explanation could be, that cytochrome *c* is distributed differently in *MIC13* KO cells. With the loss of cristae dynamics, it is possible, that cytochrome *c* mainly resides in the IMS. This however raises the question, why cytochrome *c* release is slower and not faster upon loss of MIC13. The effect of loss of MIC13 on MOMP was not studied yet. An interaction of MICOS with BAX/BAK foci is not reported, but possible, since MICOS as part of the MIB interacts with proteins in the outer membrane [157]. This interaction can possibly influence the formation of BAX/BAK foci and upon loss of MIC13 disturb the proper assembly or slow it

down. After translocation of BAX, MIC60 and MIC27 redistribute more uniformly, indicating a connection of BAX and MICOS. However, cytochrome *c* release is independent of this redistribution [108]. OPA1 was also reported to play an important part in CJ widening upon apoptosis in cooperation with MIC60. MIC60 however is not required for apoptotic redistribution of cytochrome *c* [107]. The role of MIC60 in apoptosis is also not completely understood, but some studies do also point to an antiapoptotic effect of MIC60 [108, 109}. The interplay of MIC13 with OPA1 and MIC60 in this pathway is not described yet. However, the loss of a completely assembled MICOS seems to affect the intrinsic pathway of apoptosis to some extent. The overall apoptosis however is not affected drastically, as shown by PARP cleavage. PARP cleavage, which happens downstream of cytochrome *c* release is only mildly affected (Figure 9D). PARP cleavage can also be mediated to the extrinsic pathway of apoptosis, indicating, that this pathway is not disturbed in *MIC13* KO cells.

It was shown before, that the MICOS interactor CHCHD10 is important for apoptosis. A loss of this MICOS component leads to the inhibition of apoptosis [177]. The mitochondrial ultrastructure, which is also affected to a smaller extent upon loss of CHCHD10 can unlikely be the reason, for we see apoptosis in MIC13 deficient cells. Therefore, another connection of MICOS to apoptosis can be the reason. Recently it was shown that the heme-binding protein 1 (Hebp1) interacts with MICOS. This protein was also shown to mediate heme-induced toxicity via an apoptotic pathway [202]. The influence of MICOS on apoptosis over interacting proteins would explain the different phenotypes upon loss of different MICOS subunits.

All results lead to the conclusion, that MICOS plays an important part in apoptotic cristae remodeling, but is not required for the release of cytochrome *c*. However, here I showed a minor effect on cytochrome *c* released caused by the loss of MIC13. Therefore, it is possible, that MICOS affects apoptosis not solely by the changes in ultrastructure, but by different interacting proteins, which can contribute to different mitochondrial functions.

4.4. Role of MIC13 in Respiration

Mitochondrial respiration is highly dependent on the presence of a double membrane to build a proton gradient. The cristae are suggested to be the main part of mitochondrial respiration since proteins of the OXPHOS mainly reside at CM and CJs can build diffusion barrier for protons and ADP [64, 113, 115]. F_1F_0-ATP synthase is also responsible for the tubulation of IM [57]. We found here that the absence of the MICOS components MIC10, MIC13, and MIC60 leads to a decrease in respiration [110, 111]. Upon loss of these proteins, the mitochondrial ultrastructure is drastically affected and there is a loss of CJs. This leads to the conclusion, that CJs play an important role in respiration, but are not sufficient for respiration, since there is no drastic reduction in respiration and cells are surviving. The loss of MIC13 does not lead to a reduction of ATP5L levels, as well as no difference in the stability of respiratory chain

complexes as shown by BN-PAGE. However, especially the complex IV driven respiration was affected upon loss of MIC13 [110]. Since this is not dependent on the levels or assembly of these proteins, we conclude that the loss of CJs leads to less respiration. This happens either through the isolation of the cristae, making the cristae lumen less accessible for metabolites of the OXPHOS, or through localization of the respiratory chain at the IBM instead of the CM, which provides no distinct subcompartment for the proton gradient, making diffusion much easier and therefore leading to less respiration. Also, other studies showed a defect in respiration upon MIC13 deficiency. There was less respiration upon knockdown of *MIC13* in HeLa cells observed [112]. In patient cells, the activity of respiratory chain complexes was measured with different outcomes. One study showed, that there is no change in respiratory complex activity in fibroblast, whereas others found a mild complex III and complex IV deficiency [136, 174, 181]. In muscle biopsy deficiencies across all respiratory chain complexes were found or at least a reduced activity of complex III and IV [136, 181]. In contrast, another study reported an overall normal activity of respiratory chain complexes [181]. In liver cells, the results are relatively uniform with a clear reduction in complex III and IV activity [136, 181]. The difference in tissue types can be explained by different physiological needs of the different tissue types. Differences between patients can be explained by the general mutation that causes the disease, as well as the age of the patient and the progression of the disease. A clear reduction in respiratory chain complex activity in liver cells is in line with liver dysfunction as a common symptom of MIC13 deficiency [136, 174, 181-183]. It was shown before in yeast, that Complex III and Complex IV are not properly organized or positioned upon the loss of the MICOS, leading to morphological and respiratory growth defects [75]. These results suggest a strong dependence of especially complex III and IV either on MICOS or the mitochondrial ultrastructure in general.

A recent study on MIC26 and MIC27 shows that respiration is affected upon the loss of both proteins together. In addition, MIC27 and MIC27 are required for the assembly of the F_1F_0-ATP synthase and regulate the stability of the respiratory chain complexes and supercomplexes [121]. Since there is a clear reduction of these proteins upon loss of MIC13, the decrease in respiration can also be an effect of the loss of MIC26 and MIC27. To further test this hypothesis in future studies the MIC13 variants we generated in this study can be an excellent tool [196]. With help of the MIC13 variants, one could also possibly check the contribution of MIC13 independent of MICOS and mitochondrial ultrastructure.

4.5. Conclusion

In this study, I provided insight into the molecular function of MIC13. The function of MIC13 as a bridge could be further supported by my results and I was able to decipher the conserved residues in the MIC13 sequence, which are important for this function. Also, a general

characterization of MIC13 was performed. Upon loss of MIC13, the MIC10-subcomplex is also lost, for it is no longer linked to the MIC60-subcomplex. There is also a drastic decrease of CJs and cristae upon loss of MIC13 and I show here, that MIC13 affects mitochondrial ultrastructure independent of other MICOS components. The decrease in respiration, as well as the delay in cytochrome *c* release upon loss of MIC13, is likely to be an effect of the altered mitochondrial ultrastructure or loss of other MICOS components. There is a huge potential for future studies with the generated MIC13 variants. Also, the interaction of MIC13 with proteins outside the MICOS has to be unrevealed. The contribution of MIC13 to other pathways independent of MIC13 is a huge field to discover and by finding possible interaction partners the function of MIC13 can be further deciphered. These findings can also help to understand the disease of people with MIC13 deficiency. If we know the affected pathways upon loss of MIC13, we can provide a better insight into the disease and also build a basis for better treatment of this disease. To sum this up, MIC13 is a protein of the MICOS with a bridging function, which is important for the assembly of this complex. Other functions of MIC13 are still to be discovered and are promising for further understanding of the mitochondrial function and its importance for a healthy cell and organism.

5. Summary

The integrity of the mitochondrial ultrastructure is provided by a large molecular heterooligomeric complex called mitochondrial contact site and cristae organizing system (MICOS). The evolutionary conserved MICOS complex has been shown to consist of two subcomplexes, the MIC60-subcomplex and the MIC10-subcomplex. The majority of studies have dealt with the core proteins of both subcomplex, MIC60 and MIC10, showing their importance for the formation of CJs as functional barriers to separate cristae from the inner boundary membrane and intermembrane space. This study aimed to define the function, interaction partners, and associated phenotype of the understudied protein MIC13 as part of the MICOS and independent from it. After proving that MIC13 is a part of MICOS we investigated the phenotype upon loss of this protein. We found that loss of MIC13 leads to the loss of the MIC10-subcomplex, reduced respiration, and altered mitochondrial ultrastructure accompanied by loss of CJs. Further, we studied the role of MIC13 in cristae dynamics. We found a dynamic movement of cristae inside the mitochondria, that is accompanied by continuous merging and splitting events. These cristae dynamics is highly dependent on MIC13 and a functional MICOS. These studies suggested a bridging function of MIC13 to assure the proper assembly of MICOS. MICOS is assembled in a hierarchical way with MIC60 as a docking platform. MIC13 is needed to link the MIC10-complex to the MIC60-complex and therefore without MIC13 the MIC10-complex is lost. This role of MIC13 is supported by our latest findings, where we show that two conserved regions in the MIC13 sequence are important for the interaction of MIC13 with other MICOS components. We first performed systematic deletions across the MIC13 sequence to pinpoint regions, which are important for interaction with other MICOS components by co-immunoprecipitation. We found two regions, the N-terminal region, and a middle region between aa 84 and aa 103 to be important for the interaction of MIC13 with MICOS components. With help of multiple sequence alignment, we then found conserved residues in these regions, a GxxxG motif in the N-terminal region and WN in the latter region. We show here, that these conserved regions are important for interaction with other MICOS proteins, therefore they are important for the bridging function of MIC13. Interestingly, we could find also the conserved residues RD (81-82aa), which are dispensable for the bridging function of MIC13 but are important for mitochondrial ultrastructure, showing an additional function of MIC13 independent from the other MICOS components. In additional experiments, I further show, that loss of MIC13 leads to a delayed cytochrome *c* release upon apoptosis induction, which is most likely due to the alterations in mitochondrial ultrastructure. With a proteomics approach, I found several proteins, which levels are changed upon loss of MIC13. These proteins are potential candidates for MIC13 interaction partners or hint to other functions of MIC13 outside of normal MICOS function. All in all, we showed that MIC13 is not only responsible for the connection between both MICOS

subcomplexes but also indispensable for the formation of the small subcomplex and proper mitochondrial ultrastructure independent from other MICOS components.

6. References

1. Henze, K. and W. Martin, *Evolutionary biology: essence of mitochondria.* Nature, 2003. **426**(6963): p. 127-8.
2. Ernster, L. and G. Schatz, *Mitochondria: a historical review.* J Cell Biol, 1981. **91**(3 Pt 2): p. 227s-255s.
3. Gray, M.W., G. Burger, and B.F. Lang, *The origin and early evolution of mitochondria.* Genome Biol, 2001. **2**(6): p. REVIEWS1018.
4. Gray, M.W., *Mitochondrial evolution.* Cold Spring Harb Perspect Biol, 2012. **4**(9): p. a011403.
5. Zimorski, V., et al., *Endosymbiotic theory for organelle origins.* Curr Opin Microbiol, 2014. **22**: p. 38-48.
6. Tzagoloff, A. and A.M. Myers, *Genetics of mitochondrial biogenesis.* Annu Rev Biochem, 1986. **55**: p. 249-85.
7. Boore, J.L., *Animal mitochondrial genomes.* Nucleic Acids Res, 1999. **27**(8): p. 1767-80.
8. Gray, M.W., *Rickettsia, typhus and the mitochondrial connection.* Nature, 1998. **396**(6707): p. 109-10.
9. Feagin, J.E., *Mitochondrial genome diversity in parasites.* Int J Parasitol, 2000. **30**(4): p. 371-90.
10. Sloan, D.B., et al., *Rapid evolution of enormous, multichromosomal genomes in flowering plant mitochondria with exceptionally high mutation rates.* PLoS Biol, 2012. **10**(1): p. e1001241.
11. Lang, B.F., et al., *An ancestral mitochondrial DNA resembling a eubacterial genome in miniature.* Nature, 1997. **387**(6632): p. 493-7.
12. Tarasenko, D., et al., *The MICOS component Mic60 displays a conserved membrane-bending activity that is necessary for normal cristae morphology.* J Cell Biol, 2017. **216**(4): p. 889-899.
13. Karlberg, O., et al., *The dual origin of the yeast mitochondrial proteome.* Yeast, 2000. **17**(3): p. 170-87.
14. Marcotte, E.M., et al., *Localizing proteins in the cell from their phylogenetic profiles.* Proc Natl Acad Sci U S A, 2000. **97**(22): p. 12115-20.
15. Mitchell, P., *Coupling of phosphorylation to electron and hydrogen transfer by a chemi-osmotic type of mechanism.* Nature, 1961. **191**: p. 144-8.
16. Duchen, M.R., *Mitochondria and Ca(2+)in cell physiology and pathophysiology.* Cell Calcium, 2000. **28**(5-6): p. 339-48.
17. Pizzo, P. and T. Pozzan, *Mitochondria-endoplasmic reticulum choreography: structure and signaling dynamics.* Trends Cell Biol, 2007. **17**(10): p. 511-7.
18. Rizzuto, R., P. Bernardi, and T. Pozzan, *Mitochondria as all-round players of the calcium game.* J Physiol, 2000. **529 Pt 1**: p. 37-47.
19. Contreras, L., et al., *Mitochondria: the calcium connection.* Biochim Biophys Acta, 2010. **1797**(6-7): p. 607-18.
20. Green, D.R. and J.C. Reed, *Mitochondria and apoptosis.* Science, 1998. **281**(5381): p. 1309-12.
21. Neuzil, J., et al., *Mitocans as anti-cancer agents targeting mitochondria: lessons from studies with vitamin E analogues, inhibitors of complex II.* J Bioenerg Biomembr, 2007. **39**(1): p. 65-72.
22. Harman, D., *Aging: a theory based on free radical and radiation chemistry.* J Gerontol, 1956. **11**(3): p. 298-300.
23. Veal, E.A., A.M. Day, and B.A. Morgan, *Hydrogen peroxide sensing and signaling.* Mol Cell, 2007. **26**(1): p. 1-14.
24. Meier, P., A. Finch, and G. Evan, *Apoptosis in development.* Nature, 2000. **407**(6805): p. 796-801.
25. Vaux, D.L. and S.J. Korsmeyer, *Cell death in development.* Cell, 1999. **96**(2): p. 245-54.

26. Green, D.R. and G. Kroemer, *The pathophysiology of mitochondrial cell death.* Science, 2004. **305**(5684): p. 626-9.
27. Mattson, M.P., *Apoptosis in neurodegenerative disorders.* Nat Rev Mol Cell Biol, 2000. **1**(2): p. 120-9.
28. Yuan, J. and B.A. Yankner, *Apoptosis in the nervous system.* Nature, 2000. **407**(6805): p. 802-9.
29. Favaloro, B., et al., *Role of apoptosis in disease.* Aging (Albany NY), 2012. **4**(5): p. 330-49.
30. Yivgi-Ohana, N., et al., *Utilizing mitochondrial events as biomarkers for imaging apoptosis.* Cell Death Dis, 2011. **2**: p. e166.
31. Gavathiotis, E. and L.D. Walensky, *Tracking BAX once its trigger is pulled.* Cell Cycle, 2011. **10**(6): p. 868-70.
32. Martinou, J.C. and R.J. Youle, *Mitochondria in apoptosis: Bcl-2 family members and mitochondrial dynamics.* Dev Cell, 2011. **21**(1): p. 92-101.
33. Moldoveanu, T., et al., *Many players in BCL-2 family affairs.* Trends Biochem Sci, 2014. **39**(3): p. 101-11.
34. Eskes, R., et al., *Bid induces the oligomerization and insertion of Bax into the outer mitochondrial membrane.* Mol Cell Biol, 2000. **20**(3): p. 929-35.
35. Gross, A., et al., *Enforced dimerization of BAX results in its translocation, mitochondrial dysfunction and apoptosis.* EMBO J, 1998. **17**(14): p. 3878-85.
36. Hsu, Y.T., K.G. Wolter, and R.J. Youle, *Cytosol-to-membrane redistribution of Bax and Bcl-X(L) during apoptosis.* Proc Natl Acad Sci U S A, 1997. **94**(8): p. 3668-72.
37. Grosse, L., et al., *Bax assembles into large ring-like structures remodeling the mitochondrial outer membrane in apoptosis.* EMBO J, 2016. **35**(4): p. 402-13.
38. McArthur, K., et al., *BAK/BAX macropores facilitate mitochondrial herniation and mtDNA efflux during apoptosis.* Science, 2018. **359**(6378).
39. Scorrano, L., et al., *A distinct pathway remodels mitochondrial cristae and mobilizes cytochrome c during apoptosis.* Dev Cell, 2002. **2**(1): p. 55-67.
40. Ryan, M.T. and N.J. Hoogenraad, *Mitochondrial-nuclear communications.* Annu Rev Biochem, 2007. **76**: p. 701-22.
41. Bartlett, K. and S. Eaton, *Mitochondrial beta-oxidation.* Eur J Biochem, 2004. **271**(3): p. 462-9.
42. Maechler, P., S. Carobbio, and B. Rubi, *In beta-cells, mitochondria integrate and generate metabolic signals controlling insulin secretion.* Int J Biochem Cell Biol, 2006. **38**(5-6): p. 696-709.
43. Osellame, L.D., T.S. Blacker, and M.R. Duchen, *Cellular and molecular mechanisms of mitochondrial function.* Best Pract Res Clin Endocrinol Metab, 2012. **26**(6): p. 711-23.
44. Schagger, H. and K. Pfeiffer, *Supercomplexes in the respiratory chains of yeast and mammalian mitochondria.* EMBO J, 2000. **19**(8): p. 1777-83.
45. Boekema, E.J. and H.P. Braun, *Supramolecular structure of the mitochondrial oxidative phosphorylation system.* J Biol Chem, 2007. **282**(1): p. 1-4.
46. Vogel, F., et al., *Dynamic subcompartmentalization of the mitochondrial inner membrane.* J Cell Biol, 2006. **175**(2): p. 237-47.
47. Filosto, M. and M. Mancuso, *Mitochondrial diseases: a nosological update.* Acta Neurol Scand, 2007. **115**(4): p. 211-21.
48. Cui, H., et al., *Comprehensive next-generation sequence analyses of the entire mitochondrial genome reveal new insights into the molecular diagnosis of mitochondrial DNA disorders.* Genet Med, 2013. **15**(5): p. 388-94.
49. Falk, M.J., *Introduction: Emerging research in mitochondrial disease.* Dev Disabil Res Rev, 2010. **16**(2): p. 105.
50. Scarpelli, M., et al., *Mitochondrial diseases: advances and issues.* Appl Clin Genet, 2017. **10**: p. 21-26.
51. Gerbitz, K.D., et al., *Mitochondrial diabetes mellitus: a review.* Biochim Biophys Acta, 1995. **1271**(1): p. 253-60.

52. Chan, D.C., *Mitochondria: dynamic organelles in disease, aging, and development.* Cell, 2006. **125**(7): p. 1241-52.
53. Scarpelli, M., et al., *Strategies for treating mitochondrial disorders: an update.* Mol Genet Metab, 2014. **113**(4): p. 253-60.
54. Hyslop, L.A., et al., *Towards clinical application of pronuclear transfer to prevent mitochondrial DNA disease.* Nature, 2016. **534**(7607): p. 383-6.
55. Palade, G.E., *An electron microscope study of the mitochondrial structure.* J Histochem Cytochem, 1953. **1**(4): p. 188-211.
56. Sjostrand, F.S., *Electron microscopy of mitochondria and cytoplasmic double membranes.* Nature, 1953. **171**(4340): p. 30-2.
57. Zick, M., R. Rabl, and A.S. Reichert, *Cristae formation-linking ultrastructure and function of mitochondria.* Biochim Biophys Acta, 2009. **1793**(1): p. 5-19.
58. Palade, G.E., *The fine structure of mitochondria.* Anat Rec, 1952. **114**(3): p. 427-51.
59. Daems, W.T. and E. Wisse, *Shape and attachment of the cristae mitochondriales in mouse hepatic cell mitochondria.* J Ultrastruct Res, 1966. **16**(1): p. 123-40.
60. Mannella, C.A., et al., *The internal compartmentation of rat-liver mitochondria: tomographic study using the high-voltage transmission electron microscope.* Microsc Res Tech, 1994. **27**(4): p. 278-83.
61. Mannella, C.A., et al., *Topology of the mitochondrial inner membrane: dynamics and bioenergetic implications.* IUBMB Life, 2001. **52**(3-5): p. 93-100.
62. Frey, T.G. and C.A. Mannella, *The internal structure of mitochondria.* Trends Biochem Sci, 2000. **25**(7): p. 319-24.
63. Frey, T.G., C.W. Renken, and G.A. Perkins, *Insight into mitochondrial structure and function from electron tomography.* Biochim Biophys Acta, 2002. **1555**(1-3): p. 196-203.
64. Wurm, C.A. and S. Jakobs, *Differential protein distributions define two sub-compartments of the mitochondrial inner membrane in yeast.* FEBS Lett, 2006. **580**(24): p. 5628-34.
65. Reichert, A.S. and W. Neupert, *Contact sites between the outer and inner membrane of mitochondria-role in protein transport.* Biochim Biophys Acta, 2002. **1592**(1): p. 41-9.
66. Koob, S. and A.S. Reichert, *Novel intracellular functions of apolipoproteins: the ApoO protein family as constituents of the Mitofilin/MINOS complex determines cristae morphology in mitochondria.* Biol Chem, 2014. **395**(3): p. 285-96.
67. Perkins, G.A., M.H. Ellisman, and D.A. Fox, *Three-dimensional analysis of mouse rod and cone mitochondrial cristae architecture: bioenergetic and functional implications.* Mol Vis, 2003. **9**: p. 60-73.
68. Nicastro, D., et al., *Cryo-electron tomography of neurospora mitochondria.* J Struct Biol, 2000. **129**(1): p. 48-56.
69. van Meer, G., D.R. Voelker, and G.W. Feigenson, *Membrane lipids: where they are and how they behave.* Nat Rev Mol Cell Biol, 2008. **9**(2): p. 112-24.
70. Horvath, S.E. and G. Daum, *Lipids of mitochondria.* Prog Lipid Res, 2013. **52**(4): p. 590-614.
71. Zinser, E., et al., *Phospholipid synthesis and lipid composition of subcellular membranes in the unicellular eukaryote Saccharomyces cerevisiae.* J Bacteriol, 1991. **173**(6): p. 2026-34.
72. Baile, M.G., Y.W. Lu, and S.M. Claypool, *The topology and regulation of cardiolipin biosynthesis and remodeling in yeast.* Chem Phys Lipids, 2014. **179**: p. 25-31.
73. Ikon, N. and R.O. Ryan, *Cardiolipin and mitochondrial cristae organization.* Biochim Biophys Acta Biomembr, 2017. **1859**(6): p. 1156-1163.
74. Basu Ball, W., J.K. Neff, and V.M. Gohil, *The role of nonbilayer phospholipids in mitochondrial structure and function.* FEBS Lett, 2018. **592**(8): p. 1273-1290.
75. Friedman, J.R., et al., *MICOS coordinates with respiratory complexes and lipids to establish mitochondrial inner membrane architecture.* Elife, 2015. **4**.
76. Khalifat, N., et al., *Membrane deformation under local pH gradient: mimicking mitochondrial cristae dynamics.* Biophys J, 2008. **95**(10): p. 4924-33.

77. Ban, T., et al., *Molecular basis of selective mitochondrial fusion by heterotypic action between OPA1 and cardiolipin.* Nat Cell Biol, 2017. **19**(7): p. 856-863.
78. Bustillo-Zabalbeitia, I., et al., *Specific interaction with cardiolipin triggers functional activation of Dynamin-Related Protein 1.* PLoS One, 2014. **9**(7): p. e102738.
79. Francy, C.A., et al., *Cryo-EM Studies of Drp1 Reveal Cardiolipin Interactions that Activate the Helical Oligomer.* Sci Rep, 2017. **7**(1): p. 10744.
80. Gebert, N., et al., *Mitochondrial cardiolipin involved in outer-membrane protein biogenesis: implications for Barth syndrome.* Curr Biol, 2009. **19**(24): p. 2133-9.
81. Pfeiffer, K., et al., *Cardiolipin stabilizes respiratory chain supercomplexes.* J Biol Chem, 2003. **278**(52): p. 52873-80.
82. Zhang, M., E. Mileykovskaya, and W. Dowhan, *Gluing the respiratory chain together. Cardiolipin is required for supercomplex formation in the inner mitochondrial membrane.* J Biol Chem, 2002. **277**(46): p. 43553-6.
83. McKenzie, M., et al., *Mitochondrial respiratory chain supercomplexes are destabilized in Barth Syndrome patients.* J Mol Biol, 2006. **361**(3): p. 462-9.
84. Chen, H. and D.C. Chan, *Mitochondrial dynamics in mammals.* Curr Top Dev Biol, 2004. **59**: p. 119-44.
85. Tatsuta, T. and T. Langer, *Quality control of mitochondria: protection against neurodegeneration and ageing.* EMBO J, 2008. **27**(2): p. 306-14.
86. Lackner, L.L. and J.M. Nunnari, *The molecular mechanism and cellular functions of mitochondrial division.* Biochim Biophys Acta, 2009. **1792**(12): p. 1138-44.
87. Ishihara, N., et al., *Regulation of mitochondrial morphology through proteolytic cleavage of OPA1.* EMBO J, 2006. **25**(13): p. 2966-77.
88. Scott, I. and R.J. Youle, *Mitochondrial fission and fusion.* Essays Biochem, 2010. **47**: p. 85-98.
89. Ingerman, E., et al., *Dnm1 forms spirals that are structurally tailored to fit mitochondria.* J Cell Biol, 2005. **170**(7): p. 1021-7.
90. Smirnova, E., et al., *Dynamin-related protein Drp1 is required for mitochondrial division in mammalian cells.* Mol Biol Cell, 2001. **12**(8): p. 2245-56.
91. Otsuga, D., et al., *The dynamin-related GTPase, Dnm1p, controls mitochondrial morphology in yeast.* J Cell Biol, 1998. **143**(2): p. 333-49.
92. Koshiba, T., et al., *Structural basis of mitochondrial tethering by mitofusin complexes.* Science, 2004. **305**(5685): p. 858-62.
93. Cipolat, S., et al., *OPA1 requires mitofusin 1 to promote mitochondrial fusion.* Proc Natl Acad Sci U S A, 2004. **101**(45): p. 15927-32.
94. Olichon, A., et al., *Loss of OPA1 perturbates the mitochondrial inner membrane structure and integrity, leading to cytochrome c release and apoptosis.* J Biol Chem, 2003. **278**(10): p. 7743-6.
95. Duvezin-Caubet, S., et al., *Proteolytic processing of OPA1 links mitochondrial dysfunction to alterations in mitochondrial morphology.* J Biol Chem, 2006. **281**(49): p. 37972-9.
96. Wai, T. and T. Langer, *Mitochondrial Dynamics and Metabolic Regulation.* Trends Endocrinol Metab, 2016. **27**(2): p. 105-117.
97. Anand, R., et al., *The i-AAA protease YME1L and OMA1 cleave OPA1 to balance mitochondrial fusion and fission.* J Cell Biol, 2014. **204**(6): p. 919-29.
98. Frezza, C., et al., *OPA1 controls apoptotic cristae remodeling independently from mitochondrial fusion.* Cell, 2006. **126**(1): p. 177-89.
99. Cogliati, S., et al., *Mitochondrial cristae shape determines respiratory chain supercomplexes assembly and respiratory efficiency.* Cell, 2013. **155**(1): p. 160-71.
100. Jones, B.A. and W.L. Fangman, *Mitochondrial DNA maintenance in yeast requires a protein containing a region related to the GTP-binding domain of dynamin.* Genes Dev, 1992. **6**(3): p. 380-9.
101. Chipuk, J.E., L. Bouchier-Hayes, and D.R. Green, *Mitochondrial outer membrane permeabilization during apoptosis: the innocent bystander scenario.* Cell Death Differ, 2006. **13**(8): p. 1396-402.

102. Spierings, D., et al., *Connected to death: the (unexpurgated) mitochondrial pathway of apoptosis.* Science, 2005. **310**(5745): p. 66-7.
103. Bernardi, P. and G.F. Azzone, *Cytochrome c as an electron shuttle between the outer and inner mitochondrial membranes.* J Biol Chem, 1981. **256**(14): p. 7187-92.
104. Barrera, M., et al., *OPA1 functionally interacts with MIC60 but is dispensable for crista junction formation.* FEBS Lett, 2016. **590**(19): p. 3309-3322.
105. Lee, Y.J., et al., *Roles of the mammalian mitochondrial fission and fusion mediators Fis1, Drp1, and Opa1 in apoptosis.* Mol Biol Cell, 2004. **15**(11): p. 5001-11.
106. Yamaguchi, R., et al., *Opa1-mediated cristae opening is Bax/Bak and BH3 dependent, required for apoptosis, and independent of Bak oligomerization.* Mol Cell, 2008. **31**(4): p. 557-69.
107. Glytsou, C., et al., *Optic Atrophy 1 Is Epistatic to the Core MICOS Component MIC60 in Mitochondrial Cristae Shape Control.* Cell Rep, 2016. **17**(11): p. 3024-3034.
108. Yang, R.F., et al., *Mitofilin regulates cytochrome c release during apoptosis by controlling mitochondrial cristae remodeling.* Biochem Biophys Res Commun, 2012. **428**(1): p. 93-8.
109. John, G.B., et al., *The mitochondrial inner membrane protein mitofilin controls cristae morphology.* Mol Biol Cell, 2005. **16**(3): p. 1543-54.
110. Anand, R., et al., *Mic13 Is Essential for Formation of Crista Junctions in Mammalian Cells.* PLoS One, 2016. **11**(8): p. e0160258.
111. Kondadi, A.K., et al., *Cristae undergo continuous cycles of membrane remodelling in a MICOS-dependent manner.* EMBO Rep, 2020. **21**(3): p. e49776.
112. Guarani, V., et al., *QIL1 is a novel mitochondrial protein required for MICOS complex stability and cristae morphology.* Elife, 2015. **4**.
113. Gilkerson, R.W., J.M. Selker, and R.A. Capaldi, *The cristal membrane of mitochondria is the principal site of oxidative phosphorylation.* FEBS Lett, 2003. **546**(2-3): p. 355-8.
114. Perotti, M.E., W.A. Anderson, and H. Swift, *Quantitative cytochemistry of the diaminobenzidine cytochrome oxidase reaction product in mitochondria of cardiac muscle and pancreas.* J Histochem Cytochem, 1983. **31**(3): p. 351-65.
115. Davies, K.M., et al., *Macromolecular organization of ATP synthase and complex I in whole mitochondria.* Proc Natl Acad Sci U S A, 2011. **108**(34): p. 14121-6.
116. Rabl, R., et al., *Formation of cristae and crista junctions in mitochondria depends on antagonism between Fcj1 and Su e/g.* J Cell Biol, 2009. **185**(6): p. 1047-63.
117. Arnold, I., et al., *Yeast mitochondrial F1F0-ATP synthase exists as a dimer: identification of three dimer-specific subunits.* EMBO J, 1998. **17**(24): p. 7170-8.
118. Giraud, M.F., et al., *Is there a relationship between the supramolecular organization of the mitochondrial ATP synthase and the formation of cristae?* Biochim Biophys Acta, 2002. **1555**(1-3): p. 174-80.
119. Paumard, P., et al., *The ATP synthase is involved in generating mitochondrial cristae morphology.* EMBO J, 2002. **21**(3): p. 221-30.
120. Bornhovd, C., et al., *Mitochondrial membrane potential is dependent on the oligomeric state of F1F0-ATP synthase supracomplexes.* J Biol Chem, 2006. **281**(20): p. 13990-8.
121. Anand, R., et al., *MIC26 and MIC27 cooperate to regulate cardiolipin levels and the landscape of OXPHOS complexes.* Life Sci Alliance, 2020. **3**(10).
122. Hackenbrock, C.R., *Ultrastructural bases for metabolically linked mechanical activity in mitochondria. I. Reversible ultrastructural changes with change in metabolic steady state in isolated liver mitochondria.* J Cell Biol, 1966. **30**(2): p. 269-97.
123. Hackenbrock, C.R., *Ultrastructural bases for metabolically linked mechanical activity in mitochondria. II. Electron transport-linked ultrastructural transformations in mitochondria.* J Cell Biol, 1968. **37**(2): p. 345-69.
124. Yan, L., et al., *Structural analysis of a trimeric assembly of the mitochondrial dynamin-like GTPase Mgm1.* Proc Natl Acad Sci U S A, 2020. **117**(8): p. 4061-4070.

125. Amchenkova, A.A., et al., *Coupling membranes as energy-transmitting cables. I. Filamentous mitochondria in fibroblasts and mitochondrial clusters in cardiomyocytes.* J Cell Biol, 1988. **107**(2): p. 481-95.
126. Skulachev, V.P., *Mitochondrial filaments and clusters as intracellular power-transmitting cables.* Trends Biochem Sci, 2001. **26**(1): p. 23-9.
127. Wolf, D.M., et al., *Individual cristae within the same mitochondrion display different membrane potentials and are functionally independent.* EMBO J, 2019. **38**(22): p. e101056.
128. Stephan, T., et al., *Live-cell STED nanoscopy of mitochondrial cristae.* Sci Rep, 2019. **9**(1): p. 12419.
129. Stoldt, S., et al., *Mic60 exhibits a coordinated clustered distribution along and across yeast and mammalian mitochondria.* Proc Natl Acad Sci U S A, 2019. **116**(20): p. 9853-9858.
130. Perkins, G., et al., *Electron tomography of neuronal mitochondria: three-dimensional structure and organization of cristae and membrane contacts.* J Struct Biol, 1997. **119**(3): p. 260-72.
131. Kondadi, A.K., R. Anand, and A.S. Reichert, *Cristae Membrane Dynamics - A Paradigm Change.* Trends Cell Biol, 2020.
132. Vafai, S.B. and V.K. Mootha, *Mitochondrial disorders as windows into an ancient organelle.* Nature, 2012. **491**(7424): p. 374-83.
133. Bannwarth, S., et al., *A mitochondrial origin for frontotemporal dementia and amyotrophic lateral sclerosis through CHCHD10 involvement.* Brain, 2014. **137**(Pt 8): p. 2329-45.
134. Zhou, W., D. Ma, and E.K. Tan, *Mitochondrial CHCHD2 and CHCHD10: Roles in Neurological Diseases and Therapeutic Implications.* Neuroscientist, 2020. **26**(2): p. 170-184.
135. Lamant, M., et al., *ApoO, a novel apolipoprotein, is an original glycoprotein up-regulated by diabetes in human heart.* J Biol Chem, 2006. **281**(47): p. 36289-302.
136. Godiker, J., et al., *QIL1-dependent assembly of MICOS complex-lethal mutation in C19ORF70 resulting in liver disease and severe neurological retardation.* J Hum Genet, 2018. **63**(6): p. 707-716.
137. Acehan, D., et al., *Comparison of lymphoblast mitochondria from normal subjects and patients with Barth syndrome using electron microscopic tomography.* Lab Invest, 2007. **87**(1): p. 40-8.
138. Finsterer, J., *Barth syndrome: mechanisms and management.* Appl Clin Genet, 2019. **12**: p. 95-106.
139. Agarwal, P., et al., *Phosphokinome Analysis of Barth Syndrome Lymphoblasts Identify Novel Targets in the Pathophysiology of the Disease.* Int J Mol Sci, 2018. **19**(7).
140. Chatzispyrou, I.A., et al., *Barth syndrome cells display widespread remodeling of mitochondrial complexes without affecting metabolic flux distribution.* Biochim Biophys Acta Mol Basis Dis, 2018. **1864**(11): p. 3650-3658.
141. Giorgi, C., et al., *Mitochondrial calcium homeostasis as potential target for mitochondrial medicine.* Mitochondrion, 2012. **12**(1): p. 77-85.
142. Alavi, M.V. and N. Fuhrmann, *Dominant optic atrophy, OPA1, and mitochondrial quality control: understanding mitochondrial network dynamics.* Mol Neurodegener, 2013. **8**: p. 32.
143. Blackwood, D.H., et al., *Schizophrenia and affective disorders--cosegregation with a translocation at chromosome 1q42 that directly disrupts brain-expressed genes: clinical and P300 findings in a family.* Am J Hum Genet, 2001. **69**(2): p. 428-33.
144. Pinero-Martos, E., et al., *Disrupted in schizophrenia 1 (DISC1) is a constituent of the mammalian mitochondrial contact site and cristae organizing system (MICOS) complex, and is essential for oxidative phosphorylation.* Hum Mol Genet, 2016. **25**(19): p. 4157-4169.
145. von der Malsburg, K., et al., *Dual role of mitofilin in mitochondrial membrane organization and protein biogenesis.* Dev Cell, 2011. **21**(4): p. 694-707.

146. Harner, M., et al., *The mitochondrial contact site complex, a determinant of mitochondrial architecture.* EMBO J, 2011. **30**(21): p. 4356-70.
147. Hoppins, S., et al., *A mitochondrial-focused genetic interaction map reveals a scaffold-like complex required for inner membrane organization in mitochondria.* J Cell Biol, 2011. **195**(2): p. 323-40.
148. Alkhaja, A.K., et al., *MINOS1 is a conserved component of mitofilin complexes and required for mitochondrial function and cristae organization.* Mol Biol Cell, 2012. **23**(2): p. 247-57.
149. Ott, C., et al., *Sam50 functions in mitochondrial intermembrane space bridging and biogenesis of respiratory complexes.* Mol Cell Biol, 2012. **32**(6): p. 1173-88.
150. Jans, D.C., et al., *STED super-resolution microscopy reveals an array of MINOS clusters along human mitochondria.* Proc Natl Acad Sci U S A, 2013. **110**(22): p. 8936-41.
151. Pfanner, N., et al., *Uniform nomenclature for the mitochondrial contact site and cristae organizing system.* J Cell Biol, 2014. **204**(7): p. 1083-6.
152. Xie, J., et al., *The mitochondrial inner membrane protein mitofilin exists as a complex with SAM50, metaxins 1 and 2, coiled-coil-helix coiled-coil-helix domain-containing protein 3 and 6 and DnaJC11.* FEBS Lett, 2007. **581**(18): p. 3545-9.
153. van der Laan, M., et al., *Role of MINOS in mitochondrial membrane architecture and biogenesis.* Trends Cell Biol, 2012. **22**(4): p. 185-92.
154. Zerbes, R.M., et al., *Mitofilin complexes: conserved organizers of mitochondrial membrane architecture.* Biol Chem, 2012. **393**(11): p. 1247-61.
155. Munoz-Gomez, S.A., et al., *The evolution of MICOS: Ancestral and derived functions and interactions.* Commun Integr Biol, 2015. **8**(6): p. e1094593.
156. Huynen, M.A., et al., *Evolution and structural organization of the mitochondrial contact site (MICOS) complex and the mitochondrial intermembrane space bridging (MIB) complex.* Biochim Biophys Acta, 2016. **1863**(1): p. 91-101.
157. Rampelt, H., et al., *Role of the mitochondrial contact site and cristae organizing system in membrane architecture and dynamics.* Biochim Biophys Acta Mol Cell Res, 2017. **1864**(4): p. 737-746.
158. Bohnert, M., et al., *Central role of Mic10 in the mitochondrial contact site and cristae organizing system.* Cell Metab, 2015. **21**(5): p. 747-55.
159. Darshi, M., et al., *ChChd3, an inner mitochondrial membrane protein, is essential for maintaining crista integrity and mitochondrial function.* J Biol Chem, 2011. **286**(4): p. 2918-32.
160. Weber, T.A., et al., *APOOL is a cardiolipin-binding constituent of the Mitofilin/MINOS protein complex determining cristae morphology in mammalian mitochondria.* PLoS One, 2013. **8**(5): p. e63683.
161. Koob, S., et al., *The non-glycosylated isoform of MIC26 is a constituent of the mammalian MICOS complex and promotes formation of crista junctions.* Biochim Biophys Acta, 2015. **1853**(7): p. 1551-63.
162. Michaud, M., et al., *AtMic60 Is Involved in Plant Mitochondria Lipid Trafficking and Is Part of a Large Complex.* Curr Biol, 2016. **26**(5): p. 627-39.
163. Kozjak-Pavlovic, V., *The MICOS complex of human mitochondria.* Cell Tissue Res, 2017. **367**(1): p. 83-93.
164. Ott, C., et al., *Detailed analysis of the human mitochondrial contact site complex indicate a hierarchy of subunits.* PLoS One, 2015. **10**(3): p. e0120213.
165. Callegari, S., et al., *A MICOS-TIM22 Association Promotes Carrier Import into Human Mitochondria.* J Mol Biol, 2019. **431**(15): p. 2835-2851.
166. Abrams, A.J., et al., *Mutations in SLC25A46, encoding a UGO1-like protein, cause an optic atrophy spectrum disorder.* Nature Genetics, 2015. **47**(8): p. 926-+.
167. Li, H., et al., *Mic60/Mitofilin determines MICOS assembly essential for mitochondrial dynamics and mtDNA nucleoid organization.* Cell Death Differ, 2016. **23**(3): p. 380-92.
168. Zerbes, R.M., et al., *Distinct Roles of Mic12 and Mic27 in the Mitochondrial Contact Site and Cristae Organizing System.* J Mol Biol, 2016. **428**(8): p. 1485-92.

169. An, J., et al., *CHCM1/CHCHD6, novel mitochondrial protein linked to regulation of mitofilin and mitochondrial cristae morphology.* J Biol Chem, 2012. **287**(10): p. 7411-26.
170. Hessenberger, M., et al., *Regulated membrane remodeling by Mic60 controls formation of mitochondrial crista junctions.* Nat Commun, 2017. **8**: p. 15258.
171. Sakowska, P., et al., *The Oxidation Status of Mic19 Regulates MICOS Assembly.* Mol Cell Biol, 2015. **35**(24): p. 4222-37.
172. Barbot, M., et al., *Mic10 oligomerizes to bend mitochondrial inner membranes at cristae junctions.* Cell Metab, 2015. **21**(5): p. 756-63.
173. Nijstad, N., et al., *Overexpression of apolipoprotein O does not impact on plasma HDL levels or functionality in human apolipoprotein A-I transgenic mice.* Biochim Biophys Acta, 2011. **1811**(4): p. 294-9.
174. Guarani, V., et al., *QIL1 mutation causes MICOS disassembly and early onset fatal mitochondrial encephalopathy with liver disease.* Elife, 2016. **5**.
175. Valente, E.M., et al., *Hereditary early-onset Parkinson's disease caused by mutations in PINK1.* Science, 2004. **304**(5674): p. 1158-60.
176. Tsai, P.I., et al., *PINK1 Phosphorylates MIC60/Mitofilin to Control Structural Plasticity of Mitochondrial Crista Junctions.* Mol Cell, 2018. **69**(5): p. 744-756 e6.
177. Genin, E.C., et al., *CHCHD10 mutations promote loss of mitochondrial cristae junctions with impaired mitochondrial genome maintenance and inhibition of apoptosis.* EMBO Mol Med, 2016. **8**(1): p. 58-72.
178. Chaussenot, A., et al., *Screening of CHCHD10 in a French cohort confirms the involvement of this gene in frontotemporal dementia with amyotrophic lateral sclerosis patients.* Neurobiology of Aging, 2014. **35**(12).
179. Ronchi, D., et al., *CHCHD10 mutations in Italian patients with sporadic amyotrophic lateral sclerosis.* Brain, 2015. **138**: p. E372-U11.
180. Beninca, C., et al., *Mutation in the MICOS subunit gene APOO (MIC26) associated with an X-linked recessive mitochondrial myopathy, lactic acidosis, cognitive impairment and autistic features.* J Med Genet, 2020.
181. Zeharia, A., et al., *Mitochondrial hepato-encephalopathy due to deficiency of QIL1/MIC13 (C19orf70), a MICOS complex subunit.* Eur J Hum Genet, 2016. **24**(12): p. 1778-1782.
182. Russell, B.E., et al., *Expanding and Underscoring the Hepato-Encephalopathic Phenotype of QIL1/MIC13.* Hepatology, 2019. **70**(3): p. 1066-1070.
183. Kishita, Y., et al., *A novel homozygous variant in MICOS13/QIL1 causes hepato-encephalopathy with mitochondrial DNA depletion syndrome.* Mol Genet Genomic Med, 2020: p. e1427.
184. Meurs, K.M., et al., *A QIL1 Variant Associated with Ventricular Arrhythmias and Sudden Cardiac Death in the Juvenile Rhodesian Ridgeback Dog.* Genes (Basel), 2019. **10**(2).
185. Janji, B., et al., *Phosphorylation on Ser5 increases the F-actin-binding activity of L-plastin and promotes its targeting to sites of actin assembly in cells.* J Cell Sci, 2006. **119**(Pt 9): p. 1947-60.
186. Delanote, V., J. Vandekerckhove, and J. Gettemans, *Plastins: versatile modulators of actin organization in (patho)physiological cellular processes.* Acta Pharmacol Sin, 2005. **26**(7): p. 769-79.
187. Wabnitz, G.H., et al., *Costimulation induced phosphorylation of L-plastin facilitates surface transport of the T cell activation molecules CD69 and CD25.* Eur J Immunol, 2007. **37**(3): p. 649-62.
188. Strange, R.C., et al., *Glutathione-S-transferase family of enzymes.* Mutat Res, 2001. **482**(1-2): p. 21-6.
189. Bernardini, S., et al., *Glutathione S-transferase P1 *C allelic variant increases susceptibility for late-onset Alzheimer disease: association study and relationship with apolipoprotein E epsilon4 allele.* Clin Chem, 2005. **51**(6): p. 944-51.

190. Pinhel, M.A., et al., *Glutathione S-transferase variants increase susceptibility for late-onset Alzheimer's disease: association study and relationship with apolipoprotein E epsilon4 allele.* Clin Chem Lab Med, 2008. **46**(4): p. 439-45.
191. Hanukoglu, I., *Steroidogenic enzymes: structure, function, and role in regulation of steroid hormone biosynthesis.* J Steroid Biochem Mol Biol, 1992. **43**(8): p. 779-804.
192. Lambeth, J.D. and D.R. Mccaslin, *Adrenodoxin Adrenodoxin Reductase Complex - Catalytic Properties and Titration with Nadh and Dithionite.* Federation Proceedings, 1976. **35**(7): p. 1599-1599.
193. Paul, A., et al., *FDXR Mutations Cause Sensorial Neuropathies and Expand the Spectrum of Mitochondrial Fe-S-Synthesis Diseases.* Am J Hum Genet, 2017. **101**(4): p. 630-637.
194. Perocchi, F., et al., *MICU1 encodes a mitochondrial EF hand protein required for Ca(2+) uptake.* Nature, 2010. **467**(7313): p. 291-6.
195. Mallinder, P.R., A. Pritchard, and A. Moir, *Cloning and Characterization of a Gene from Bacillus-Stearothermophilus Var Non-Diastaticus Encoding a Glycerol Dehydrogenase.* Gene, 1992. **110**(1): p. 9-16.
196. Urbach, J., et al., *Conserved residues of the MICOS subunit MIC13 are important for its function to bridge MICOS subcomplexes.* unpublished.
197. Brenig, K., et al., *The Proteomic Landscape of Cysteine Oxidation That Underpins Retinoic Acid-Induced Neuronal Differentiation.* J Proteome Res, 2020. **19**(5): p. 1923-1940.
198. Teese, M.G. and D. Langosch, *Role of GxxxG Motifs in Transmembrane Domain Interactions.* Biochemistry, 2015. **54**(33): p. 5125-35.
199. Baloyannis, S.J., *Mitochondrial alterations in Alzheimer's disease.* Journal of Alzheimers Disease, 2006. **9**(2): p. 119-126.
200. Ansell, R., et al., *The two isoenzymes for yeast NAD+-dependent glycerol 3-phosphate dehydrogenase encoded by GPD1 and GPD2 have distinct roles in osmoadaptation and redox regulation.* EMBO J, 1997. **16**(9): p. 2179-87.
201. Matesanz-Isabel, J., et al., *Functional roles of MICU1 and MICU2 in mitochondrial Ca(2+) uptake.* Biochim Biophys Acta, 2016. **1858**(6): p. 1110-7.
202. Yagensky, O., et al., *Increased expression of heme-binding protein 1 early in Alzheimer's disease is linked to neurotoxicity.* Elife, 2019. **8**.

7. Publications

Anand, R., Strecker, V., Urbach, J., Wittig, I., and Reichert, A.S. (2016). Mic13 Is Essential for Formation of Crista Junctions in Mammalian Cells. PLoS One *11*, e0160258.

Contribution of Jennifer Urbach to the manuscript:
Investigation, methodology and visualization of Figure 5C and 5D.

Kondadi, A.K., Anand, R., Hansch, S., Urbach, J., Zobel, T., Wolf, D.M., Segawa, M., Liesa, M., Shirihai, O.S., Weidtkamp-Peters, S.*, et al.* (2020). Cristae undergo continuous cycles of membrane remodelling in a MICOS-dependent manner. EMBO Rep *21*, e49776.

Contribution of Jennifer Urbach to the manuscript:
Investigation, visualization and methology of all co-immunoprecipitation and blue native PAGE experiments.
Preparation of HeLa *MIC13* KO cells. Data analysis and statistic for Figure EV1B.
Preparation of first version of figure EV2.

Urbach, J., Kondadi, A.K., David, C., Deinert, K., Reichert, A.S., Anand, R. (2020). Conserved protein residues of MICOS component MIC13 are important for its bridging function. Unpublished.

Conceptualization, writing of the original draft, finalization with help of R. Anand.
Visualization, except STED nanoscopy (figure 3). Methodology and investigation of all experiments except for EM pictures, STED nanoscopy, Co-IP in Figure 4C of decoration with MIC10, western blot and Co-IP in Figure 6B, 6C and S2B. Data analysis and statistical analysis.

Further contribution to thesis manuscript:

Proteomics measurement and data analysis was performed at the Molecular Proteomics Laboratory (MPL) from the BMFZ by Gereon Poschmann, AG Stühler, Institute of Molecular Medicine I, Heinrich Heine University, Düsseldorf.

8. Acknowledgements

During my time as a Ph.D. student, many people contributed and helped me with my project in different ways. First of all, I want to thank Prof. Dr. Andreas Reichert for being a very kind, patient, supportive, and understanding supervisor. He created a very nice working environment and cared about us and our work.

Second, I want to thank my mentor Prof. Dr. Lutz Schmitt for his support in our annual meetings.

A big thank you to Dr. Ruchika Anand, who was my direct supervisor and always helped out with ideas and often believed more in my data than I did. She gave me the confidence to trust my work.

Thanks go to Dr. Marcel Zimmermann and Dr. Arun Kondadi for their scientific support in many different ways and also for making the lab a little bit more fun.

Many thanks go to Dr. Leonie Drews, my fellow Ph.D. student and friend, who helped me survive the hard times when all was lost. Even if I am not going to publish in nature, we had the best time together and everything will be alright (so say we all). Also, many thanks for helping me by correcting my thesis and the very confused first outline of this work.

Also, a huge thanks to the whole Institute of Biochemistry and Molecular Biology I, including the groups of Prof. Dr. Wilhelm Stahl and Prof. Dr. Peter Brenneisenfor many scientific discussions, workshops, as well as all the fun we had at the Christmas party, birthday parties, barbeques, and other occasions.

Special thanks go to the technicians Andrea Borchardt, Tanja Protugall, and Gisela Pansegrau for their continuous help and support and their excellent technical assistance in many experiments. Especially a big thanks to Andrea, who helped me a lot in cell culture and did the EM experiments for my work.

Thanks to Laura Bierwald for being the world's best secretary. You were always there for us when we had paperwork and without you, this whole institute would not be able to work properly.

Also, thanks to Kim Deinert, my bachelor student, and Céline David, another bachelor student at our institute, who contributed directly to this work.

Thanks to my former fellow students Laura Bergmann and Oliver Reiners, also known as the Lunch Club, for sharing the same fate of a Ph.D. student. And a veeeeery big thank you to Dr. Lindolf Goli for the excellent help by correcting my first confused draft of this thesis and making me understand how to express my ideas properly.

Vielen Dank auch an meine Eltern, die mir die Möglichkeit gegeben haben zu Studieren und mich stets emotional und finanziell unterstützt haben. Außerdem danke ich meinem Freund Daniel und all meinen engsten Freunden, insbesondere Steffie und Thobi. Ihr alle durftet euch

mein Gejammer lang genug anhören und habt euch niemals darüber beschwert, sondern wart immer sehr verständnisvoll und unterstützend. Das Leben ohne so großartige Freunde ist möglich, aber nicht sinnvoll. Zuletzt, wenn es die Kleinsten unter uns schaffen, die größten und schwierigsten Taten zu vollbringen, dann sollte eine Doktorarbeit nicht viel schwieriger sein, als ein Spaziergang nach Mordor.

Eidesstattliche Erklärung

Ich versichere an Eides Statt, dass die vorliegende Dissertation von mir selbständig und ohne unzulässige fremde Hilfe unter Beachtung der Grundsätze zur Sicherung guter wissenschaftlicher Praxis an der Heinrich-Heine-Universität Düsseldorf erstellt worden ist. Die aus fremden Quellen übernommenen Gedanken sind als solche kenntlich gemacht. Die Dissertation wurde in der vorgelegten oder in ähnlicher Form noch bei keiner anderen Institution eingereicht. Ich habe bisher keine erfolglosen Promotionsversuche unternommen.

Düsseldorf, den Jennifer Urbach